

Sulphur-Rich Molecular Magnetic Materials



**A thesis submitted for the degree of Doctor of
Philosophy**

by

Sarah S Staniland

**School of Chemistry
Faculty of Science and Engineering
University of Edinburgh
April 2005**



Declaration

Since graduating from the University of Edinburgh in 2001 with a Mchem. (Hons) degree in chemistry, the author has been engaged in a programme of full-time research under the supervision of Dr. Neil Robertson and Prof. Andrew Harrison at the University of Edinburgh.

No part of the work referred to in this thesis has been submitted in support of an application for another degree or qualification and all the work herein, unless otherwise specifically stated is the original work of the author.

Sarah S. Staniland.

Abstract

Cooperative magnetic effects exist in molecular materials as well as infinite lattice solids. Magnetic interactions occur within the individual molecules as well as being conveyed through intermolecular short contacts between magnetic molecules.

Magnetism in molecular materials has enjoyed increasing interest over the last 40 years as greater understanding of the mechanisms at work within these systems has developed. With this understanding came the pioneering synthesis of novel materials such as organic ferromagnets and superconductors.

Magnetic exchange through molecular inorganic materials relies on a mechanism called superexchange where magnetic cooperation is translated between magnetic centres via intermediate ligands. An examination of molecular magnetic materials indicates that materials that are rich in sulphur generally have a greater magnetic coupling than similar non-sulphurous materials. This is attributed to the fact that sulphur has large diffuse orbitals that can facilitate a good magnetic overlap.

The work within this thesis is concerned with several different magnetic systems all involving materials that are rich in sulphur and are thus predicted to have strong magnetic coupling through these sulphur atoms.

Firstly, a range of molecular salt materials of $[\text{dithiazolyl}]_x[\text{M}(\text{dithiolene})_2]$ were synthesised and their magnetic behaviour analysed. Dithiolene complex salts of $[\text{BDTA}]^+$ (benzo-1,3,2-dithiazolyl) [2]-[6] were found to have a mainly mixed anion-cation stacked structural motif and show a number of interesting magnetic properties, such as an almost perfect one-dimensional antiferromagnetic chain system

[BDTA]₂[Cu(mnt)₂] [2] (mnt = maleonitriledithiolate), as well as the conducting charge transfer salt [BDTA][Ni(dmit)₂]₂ [3] (dmit = 1,3-dithiol-2-thione-4,5-dithiolate) that is the first example of the [BDTA]⁺ cation behaving as an open shell conductor. The [BDTA]₂[Fe(tdas)₂Cl] (tdas = 1,2,5-thiazole-3,4-dithiol) salt [5] has the first mixed stacking structural motif of this anion (as it usually dimerises) and this material was found to be paramagnetic.

The paramagnetic radical dithiazolyl cation [BBDTA]^{•+} (benzo-bis-1,3,2-dithiazolyl) was also co-precipitated with dithiolene complexes to create magnetic salts [11]-[15]. These all showed mixed magnetic effects with some unusual magnetic interactions occurring.

[BDTA]⁺ was also co-crystallised with MCl₄²⁻ anions to form molecular materials containing a two-dimensional magnetic structure with a square lattice magnetic pathway. This magnetic mechanism provides ideal materials for the study of ground state quantum magnetic effects that are thought to relate to the fundamental mechanism of superconductivity.

This work also contains the study of the non interacting magnetic molecular thiophosphine complexes of the form [M((SPR^{1,2})₂N)₂] (M = Mn, Co, Ni, R¹ = R² = Ph, ⁱPr and R¹=Ph & R²=ⁱPr) which behave as simple paramagnets ([16]-[24]). All M = Mn and Co complexes were found to be simple paramagnetic materials with a strong ligand field splitting. However, the magnetic study of the M = Ni materials, along with structural and spectroscopic analysis, show a large amount of spin density on the ligands due to their non-innocent nature. This unusual electronic behaviour could explain the previously unpredicted tetrahedral geometries of these complexes.

Acknowledgements

Like actors receiving an Oscar; I am grateful to a large number of people for their help and encouragement and want to thank them all for everything. However, just as with Oscar speeches, this can be lengthy and tedious for all concerned. I will thus try to be concise and so if I miss someone out, sorry.

Firstly, of course, I must thank my supervisors Dr. Neil Robertson and Prof. Andrew Harrison for everything they have done for me and this thesis. For the constructive and educational conversations, ideas, encouragement and honesty, as well as the little things, like teaching me the benefits of proof reading. I would also like to thank my group, i.e. Elaine, as well as the Tasker group for their support, help, general chat and merriment that made the time in lab N2.17 so enjoyable, especially Jenny for all the cakes and Mexican adventures, and Dave Henderson for all his chemical knowledge and experience.

I must also say a big thank you to all the people who trained me to use instruments and have performed measurements, calculations, refined structures, and synthesised products, all of which contributed to this work. So thank you to Dr. Simon Parsons and his crystallographic group, thanks to Konstantin Kamenev and Fiona Coomer for SQUID room fun, help and advice, as well as Nic Meller for diffractometer training. Thanks to Dr. Philip Camp for help with the fitting of low temperature magnetic data, Paul Murray for EPR expertise and Mark De Vries for help refining X-ray data.

This Thesis is made up of several collaborations. One such collaboration was with the group of Prof. Kunio Awaga, and it is individuals within this group I am

especially grateful to, for academic help as well as friendship. I would therefore like to thank Prof. Kunio Awaga, Sayuri Handa, Watura Fujita, Yoshikatsu Umezono, Kenta Hayashida and everyone else in Kunio's group for making me most welcome on the other side of the world. I would also like to thank all those from the University of Athens involved in the collaboration that has brought about the work in Chapter 6, namely Dr. Panyotis Kyritsis and Dimitrios Maganas. Last of our collaborators, I would like to thank Dr. Stewart Clarke for all the DFT calculation he performed for Chapter 3.

Lastly, I would like to thank all those who have been so personally supportive throughout this venture. All those people who have listened to my chat about this work but have little idea what I'm talking about; I thank you for your patience. Thanks to my parents and siblings for humouring my rubbish explanations as to what it is I actually do, as well being proud of my achievements. Thanks to the technical staff in the chemistry department for a very enjoyable and paid last few months that has been a godsend for writing up. Lastly, and most of all, I'd like to thank my husband Luke who has tried to, and pretended to, understand to my chemistry ramblings as well as proof reading this thesis. For all his day to day support, love, encouragement and much much more I am eternally grateful.

Contents

Declaration.....	i
Abstract.....	ii
Acknowledgements.....	iv
Contents.....	vi
Abbreviations.....	xi
Structures of abbreviated chemical.....	xiv
Table of products.....	xvi

Chapter 1. Introduction..... 1

1.1 Introduction.....	2
1.2 Magnetism tutorial.....	3
1.2.1 Atomic magnetism.....	3
1.2.2 Spin-orbit coupling.....	5
1.2.3 The Curie Law.....	7
1.2.4 Curie-Weiss Law.....	8
1.2.5 Mechanism of coupling in magnetic systems.....	11
1.3 Examples of magnetic materials.....	18
1.3.1 Metallic centred magnetic materials (1D-3D lattices).....	18
1.3.2 Charge transfer salts.....	26
1.3.3 Organic magnetic materials.....	29
1.4 Conclusions & aims.....	32
1.5 References.....	34

Chapter 2. Experimental methods..... 35

2.1 Introduction.....	36
2.2 Analysis methods of electronic properties.....	36

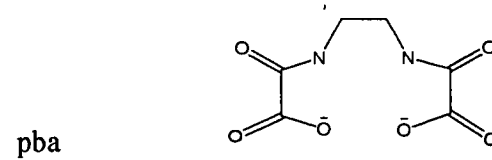
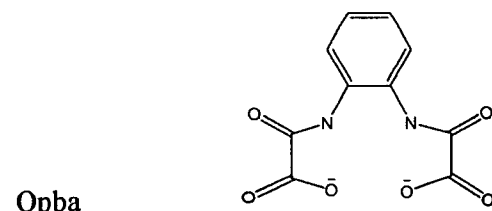
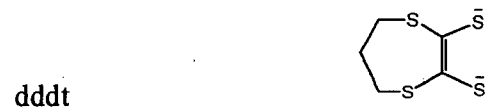
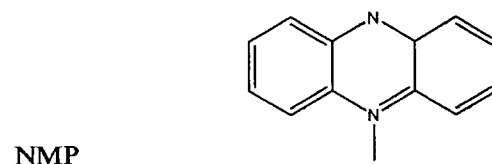
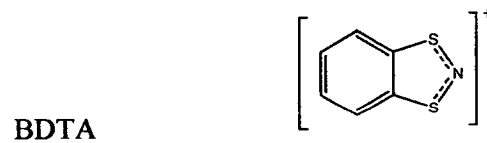
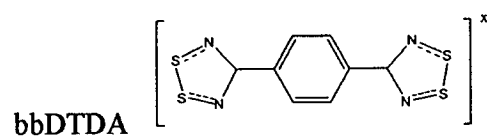
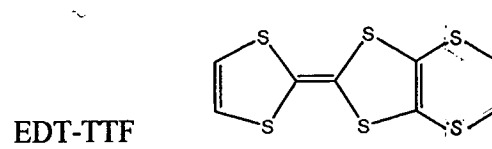
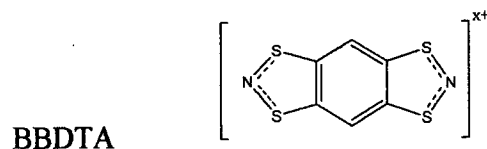
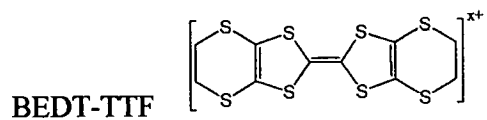
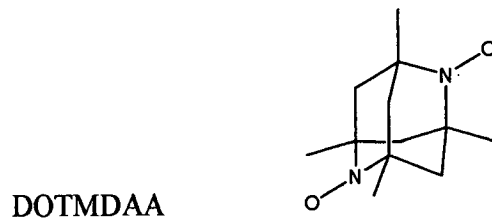
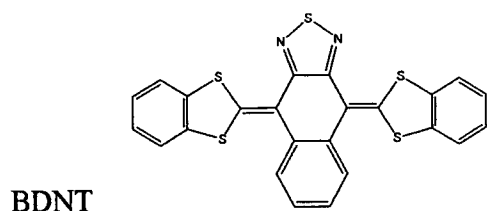
2.2.1	Magnetic analysis using a SQUID magnetometer.....	36
2.2.2	Analysis using a PPMS.....	37
2.2.3	EPR Spectroscopy.....	38
2.2.4	Conductivity measurements.....	40
2.2.5	DFT plane wave calculations.....	41
2.2.5.1	Computational chemistry.....	41
2.2.5.2	Hartree-Fock <i>ab initio</i> calculations.....	42
2.2.5.3	Density functional theory plane wave calculations.....	44
2.3	Structural refinement from X-ray diffraction.....	46
2.3.1	Single crystal X-ray diffraction.....	47
2.3.2	X-ray powder diffraction.....	48
2.4	References.....	50
 Chapter 3. Complexes of [BDTA]_x[M(dithiolenes)₂]		51
3.1	Introduction.....	52
3.1.1	Dithiolenes.....	52
3.1.1.1	[M(dmit) ₂] ^{x-}	54
3.1.1.2	[M(tdas) ₂] ^{x-}	56
3.1.1.3	[M(mnt) ₂] ^{x-}	59
3.1.2	Dithiazolyls.....	63
3.1.2.1	Schematics and reactivity of dithiazolyl cations.....	65
3.2	Results and discussion of [BDTA]₂[M(dithiolenes)₂]	68
3.2.1	[BDTA] ₂ [Cu(mnt) ₂] [2]	68
3.2.1.1	Preparation.....	68
3.2.1.2	Crystal structure.....	69
3.2.1.3	Magnetic and EPR studies.....	70
3.2.1.4	Magnetic susceptibility.....	72
3.2.1.5	DFT calculations.....	77
3.2.1.6	Conclusion.....	79
3.2.2	[BDTA] ₂ [Ni(dmit) ₂] ₂ [3].....	80

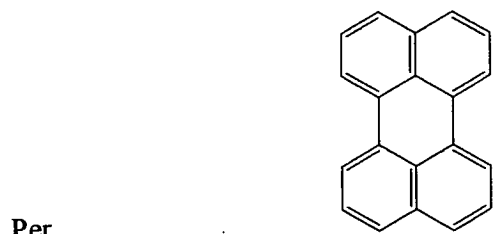
3.2.2.1	Preparation and X-ray structure.....	80
3.2.2.2	Conductivity.....	83
3.2.2.3	Magnetic susceptibility.....	86
3.2.2.4	Conclusion.....	89
3.2.3	[TBA] ₄ [Pd ₈ (dmit) ₁₀] [4].....	89
3.2.3.1	Preparation and X-ray crystal structure.....	89
3.2.4	[BDTA] ₂ [Fe(tdac) ₂ Cl] [5].....	91
3.2.4.1	Preparation and X-ray crystal structure.....	91
3.2.4.2	Magnetic susceptibility.....	94
3.2.5	[BDTA] ₂ [Ni(tdac) ₂] [6].....	96
3.2.5.1	Preparation and X-ray structure.....	96
3.3	Summary and conclusion	97
3.4	Experimental	101
3.4.1	Preparation of [BDTA] ₂ [M(dithiolene) ₂] [1]-[6].....	101
3.4.2	Analysis and structure.....	102
3.5	References	106
 Chapter 4. Complexes of [BDTA]₂[MCl₄]		109
4.1	Introduction	110
4.2	Results and discussion of [BDTA]₂[MCl₄] (M = Cu [7], Co [8] & Mn [9])	114
4.2.1	Preparation and X-ray structure.....	114
4.2.2	Magnetic analysis.....	122
4.3	Conclusion	136
4.4	Experimental	137
4.4.1	Preparation of [BDTA] ₂ [MCl ₄].....	137
4.4.2	Analysis and structure.....	138
4.5	References	140

Chapter 5. Complexes of [BBDTA]_x[M(dithiolene)₂]	141
5.1 Introduction	142
5.2 Results and discussion of [BBDTA]_x[M(dithiolene)₂]	142
5.2.1 Preparation and X-ray analysis	143
5.2.2 Magnetic and EPR studies	148
5.2.2.1 EPR analysis	148
5.2.2.2 Magnetic susceptibility	149
5.3 Conclusion	156
5.4 Experimental	157
5.4.1 Preparation of [BBDTA]_x[M(dithiolene)₂] [11]-[15]	157
5.4.2 Analysis	158
5.5 References	161
Chapter 6. Thiophosphine complexes	162
6.1 Introduction	163
6.2 Results and discussion	166
6.2.1 Literature crystal structures of [M((SPR₂)₂N)₂] [16], [19], [20], [22] & [23] and the structural determination for [17], [18], [21] & [24]	167
6.2.1.1 Crystal structure of [Mn((SP(ⁱPr)₂)₂N)₂] [17]	169
6.2.1.2 Crystal structure of [Mn(SP(Ph)₂)(SP(ⁱPr)₂)N)₂] [18]	170
6.2.1.3 Crystal structure of [Co(SP(Ph)₂)(SP(ⁱPr)₂)N)₂] [21]	171
6.2.1.4 Crystal structure of [Ni(SP(Ph)₂)(SP(ⁱPr)₂)N)₂] [24]	172
6.2.2 Magnetic, EPR and spectroscopic analysis	173
6.2.2.1 Analysis of Co²⁺ and Mn²⁺ complexes [16]-[21]	174
6.2.2.2 Analysis of Ni²⁺ complexes [22]-[24]	179
6.2.2.3 Orientated crystal magnetic analysis	183
6.2.2.4 Structural analysis of Ni compounds	190
6.3 Conclusion	194

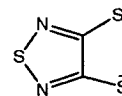
6.4	Experimental	197
6.5	References	198
Chapter 7.	[M(C_nH_{2n}(C₃S₅))₂] materials	199
7.1	Introduction	200
	7.1.1 Low dimensional magnetic materials and spin ladders.....	200
	7.1.2 New molecular approach using modified dithiolene ligands.....	203
7.2	Results and discussion	206
	7.2.1 Preparation and structure of ligands (C _n H _{2n} (C ₃ S ₅) ₂) ²⁻ [25]-[28].....	206
	7.2.2 Preparation and structure of [M(C _n H _{2n} (C ₃ S ₅) ₂)] [29]-[32].....	209
	7.2.3 Magnetic and EPR analysis.....	211
7.3	Conclusion	215
7.4	Experimental	216
7.5	References	223
Chapter 8.	Appendices	224
	Appendices on CD	
	Chapter 3, CIF files for products [1]-[6]	
	Chapter 4, CIF files for products [7]-[9]	
	X-ray powder diffraction data for products [7]-[10]	
	Chapter 5, X-ray powder diffraction data for products [11]-[13]	
	Chapter 6, CIF files for products [17], [18], [21] and [24]	
	CIF files of other literature cobalt and nickel thiophosphines	
	Excel spread sheet of bond length comparisons	
	Computer program to model distorted nickel system	
List of Publications		225

Structures of abbreviated chemicals



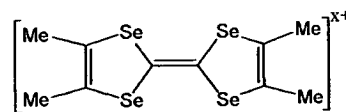


tdas

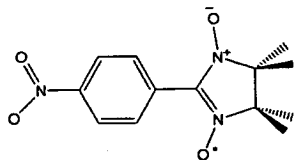


Per

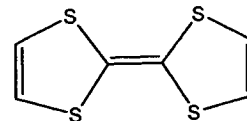
TMTSF



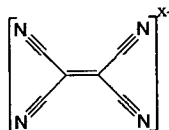
p-NPNN



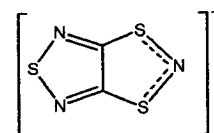
TTF



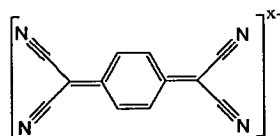
TCNE



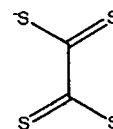
TTTA



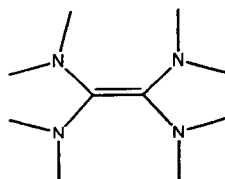
TCNQ



tto



TDAE



Abbreviations

Chemicals, ligands and solvents

Also see page xiv for structures of compounds

BDNT	4,9-bis(1,3-benzodithiol-2-ylidene)-4,9-dihydronaphtho[2,3-c][1,2,5]thiadiazole
BEDT-TTF	bisethylenedithiolenetetrathiafulvalene
BBDTA	benzo-bis-1,3,2-dithiazolyl
bbDTDA	1,4-phenylene-bis(dithiadithiazolyl)
BDTA	benzo-1,3,2-dithiazolyl
bipy	bipyridine
DCM	dichloromethane
ddd	5,6-dihydro-1,4-dithiin-2,3-dithiolate
DMF	dimethylformamide
dmid	2-oxo-1,3-dithiol-2-thione-4,5-dithiolate
dmit	1,3-dithiol-2-thione-4,5-dithiolate
DMSO	dimethyl sulfoxide
DOTMDAA	dupeyredioxyl (1,3,5,7-tetramethyl-2,6-diazaadamantane-N,N'-dioxyl)
dto.	dithiooxalate
EDT-TTF	ethylenedithiolenetetrathiafulvalene
EtOH	ethanol
Etpy ⁺	ethylpyridinium
IPA	isopropyl alcohol
IPE	isopropyl ether
mnt	maleonitriledithiolate
MeCN	acetonitrile
MeOH	methanol
NIT-R	R-substituted-nitronylnitroxide
NMP	bis(N-methylphenazinium)
OM-TTF	octamethyl-tetrathiafulvalene
Opba	<i>o</i> -phenylenebis(oxamate)
ox	oxalate
pba	1,3-propylene-bis(oxamate)

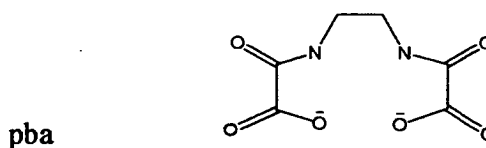
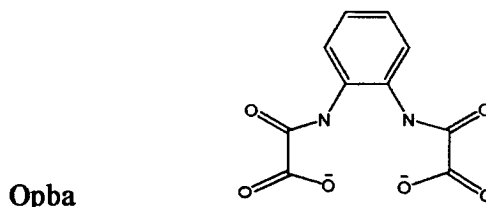
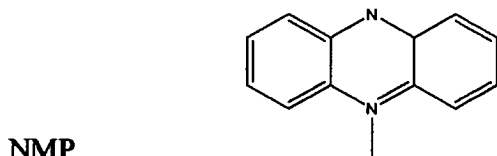
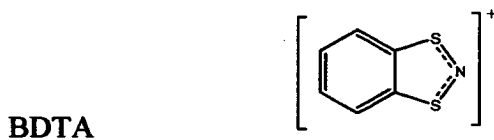
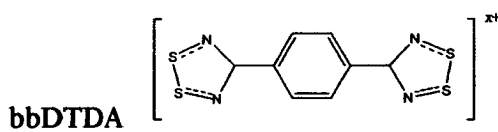
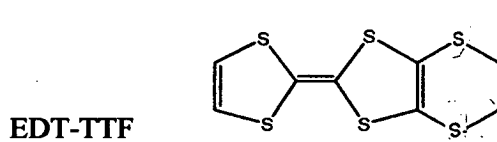
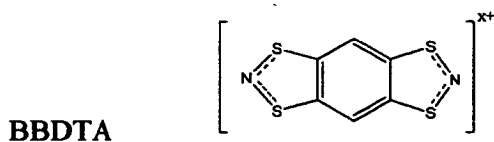
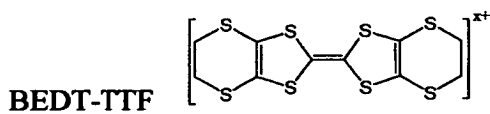
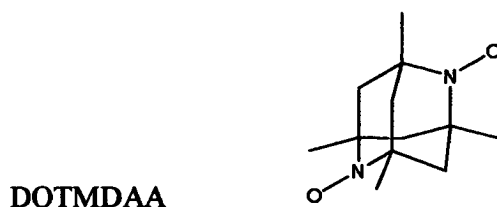
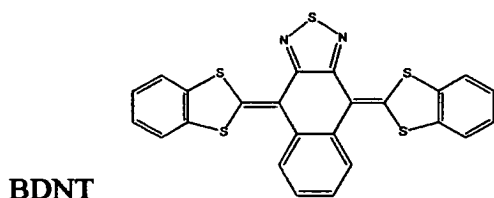
<i>p</i> -EPYNN	<i>p</i> -ethylpyridinium-nitronyl nitroxide
Per	perylene
<i>p</i> -NPNN	<i>p</i> -nitrophenyl nitronyl nitroxide
TBA	tetrabutylammonium
TCNE	tetracyanoethylene
TCNQ	7,7,8,8-tetracyanoquinodimethane
TDAE	tetrakis(dimethylamino)ethylene
tdas	1,2,5- thiadiazole-3,4-dithiol
TBA	tetrabutylammonium
TEA	tetraethylammonium
THF	tetrahydrofuran
TMA	tetramethylammonium
TPMTPP	triphenylmethyltriphenylphosphonium
TMTSF	tetramethyltetraselenafulvalene
TTF	tetrathiafulvalene
TTTA	1,3,5-trithia-2,4,6-trizapentalenyl
tto	tetrathiooxalate

Other abbreviations

CHN	carbon, hydrogen and nitrogen analyses
cm ⁻¹	wavenumbers
E _a	activation energy
emu	empirical mass units
EPR	electron paramagnetic resonance
eV	electron volt
g	g-value
HOMO	highest occupied molecular orbital
ICP-AES	induced coupled plasma atomic emission spectroscopy
IR	infra-red
J	magnetic coupling constant
k	Boltzmann constant
k	orbital reduction factor
K	Kelvin
L	orbital angular momentum

LUMO	lowest unoccupied molecular orbital
N	Avagadro's number
NMR	nuclear magnetic resonance
PPMS	physical properties measurements system
S cm ⁻¹	Siemens wavenumber
S	spin
SQUID	superconductive quantum interference device
T	temperature
T _c	Curie temperature (ordering temperature)
UV-vis	ultra-violet- visible
Å	Angstroms
β	Bohr magneton
σ	conductivity
σ _{RT}	room temperature conductivity
μ	magnetic moment
μ _{eff}	effective magnetic moment
χ	magnetic susceptibility
χ _{mol}	molar magnetic susceptibility
λ	spin-orbit coupling constant

Structures of abbreviated chemicals



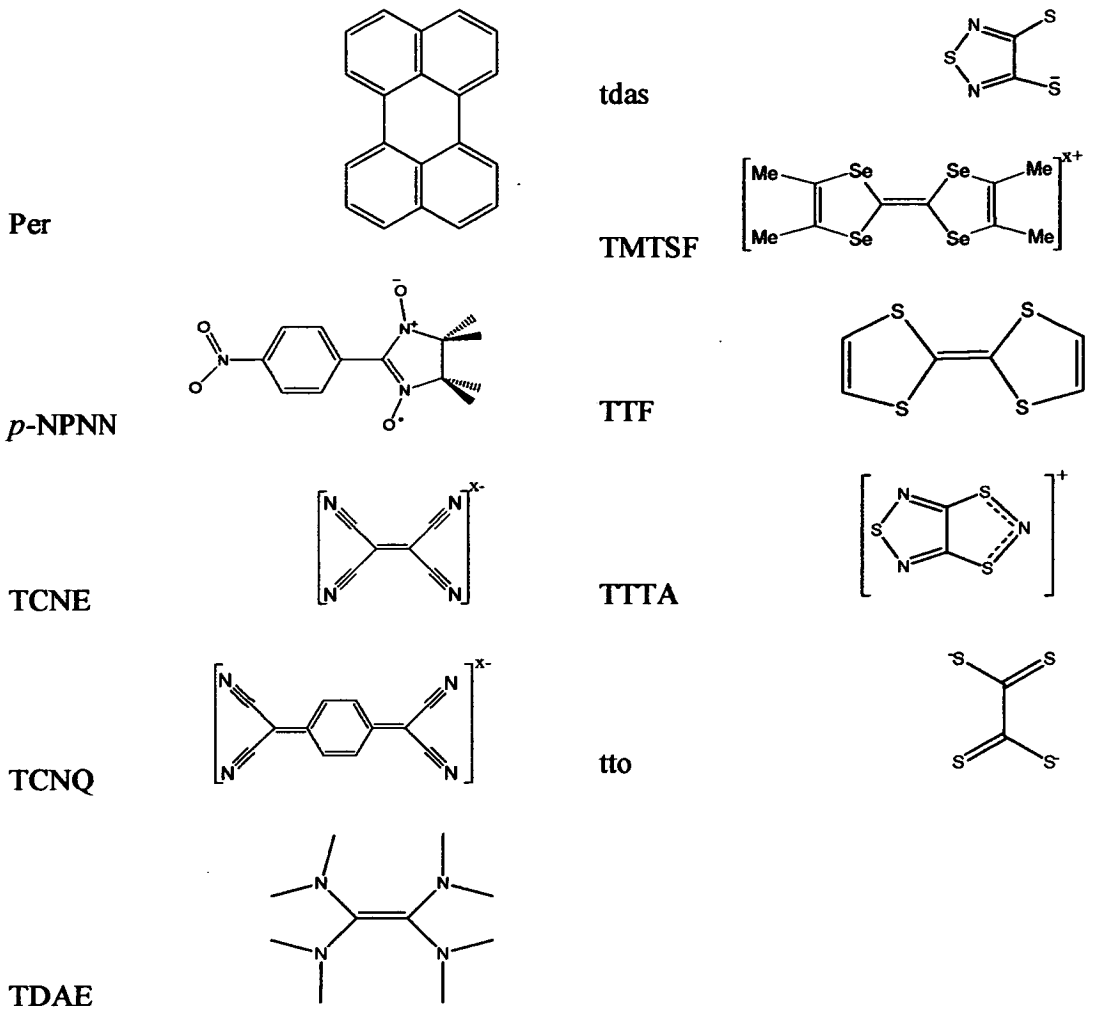
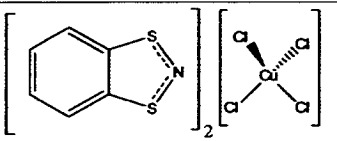
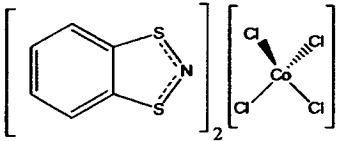
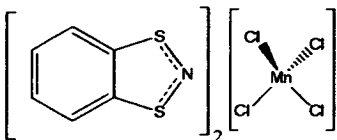
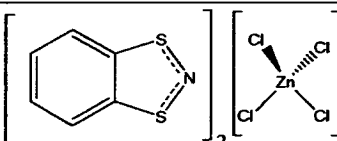
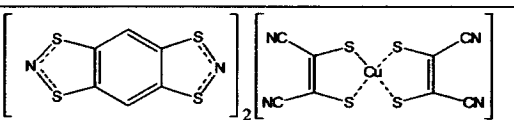
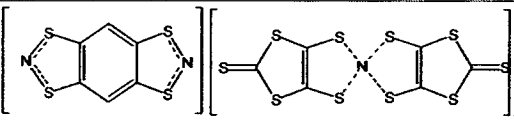
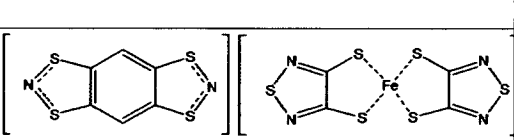
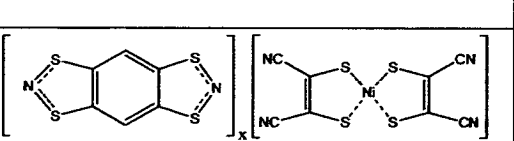
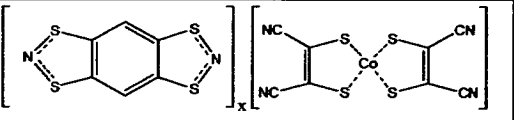
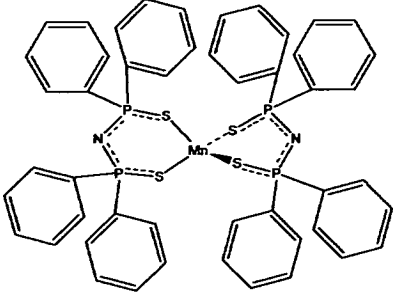
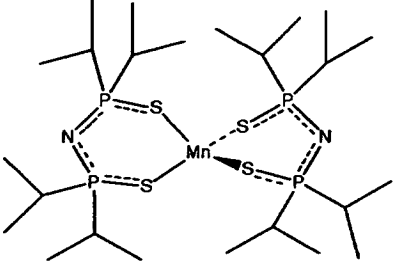
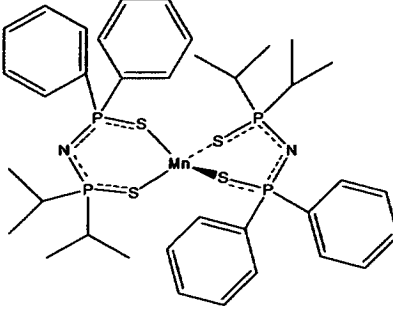
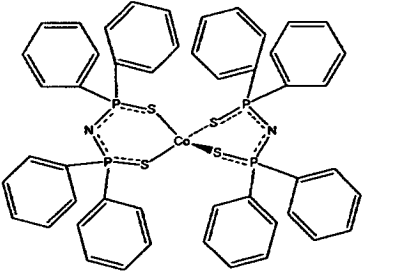
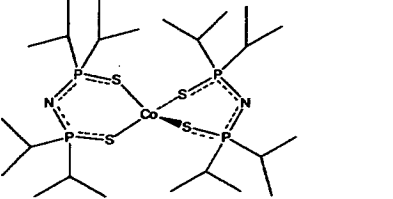


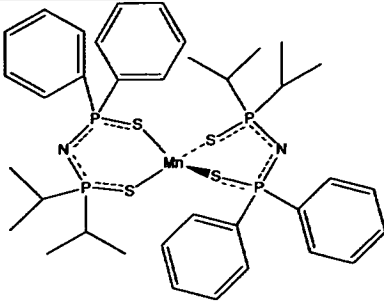
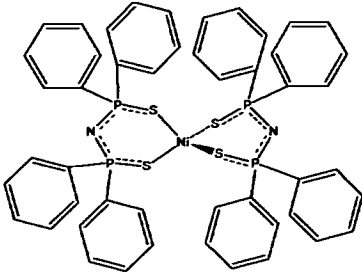
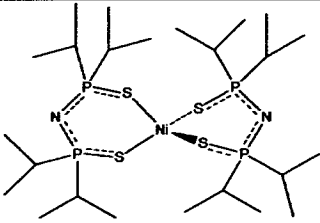
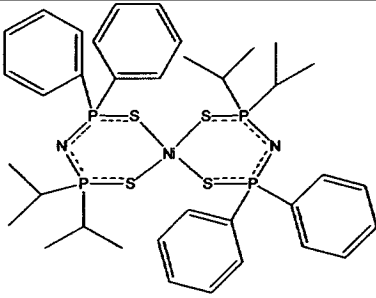
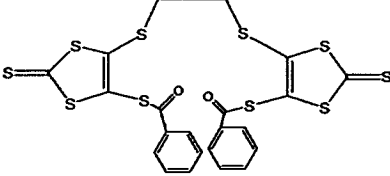
Table of Products

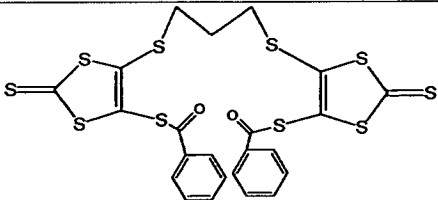
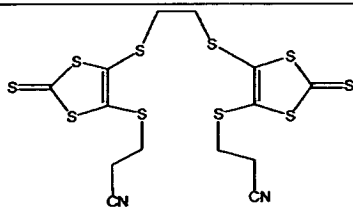
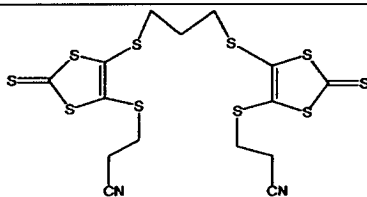
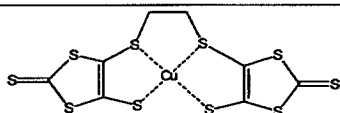
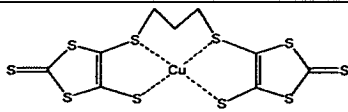
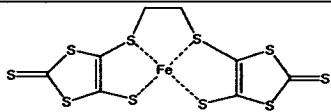
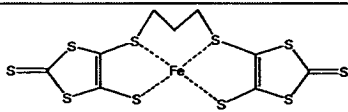
Each chapter in this work is written as a separate entity with regards to figures, tables and references. However, the products synthesised in this work are continuously numbered throughout the thesis and these are shown below.

	Name	Structure	Chapter
[1]	[Ni(ddd _t) ₂]		3.1.2.1
[2]	[BDTA] ₂ [Cu(mnt) ₂]		3.2.1
[3]	[BDTA][Ni(dmit) ₂] ₂		3.2.2
[4]	[TBA] ₄ [Pd ₈ (dmit) ₁₀]		3.2.3
[5]	[BDTA] ₂ [Fe(td _{as}) ₂ Cl]		3.2.4
[6]	[BDTA] ₂ [Ni(td _{as}) ₂]		3.2.5

[7]	[BDTA] ₂ [CuCl ₄]		4.2
[8]	[BDTA] ₂ [CoCl ₄]		4.2
[9]	[BDTA] ₂ [MnCl ₄]		4.2
[10]	[BDTA] ₂ [ZnCl ₄]		4.2
[11]	[BBDTA] ₂ [Cu(mnt) ₂]		5.2
[12]	[BBDTA][Ni(dmit) ₂]		5.2
[13]	[BBDTA][Fe(tdas) ₂]		5.2
[14]	[BBDTA] _x [Ni(mnt) ₂]		5.2
[15]	[BBDTA] _x [Co(mnt) ₂]		5.2

[16]	[Mn((SP(Ph)₂N)₂)₂]		6.2
[17]	[Mn((SP(ⁱPr)₂N)₂)₂]		6.2 (6.2.1.1)
[18]	[Mn((SP(Ph)(ⁱPr)₂N)₂)₂]		6.2 (6.2.1.2)
[19]	[Co((SP(Ph)₂N)₂)₂]		6.2
[20]	[Co((SP(ⁱPr)₂N)₂)₂]		6.2

[21]	[Co((SP(Ph)(ⁱPr))₂N)₂]		6.2 (6.2.1.3)
[22]	[Ni((SP(Ph))₂N)₂]		6.2
[23]	[Ni((SP(ⁱPr))₂N)₂]		6.2
[24]	[Ni((SP(Ph)(ⁱPr))₂N)₂]		6.2 (6.2.1.4)
[25]	(C₂H₄(C₃S₅COPh)₂)		7.2.1

[26]	$(C_3H_6(C_3S_5COPh)_2)$		7.2.1
[27]	$(C_2H_4(C_3S_5C_2H_4CN)_2)$		7.2.1
[28]	$(C_3H_6(C_3S_5C_2H_4CN)_2)$		7.2.1
[29]	$[Cu(C_2H_4(C_3S_5)_2)]$		7.2.2
[30]	$[Cu(C_3H_6(C_3S_5)_2)]$		7.2.2
[31]	$[Fe(C_2H_4(C_3S_5)_2)]$		7.2.2
[32]	$[Fe(C_3H_6(C_3S_5)_2)]$		7.2.2

Chapter 1

Introduction

1.1 Introduction

The field of molecular magnetism is a relatively new discipline. Although Faraday discovered magnetism in the 1800's, there had been little investigation into the solid state phenomenon until the 1930's when new theoretical advances about the mechanisms of magnetic interactions started to emerge. These mechanisms were proposed first by Néel, then later (in the 50's and 60's) Mott, Anderson and Goodenough.¹ However, the subject area of molecular magnetism was only truly born when the first molecular magnetic material (bis-(N,N-diethyldithiocarbamato)Fe³⁺Cl) was synthesised by Wichman *et. al* in 1967, showing long-range order at 2.5 K.² This in turn led to the experimental realisation that magnetic communication through this solid arose from molecular orbital interactions, as predicted in the 50's and 60's.

This thesis is concerned with the molecular and bulk magnetic behaviour of materials composed of metal complexes with sulphur-rich ligands. The theoretical and historical background of molecular magnetism reveals both the significance of this field of study and the logic of investigating sulphur-rich molecular magnets. Thus, the introduction to this work will be comprised of a brief tutorial covering the fundamentals of magnetism and magnetic interaction in the solid state, and a historical review of the advances in molecular magnetism over the past 30 years. Within the tutorial attention will be paid to mechanisms of molecular magnetic interactions through ligands in inorganic materials, providing the reader with a good background to understand later discussion. The historical review will discuss molecular magnetic systems that have advanced this field, paying particular attention to materials relevant to this work. Through these introductory discussions the relevance of this thesis and its relationship to current research will become apparent.

1.2 Magnetism tutorial

1.2.1 Atomic magnetism

All materials have a magnetic property of some form as all materials contain electrons. On a basic level a magnetic field is created when a charge moves. Electrons are particles with a negative charge that spin on their own axis (**spin angular momentum S**) and move in orbitals around the nucleus of an atom (**orbital angular momentum L**), thus anything containing electrons has some form of magnetism.

The most common atomic magnetic effect is **diamagnetism**. This is where electrons of opposing spins (S) couple within an orbital and consequently the magnetic moments of the paired spins cancel. However, diamagnetic materials are not simply unaffected by a magnetic field; the paired electrons behave as a current loop and thus actually repel a magnetic field. This effect is very weak and can be considered to be independent of temperature. Diamagnetism is present in all matter as there will be paired electrons present in any material. The approximate diamagnetic component of a magnetic system can be easily obtained, as the diamagnetic susceptibility of a given compound will not vary with temperature. Diamagnetic constants (normally in the region of $10^{-6} \text{ cm}^3 \text{ mol}^{-1}$) for molecules and atoms can be added together to obtain the diamagnetism of a material.³

The other form of atomic magnetic effect is **paramagnetism**. This occurs when there are unpaired electrons in the atomic orbitals. The magnetic moment of an atom (μ) is a combination of the spin and orbital angular momentum and is expressed as:

$$\mu = g\sqrt{J(J+1)}$$

Equation 1. 1

where J is the total angular momentum ($S + L$), and g is the Landé g-factor (this varies when the atom has orbital angular momentum but is 2.0023 for a free electron). The value of g is given in Equation 1. 2.

$$g = \frac{3J(J + 1) + S(S + 1) - L(L + 1)}{2J(J + 1)} \quad \text{Equation 1. 2}$$

When a paramagnetic system is subject to a magnetic field the energy distribution of the unpaired electrons alter as they can occupy a lower energy level that aligns with the field, increasing the net magnetisation. Paramagnetic effects are of the order of 10^3 - 10^6 times larger than diamagnetic effects and as such typically dominate any signal. In a weak field (before magnetic saturation is achieved) the paramagnetic susceptibility is independent of field strength but is usually heavily dependent on temperature.

A material that has an attraction to a magnetic field is said to acquire magnetisation (M) in a magnetic field (H). The amount of magnetisation achieved for one mole of material in a field is called the **molar magnetic susceptibility** (χ) shown by Equation 1. 3. In a weak field the equation can be simplified to Equation 1. 4.

$$\frac{\partial M}{\partial H} = \chi \quad \text{Equation 1. 3}$$

$$M = \chi H \quad \text{Equation 1. 4}$$

The magnetisation term is equivalent to the sum of the magnetisation of electrons over a Boltzmann distribution of the energy levels for one mole of material at a given temperature. This takes on the form of the Van Vleck's susceptibility equation depicted in Equation 1. 5.⁴

$$\chi = \frac{N \sum_i (w_i^{(0)2} / kT - 2w_i^{(2)}) \exp(-w_i^0 / kT)}{\sum_i \exp(-w_i^0 / kT)} \quad \text{Equation 1. 5}$$

In this equation χ is the molar susceptibility of the material, N is Avogadro's number, k is the Boltzmann constant, T is the temperature and $w_i^{(0)}$, $w_i^{(1)}$ and $w_i^{(2)}$ are coefficients that are determined by perturbation theory. $w_i^{(0)}$ is the energy of the system in the absence of a field and $w_i^{(1)}$ and $w_i^{(2)}$ are the first and second order Zeeman coefficients that occur as a result of the field. The equation is derived by assuming that the value of H/kT is small (H is not too large and T is not too small). This equation can be simplified in specific circumstances to give results that provide the quantum justification for previously intuitive laws of magnetism. This will be demonstrated in subsequent sections. The solutions of the equation, by finding values of w_i for specific crystal field situations, are also utilised in following sections.

1.2.2 Spin-orbit coupling

The simplest paramagnetic system is a "spin-only" system where there is no orbital angular momentum ($L = 0$) and a large separation between the ground state and the first excited state (so that only the ground state is considered). This system will be considered in the next section. However, when there is an orbital angular momentum ($L \neq 0$) the spin moment and the orbital moment can interact displaying a phenomenon known as **spin-orbit coupling**. Spin-orbit coupling is dependent on the atomic orbitals that the unpaired electrons occupy and thus the symmetry of the magnetic centre. Spin-orbit coupling can be

quantified using the spin-orbit coupling constant (λ), which represents the energy of the interaction between the spin angular momentum and the angular momentum of the orbitals. Spin-orbit coupling normally increases dramatically with atomic number, making λ much larger for heavier elements. Spin-orbit coupling occurs when the magnetic effect created by the momentum of the electron spin (S) interacts with the magnetic effect created by the orbital motion (L). This is only possible if there are orbitals related by symmetry of the same energy levels with vacancies to accommodate the unpaired electron. Thus, quenching of spin-orbit coupling can occur when there is no degenerate state (orbitals of the same energy) to transfer an unpaired electron across to. Spin-orbit coupling is often reduced or quenched in first row transition metal complexes. This is because complexation results in a crystal field that often yields non-degenerate energy levels, usually with large energy gaps between each state. However, spin-orbit coupling need not be fully quenched in these situations it may also occur through mixing in of low-lying excited states. This reduced spin-orbit coupling is called second order spin-orbit coupling. For example, a d^8 ion can complex in a tetrahedral or octahedral geometry. Within an octahedral complex first order spin-orbit coupling is quenched so any reduced spin-orbit coupling could only arise from a second order effect. This is because the e_g orbitals have no vacant sites to transfer an electron across to. The tetrahedral complex will display first order spin-orbital coupling as there is one electron that can be translated across the three t_2 orbitals (Figure 1. 1).

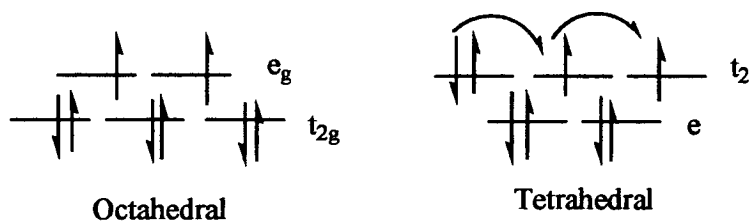


Figure 1. 1. Schematic of Ni(II) electronic configurations in two crystal fields.

Spin-orbit coupling is often reduced or quenched for the type of complexes discussed in this work. However, when it does arise the spin-orbit coupling constant can often be determined by fitting the data to the appropriate form of the Van Vleck equation.

1.2.3 The Curie Law

The Curie Law can be used to describe the behaviour of an ideal paramagnet with no spin-orbit coupling or intermolecular interactions. The Curie law was proposed by Pierre Curie in 1910, as an observation of experimental data from spin-only paramagnets, before the quantum treatment was realised. Curie noticed that $\chi T = C$, where C is the Curie constant.⁵ From a simplification of the Van Vleck equation, it could then be expressed in quantum mechanical terms as:

$$\chi = \frac{Ng^2\beta^2}{3kT} J(J+1) \quad \text{Equation 1. 6}$$

In this equation N is Avogadro's number, β is the Bohr Magneton, and k is Boltzmann's constant. If the material is spin-only (i.e. $L = 0$) then the equation can be simplified as J can be replaced with S to give the Curie constant as:

$$C = \frac{Ng^2\beta^2}{3k} S(S+1) \quad \text{Equation 1. 7}$$

This can be used to calculate the number of unpaired electrons from the value of S in a spin-only paramagnet as the only other variable in C is g and this usually only varies slightly from the free electron value.

For a spin-only magnet Equation 1. 1 and Equation 1. 6 can be combined and rearranged to obtain Equation 1. 8.

$$\mu_{\text{eff}} = \sqrt{\frac{3kT\chi}{N\beta^2}} \approx \sqrt{8T\chi}$$

Equation 1. 8

This equation is also a useful term to predict expected values of both μ_{eff} and χ for spin-only paramagnets.

1.2.4 Curie-Weiss Law

The Curie law fails to explain intermolecular interactions between magnetic centres. To account for this sort of deviation a Weiss constant (θ) is added. This modifies the Curie Law to give the Curie-Weiss Law shown in Equation 1. 9.

$$\chi = \frac{C}{(T - \theta)}$$

Equation 1. 9

The Weiss constant has units of temperature and can be either positive or negative. The magnitude and the sign depend respectively on the strength and type of intermolecular interactions.

Within magnetic materials intermolecular interactions between paramagnetic centres yield a bulk magnetic effect that can lead to magnetic order (at a certain temperature). When magnetic order is achieved in a material the paramagnetic centres align. If the magnetic centres all align parallel the material has **ferromagnetic interactions**, and the sign of θ is generally positive. If these interactions extend to form a magnetic material with long-range ferromagnetic order the material is know as a **ferromagnet**.

Likewise, if the magnetic centres all align antiparallel the material has **antiferromagnetic interactions**, and the sign of θ is generally negative. When there are an equal number and magnitude of spins in each direction no net magnetic moment is observed. Again, if long-range order is achieved through these antiferromagnetic interactions the material is known as an **antiferromagnet**. There is a special case of antiferromagnetism that also needs to be considered, called **ferrimagnetism**. This occurs in situations where neighbouring magnetic centres have unequal moments, so although the spins are still aligned antiparallel, they only partially cancel, and there is an overall net magnetic moment. These terms are shown schematically in Figure 1. 2.

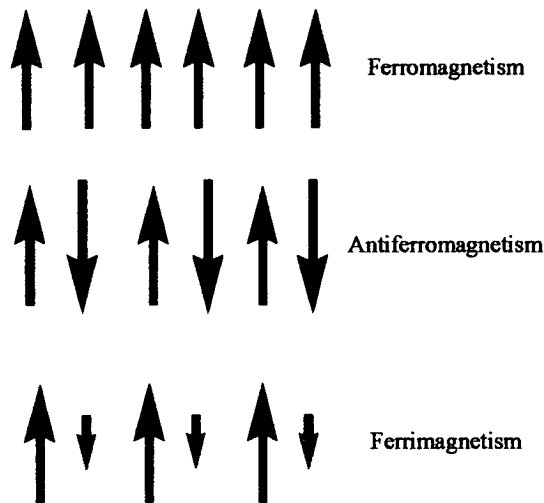


Figure 1. 2 Representation of magnetic interaction in one-dimension.

Deviation from the Curie-Weiss law occurs when the temperature approaches the value at which long-range magnetic order is achieved. The Curie-Weiss law is therefore only valid for paramagnetic systems above a temperature T , such that kT is well above the energy of dominant magnetic intermolecular interactions. This ordering temperature is called the Curie temperature (T_c) or the Neel temperature (T_N) for a ferromagnetic or an

antiferromagnetic system respectively, although more often T_c is used for both situations and will be generally used to represent both systems in this work. In specific simple systems this temperature can be approximated by the value of θ . A plot of χ^{-1} vs. T will form a straight line with gradient $1/C$ and an intersection at the origin for the Curie Law. The graph will be the same for the Curie-Weiss Law but an extrapolated line down to 0 will intersect at $\chi^{-1} = 0$ and $T \neq 0$. If the value of T is negative then θ is negative and the material has dominant antiferromagnetic interactions. Likewise, if the intersect is positive then the material has dominant ferromagnetic interactions.⁵ This is demonstrated in Figure 1. 3. It must be remembered that below the ordering temperature the Curie-Weiss law is not obeyed and the χ^{-1} graphs of ferro- and antiferromagnetism deviate from this perfectly straight line. In the ferromagnetic case at T_c the χ^{-1} graph plummets vertically down close to zero, and then gradually declines thereafter. At T_N for an antiferromagnet a small bump below the extrapolated straight line occurs, and then the graph slowly increases with decreasing temperature. This can firstly be explained by the assumptions used to derive the Van Vleck equation, as T cannot be too small as the equation breaks down. In a more literal sense the deviation from the Curie-Weiss law can be appreciated if magnetisation at 0 K is considered. χ^{-1} below $T_N \rightarrow \infty$ at $T = 0$ so that χ below $T_N = 0$ at $T = 0$. This is because antiferromagnets have no net magnetisation at $T = 0$. Likewise, χ^{-1} below $T_c \rightarrow$ a finite small value as χ below $T_c =$ a finite value at $T = 0$ as there is a net magnetisation. Above these temperatures the long-range magnetic order is lost so the straight line of the Curie-Weiss Law is upheld.

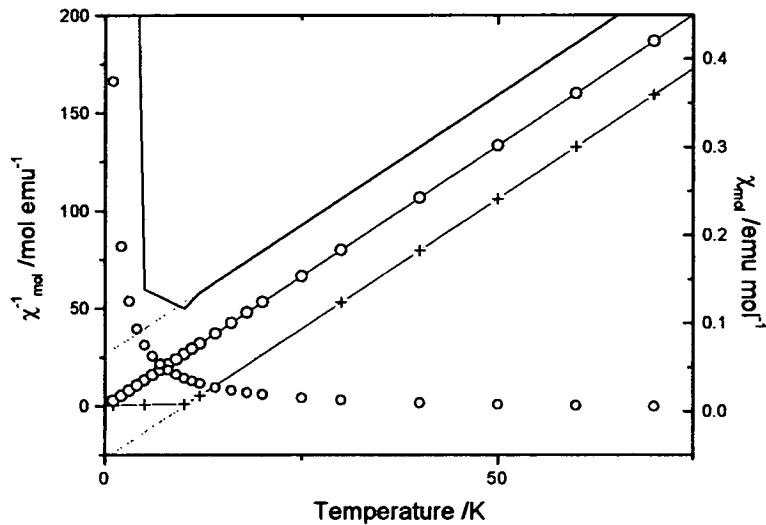


Figure 1. 3. The Curie and Curie-Weiss laws. χ shown for $C = 0.375$, $\theta = 0$, (○), against χ^{-1} for $C = 0.375$, $\theta = 0$ (◐), $\theta = -10$ K (—) and $\theta = +10$ K (-+-).

1.2.5 Mechanisms of coupling in magnetic systems

Bulk iron was the original ferromagnetic material studied by Faraday. In iron the magnetic interaction is transmitted inter-atomically, aligning the magnetic moments, turning individual paramagnets into a bulk magnetic effect (ferromagnetism). An area of the material with all moments aligned in the same direction is called a ferromagnetic domain. Iron, nickel and cobalt are the only elements that possess this bulk property. The metals are stabilised as positive ions in a “sea” of delocalised electrons all magnetised in the same direction within these domain areas. These three metals, a small number of alloys, a handful of metal oxides/halides, and some molecular systems are the only materials to be

ferromagnetic. Ferromagnetic interactions are therefore very rare as antiferromagnetic interactions most commonly occur. This is explained by the Pauli Exclusion Principle. This principle determines that electrons cannot couple ferromagnetically unless their orbitals are orthogonal. As it is far more common to have non-orthogonal orbitals utilised in magnetic exchange, antiferromagnetism dominates

The type of magnetic exchange that can occur in an inorganic material will now be discussed, before antiferromagnetic and ferromagnetic systems are examined.

The first and most simple magnetic interaction is **direct exchange**. This is when the orbitals of two magnetic centres overlap directly (examples shown in Figure 1. 4). These couple antiferromagnetically and form a spin singlet ground state. This is demonstrated by the $\text{Cu}_2(\text{Ac})_4$ dimer (Ac = acetate) that utilises the direct exchange shown in figure 1. 4a, as well as $\text{Mn}_2(\text{CO})_{10}$ that is an example of the type of direct exchange shown in figure 1. 4b.³

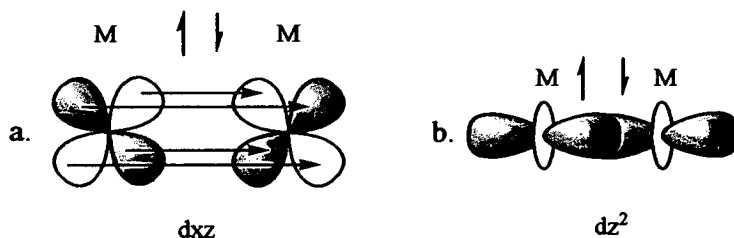


Figure 1. 4. Direct exchange via a) dxz orbitals and b) dz^2 orbitals.

The next type of exchange is very similar but utilises an intermediate ligand between the magnetic centres, called **superexchange**. Examples of this are shown in Figure 1. 5. The majority of superexchange systems are antiferromagnetically coupled as shown in Figure 1. 5. It can be seen that the diamagnetic ligand will still have a preference to order the system antiferromagnetically (Figure 1. 5a. and b.) unless orthogonal orbitals are utilised. Thus, in the case of Figure 1. 5c, ferromagnetic interactions can be achieved if the

M-L-M configuration is at an angle of 90° (the coupling orbitals are orthogonal to one another) and thus favour a parallel alignment of spins on adjacent ligands and adjacent metal centres. This is seen to be the case when $L = \text{Cl}$ and $M = \text{Fe}$ in FeCl_2 in a 2 dimensional lattice. This also occurs in some oxides, e.g. LiNiO_2 , however, the antiferromagnetically coupled examples are the most common interaction in general, particularly in metal oxides and fluorides.

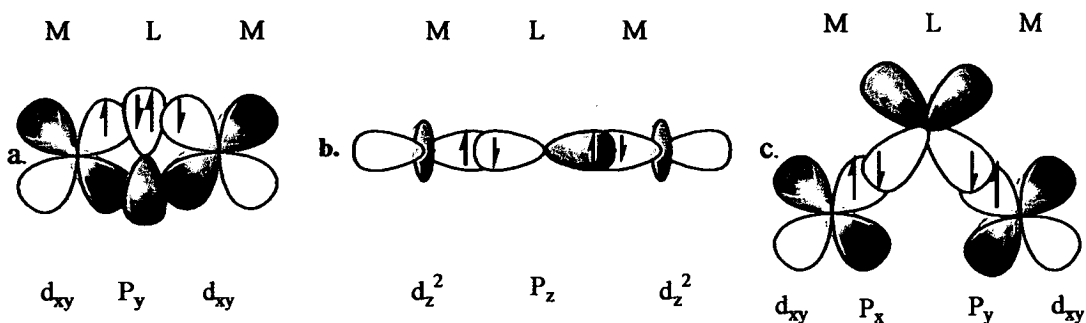


Figure 1. 5. Super exchange via ligand intermediates of the form a) P_y (or P_x), b) P_z and c) $P\sigma$.

The importance of orthogonality to propagate ferromagnetic superexchange has been emphasised here and as such the geometry of the structure is also imperative.

The simplest form of magnetic interaction occurs when two magnetic centres interacting with one another and this is known as a dimer. The mathematical model for a material with dimer interactions was reported in 1952 by Bleaney and Bowers.⁵ If the magnetic centres are coupled antiferromagnetically (and this is the case in most situations described above) then the coupling constant (J) between the centres is negative. Likewise, a ferromagnetic interaction has a positive value of J . The size of this constant is an energy term and thus represents the strength of the interaction. The Bleaney-Bowers model is shown in Equation 1. 10 and is plotted in Figure 1. 6.

$$\chi = \frac{2Ng^2\beta^2}{kT[3 + \exp(-J/kT)]} \quad \text{Equation 1. 10}$$

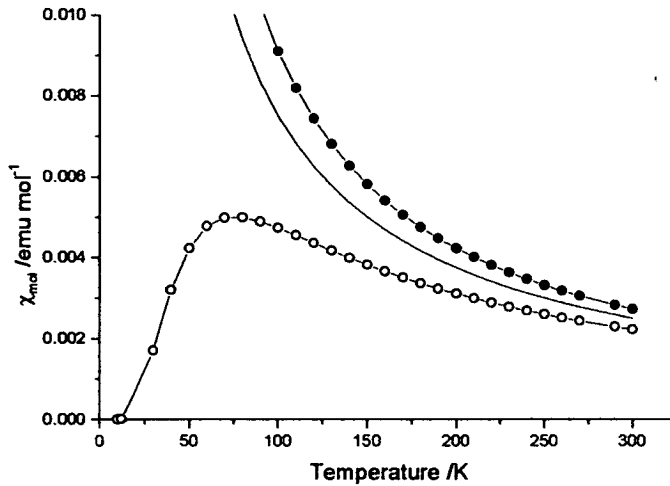


Figure 1. 6. Bleaney-Bowers model for a dimer coupled a) ●-●- = ferromagnetically ($J = 100 \text{ cm}^{-1}$), b) ○-○- = Antiferromagnetically ($J = -100 \text{ cm}^{-1}$) and c) — = not coupled (paramagnet, $J = 0$)

In the antiferromagnetic dimers (approximately 95% of cases) the graph shows a broad maximum where $|J|/kT_{max} = 1.599$. At lower temperatures the susceptibility tends to zero as only the diamagnetic ground state is populated. Above the temperature of maximum susceptibility the plot follows the same trends as the Curie law. It can be seen that the susceptibility of the ferromagnetic dimer looks very similar to that of a plot of a paramagnetic Curie system. The ferromagnetic example has a sharper increase of susceptibility at lower temperatures, as the ferromagnetic ground state is increasingly populated. However, the best way to separate the two is by comparing the plot of χT against T . In a Curie paramagnetic example a constant value of χT is obtained ($\chi T = C$), but for a ferromagnetic dimer the value of χT increases towards zero temperature and for an antiferromagnetic dimer the value decreases at low temperature, as respective magnetic and

non-magnetic ground states are populated. It is also common to see a small increase in susceptibility close to zero temperature in the antiferromagnetic example. This increase is called a “Curie tail” and can be ascribed to a small amount of paramagnetic impurity, which follows the Curie law and can only become visible if the rest of the material’s susceptibility tends to zero.

In a magnetic material there may be more interactions than with just one nearest neighbour and these more complex systems will now be considered. Magnetic communication in one direction only will form a one-dimensional chain of interactions, insulated from any further interactions. The concept of a 1D magnetic chain and the theoretical calculations for it were proposed as early as 1925.⁵ Theoretically the 1D magnet is of fundamental importance and Ising and his contemporaries found that a perfect 1D magnet only has long-range order at 0 K. This is because the chain thermally disorders at higher temperatures, with only short-range order above 0 K. However a *perfect* 1D magnet cannot exist, as there will always be some level of interaction between chains, so real 1D magnetic materials achieve long-range order above 0 K. A 1D magnetic chain is well understood and has been solved exactly with several different models accounting for atomic anisotropy, superexchange, dipolar interactions etc.

There are three standard models that are considered when analysing a 1D magnetic chain. These differ depending on the anisotropy of the magnetic centre and thus the orbital contribution. The first model is the simplest and is an isotropic system where the magnetic centre has no preference for any axial orientation of spins (i.e. if axial orientation preferences are α for the a-axis, β for the b-axis and γ for the c-axis, $\alpha = \beta = \gamma = 1$) and is called a Heisenberg system. The next system to consider is the Ising model. This applies where there is a uniaxial anisotropy arising from orbital contributions to the single ion

moment that gives a preferred spin orientation along one axis ($\alpha = \beta = 0$ & $\gamma = 1$). The third model is called the XY system, and applies where there is an electronic preference to align in both the x and y direction, making $\alpha = \beta = 1$ & $\gamma = 0$. In real systems that have significant orbital contributions the latter two models provide extreme-limiting cases that will not be ideally met. Thus, most materials of this kind are treated as approximations to these models and only in restricted temperature ranges where the model applies to that orbital population. The latter two models can only describe a limited number of systems and so do not feature in this thesis, and as such will not be discussed further. This discussion will be based on an isotropic Heisenberg system.

The first model to describe the simplest system of a spin $\frac{1}{2}$ isotropic Heisenberg antiferromagnetically coupled chain was reported in 1964 by Bonner and Fisher⁶ and a closed-form expression to describe this model was later presented by Estes *et al.*⁷ (Equation 1. 11). This model predicts a plot of susceptibility versus temperature as a curve, with a broad maximum at a temperature $\approx 0.641 |J|/k$ and with maximum susceptibility $\approx 0.0367 Ng^2\mu^2/|J|$, and this was later found to accurately model real systems of this sort.

$$\chi = \frac{Ng^2\beta^2}{kT} \frac{0.25 + 0.074975x + 0.075235x^2}{1.0 + 0.9931x + 0.172135x^2 + 0.757825x^3} \quad x = \frac{|J|}{kT} \quad \text{Equation 1. 11}$$

The Bonner-Fisher model breaks down at lower temperatures because it was originally developed by considering finite chains of 3-11 magnetic centres long. The results were then extrapolated to an infinite chain. This mathematical model is a classical system that did not take into account quantum effects at low temperatures that occur within an infinitely long magnetic chain. The Bethe Ansatz approximation⁸ utilises quantum mechanics to fit the whole temperature range of data, but must be calculated numerically.

However, recently the low temperature part of the Bethe Ansatz approximation has been formulated into an equation using quantum field theory by Eggert *et al.*⁹ This new model has a small inflection just before zero temperature, giving the infinite chain a finite susceptibility at 0 K = $Ng^2\beta^2/J\pi^2$.

Antiferromagnetic systems described by the above model have $J < 0$. For a ferromagnetically coupled chain $J > 0$. In this latter case χ increases as temperature decreases but there is no precise mathematical equation to describe this. The nearest analytical fit to such a situation is described by a high temperature expansion that was proposed by Baker, Rushbrooke and Gilbert in 1964.¹⁰ This approximation can be used for both signs of J and is shown in Equation 1. 12.

$$\chi = \frac{Ng^2\beta^2}{4kT} \left[\frac{N}{D} \right]^{2/3} \quad \text{Equation 1. 12}$$

Where

$$\begin{aligned} N &= 1.0 + 5.79799y + 16.90265y^2 + 29.37689y^3 + 29.83296y^4 + 14.03692y^5 \\ D &= 1.0 + 2.79799y + 7.008678y^2 + 8.653864y^3 + 4.574311y^4 \\ y &= J/2kT \end{aligned}$$

This example is the simplest type of 1D chain. Subsequently new materials were synthesised that were not so simple, so theoretical models were improved to fit new data and to take these modifications into account.³

A two dimensional lattice is formed when a further magnetic interaction occurs orthogonal to the first. As with the 1D chain the ideal Heisenberg and XY models do not yield long-range order above $T = 0$. It is only the Ising model that has a finite value of T_c for an ideal model 2D system. However, just as before, there are no real, truly ideal systems due to weak interactions in the third dimension, so values of T_c can be obtained for all 2D

lattices, although the transition may be at too low a temperature to observe experimentally. A change in dimensionality of a material has very dramatic effects on the thermodynamic properties and this is seen when comparing the characteristic graphs of heat capacity versus temperature. A sharp spike/ discontinuity is seen when 2D ordering is achieved for an Ising 2D lattice instead of a broad maximum (seen in a 1D system). For a Heisenberg system 2D magnetic order gives rise to a broad peak with a sharp spike showing the onset of 3D order. The magnetic susceptibility of a perfect square lattice has been modelled using a range of high temperature series expansions depending on the type of system pioneered by Kramer and Opechowsky.¹¹ An Ising lattice has been modelled the most successfully with a Heisenberg square lattice being the most difficult to model producing a long series expansion to calculate, Equation 1.13.

$$\chi = \frac{Ng^2\beta^2 S(S+1)}{k_B T} \left(1 + \sum_{n=1}^{\infty} a_n \left(\frac{J}{k_B T} \right)^n \right) \quad \text{Equation 1. 13}$$

2D magnetic materials are an area of much interest as many superconducting materials are based on 2D antiferromagnetic lattices and the phenomenon of superconductivity is still not completely understood.

1.3 Examples of magnetic materials

1.3.1 Metallic centred magnetic materials (1D -3D lattices)

There have been many examples of 1D chain materials, some more ideal than others. CuCl_2 was the first magnetic chain material to be analysed, however, it is quite a

poor magnetic chain as there are significant interchain interactions, so it does not compare well to the theoretical model.¹² $\text{CuCl}_2 \cdot 2\text{H}_2\text{O}$ and then later $\text{CuCl}_2 \cdot 2\text{NC}_5\text{H}_5$ proved to be better 1D systems, with $\text{CuCl}_2 \cdot 2\text{NC}_5\text{H}_5$ being the best, as NC_5H_5 units separated the chains and inhibited interchain interactions. However, it is still not a good example of a 1D magnet as 3D order is achieved at 1.13 K.¹² $\text{CoCl}_2 \cdot 2\text{NC}_5\text{H}_5$ is isomorphic with $\text{CuCl}_2 \cdot 2\text{NC}_5\text{H}_5$ but is different magnetically. This 1D ferromagnetic system has anisotropic Co(II) centres that can be fitted to the Ising model. Other 1D systems (e.g. CsNiCl_3) belong to a general class of chain materials of the form AMX_3 . These materials are antiferromagnetic Heisenberg chains of face-sharing octahedra with $J/k = -13$ K for the example compound and $J/k = -17$ K for the $\text{A} = \text{Rb}$ equivalent compound.¹² At very low temperatures the 1D model is not satisfied, as a triangular array of coupled chains form as a consequence of intermolecular exchange. Both CsCuCl_3 and CsCoCl_3 are isomorphic with CsNiCl_3 , but the former forms a Heisenberg ferromagnetic chain system with large antiferromagnetic interchain interactions, while the latter forms one of the best examples of a 1D Ising antiferromagnetic chain with $J/k = -115$ K and $T_c = 8$ K. Another good example of a 1D magnetic system within this metal-halogen family is $[\text{Me}_4\text{N}][\text{MnCl}_3]$. This system has negligible $[\text{MnCl}_3]^-$ interchain interactions as they are well separated by the $[\text{Me}_4\text{N}]^+$ counterions. It is an antiferromagnetically coupled chain with $J/k = -6.3$ K with a $T_c = 0.84$ K.¹²

Fluoride compounds have also been synthesised to yield 1D magnetic systems. KCuF_3 has a perovskite structure analogous to KNiF_3 . This structure is 1D because of a special alignment of the d-orbitals in the Cu^{2+} ion that propagates a strong overlap along the c-axis and prevents exchange through F along the a- axis. Simpler systems of the form MF_2 yield 1D chain materials with $\text{M} = \text{V}, \text{Mn}, \text{Fe}, \text{Co}, \text{Ni}$. The magnetic structure takes the

form of a spiral around the c-axis with the spins aligning perpendicular to the c-axis.¹²

These families of metal halide 1D materials are really a starting point for constructing low dimensional magnetic materials as the synthesis of 1D material can be greatly improved by designing a structural motif. Once the theoretical side was better understood, new types of low dimensional molecular materials were designed to try to improve the magnetic overlap (J). In 1988 Gatteschi *et al* synthesised ferrimagnetic manganese chains with bridging radical ligands (Figure 1.7).¹³

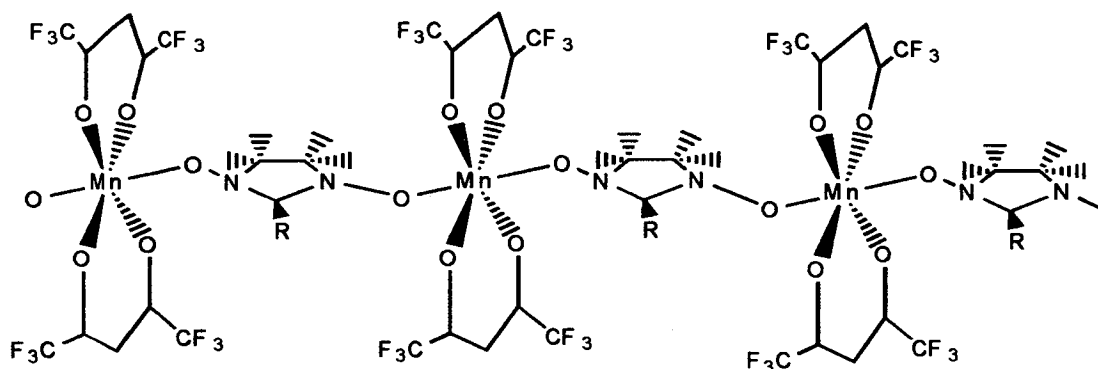


Figure 1. 7. chain of $\text{Mn}(\text{hfac})_2\text{NIT-R}$

These chain materials were ferrimagnetic as the spin density on the Mn^{2+} ($S = 5/2$) coupled antiferromagnetically with the radical spin ($S = 1/2$) on the NIT-R ligand creating an overall net spin of 2 per formula unit. This coupling was also found to be very strong with values of $J = 329.8\text{-}208.2 \text{ cm}^{-1}$ depending on the R group. This system was reproduced with $M = \text{Ni}$ or Cu , yielding another ferrimagnetic system for $M = \text{Ni}$ and a ferromagnetic system for $M = \text{Cu}$.

This dramatic increase in J , created by the use of specifically designed ligands for ferrimagnetic 1D materials, led to other such ligands been explored. The ligand 1,3-

propylene-bis(oxamate) (pba) and derivatives such as the 2-hydroxide (pbaOH)¹⁴ and the phenyl derivative (opba) have been extensively researched.^{3, 15, 16} These ligands will chelate around a metal centre, usually copper (Figure 1. 8) and can then form an extended structure with an alternation of different metals resulting in ferrimagnetic interactions. The ligand has the added benefit of extensive delocalisation so spin density is high (10%) around the outer oxygen atoms. It is also favourable as the ligand is perfectly planar and conjugated.

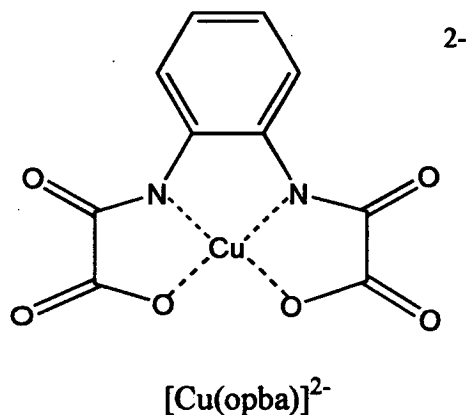


Figure 1. 8. Copper *o*-phenylenebis(oxamato) $[\text{Cu}(\text{opba})]^{2-}$

$[\text{Cu}(\text{pba})]^{2-}$ and $[\text{Cu}(\text{pbaOH})]^{2-}$ create ferrimagnetic chain systems with Mn^{2+} . The magnetic properties of both are the same down to 30 K, then the former is found to form antiferromagnetic interchain interactions forming a 2D lattice with $J/k = -2.2$ K, with the latter forming ferromagnetic interchain interaction to create a 2D lattice with $J/k = 5$ K. This is due to the shortest distance between chains in the a-axis being between Mn-Mn units for $[\text{Cu}(\text{pba})]^{2-}$ and between Mn-Cu units for $[\text{Cu}(\text{pbaOH})]^{2-}$. In order to prevent interchain interactions of this sort, the bulky Ph group was added in $[\text{Cu}(\text{opba})]^{2-}$. This building block combined with manganese, forms ferrimagnetic chains that are linear with addition of 2 ligating H_2O (on manganese) and forms a zigzagged chain when two DMSO

molecules replace the water (due to the *cis* addition of DMSO). These chains have ferrimagnetic interactions between the metal centres with long-range order up to 5 K. These building blocks can also create a 2D lattice structure in the form of a honeycomb motif for $[\text{Cu}(\text{opba})]^{2-}$ coordinated to Mn and Co when in an octahedral geometry, with magnetic ordering at 15 K and 30 K respectively.

2D magnetic materials were synthesised before 1D materials, the first being transition metal halides. The most well studied 2D magnetic systems are of the form A_2MX_4 , $\text{A} = \text{K}^+, \text{Rb}^+, \text{Cs}^+$ as well as a range of organic cations, $\text{M} = \text{Ni}^{2+}, \text{Mn}^{2+}, \text{Co}^{2+}$ and Cu^{2+} , $\text{X} = \text{F}^-$ and Cl^- . These systems usually have a perovskite structure with an AX non-magnetic layers separating the MX_2 magnetic layer to form 2D magnetic lattices with ordering temperatures as high as 42.3 K ($\text{A} = \text{K}$, $\text{M} = \text{Mn}$ & $\text{X} = \text{F}$).¹²

Another interesting 2D system is CoCs_3Br_5 . The chloride analogue is an Ising 3D magnet, but the bromide ions in CoCs_3Br_5 block the interaction in the third dimension and thus give a very good example of an antiferromagnetic, Ising, 2D lattice.¹²

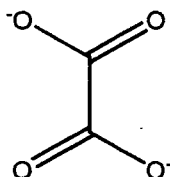


Figure 1. 9. Oxalate ligand.

Oxalate (Figure 1. 9) is a useful linking ligand to propagate superexchange and tends to form 2 and 3D ferrimagnetic lattices with a range of transition metals. These materials tend to form hexagonal layer structures with geometries that are dependent on the cation.^{15, 17} Bimetallic compounds using oxalate bridges were first synthesised in 1990 by

Okawa *et al* then Tamaki *et al*¹⁸ and were found to have three dimensional ferrimagnetic order.¹⁷ Combinations of metals such as nickel, iron, manganese, zinc and chromium were used and made ferrimagnetic materials with Curie temperatures between 4 and 45 K. The Cr(ox)₃Ni bridged lattice compound was found to be ferromagnetic as the magnetic orbitals on the two metals are orthogonal. All the compounds were found to be soft magnets with the hardest being the Fe(II)Cr(III) system with a coercive field of 320Oe.

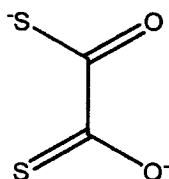


Figure 1. 10. Dithiooxalate ligand.

Dithiooxalate (dto) (Figure 1. 10) is analogous to oxalate but replaces two oxygen atoms with two sulphur atoms, and these bimetallic lattices were compared to oxalate lattices by Okawa *et al*.¹⁹ These take the form of $[NPr_4][MCr(dto)_3]$ where M is iron, cobalt, nickel and zinc (the copper and manganese products stayed molecular). The Cr(III) always bonds to the sulphur atom and the M(II) to the oxygen, due to the fact that sulphur is the stronger more attractive donor atom and Cr(III) is complexed first. This mode of complexation is unusual as sulphur is a soft ligand and will normally complex with softer metals. All the Cr(dto)M compounds are ferromagnetic as with the oxalate counterparts, with the exception of the zinc compound that shows no magnetic interaction. The T_c of both systems are directly compared and the results are shown in Table 1. 1.

M	[NPr ₄][MCr(dto) ₃]		[NPr ₄][MCr(ox) ₃]	
	T_c (K)	J (cm ⁻¹)	T_c (K)	J (cm ⁻¹)
Fe	8	+1.2	12	+0.8
Co	16	+3	10	+1.3
Ni	23	+5.8	14	+2.7

Table 1. 1. Ferrimagnetic Curie temperatures and coupling constants of the bimetallic compounds.¹⁹

It can be seen that the coupling constants are approximately double for the dithiooxalate compounds compared to the oxalates, and that the dto compounds also show increased values of T_c . The exception is the Fe(II) compound and this is because the magnetic interaction is a mixture of ferromagnetism and antiferromagnetism that gives an overall ferromagnetic interaction. In the Fe-Cr interaction the antiferromagnetic component is larger than in the others examples and thus the overall coupling is reduced. The fact that there is both a ferromagnetic and antiferromagnetic interaction shows that both π and σ orbitals on the sulphur are used for spin exchange as the π orbital mediates the antiferromagnetic interaction and the σ orbital mediate the ferromagnetic interaction.

From these examples it can be seen that sulphur has the ability to have a larger overlap and magnetically couple metals with a greater strength than oxygen. This has been ascribed to the “diffuseness” of the sulphur p-orbitals.²⁰

An increase in magnetic coupling (in all three dimensions) increases the magnetic stability of a material and this helps to increase the temperature of magnetic ordering to higher temperatures such as room temperature. A goal in the field of magnetic materials is to increase the ordering temperatures of materials so they can be utilised for practical

applications.

With respect to the synthesis of high T_c magnetic materials, there have been two such materials reported with T_c at or above room temperature. $V(TCNE)_x \cdot yCH_2Cl_2$ ($x \sim 2$, $y \sim 1/2$) was synthesised in 1991 by Manriquez *et al*²¹ with a remarkable T_c estimated at 350 K (depending on the solvent of crystallisation). Very little is understood about the material, as it is amorphous and fragile. The structure is not fully understood but it seems that TCNE is a negative radical and vanadium is in the 2+ oxidation state. The second high temperature molecular magnet was discovered in 1995 by Ferlay *et al* and is an organometallic magnet from the Prussian Blue family.²² Here chromium(III) hexacyano complexes are bridged by vanadium through the cyano ligands to make a ferrimagnetic lattice. $V[Cr(CN)_6]_{0.86} \cdot 2.8H_2O$ is found to be of the composition $(V^{2+}_{0.42}V^{3+}_{0.58}[Cr^{3+}(CN)_6]_{0.86} \cdot 2.8 H_2O)$ with a $T_c = 315$ K, but it is again amorphous.

It can be seen from this material that, not only is ferrimagnetism a good strategy for building a room temperature molecular magnet, but also that the bridging ligand is important. A cyano ligand is advantageous as it is linear, small, and conjugated, and thus a good electronic communicator. Miller and Manson²³ researched this further and found that the shorter the bridge the stronger the interaction: $-C=N- > -N=C-N- \gg -N=C-N-C=N$. In this study it was also noted that the earlier transition metals had stronger coupling than the later ones. The cyano groups are even more useful as they are rigid and retain their linearity, so they can connect various spin carriers without the possibility of chelation.

1.3.2 Charge transfer salts

Molecular systems called charge transfer salts were the first molecular materials to display electrical conduction (electronic communication through non-bonded interactions). A charge transfer salt is an anion-cation system in a lattice with unpaired electrons (or fractional charges) on one or both components at a distance near enough to interact. Charge transfer salts can have exciting and easily manipulated electronic properties, enabling the development of molecular materials with properties such as, conductivity, molecular magnetism and superconductivity.

The first groundbreaking magnetic salt of this type was $[\text{FeCp}_2^*][\text{TCNE}]$ (Figure 1.11). It was discovered in 1979 and showed 3D ferromagnetic behaviour with a Curie temperature (T_c) of 4.8 K.²⁴ The magnet was also shown to be hard with the ability to attract a Co_5Sm magnet and have a strong hysteresis (1000 Oe) which exceeds that of standard data storage devices. It was also found that this material has a magnetisation 37% greater than elemental iron on a per mole basis (not per gram or volume).²⁵ Considering these factors it would be very desirable to raise T_c to room temperature or near room temperature to utilise these features as a very promising data storage system.

The structure was found to be an alternating chain of donors ($[\text{FeCp}_2^*]^{+}$) and acceptors ($[\text{TCNE}]^{-}$) with a Fe-Fe distance of 10.42 Å. The crystal structure however is that of the solvated material. When the MeCN solvent is lost it forms an orthorhombic phase that has not been characterised fully and it is on the desolvated phase that the magnetic measurements have been performed. It was found that there is a strong magnetic coupling of 26 cm^{-1} through the chain stacks with a weaker interchain interaction that forms a 3D ferromagnet at 4.8 K. A whole family of this type of salt was investigated, changing

the metal and anion. The two most studied anions are [TCNE]^{•-} and [TCNQ]^{•-} (Figure 1.11). Initially six materials were studied, comprised of each anion with cations of M = Fe, Mn, and Cr, and were shown to have the same structure as the M = Fe, acceptor = [TCNE]^{•-} analogue. They have T_c values of 4.8 K, 8.8 K and 3.65 K respectively for the [TCNE]^{•-} anion and 2.55 K, 6.3 K and 3.3 K respectively for the [TCNQ]^{•-} anion. There are a number of observations to be made about this set of 6 salts. Firstly, the Fe salt of [TCNQ]^{•-} is not ferromagnetic but is a metamagnet. It has an antiferromagnetic ground state that has a transition to a ferromagnetic state above a critical field of 1500 Oe. Secondly, the [TCNE]^{•-} salt can be seen to display higher T_c values than the [TCNQ]^{•-} counterpart. Both of these observations are thought to be due to the fact that the same spin is delocalised over fewer atoms in [TCNE]^{•-} and thus “concentrate” the spin. Another trend to notice is that T_c varies for each metal as Mn > Fe > Cr, which is unusual as it does not follow the predicted trend of Cr > Mn > Fe where the earlier transition metal has the higher T_c .²⁵ The ferromagnetic mechanism of interaction within this material is under debate, however, the most likely explanation seems to be a spin polarisation effect.²⁵ Here a positive spin density on the metal encourages a negative spin density on the aromatic ring and subsequently promotes a positive spin density on the anion where the remaining unpaired electron lies. Thus the magnetic centres couple ferromagnetically.

Analogues of this salt design have been synthesised with the aim of increasing T_c , but unfortunately one of the earliest synthesised, [MnCp*₂][TCNE], remains the material with the highest T_c .

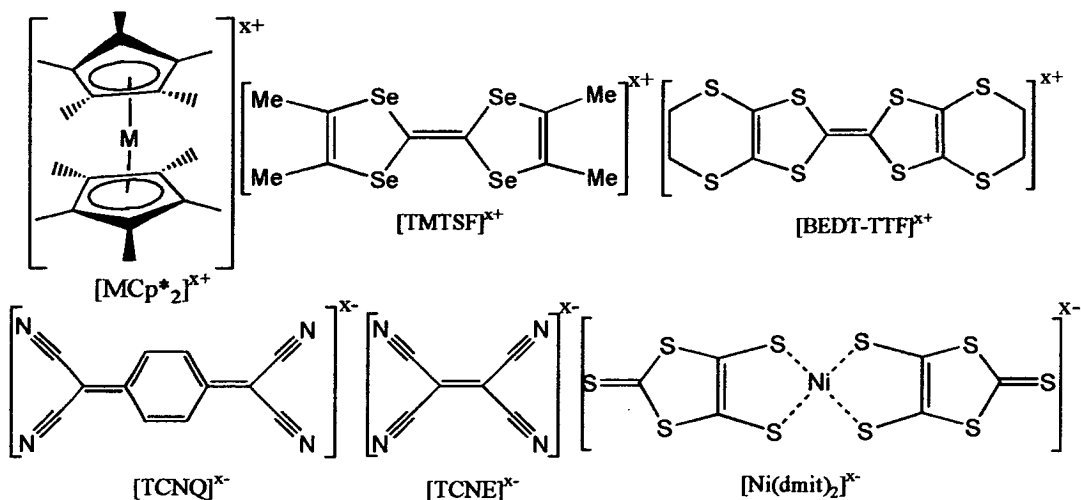


Figure 1. 11. Example components of charge transfer salts.

Charge transfer salts have, however, shown more promise in other research areas. Due to the fact that partial charge can transfer in these materials, they can be highly conducting. They were also found to be the first molecular materials to display superconductivity. The first examples were discovered in the mid 80's and took the form $[TMTSF]_2X$ followed by $[BEDT-TTF]_2X$ (where $X = PF_6^-, BF_4^-, AuI_2^-$ etc.) shown in Figure 1. 11.

These organic charge transfer salts utilise their large chalcogen intermolecular overlap to conduct electronic charge. Other materials similar in appearance and structure are also found to be conducting. Namely the salts of the metal bis-dithiolene anion $[Ni(dmit)_2]^{x-}$. As this complex is anionic it can form charge transfer salts with the conducting cationic counterparts above. These types of materials show high conductivity and can be metallic at room temperature.²⁶

1.3.3 Organic magnetic materials

Magnetism is a phenomenon associated with unpaired electron spins, and so it becomes apparent that metals are not the only materials that can be used as a magnetic centre to create a magnetic material. Organic magnets have been synthesised that involve huge polymeric systems with benzene molecules to bridge the spin carriers. The spin carriers are created by partial oxidation of bridging carbon atoms to yield free radicals of high spin triplets, due to the fact that the spins reside in orthogonal orbitals. The concept that large planar hydrocarbons of meta substituted triplets would ferromagnetically couple was theoretically suggested in 1968 by N. Mataga.²⁷ The theory was realised when large polymeric, aromatic systems were synthesised at the beginning of 1986^{28, 29} (Figure 1. 12). These were found to ferromagnetically couple along the polymer chain; however, their lack of stability meant that no long-range order was achieved due to their disordered structure and flexibility.

The first organic ferromagnet was synthesised in 1991 by Tamura *et al* and is composed of a nitronylnitroxide, *p*-NPNN³⁰ (Figure 1. 13a). This can be crystallised in several polymorphs and the α -phase, discovered in 1989, was later found to have ferromagnetic interactions with a $T_c = 0.9$ K. The β -polymorph has a strong ferromagnetic interaction between the oxygen radical and the nitrogen of the NO₂ group on a neighbouring molecule.

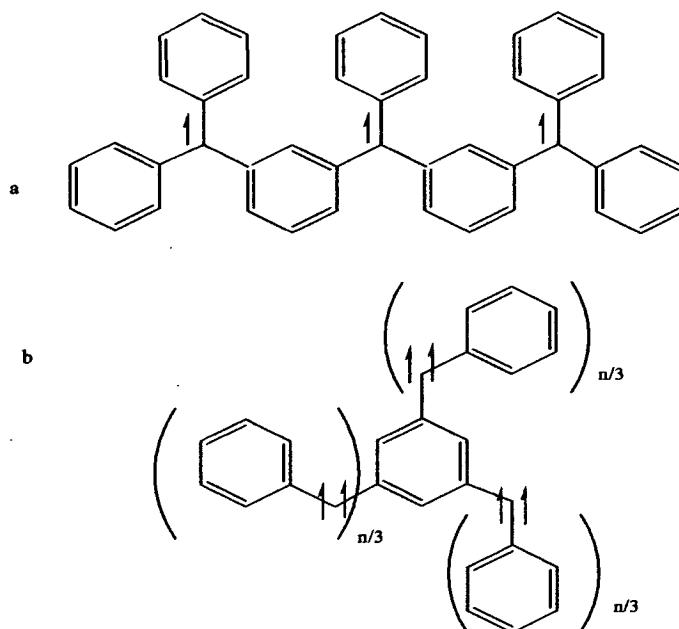


Figure 1. 12. Examples of polymeric organic magnets. Poly-metaquinodimethanes.

The interaction is ferromagnetic, as the magnetic orbitals are held in the crystal structure orthogonal to each other. This formed the first non-metallic 2D bulk magnet with a Curie temperature of 0.6 K. Within two years the Curie temperature of such materials was doubled with the discovery of the subsequent nitroxide-based diradical DOTMDAA with a $T_c = 1.48$ K (Figure 1. 13b.)

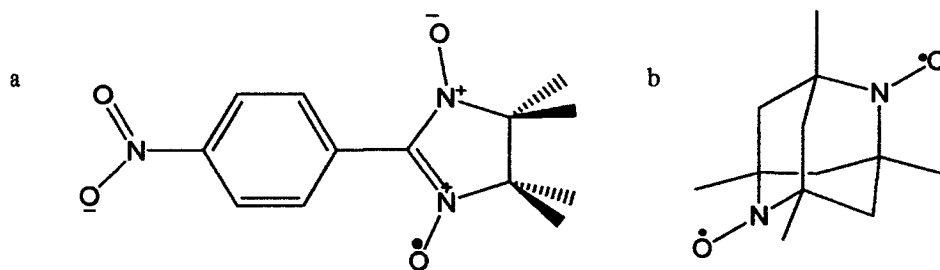


Figure 1. 13. Ferromagnetic organic radicals. a) *p*-NPNN, b) DOTMDAA

Around the same time other ferromagnetic, non-metal containing materials were also being discovered. These included fullerene[TDAE]³¹ and [BBDTA]GaCl₄³² which order ferromagnetically at 19 K and 6.7 K respectively. These values are much greater than the nitroxide-based compounds and it must be noted that these are radical cation salts as opposed to neutral radical systems.

From the same dithiazolyl family as [BBDTA]^{x+}, a new, neutral radical, ferromagnet was discovered in 1996 that far exceeded the Curie temperature of any other organic ferromagnet.³³ The complex is *p*-NCC₆F₄CNSSN (Figure 1. 14) and has two polymorphic crystal structures. The α -polymorph phase was found to be antiferromagnetic with $T_c = -8$ K. However the β -phase was found to be a canted antiferromagnet with a $T_c = 36$ K, more than an order of magnitude greater than any other neutral radical compound. The Curie temperature of the material was greatly increased to $T_c = 65$ K when 16 kbars of pressure were applied.³⁴ However, the net moment is suppressed by this large pressure.

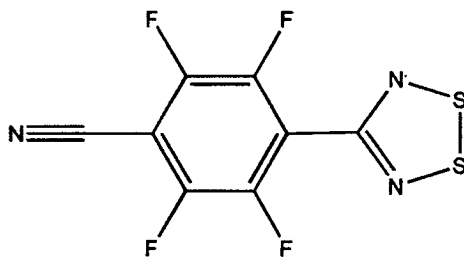


Figure 1. 14. *p*-NCC₆F₄CNSSN.

It was found that the spin density lies predominantly on the sulphur and nitrogen atoms and that ferromagnetic exchange was mediated by contacts between the sulphurs and the nitrogen on the heterocycle in adjacent molecules.³⁵ It is interesting to note that both *p*-NPNN and *p*-NCC₆F₄CNSSN magnetically couple intermolecularly through nitrogen atoms. Nitroxide-based compounds utilising a N-O interaction have magnetic ordering 60

times less than the dithazoyl utilising an N-S interaction to propagate magnetic coupling. This is partly due to the larger atomic orbitals of the sulphur atom compared to the oxygen atom, leading to greater interaction through a larger overlap.

1.4 Conclusions & aims

It can be concluded from this survey, particularly the comparative work between oxalates and dithiooxalates done by Okawa *et al* discussed in section 1.3.1, that sulphur atoms can mediate strong exchange coupling between magnetic centres due to a large overlap that increases the magnetic coupling constant J (compared to Oxygen and Nitrogen atoms) as well as increasing the T_c of the material. This effect is reiterated in section 1.3.3 when comparing the organic magnets p -NPNN and p -NCC₆F₄CNSSN. The magnetic coupling is communicated through N-O and N-S interaction respectively, leading to a dramatic increase in the ordering temperature of p -NCC₆F₄CNSSN. Due to sulphur's ability to increase magnetic interactions and the small amount of previous work carried out on the magnetic properties of sulphur-rich materials, this thesis will be concerned with magnetic materials with magnetic interactions propagated by sulphur atoms.

The target materials in this thesis will be synthesised by a "molecular approach" as opposed to high temperature "shake and bake" methods which are common in solid state chemistry. With the molecular approach precise building blocks or molecules are synthesised using solution chemistry methods then built up to create the desired material. This method has the advantage of precision design in the molecule and thus a larger degree of design in the overall material. Another advantage is that single crystals can often be grown, so structural information can be obtained easily.

The molecular materials that will be studied will be firstly, magnetic complexes with sulphur-donor ligands such as dithiolenes and thiophosphines. These are families of bidentate ligands that form complexes with metals through two sulphur bonds. The sulphur atoms are bonded to a conjugated system that makes up the non-innocent ligand. Dithiolenes have been researched extensively because of their solid state electronic properties, whereas thiophosphines have not yet been considered in a magnetic materials context, with most research into this family being orientated around enzymatic mimicing. A family of sulphur-rich cations (dithiazolyl) will be studied as they have proven to have extensive magnetic properties and one such example forms the molecular magnetic material with the highest T_c for an organic magnet (section 1.3.3). Dithiolenes, thiophosphines and dithiazolyls are ideal to propagate magnetic interactions as they are conjugated and delocalised, encouraging electronic communication.

The primary objectives are therefore:

- To synthesise charge transfer salts of dithiolene anions and dithiazolyl cations and explore the resulting magnetic properties.
- To study the magnetic effects in materials of MCl_4 with dithiazolyl cations.
- To study the magnetic properties of a range of thiophosphine complexes.

1.5 References

- 1 J. B. Goodenough, *Phys. Rev.*, 1955, **100**, 564.
- 2 H. H. Wickman, A. M. Trozzolo, H. J. Williams, G. W. Hull, and F. R. Merritt, *Phys. Rev.*, 1967, **155**, 563.
- 3 O. Kahn, 'Molecular Magnetism', New York, VCH, 1993.
- 4 F. E. Mabbs and D. J. Machin, 'Magnetism and Transition Metal Complexes', London, Chapman and Hall, 1973.
- 5 R. L. Carlin, 'Magnetochemistry', Berlin, Springer-Verlag, 1986.
- 6 J. C. Bonner and M. E. Fisher, *Phys. Rev. A*, 1964, **135**, A640.
- 7 W. E. Estes, D. P. Gavel, W. E. Hatfield, and D. J. Hodgson, *Inorg. Chem.*, 1978, **17**, 1415.
- 8 M. Karbach and G. Muller, *Phys. Rev. B*, 2000, **62**, 14871.
- 9 S. Eggert, I. Affleck, and M. Takahashi, *Phys. Rev. Lett.*, 1994, **73**, 332.
- 10 G. A. Baker, Jr., H. E. Gilbert, J. Eve, and G. S. Rushbrooke, *Phys. Lett.*, 1966, **22**, 269.
- 11 R. Navarro, in 'Magnetic Properties of Layered Transition Metal Compounds', ed. L. J. De Jongh, Dordrecht, Kluwer Academic, 1990.
- 12 L. J. De Jongh and A. R. Miedema, *Adv. Phys.*, 1974, **23**, 1.
- 13 A. Caneschi, D. Gatteschi, P. Rey, and R. Sessoli, *Inorg. Chem.*, 1988, **27**, 1756.
- 14 C. T. Chen and K. S. Suslick, *Coord. Chem. Rev.*, 1993, **128**, 293.
- 15 D. Gatteschi, *Adv. Mater.*, 1994, **6**, 635.
- 16 O. Kahn, *Acc. Chem. Res.*, 2000, **33**, 647.
- 17 O. Kahn, *Adv. Inorg. Chem.*, 1995, **43**, 179.
- 18 H. Tamaki, Z. J. Zhong, N. Matsumoto, S. Kida, M. Koikawa, N. Achiwa, Y. Hashimoto, and H. Okawa, *J. Am. Chem. Soc.*, 1992, **114**, 6974.
- 19 H. Okawa, M. Mitsumi, M. Ohba, M. Kodera, and N. Matsumoto, *Bull. Chem. Soc. Jpn.*, 1994, **67**, 2139.
- 20 A. Gleizes and M. Verdaguer, *J. Am. Chem. Soc.*, 1984, **106**, 3727.
- 21 J. M. Manriquez, G. T. Yee, R. S. McLean, A. J. Epstein, and J. S. Miller, *Science*, 1991, **252**, 1415.
- 22 S. Ferlay, T. Mallah, R. Ouahes, P. Veillet, and M. Verdaguer, *Nature*, 1995, **378**, 701.
- 23 J. S. Miller and J. L. Manson, *Acc. Chem. Res.*, 2001, **34**, 563.
- 24 J. S. Miller and A. J. Epstein, *Angew. Chem.*, 1994, **106**, 399.
- 25 J. S. Miller, *Inorg. Chem.*, 2000, **39**, 4392.
- 26 N. Robertson and L. Cronin, *Coord. Chem. Rev.*, 2002, **227**, 93.
- 27 N. Mataga, *Theor. Chim. Acta*, 1968, **10**, 372.
- 28 H. Iwamura, *Pure Appl. Chem.*, 1986, **58**, 187.
- 29 H. Iwamura, *Adv. Phys. Org. Chem.*, 1990, **26**, 179.
- 30 M. Tamura, Y. Nakazawa, D. Shiomi, K. Nozawa, Y. Hosokoshi, M. Ishikawa, M. Takahashi, and M. Kinoshita, *Chem. Phys. Lett.*, 1991, **186**, 401.
- 31 F. Wudl and J. D. Thompson, *J. Phys. & Chem. Solids*, 1992, **53**, 1449.
- 32 W. Fujita and K. Awaga, *Chem. Phys. Lett.*, 2002, **357**, 385.
- 33 A. J. Banister, N. Bricklebank, I. Lavender, J. M. Rawson, C. I. Gregory, B. K. Tanner, W. Clegg, M. R. J. Elsegood, and F. Palacio, *Angew. Chem., Int. Ed. Engl.*, 1996, **35**, 2533.
- 34 M. Mito, T. Kawae, K. Takeda, S. Takagi, Y. Matsushita, H. Deguchi, J. M. Rawson, and F. Palacio, *Polyhedron*, 2001, **20**, 1509.
- 35 F. Palacio, G. Antorrena, M. Castro, R. Burriel, J. Rawson, J. N. B. Smith, N. Bricklebank, J. Novoa, and C. Ritter, *Phys. Rev. Lett.*, 1997, **79**, 2336.

Chapter 2

Experimental Techniques

2.1 Introduction

This work is concerned with the synthesis and analysis of new molecular magnetic compounds. This will involve a number of experimental techniques that will be outlined in this chapter. The electronic properties were analysed using a Superconducting Quantum Interference Device (SQUID), four probe conductivity measurements, Electron Paramagnetic Resonances (EPR) and a Physical Properties Measuring System (PPMS). Structural determination was carried out using single crystal X-ray crystallography and X-ray powder diffraction with electronic and spin densities being computationally modelled using plane wave density functional theory calculations. The molecules and materials were also characterised using CHN elemental analysis, ^1H and ^{31}P NMR, IR and mass spectrometric techniques. Key methods mentioned here will be outlined and the equipment and parameters identified herein, with the exceptions of the common methods of CHN analysis, NMR, IR and mass spectroscopy. An in-depth explanation of these techniques can be found elsewhere.¹

2.2 Analytical methods of electronic properties

2.2.1 Magnetic analysis using a SQUID magnetometer

The Superconductive Quantum Interference Device (SQUID) is a highly sensitive machine that measures magnetisation (M), across varying temperatures and magnetic fields, and thus the magnetic susceptibility. The measurement of

magnetisation is achieved using the “Josephson Effect.” This is the phenomenon whereby a superconducting circuit has a weak point called a “Josephson Junction.” At this weak point the electrons tunnelling through the junction are very sensitive to any change in magnetic field, which alters their wavefunction. In the SQUID the supercurrent is split to travel down two separate Josephson junctions. One side is a control, whereas the other passes a sample in which a net magnetisation has been induced by a field. Thus when the supercurrent is recombined the wavefunctions are no longer coherent and the magnitude of the magnetisation can be determined and susceptibility calculated.

In this work magnetic measurements were carried out typically at 0.1 T over varying temperatures. A variable field measurement was performed from 0-5 T at 2 K to ensure that the magnetism was not saturated. Variable temperature magnetic susceptibility measurements were performed from 300-2 K using a Quantum Design MPMS₂ SQUID magnetometer with MPMS MultiVu Application software to collect the data.

2.2.2 Analysis using a PPMS

The Quantum Design Physical Properties Measurement System (PPMS) provides a platform on which one can carry out a range of electronic analytical techniques within one system. This is because there is a sample chamber into which a variety of equipment can be set up with a temperature control within the external case. Equipment to measure ac and dc magnetic susceptibility, conduction and heat capacity can then be used at variable temperatures. An advantage of the PPMS is that ³He can be

used to cool the system to reduce the temperature down to 0.35 K as well as being capable of reaching fields of 7 T. A further advantage of the PPMS is that several measurements can be performed simultaneously.

2.2.3 EPR spectroscopy

Electron paramagnetic resonance (EPR) spectroscopy is analogous to NMR spectroscopy. In this spectroscopic method it is the energy absorbed from the reversal of an unpaired electron's spin in a magnetic field that is observed (as opposed to nuclear spin in NMR). The method also differs from NMR as the frequency is set to a constant and the magnetic field is varied. For EPR spectroscopy a sample is placed in an electromagnetic field in the centre of a standing wave across a cavity at the point where the magnetic field is the strongest and the electronic field is the weakest. The frequency is fixed and this value determines the region of the electromagnetic spectrum in which the spectrum is run. All the EPR spectra in this work were taken in the microwave region, known as X-band EPR spectra, with a frequency set within the range of 9.4-9.7 GHz. Q-band EPR spectra can also be performed at 35 GHz. An absorption signal occurs when the energy is reached to flip the unpaired electron from the energy state where it is aligned parallel to the magnetic field to the higher energy state where it aligns antiparallel to the field. This energy is determined by Equation 2.1.

$$\Delta E = h\nu = g\beta B_0 \quad \text{Equation 2. 1}$$

The energy is obtained from the microwave radiation frequency (ν). β is the Bohr magneton, B_0 is the magnetic field, and g is a proportionality factor, otherwise known as

the Landé g -factor. Once the sample is placed in the cavity the magnetic field is varied while the radiation frequency is kept constant. When the field is at such strength that the energy needed to flip the unpaired electron matches the microwave frequency, an absorption signal is recorded (typically around 3000 Gauss (G) for an X-band spectrum). The signal that is usually recorded is the first derivative of the absorption curve and thus the peak of absorption lies on the baseline. The value of g is obtained from the field where the absorption occurs (the central point of the spectrum on the baseline) and can be calculated from equation 2.2.

$$g = \frac{714.48 \times \nu(\text{GHz})}{\text{Signal}(G)} \quad \text{Equation 2. 2}$$

The value of g gives information about the system. A free electron has $g = 2.0023$ and an unpaired electron on an organic radical has a value of g very close to this. However, due to delocalisation, spin orbit coupling and ligand shielding, the value of g for a transition metal complex normally lies between 1.4 and 3, but can be as high as 9 for some complexes.²

The signal is dependent upon two contributions to the electronic magnetic field: the electron rotation on its own axis (the spin angular momentum S), and the electron interaction with the nucleus spin (I). If the unpaired electron couples with the nuclear magnetic spin a hyperfine splitting is observed. Hyperfine coupling gives a signal of $(2I+1)$ peaks. Nuclei with an even number of protons and neutrons have $I = 0$ and thus no hyperfine coupling is seen. Nuclei with an odd number of both protons and neutrons have an integral value of I and nuclei with an odd number of either protons or neutrons

have a half integral value of I . Hyperfine coupling can give information on the spin density distribution over the molecule.

EPR spectroscopy is a very useful tool as it gives detailed information about the number and location of unpaired electrons in a system. It is also very useful as it can be used at variable temperature across a range of states such as solid, liquid and frozen liquids. The technique is also advantageous as it is very sensitive, with signals over 700x the intensity of an NMR spectrum.

In this work temperature dependent EPR measurements performed in Nagoya University, Japan, were carried out on JES-FA200 spectrometer in a temperature range of 4-300K by means of a variable temperature helium gas flow.

EPR measurements carried out in the University of Edinburgh, UK, were performed on an X-band Bruker ER200D-SCR spectrometer connected to a Datalink 486DX PC running EPR Acquisition System, version 2.42 software. This is fitted with a Bruker ER4111VT variable temperature probe using a nitrogen gas flow with the capacity to reach 160 K. However, low temperature experiments were also carried out within a liquid nitrogen filled glass dewar cooled to 77 K.

2.2.4 Conductivity measurements

The conductivity of a sample can be easily measured by passing a current across a sample and measuring the resistance and the distance between the probes. This is known as a two-probe system. This may be limited in accuracy as resistance from the contacts and the cables is not taken into account in this method. Thus, a four-probe

method is generally preferred. In this system a current is passed through one pair of contacts while the potential is measured across the other pair to minimise the effect of contact resistance.

Ideally a single crystal is used that is large enough to mount four probes (made of copper wires mounted with graphite paste). An advantage of a single crystal measurement is that the conduction can be measured along different crystal axes. If single crystals are not available, conduction of a powder sample can be measured in the form of a pressed pellet. This has the disadvantage of being made up of many solid state components and so the conduction is reduced by the resistance from grain boundaries. This can be reduced by measuring the conduction using an a.c. current as opposed to a d.c. current. There is also the added disadvantage that there is no specific orientation to the particles, so no directional conduction can be inferred.

2.2.5 DFT plane wave calculations

2.2.5.1 Computational chemistry

DFT plane wave calculations is a method used in computational chemistry that was born out of the field of theoretical chemistry. Theoretical chemistry uses mathematical systems to model chemical systems to predict analytical outcomes, such as calculating predicted coupling constants, rates of reactions and geometries. Due to the complex nature of atomic systems it is only possible to gain an exact solution for a

one or 2 molecule problem whilst numerical approximate solutions can be obtained for more complex many bodied problems. The solution to such complex problems uses a very large number of mathematical operations that need a large amount of computing power. As the performance of computers has grown, so too has the speed and number of operations the computer can calculate, increasing the range and complexity of chemical problems that could be solved, and thus the subfield of computational chemistry has developed.

Initial calculations were modelled on a classical mechanical picture of molecular systems, approximating bonds to springs and other such analogies. This is called force field theory. This has many limitations as molecular systems and electronic distributions are inherently quantum and thus better models are based on quantum mechanics. The specific cases dealt with in the subsequent two sections along with more in-depth information on computational chemistry are covered by Jensen.³

2.2.5.2 Hartree-Fock *ab initio* calculations

Ab initio calculations were the first quantum computational technique used to calculate electronic distributions within a molecular system. The term *ab initio* means “from the beginning” and with this method solutions are calculated from the electronic contribution of the time independent Schrödinger equation, with no reference to experimental results. The Schrödinger equation can only be solved exactly for a one-electron system and so the Hamiltonian needs to be simplified by approximations. The Adiabatic and Born-Oppenheimer approximations are applied to simplify the calculations, but these have drawbacks. An Adiabatic approximation confines the

system to only one electron surface meaning that all coupling interactions and avoided crossings are neglected, effectively discounting any electron-electron correlation. The implementation of the Born-Oppenheimer approximation fixes the position of the nuclei in the material. In practice these are accommodated by the addition of correction terms, but these give no information as to the real interactions of these parts of the system.

Once the Hamiltonian is simplified it can then be put into the Hartree-Fock equation to form an initial description of the system. A basis set is then applied to enable the Hartree-Fock equations to be solved. This is a mathematical function that mimics the physical behaviour of the electronic density and will thus converge on the correct solution. Usually a Gaussian basis set is chosen for ease of processing. A self consistent field theory is then applied to solve the system. This is when a field is applied to the system and iteration is performed to obtain an electron density matrix. This is used to calculate the new field, which is then used to calculate the new density matrix, until the lowest energy convergence is achieved. This method makes no distinction between singlet and doublet states, so when this is relevant, the unrestricted Hartree-Fock is used.

This method is very successful for smaller organic molecules where electron density is mainly localised. However, it is not so applicable for electronically delocalised lattice systems. The Hartree-Fock model positions electrons in specific atomic orbitals and takes limited account of diffused orbital systems or electronic interaction. Indeed, electronic correlation is often accounted for by an average interaction correction. Electronic correlation can be calculated using configuration interactions but this is an iterative method and as such is not very accurate and is extremely time consuming.

2.2.5.3 Density functional theory plane wave calculations

Density functional theory is based on the proven physical phenomenon that the ground state electronic energy is determined completely by the electron density of the system. Thus the lowest optimum energy can be found by iteration of the electronic density. This has many advantages. Firstly there are less parameters to calculate, as the electronic density function is independent of the number of electrons, whereas the position of each electron has parameters associated with it for the Hartree-Fock method. This reduction of parameters reduces calculation time and energy greatly. Secondly, and perhaps most importantly, electron-electron interaction, correlations, delocalisation, and the total energy of the system, are all implicitly included in this model. Density functional theory can also take into account non-bonded interaction, which is difficult to accommodate in Hartree-Fock calculations. This is the main reason that the DFT model was selected, as the systems in this work are inherently delocalised and involve magnetic interaction through non-bonded contacts.

In order to model a system using DFT calculations, approximations must be made for electron correlations. The original method of doing this used the local density approximation (LDA) that assumes that local density can be treated as a uniform electron gas. However, this approximation does not model the system well and has been replaced with the local spin density approximation (LSDA) which takes into account the spin quantum number. Thus for a closed shell system LDA and LSDA are the same. Both these approximations are not adequate to describe a real system, as electron correlation is not usually uniform. Thus a new, superior, approximation is now used that takes into account the variations that occur. This correction is called the generalised

gradient approximation (GGA) and gives a more accurate picture as the exchange and correlation energy are now dependent on the derivative of the electron density, not just the electron density. Another approximation introduced into the system is the concept that the core (non-valence) electrons are introduced with the nucleus potential and thus are not subject to any mathematical treatment. This is a large simplification to the calculation but has only a small effect on the accuracy of the results, as the core electrons play a very limited role in the chemistry of the materials. This is known as a frozen core approximation. The total elimination of these effects can actually have an effect on the valence orbitals, so in this case it is worth introducing an ultrasoft pseudo potential correction to represent any core electrons.

The calculations in this work use a plane wave basis set, as opposed to a Gaussian basis set, as mentioned previously. The plane wave basis set is constructed from continuous sine waves. This has many advantages over a Gaussian basis set. The sine wave function used to model the entire system is far simpler to describe than Gaussian functions. Thus many thousands of waves can be used to accurately model the systems, with little cost to calculation time and energy. As the plane waves are so simple to process, as many functions as are needed can be used (until the energy of the system converges to a cut off point). Whereas basis sets using Gaussian functions generally have to be simplified rendering them more inaccurate. A plane wave basis set also has the advantage of suiting the type of materials in this work. In this work the materials that will be subjected to computational calculation will be systems with infinite repeat unit lattices, needing calculations to span the entire structure. Plane wave basis sets are continuous functions, making them ideal to use over large lattices.

The calculations in chapter 3 were performed using the density functional formalism within the generalised gradient approximation using the CASTEP code.⁴ The electronic wavefunctions were expanded in a plane wave basis set up to a kinetic energy cut off of 380eV, which converged the total energy of the system to better than 1meV/atom. The valence electron and ion interactions were described using ultrasoft pseudo potentials. Integrations over the Brillouin zone were performed on a grid which also converges the total energy of the system to 1meV/atom.

Geometry optimisations were performed by relaxing the positions and unit cell parameters under the influence of the Hellmann-Feynman forces and stresses respectively. The calculations on [2] were performed by constraining the magnetic properties to investigate their relative energies: ferromagnetic and various antiferromagnetic configurations.

2.3 Structural refinement from X-ray diffraction

Both techniques discussed herein are diffraction methods that obtain structural data from the diffraction of X-rays by electron density surrounding each atom within a material. X-ray diffraction scatters radiation elastically and as such is non intrusive and gives data about the entire structure. X-rays have a wavelength comparable to the distance between atoms in a molecule and it is this similarity that allows the X-rays to diffract. As a crystal structure has a repeat unit a pattern emerges that is directly related to the planes in which atoms lie in the material, and this pattern conforms to Braggs law (Equation 2. 3)

$$n\lambda = 2d \sin \theta$$

Equation 2. 3

where n is an integer, λ is the wavelength of the X-rays (which are known). θ is the angle of diffraction that can be measured and so d , the distance between planes, can be calculated. This is a simplistic 1D model that is extended to 3D to obtain a structure. Thus a diffraction pattern yields exact inter-plane distances that can be refined into complete structures.

2.3.1 Single crystal X-ray diffraction

Diffraction intensities are collected at all angles in 3 dimensions around the single crystal. From the diffraction pattern obtained, a unit cell is first found. There are several complications in solving the entire structure from this point (which will not be discussed in this brief account) but these can be overcome by using one of two solution methods. The first is the Patterson method, this method finds the heavy atoms first and then solves the structure on a trial and error basis. The second method, and the one used by all the crystallographers that solved structures in this work, is the direct method. In this method all planes are calculated and the position that planes intersect is said to have an atom on it, or very near it. Both these methods lead to an electron density map that is then refined further to a complete structure. For the crystal structures collected at Nagoya University, Nagoya, Japan, ([1] and [2]) the X-ray diffraction intensities were collected on a MacScience DIP-Labo 3200 imaging plate type diffractometer with monochromatic Mo-K-alpha radiation at 50 kV at room temperature. A further crystal structure solved in Japan [3] was performed by H.

Kobayashi at the Institute for Molecular Science and CREST, JST, Okazaki, Japan. The X-ray diffraction intensities for this measurement were collected on a new Rigaku X-ray diffractometer equipped with confocal X-ray mirror system and a CCD detector with Mo-K-alpha radiation at room temperature.

X-ray crystal diffraction at the University of Edinburgh's chemistry facility (for all the remaining structures in this work) were performed on a Bruker SMART APEX CCD area detector diffractometer equipped with an Oxford Cryosystems low-temperature device with monochromatic Mo-K-alpha radiation (wavelength = 0.71073Å) at 50 kV at 150 K.

For all data collected an absorption correction was not carried out. The structures in this work were solved by direct methods and refined by full-matrix least squares against F^2 using all data (SHELXTL). H-atoms were placed in calculated positions and allowed to ride on their parent atoms (with the exception of [3] which did not include any H atoms). All non-H atoms were modelled with anisotropic displacement parameters.

2.3.2 X-ray powder diffraction

A powder is a material composed of lots of randomly orientated tiny microcrystalline particles, so when a diffraction pattern is recorded from a powder sample all orientations are recorded simultaneously and 3 dimensions of data are thus reduced into 1 dimension. This has obvious disadvantages compared to the single crystal diffraction techniques, due to the loss of so much information. It is therefore much harder to solve and refine a full structure from X-ray powder diffraction. To

improve the pattern the sample can be packed into a capillary tube and rotated in the X-ray beam. This makes the sample truly randomly orientated, so all diffraction angles can be observed. This eliminates any preferred orientations that would give incorrect intensities of peaks.

The diffraction intensities are collected in an arc around the sample, aligned with the beam. Structural solution, until very recently, has only been performed by a system of trial and error. A known structure, similar to the sample, is used as a starting point and the similar intensities are refined to the new data peaks. More recently, improvements in computing and refinement methods have seen the structural solution from powder diffraction data where a preliminary structural starting point is not known. The most difficult aspect of this is indexing the unit cell and identifying the space group. Once this has been achieved, and if the molecules in question are rigid and thus have limited degrees of freedom (which is the case for the materials in this work), then it should then simply be a case of determining the molecules' position in the cell to correspond to the pattern.

All X-ray powder diffraction measurements were carried out on a Bruker-AXS D8 series 2 diffractometer, set up to a Bragg Brentano Parafocussing Geometry. Monochromatic X-rays were generated at 40 kV from a Cu-K-alpha source at room temperature. Samples [3], [5], [6], [11]-[15] and [29]-[32] were loaded into a 0.5 or 0.7mm diameter lime soda glass capillary and rotated in an X-ray beam that had passed through a 1 mm exit slit. Samples [2], [7]-[10] were spread onto a silica flat-plate and mounted onto a 9 position sample stage and rotated in an X-ray beam that had passed through a 2 mm exit slit and an automatic divergence slit of 0.2° . Intensities were collected between $2\theta = 5$ and 80° on a Braun position sensitive detector over 12 or 8

hours (10563 steps of 0.0071° for 3.5 or 2.4 sec/step). The data were processed by Bruker-AXS Commander and Bruker-AXS EVA software.

2.4 References

- 1 E. A. V. Ebsworth, D. W. H. Rankin, and S. Craddock, 'Structural Methods in Inorganic Chemistry', Oxford, Blackwell Scientific, 1987.
- 2 B. A. Goodman and J. B. Raynor, *Adv. Inorg. Chem. Radiochem.*, 1970, **13**, 135.
- 3 F. Jensen, 'Introduction to Computational Chemistry', Chichester, John Wiley & sons, 1999.
- 4 M. D. Segall, P. J. D. Lindan, M. J. Probert, C. J. Pickard, P. J. Hasnip, S. J. Clark, and M. C. Payne, *J. Phys.: Condens. Matter*, 2002, **14**, 2717.

Chapter 3

Complexes of [BDTA]_x[M(dithiolene)₂]



3.1 Introduction

Chapters 3, 4 and 5 contain common cations or anions, therefore chapter 3 will provide an introduction to both this and the following two chapters. This introduction provides a general discussion of 1,2-bisdithiolene anions as well as dithiazolylium cations. The salts composed of these two components will be the subject of chapters 3 and 5 with dithiazolylium chlorometallate salts being the subject of chapter 4.

3.1.1 Dithiolenes

Bis-1,2-dithiolenes are bidentate, sulphur-rich, non-innocent ligands that complex through two sulphur atoms to form a 5-membered ring chelate complex. Metal bis-1,2-dithiolene complexes typically possess a square-planar, electronically conjugated system and have been studied extensively due to exciting properties such as superconducting¹, conducting², non-linear optical³ and magnetic behaviour.² These properties arise due to extensive electronic delocalisation of the HOMO and LUMO over the complex, as well as longer ranging electronic interactions through the material by extensive intermolecular overlap facilitated by the large π -orbitals of the sulphur atoms. Electronic bulk properties are readily seen in dithiolene complexes due to the propensity of the planar complexes to form stacking structures with intermolecular interactions in the stacking direction.² This interaction alone will form a one-dimensional material and such structures are typically obtained by segregating the stacks with counterions to hinder further electronic communication. Side-by-side interactions have also been observed between sulphur atoms on complexes in adjacent

stacks, as well as networks of interactions between the metal dithiolene complexes and participating cations to yield many examples of 2D or 3D metal dithiolene materials.⁴

Dithiolenes ligands have enjoyed an explosion of interest over the last 20 years as their role as the building blocks for new functional materials has been realised. Initially charge transfer salts of [perylene][Pt(mnt)₂] yielded conducting materials, but the conduction was thought to be due to the perylene. The first 1D metallic material with conduction based solely on the dithiolene complex was Li_{0.82}(H₃O⁺)_{0.33}[Pt(mnt)₂].1.67H₂O in 1981,⁵ sparking increased interest in these complexes. Later in the 80's, molecular conductors, superconductors,¹ and molecular magnetic materials with 3D ferromagnetic ordering⁶ were synthesised from dithiolene complexes. This work focuses on 3 such dithiolene complexes; [M(dmit)₂]^{x-}, [M(tdas)₂]^{x-} and [M(mnt)₂]^{x-}, shown in figure 3.1

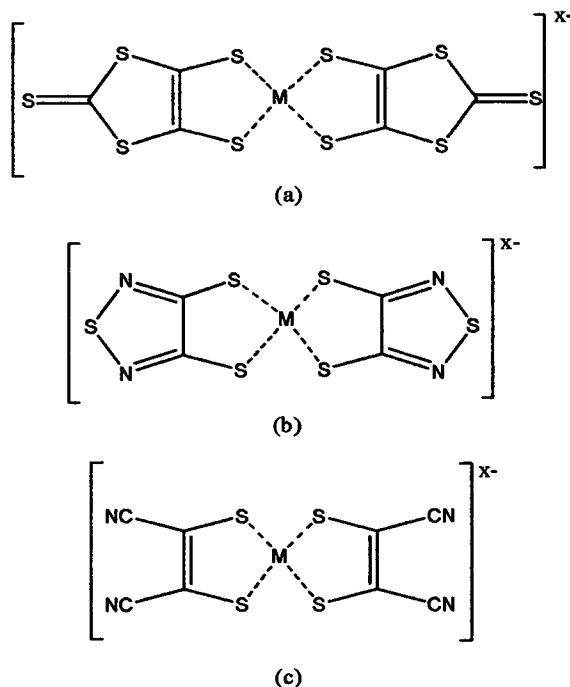


Figure 3. 1 (a) [M(dmit)₂]^{x-}, (b) [M(tdas)₂]^{x-} and (c) [M(mnt)₂]^{x-}.

3.1.1.1 [M(dmit)₂]^{x-}

The ligand dmit (acronym derived from the old name dimercaptoisotrithione) was first synthesised by Steimecke *et al* in 1975.⁷ This was some two years after the first organic molecular metal [TTF-TCNQ] had been reported. The development of this functional, organic, molecular material shifted the attention in the research field towards more sulphur-rich molecular systems similar to [TTF]^{x+}. [M(dmit)₂]^{x-} complexes were thus considered prime candidates to be the building blocks of a molecular conductor, as they are very similar in structure to the organic electron donor [BEDT-TTF]^{x+}. [M(dmit)₂]^{x+} could show similar electronic properties to [BEDT-TTF]^{x+}, with the added variation of containing a metal centre, as well as being typically anionic as opposed to a cationic (ideal for crystallising with organic π -donors). [M(dmit)₂]^{x-} complexes are ideal contenders for conducting materials as they are delocalised, planar and conjugated systems with large sulphur orbitals that give them the capability to form stacks with considerable intermolecular overlap. They can also be partially oxidised to yield a system with unpaired electrons delocalised through the stacked structure.

The complexes generally show a large number of intermolecular sulphur contacts through the stack, as well as between stacks, that increase structural stability. This is favourable for conducting materials as low dimensional conducting materials generally lose their conduction at lower temperatures due to Peierl's distortion. This instability causes stacking systems to dimerise, forming a band gap in the conductor. Thus, [M(dmit)₂]^{x-} could form materials with improved conductivity down to lower temperatures, increasing the chance of a superconducting transition.⁸

This indeed turned out to be the case when it was found that [TTF][Ni(dmit)₂]₂ has a very high room temperature conductivity of 300 S cm⁻¹ and is metallic down to a

very low temperature of 1.4 K.⁹ [TTF][Ni(dmit)₂]₂ was found to be superconducting below 47 mK and under a pressure of 7 kbar with a $T_c = 1.62$ K.¹⁰ Unusually, decreasing the pressure decreases the superconducting T_c , making it the opposite of all other organic molecular superconductors reported in the TTF family. The discovery of [TTF][Ni(dmit)₂]₂ inspired activity in this field to find similar materials, and so a very large number of analogous materials were reported in subsequent years.⁸ For example, the first ambient pressure superconducting molecular material was reported by Tajima *et al* in 1993.¹¹ The complex [α -EDT-TTF][Ni(dmit)₂] has segregated stacks of each ion in different planes. It was found to be metallic down to 20 K and superconducting with a $T_c = 1.3$ K.

Both of these materials incorporate open shell cations that have the capacity to be the sole conducting element in the materials. It was therefore encouraging to find the first conducting [Ni(dmit)₂]^{0.5-} material with a closed shell (spectator) cation [Me₄N]⁺ and thus the conductivity was found¹² to be solely due to [Ni(dmit)₂]^{0.5-}. [Me₄N][Ni(dmit)₂]₂ has $\sigma_{RT} = 60$ S cm⁻¹ and is also found to be superconducting under a pressure of 7 k bar with $T_c = 5$ K.¹³ This was surprising as closed shell systems are assumed to be more susceptible to a metal-insulator transition than open shell cation materials as they have less bands in the band structure.¹³ For example, the multi-conduction band system of [TTF][Ni(dmit)₂]₂ has additional conduction bands contributed by [TTF]^{x+}. The [TTF]^{x+} band structure is very stable and shows no band gaps down to 1.5 K. Thus the [TTF]^{x+} bands increase the overall stability of the conduction. This point is demonstrated by the fact that [Me₄N][Ni(dmit)₂]₂ has a metal-to-semimetallic transition at 100 K. Multifunctional hybrid materials have also been synthesised taking advantage of the conducting properties of [Ni(dmit)₂]^{x-}. For example,

$\text{Li}_{0.6}(\text{15-crown-5-ether})[\text{Ni}(\text{dmit})_2]_2$ is a conductor of both electricity and cations.¹⁴

Within the structure each component forms a segregated stack so that conduction of electricity ($\sigma_{RT} = 240 \text{ S cm}^{-1}$) occurred through the $[\text{Ni}(\text{dmit})_2]^{x-}$ stacks and the crown ethers stacks formed an ion channel that conducted the Li^+ cation.

Stoichiometric salts of $[\text{Ni}(\text{dmit})_2]^{x-}$ have also yielded molecular magnetic materials, as an integral ratio of cations to anions leads to localised unpaired electrons. One such example is the molecular spin ladder system $[p\text{-EPYNN}][\text{Ni}(\text{dmit})_2]$.¹⁵ In this material $p\text{-EPYNN}$ forms a one dimensional ferromagnetic chain, whilst the $[\text{Ni}(\text{dmit})_2]$ units form the first molecular antiferromagnetic spin ladder.

3.1.1.2 [M(tdas)₂]^{x-}

The dithiolene ligand $(\text{tdas})^{2-}$ was first synthesised in 1987 by Morris *et al.*¹⁶ However, a simpler synthetic route was executed by Wolmerhaeuser *et al* in 1989.¹⁷ This led to the synthesis of $[\text{NR}_4][\text{M}(\text{tdas})_2]$ ($\text{M} = \text{Ni}, \text{Pd}, \text{Pt}, \text{and Cu}$) in 1990 by Underhill and co-workers using this simple preparative procedure.¹⁸ The potential was immediately seen to utilise this dithiolene complex as a conducting material. Thus the nickel complex was co-crystallised with $[\text{TTF}]^{x+}$ and the resulting $[\text{TTF}]_2[\text{Ni}(\text{tdas})_2]$ was found¹⁸ to have $\sigma_{RT} = 0.1 \text{ S cm}^{-1}$. Complexes of $[\text{TTF}]_x[\text{M}(\text{tdas})_2]$ ($\text{M} = \text{Fe \& Cu}, x = 2, \text{M} = \text{Au}, x = 1$) were crystallised and conducting and magnetic properties analysed. $[\text{M}(\text{tdas})_2]^{x-}$ was found to dimerise in all the structures obtained. No structural data were gathered for the Cu complex, but in the Au complex both the $[\text{Au}(\text{tdas})_2]^-$ and the $[\text{TTF}]^+$ units were shown to be dimerised.¹⁹ $[\text{TTF}]_2[\text{Fe}(\text{tdas})_2]$ shows a hybrid system,²⁰ with a dimeric alternating chain of $[\text{Fe}(\text{tdas})_2]^-$ that shows an antiferromagnetic, $S = 3/2$,

dimer interaction. The [TTF]^{0.5+} cation forms a segregated stack at right angles to the anion, through which the conduction is thought to be propagated. The material shows $\sigma_{RT} = 0.03 \text{ S cm}^{-1}$, yielding a system with coexisting delocalised (conducting) and localised (magnetic) unpaired electrons. It seems to be the general case that [M(tdas)₂]^{x-} complexes form dimeric 5-coordinated structures with strong M-S interactions with adjacent complexes. This propensity to dimerise, as opposed to forming regular stacks, deems it an unsuitable candidate for new conducting materials. Systems containing [Ni(tdas)₂]²⁻ have yielded structures that do not contain dimeric [Ni(tdas)₂]²⁻ units. The materials [R₄N]₂[Ni(tdas)₂] (R = Et and Bu) do not contain dimer units but a layered ribbon structure of [Ni(tdas)₂]²⁻ and loosely stacked [Ni(tdas)₂]²⁻ units respectively.²¹ Thus, the pursuit of materials containing open shell conducting cations (other than TTF) continued with the hope that dimers would not form in the crystal structure. One such literature example is; [OM-TTF]₂[Ni(tdas)₂] in which it is the donor radical cation that dimerises with isolated [Ni(tdas)₂]⁻ units between each pair.²² This salt has a very poor room temperature conductivity = $3.7 \times 10^{-9} \text{ S cm}^{-1}$. Other examples proved to be slightly better conductors with [BEDT-TTF][Ni(tdas)₂] displaying a room temperature conductivity of 0.018 S cm^{-1} . In this system the electricity is conducted through a [Ni(tdas)₂]⁻ ribbon that runs through the structure via end on interactions. These ribbons are separated by isolated [Ni(tdas)₂]⁻ and dimerised [BEDT-TTF] units.²³ The material is found to have a semiconductor transition at 200 K and magnetic $S = \frac{1}{2}$, weak, antiferromagnetic interactions through the ribbon of [Ni(tdas)₂]⁻. This material is interesting as conductivity is seen to use a [Ni(tdas)₂]⁻ pathway. However, the best conductor in this family is the Fe analogue. [BEDT-TTF]₂[Fe(tdas)₂] has $\sigma_{RT} = 1 \text{ S cm}^{-1}$ although this is through a [BEDT-TTF]^{0.5+} 2D layer and not through the [Fe(tdas)₂]⁻.²⁴

Between each cationic layer is a stacks of dimerised alternating chains of [Fe(tdas)₂]⁻ that shows antiferromagnetic coupling with weak interchain interactions. Thus, unpaired electrons are found on both the conducting cations and the magnetic anions, just as was the case in the previous Fe example.²⁴

Although dimerisation seems to be the most common situation for [M(tdas)₂]^{x-} anions and this is problematic for conduction, dimerised [Fe(tdas)₂]⁻ has formed materials with interesting magnetic properties. [TBA][Fe(tdas)₂] has the dimeric structure and is found to be a $S = 3/2$ antiferromagnetic dimer ($J/k_b = 118$ K) that shows a peculiar result between 190 and 240 K.²⁵ In this temperature range there is a sudden increase in susceptibility yielding a $J/k_b = 108$ K, and then there is reentry back to the previous curve at 220 K. There is also quite a large degree of hysteresis in this transition.

Thus it can be seen that [M(tdas)₂]^{x-} has proved to be quite an unsuccessful building block for conducting materials, due to the presence of dimerisation in the structure. That said, even when there is no dimerisation, only weak end-on interactions were achieved propagating a small conductivity compared to [M(dmit)₂]^{x-} systems. It is probably for this reason that there are very few materials with [M(tdas)₂]^{x-} anions in the literature. [M(tdas)₂]^{x-} has however exhibited some interesting magnetic properties and is worth pursuing as an anion for magnetic materials. A [M(tdas)₂]^{x-} material would be much improved if it could be crystallised without a tendency to form dimers, and so form a uniform stack instead.

3.1.1.3 [M(mnt)₂]^{x-}

[M(mnt)₂]^{x-} is the most extensively studied bis-dithiolene complex. There are thousands of literature studies of conducting and magnetic [M(mnt)₂]^{x-} materials. As stated previously, Li_{0.82}(H₃O⁺)_{0.33}[Pt(mnt)₂].1.67H₂O was found to be the first metallic dithiolene material and was also found to have a one dimensional structure.²⁶ As [M(mnt)₂]^{x-} was one of the first dithiolene complexes discovered to have such functional properties there have been extensive studies of the mechanism of interaction. It is found that large π orbitals can interact strongly with adjacent complexes, enabling strong interaction through stacked motifs.²⁷ The counterion selected is of key importance, as larger counterions tend to lead to materials containing isolated or dimerised [M(mnt)₂]^{x-} units, as opposed to stacks. The examples of [NEt₄]₂, [NPr₄]₂ and [NBu₄]₂[Cu(mnt)₂] salts illustrate this point. The first example is the salt that utilises the smallest of these cations, [NEt₄]⁺. This exhibits semiconducting properties as well as 1-dimensional magnetic interactions.²⁸ The second salt containing [NPr₄]⁺ is only poorly conducting with a negligible magnetic exchange coupling constant²⁹ and the third of the series that has the biggest cation [NBu₄]⁺, has only a negligible magnetic coupling constant at low temperatures.³⁰ In this example the distance between the [M(mnt)₂]^{x-} units becomes too great for strong interaction to occur. Thus, predominately, it has been materials that contain smaller counterions that have yielded the most exciting properties, as they promote intermolecular interactions between the dithiolene complexes through the stack. Inorganic single metal ions are the smallest cations and the Cs_{0.83}[Pd(mnt)₂].0.5H₂O was found to be metallic under a pressure of 12 kbars down to 30 K. This was due to a large number of intermolecular interactions that gives the material 2-dimensionality.³¹ Another example of a material that contains the small

cation NH_4^+ is the salt $[\text{NH}_4][\text{Ni}(\text{mnt})_2]\cdot\text{H}_2\text{O}$, which was found to exhibit a ferromagnetic ground state.^{6, 32} This dithiolene complex formed a uniform stacked system yielding a material that shows ferromagnetic ordering at 4.5 K at atmospheric pressure, with T_c rising under pressure by 0.4 K kbar^{-1} until ferromagnetism was lost at 6.8 kbar. Long-range ferromagnetism is thought to be lost at higher pressure due to the competing factors of ferromagnetic coupling through the intermolecular Ni-S interaction and antiferromagnetic coupling between adjacent nickel centres, when they are close enough. Thus, long-range ferromagnetic order is increased with the reduction of intermolecular distance until an alternative mechanism supercedes this interaction.

Other materials containing stacked $[\text{M}(\text{mnt})_2]^x$ complexes have been found to display varied and unusual magnetic properties. The charge transfer salt $[\text{Etpy}][\text{Ni}(\text{mnt})_2]^{33}$ has a magnetic transition at 50 K. Above this temperature it exhibits strong antiferromagnetic coupling, whereas below it displays a ferromagnetic interaction with long-range ordering at 285 mK. The magnetic behaviour can be ascribed to the stacking motif as the behaviour is extremely similar to that of $[\text{NH}_4][\text{Ni}(\text{mnt})_2]\text{H}_2\text{O}$.

Other such examples within the same pyridinium family are [1-(4-bromo-2-fluorobenzyl)pyridinium][Ni(mnt)₂],^{34, 35} [1-(4-fluorobenzyl)-4-aminopyridinium][Ni(mnt)₂],³⁶ [(1-(4-R-benzyl)-pyridium)[M(mnt)₂] where M = Ni and R = F,³⁷ Cl, Br and NO₂,³⁸ M = Pt and R = Cl, Br, NO₂,³⁹ and CN.⁴⁰ In all of these systems the anion and cations form segregated stacks. In the first material a 1-D ferromagnetic interaction is formed down the $[\text{Ni}(\text{mnt})_2]^-$ stack with a strong ferromagnetic coupling of 42.2 cm^{-1} . There also exists a weaker antiferromagnetic interaction of -4.78 cm^{-1} between stacks. The second example is a metamagnet with antiferromagnetic interaction below 2.5 K in

a low field and ferrimagnetic interaction in a high field (1000 Oe). Interestingly, the addition of the amino group to cation changes the principle magnetic interactions of the material dramatically. This next material is paramagnetic down to 90 K, where it undergoes a phase transition and then becomes diamagnetic. This is due to dimerisation of the [Ni(mnt)₂]⁻ anions. Of the remaining M = Ni & Pt and R = Cl, Br and NO₂ materials, the Ni complexes all show long-range antiferromagnetic order (with the exception of R = Cl, which is weakly ferromagnetic) with a phase transition to a diamagnetic phase at lower temperatures of 101.7 K, 109.6 K and 181.7 K respectively. The Pt complexes follow the same phase transition to diamagnetism, with the exception of R = Br that becomes weakly ferromagnetic at low temperatures due to spin canting in this complex that can be seen in the crystal structure. These complexes show phase transitions at 274.6 K, 269.5 K and 179.6 K respectively. The final complex M = Pt and R = CN exhibits very different behaviour and is strongly antiferromagnetic.

It should be noted here that even very subtle changes in the cation affect the properties of the material. This is due to how the change affects the packing in solid-state structure. It can be seen from these examples that when the cation is planar and forms stacks in the structure, the [M(mnt)₂]^{x-} can also form a close stack. It is interesting that the properties of the [Etpy]⁺ and the [NH₄]⁺ salt are comparable, as [Etpy]⁺ is not as small as [NH₄]⁺, but is planar and forms stacks and so is small in the stacking direction.

New functional, planar cations can be explored to yield a hybrid material with mixed properties. There are several examples of such materials, including (Per)₂[M(mnt)₂] (M = Cu and Ni). Perylene is a planar molecule that stacks to form a semiconductor material. In this hybrid material the anion and cation form segregated

stacks. The materials were found to be conducting down the perylene stacks, with localised unpaired spins on the anion stacks.⁴¹

[BDNT]₂[Ni(mnt)₂] is another hybrid material. BDNT is a butterfly shaped electron donor capable of stacking, that has been studied extensively due to its conducting properties.⁴² The salt was found to be conducting due to [BDNT]^{0.5+}, as well as displaying a ferromagnetic interaction ($J/k = 3.4$ K) along the [Ni(mnt)₂]⁻ stack. The stacking motif is only assumed as the structure has not yet been determined.⁴²

A further interesting class of materials involves a hybrid system where the planar cations and anions form an alternately stacked motif giving a material with mixed properties. One material of this kind is [(NMP)₂][Cu(mnt)₂]. This forms 1-dimensional antiferromagnetic chains through an alternating stack. However, the interaction is very weak, as there are two stacked NMP cations between each [Cu(mnt)₂] anion.⁴³

This is a brief selection of [M(mnt)₂]^{x-} materials from which a variety of different functional properties have been achieved. This, however has only been the case when the counterions are small enough to allow a close stacking of the [M(mnt)₂]^{x-} units. A planar cation can be used as it too can stack, making it very small in the stacking direction. The scope for exploitation of this approach is vast, as there are a large number of planar cations, where small non-planar cations are limited.

To conclude, it would be desirable to obtain salts of these dithiolenes that yield structures with long-range intermolecular interactions, preferably via a stacking system, as past examples of this sort of structure have shown the most promise for new functional materials. It is the aim of this work to utilise a planar cation for this purpose.

3.1.2 Dithiazolylys

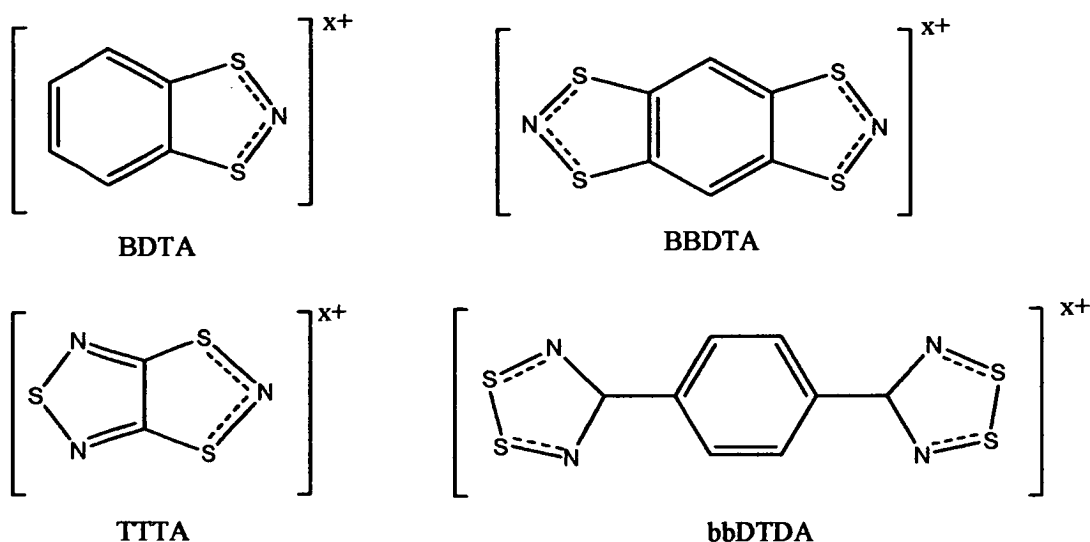


Figure 3. 2 Selection of dithiazolylium molecules and cations. (BDTA can be $0/1+/2+$, BBDTA can be $1+/2+$, TTTA can be $1+/2+$ And bbDTDA can be $0/1+/2+$)

Many of the most exciting examples of dithiolene-based magnetic and conducting materials have utilised open shell cations such as $[TTF]^{x+}$ and $[BEDT-TTF]^{x+}$. This is because they can form conducting materials in their own right and as such have extensive delocalised systems and can be partially oxidised. They are also desirable because they contain a large number of sulphur atoms that can form strong intermolecular interactions with sulphur atoms in the dithiolene anion and thus an extensive network can be achieved, such as in $[TTF][Ni(dmit)_2]$. It would therefore be desirable to include these features in the cations of the materials in this project. It would also be ideal to take advantage of a planar cation that has the ability to form a segregated or mixed stacking system with the dithiolene to achieve novel properties.

Dithiazolylium cations have been chosen for the formation of new molecular magnetic salts as this family is composed of extensive phenyl and N,S-heterocyclic rings

fused together (Figure 3. 2). Thus they are generally planar, conjugated, sulphur-rich and delocalised. They display interesting magnetic properties due to their strong intermolecular π - π interactions.⁴⁴ Members of the dithiazolyl family have also shown features such as organic paramagnetism.^{45, 46}

Dithiazolyls and the greater family that includes dithiadthiazolyls have been studied extensively, as members of this family form materials that are celebrated to be some of the first organic ferromagnets, with one example having the highest T_c for an organic magnet of 36 K.⁴⁷ This family of radicals and cations have nitrogen and sulphur heterocyclic rings with up to four heteroatoms and it is these ring systems that attract nearly all the spin-density of the molecule.⁴⁸ This can favour dimerisation of the molecules, removing any paramagnetic effect. This propensity to dimerise has been overcome by the addition of bulky R groups,⁴⁹ as well chlorination of the thiazyl ring.⁵⁰ Thus many bistable dithiazolyl radicals have been isolated.⁵¹ The organic ferromagnet $[BBDTA][GaCl_4].MeCN$ has a ladder like dimer array of $[BBDTA]^{*+}$ radicals and is diamagnetic. However, when the solvent of crystallisation is lost, the material changes from diamagnetic to paramagnetic, reaching long-rang ferromagnetic order at 6.7 K.⁵² $[BBDTA]^{*+}$ (figure 3. 2) has been the cation in many unusual materials as it is a paramagnetic radical. The molecular organic magnetic material currently with the highest T_c is the compound $p-NCC_6F_4CNSSN$ and is shown in figure 1. 14, and is discussed in section 1.3.3.

The counterions in this study are primarily the diamagnetic mono-cation $[BDTA]^+$ and the paramagnetic radical mono-cation $[BBDTA]^{*+}$. $[BDTA]^+$ (figure 3. 2) was chosen for its stability as well as the fact it has displayed unusual properties. Although the radical BDTA is diamagnetic at room temperature, there is a transition

above 346 K to a paramagnetic liquid, and above 360 K a double melt occurs that on cooling returns to a paramagnetic solid, with antiferromagnetic ordering at 11 K.⁵³

Crystallisations with other dithiazolyls were attempted (shown in figure 3. 2) and rejected due to solubility and stability issues. This will be discussed in the next section.

3.1.2.1 Schematics and reactivity of Dithiazolyl cations.

The general scheme of work followed in this thesis involved the co-crystallisation of each cation with each anion (shown in figure 3.3) to obtain as many novel functional materials as possible.

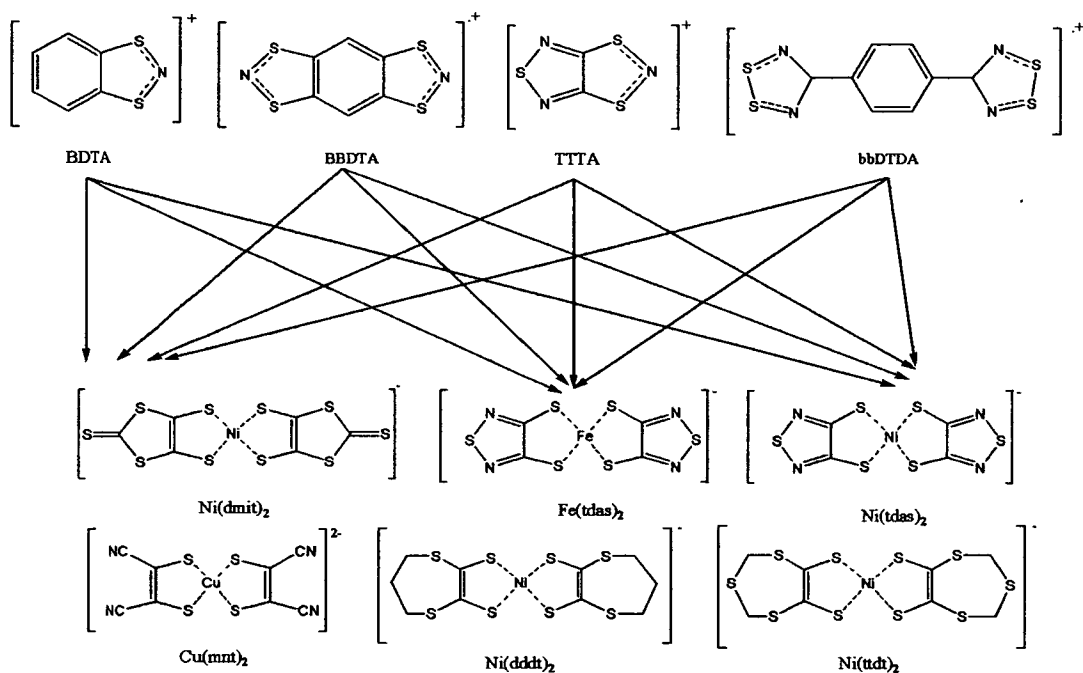


Figure 3. 3 Scheme of work. To co-crystallise each cation with each anion.

In general the process of co-crystallisation, by diffusing solutions of starting materials into one another, was a success and seven of these [dithiazolylium]_x[M(dithiolene)₂] salts were synthesised and are reported herein. These products are all salt of dithiazolyliums [BDTA]⁺ or [BBDTA]⁺ as problems were encountered with the other two thiazyl ring cations. Firstly, the cation [bbDTDA]^{x+} was found to be extremely insoluble. Both 1,3-bbDTDA and 1,4-bbDTDA were tested for solubility and yielded negative results. It is stated in the literature that both these compounds can be oxidised with a halogen by high temperature sublimation techniques.⁵⁴ This was carried out to yield [1,3-bbDTDA]Cl which was slightly soluble in nitrobenzene. However, to fully dissolve this complex heating was required and this was deemed to be impractical for the crystallisation method undertaken. The cation [TTTA]^{x+} was found to be very soluble and dissolved in all common solvents. However, this cation was not very robust, decomposing over time from a dark blue solid to a white powder. It was also not stable in solution and so any attempts to co-crystallise this cation yielded crystals of decomposition products.

Also, not all the [M(dithiolenes)₂]^{x-} proposed in scheme 3. 3 were used. The starting material [TBA][Ni(ttdt)₂] proved to be difficult to purify and only a very small quantity was obtained, which was deemed impractical to continue with. The only other [M(dithiolene)₂]^{x-} that could not be used to synthesise these salts was [TBA][Ni(dddt)₂]. In this co-crystallisation single crystals were produced of the neutral dithiolene [Ni(dddt)₂]⁰ [1] (shown in figure 3. 4b) that has dimeric stacks along the a-axis. Thus, it seems that the redox activity of this complex means that it will not form dithiazolylium salts to yield any novel materials. Therefore co-crystallisations were attempted with all

the dithiolene anions with the exception of $[\text{Ni}(\text{ttdt})_2]^-$ with all the dithiazolylum cations with the exception of bBDTDA.

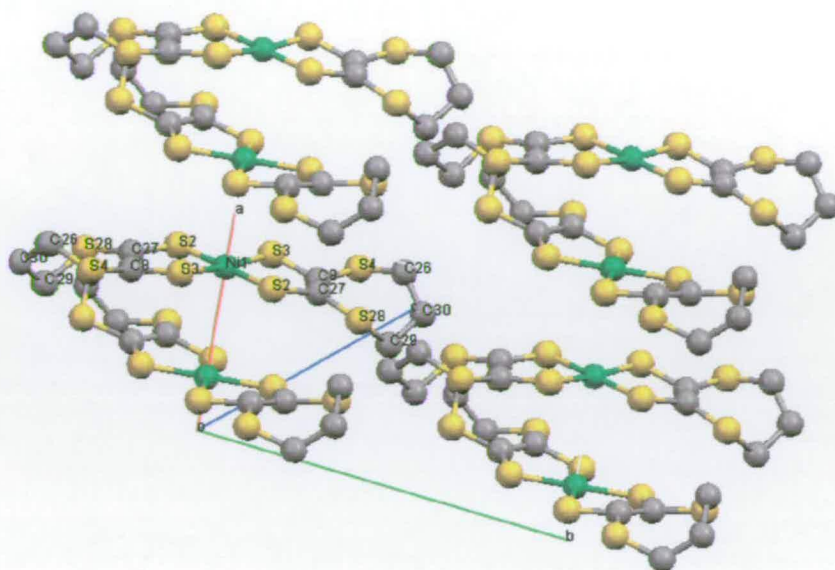


Figure 3. 4 Crystal structures of $[\text{Ni}(\text{dddtd})_2]^0$ [1]

The salts that were successfully prepared are $[\text{BDTA}]_2[\text{Cu}(\text{mnt})_2]$, $[\text{BDTA}][\text{Ni}(\text{dmit})_2]_2$, $[\text{BDTA}]_2[\text{Fe}(\text{tdas})_2\text{Cl}]$, $[\text{BDTA}]_2[\text{Ni}(\text{tdas})_2]$, $[\text{BBDTA}]_2[\text{Cu}(\text{mnt})_2]$, $[\text{BBDTA}][\text{Ni}(\text{dmit})_2]$ and $[\text{BBDTA}][\text{Fe}(\text{tdas})_2]$. This chapter will show the resulting $[\text{BDTA}]_x[M(\text{dithiolene})_2]$ materials, with chapter 4 describing $[\text{BDTA}]_2[\text{MCl}_4]$ materials and chapter 5 reporting the $[\text{BBDTA}]_x[M(\text{dithiolene})_2]$ salts.

3.2 Results and discussion of [BDTA]_x[M(dithiolenes)₂]

3.2.1 [BDTA]₂[Cu(mnt)₂] [2]

3.2.1.1 Preparation

Single crystals of [2] were prepared by layering a solution of [BDTA]Cl dissolved MeCN on top of [TBA]₂[Cu(mnt)₂] in a DCM solution. Needle-shaped black crystals were collected after 4 days.

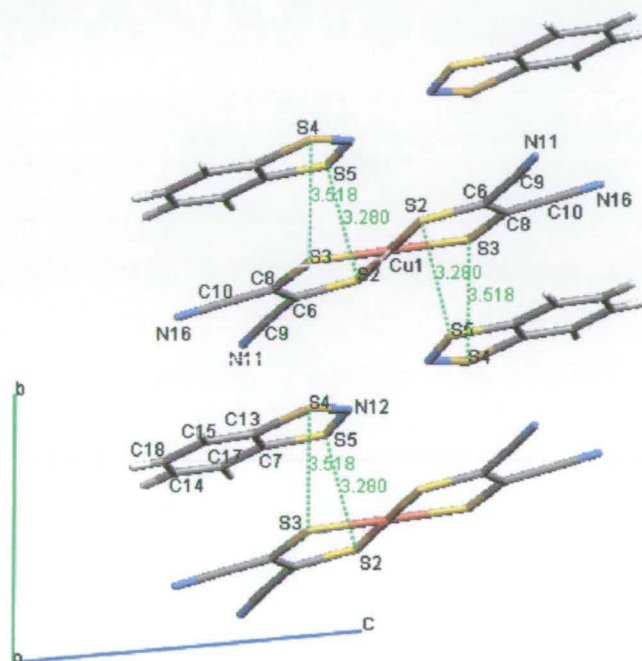


Figure 3. 5 Crystal structure of [2] viewed along the a-axis, with intermolecular distances (Å) smaller than the sum of the Van der Waal radii (S-S = 3.7 Å) shown.

3.2.1.2 Crystal structure

[BDTA]₂[Cu(mnt)₂] crystallises in the space group $P\bar{1}$ and has an inversion centre on the copper atom. The structure shows an alternating, diagonal stacked system in the b-c plane, with a single [Cu(mnt)₂]²⁻ anion sandwiched between two [BDTA]⁺ cations. Intermolecular contacts shorter than the sum of the Van der Waal radii (taken to be 3.7Å) are seen between S5 on BDTA and S2 on [Cu(mnt)₂]²⁻ along with the symmetry inverse. This creates a discrete unit of [Cu(mnt)₂]²⁻ with a [BDTA]⁺ above and below in this b-c plane (figure 3. 5). Extended interactions throughout each stack are not achieved as most of the inter-stack distances are large. Each stack is however tilted by 28.20° out of the a-b plane, allowing short intermolecular contacts between stacks along the a-axis, between a [Cu(mnt)₂]²⁻ anion and the adjacent [BDTA]⁺ cations. An S-S short intermolecular interaction is seen from S5 on [BDTA]⁺ to S3 and S2 on [Cu(mnt)₂]²⁻ in the adjacent stack (intermolecular distances of 3.418 and 3.397Å respectively). Thus the discrete units within each stack in the b-c plane form S-S interactions along the a-axis and allow a chain of contacts to form (figure 3. 6). There are no other intermolecular distances small enough to provide significant interactions, so a 1-dimensional chain is observed.

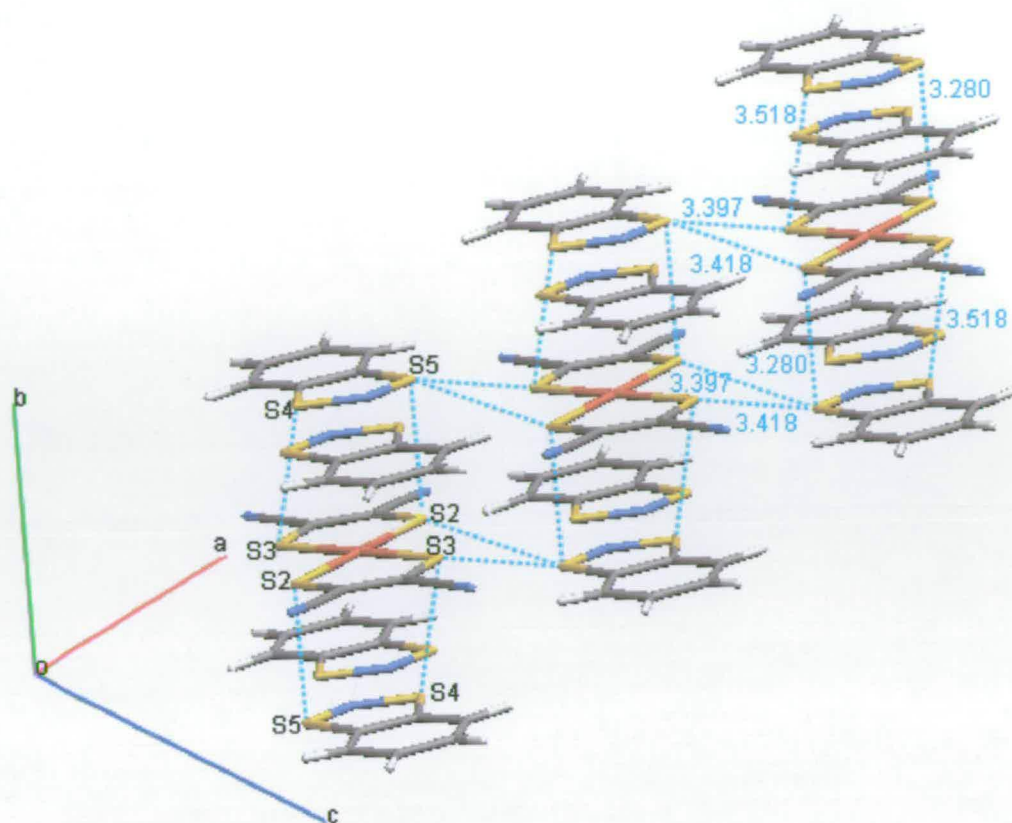


Figure 3. 6 Crystal structure of [2] viewed to show interactions along the a-axis. Intermolecular distances (Å) smaller than the ionic radii (S-S = 3.7 Å) shown.

3.2.1.3 Magnetic and EPR studies

EPR studies were performed on a solid sample of [2] at variable temperatures from 4 – 300 K (figure 3. 7). The spectrum has a principle feature at $g = 2.022$, with small positive peaks at lower fields that can be assigned to parallel and perpendicular g values respectively. This is a very typical pattern for a square-planar Cu^{2+} complex.

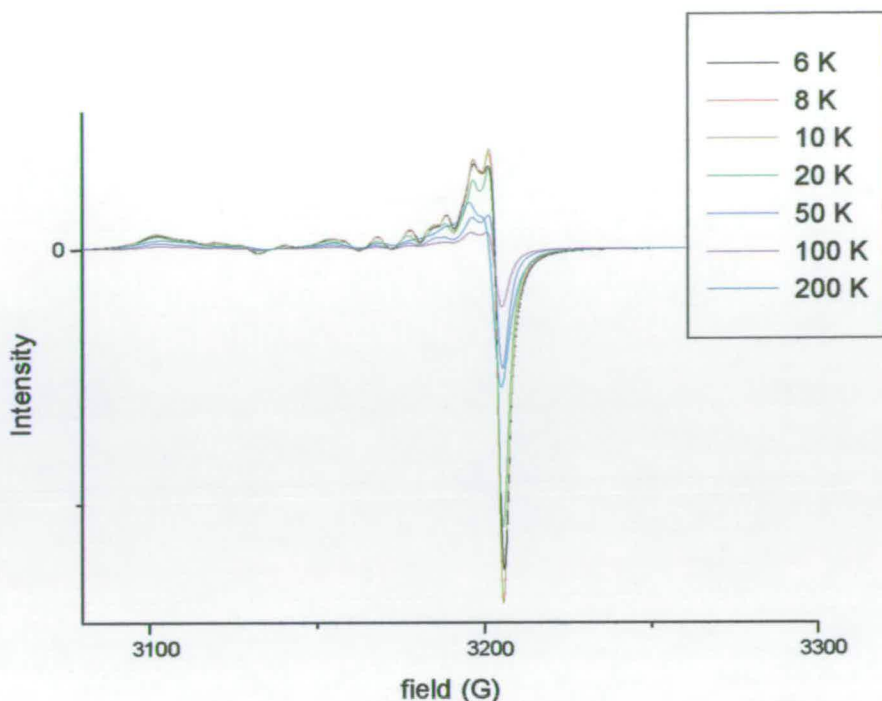


Figure 3. 7 EPR spectra of solid sample of [2] at varying temperatures.

However, the smaller peaks are poorly resolved and further discussion will focus on the principle peak. The linewidth and $g_{//}$ -value for each temperature were plotted (Figure 3. 8). Both the line width and $g_{//}$ -values decrease with temperature to a negative peak at 10 K and then increase again at lower temperatures. The value of $g_{//}$ ranges from 2.016 - 2.022 and the line width from 6.31 - 7.79 mT. At room temperature $g_{//} = 2.022$ which is comparable with literature values obtained for other $[Cu(mnt)_2]^{2-}$ complexes. For example, $[NMP]_2[Cu(mnt)_2]$ has $g_{av.} = 2.043$ ⁴³ and $[NBu_4]_2[Cu(mnt)_2]$ has $g_{av.} = 2.047$.⁵⁵ All these values are seen to be greater than the free electron value (g_o) of 2.0023, as Cu^{2+} has a more than half filled orbital configuration.⁵⁶ The deviation of g from g_o for such $[Cu(mnt)_2]^{2-}$ species is small however, indicating that a large

proportion of the electron density is delocalised across the complex.⁵⁷ In comparison, [NH₄]₂[CuCl₄] has most of the spin density on the metal and has a value of $g = 2.109$, deviating much more significantly from g_0 .

Over the temperature range studied, the value of g and the line width have a small variation of 0.0058 and 1.48 mT respectively (see figure 3. 8). A lattice of anisotropic magnetic centres will show a large shift at the ordering temperature and so the small shift in g -value observed indicates that the anions can be considered as possessing approximately isotropic Heisenberg spins.⁵⁸ The decreasing values that occur with reduced temperature can be ascribed to demagnetisation^{59, 60} as well as the fact that the copper centre is not perfectly isotropic. The value of g at low temperatures increases again as short-range magnetic ordering is achieved. The shape of the line width versus temperature curve concurs with reported 1-D and quasi 1-D antiferromagnet systems.⁶¹⁻⁶³ Thus the EPR data shows the expected pattern for a square-planar Cu²⁺ approximately Heisenberg centre with electron density delocalised across the ligand and has short-range magnetic ordering occurs around 10 K.

3.2.1.4 Magnetic susceptibility

The molar magnetic susceptibility (χ_M) of [2] is presented in Figure 3. 8 as a function of temperature. It was confirmed that at a temperature = 2 K, the magnetisation increased linearly with applied magnetic fields in the range $0 \text{ T} \leq B \leq 5 \text{ T}$. The susceptibility was recorded at a field of 0.1 T. The magnetic data showed an increase in magnetic susceptibility with reducing temperature to a maximum susceptibility at approximately 10.7 K, a position consistent with the peak displayed in the EPR data.

The temperature-dependent magnetic susceptibility was fitted with the theoretical susceptibility of a $S = \frac{1}{2}$ isotropic Heisenberg chain, known as the Bonner-Fisher model. The closed expression of this model can be found in chapter 1, Equation 1. 11. According to Equation 1. 11, the peak in the magnetic susceptibility occurs at $T_{\max} = 0.6475J/k_B$ and has height $\chi(T_{\max}) = 0.1468Ng^2\beta^2/J$. When the experimental results were fitted over the temperature range $5\text{ K} < T < 300\text{ K}$ they gave a value of $J/k_B = (-16.72 \pm 0.068)\text{ K}$, $T_{\max} = (10.8 \pm 0.044)\text{ K}$, and $\chi(T_{\max}) = (0.0125 \pm 0.00055)\text{ emu mol}^{-1}$

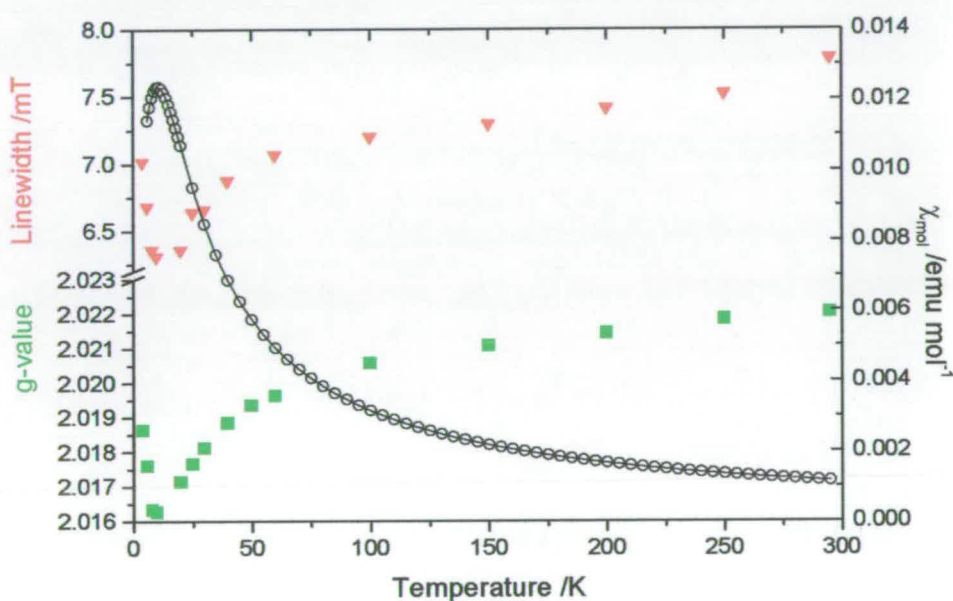


Figure 3. 8 Magnetic properties of [2] as functions of temperature $2 \leq T \leq 300\text{ K}$: g-value (■) and linewidth (▼) from variable temperature EPR studies; molar magnetic susceptibility, χ , from experiments (○), and as fitted by the Bonner-Fisher model (1) with $J/k_B = (-16.718 \pm 0.068)\text{ K}$

(—).

Figure 3. 9 shows the low temperature magnetic susceptibility in the range $0 \text{ K} < T < 18 \text{ K}$. The Bonner-Fisher fit in this restricted temperature range yielded $J/k_B = (-16.165 \pm 0.055) \text{ K}$; the deviation between this value and that obtained from fitting in the range $5 \text{ K} < T < 300 \text{ K}$ is only 3%, and therefore insignificant. It can be seen in Figure 3. 9 that an extrapolation of the Bonner-Fisher model (Equation 1. 11) does not fit the experimental data below 5 K. This was anticipated, as the Bonner-Fisher model breaks down at low temperatures (discussed in section 1.2.4). This section also describes an equation derived by Eggert *et al* that can be used to fit Heisenberg, antiferromagnetic, $S = \frac{1}{2}$ 1D magnetic data to very low temperatures using quantum field theory. This expression is shown in Equation 3. 1. ⁶⁴

$$\chi(T) \approx \chi(0) \left[1 + \frac{1}{2 \ln(T_0/T)} \right], \quad \text{Equation 3. 1}$$

$T_0 \approx 7.7 J/k_B$, and $\chi(0) = Ng^2 \beta^2 / J\pi^2$ is the exact zero-temperature value of the susceptibility.^{65, 66} The equation derived by Eggert *et al* has been shown to be very useful in describing the low-temperature susceptibility of Sr_2CuO_3 which behaves like an almost perfect one-dimensional Heisenberg antiferromagnet with $J/k_B \approx 1700 \text{ K}$.⁶⁷ The low temperature experimental data of [2] (range $0 \text{ K} < T < 3 \text{ K}$) was fit to Equation 3. 1 by Dr. Philip Camp to yield $\chi(0) = (0.00935 \pm 0.000048) \text{ emu mol}^{-1}$, $J/k_B = (-15.4 \pm 2.0) \text{ K}$, and $\chi(T_{\text{max}})/\chi(0) = 1.340 \pm 0.059$, as shown in Figure 3. 9. The observed low-temperature susceptibility exhibits a 'crossover' from the Bonner-Fisher model (Equation 1. 11) to the low temperature Eggert expression (Equation 3. 1) with both fitting parameters seen to be in very good agreement with one another. Thus it

can be said that the magnetic behaviour of [2] is consistent with that of an ideal one-dimensional Heisenberg antiferromagnet down to the lowest measured temperature. This indicates that the magnetic chains within the material are well segregated from one another, giving negligible interchain interactions.

It must be noted that the Eggert model can only be fit to a very small temperature range and the data do not go down to low enough temperatures to observe the inflection characteristic of this model. Without seeing this the deviation from the Bonner-Fisher fit at low temperature could be due to a Curie tail. Thus the magnetic susceptibility needs to be measured down to lower temperatures to see if the low temperature susceptibility decrease to follow the Eggert model or increases due to a Curie tail.

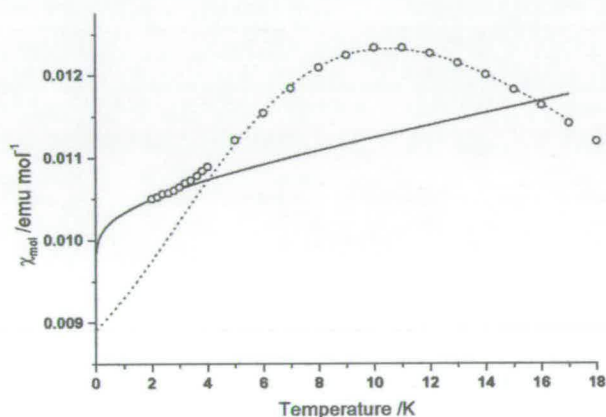


Figure 3. 9 Magnetic susceptibility, χ , of $[BDTA]_2[Cu(mnt)_2]$ in the temperature range

$0 \text{ K} < T < 18 \text{ K}$: experimental results (\circ); Bonner-Fisher curve with
 $J/k_B = (-16.165 \pm 0.055) \text{ K}$ (—); exact low-temperature curve with
 $J/k_B = (-15.4 \pm 2.0) \text{ K}$ (---).

The magnetic interaction within [2] of $J/k_B = (-16.718 \pm 0.068)K$ is surprisingly large compared with other intermolecular, non-bonded magnetic interactions. The crystal structure of the salt suggests that the magnetic exchange pathway lies along the a-axis and is communicated through a long pathway involving the non-magnetic cation as well as the dithiolene ligand. An example of a material that displays magnetic exchange mediated through a non-magnetic counterion is $[NH_4][Ni(mnt)_2] \cdot H_2O$ ^{6, 32} with 3-D ferromagnetic order at $T_c = 4.5 K$. In this example, magnetic exchange between $[Ni(mnt)_2]^-$ through non-magnetic cations appear to give rise to interactions of just a few Kelvin. However, the antiferromagnetic exchange constant for [2] of $J/k_B = (-16.718 \pm 0.068)K$ is significantly larger.

Side-by-side interactions are unusual in metal dithiolene salts, where strong interactions occur more typically within stacks. However, side-by-side interactions have been reported for the $[BEDT-TTF]^{x+}$ cation in $[BEDT-TTF][Ni(dmit)_2]$,⁶⁸ which was found to have semiconducting properties communicated by interaction between $[BEDT-TTF]^{x+}$ molecules, transverse to the alternate stack. Although side-by-side interaction are usually considered to be weak, in this example the calculated overlap integrals in the material showed that the interaction between $[BEDT-TTF]^{x+}$ molecules was over twice as large in the lateral direction as in the stacking direction. Thus giving credibility to the side-by-side pathway in system [2].

3.2.1.5 DFT Calculations

Plane-wave DFT calculations were carried out by Dr. Stewart Clarke on [2] with varying restraints on the magnetic structure. A 1-D antiferromagnetic ground state with the chain lying in the stacking direction was compared with a 1-D antiferromagnetic ground state with side-by-side interactions along the a-axis. It was found that the a-axis 1-D chain gave a lower energy by 0.2 meV, consistent with our analysis of the short intermolecular contacts in the X-ray structure that lie in this direction. In turn the system was restrained to yield a ferromagnetic ground state and the comparison showed the antiferromagnetic ground state was lower in energy than the ferromagnetic ground state by 1.0 meV. The antiferromagnetic interaction along the a-axis was calculated to have a value of $J = -12$ K and remarkably it can be seen to have not only the same sign, but also the same order of magnitude as the measured magnetic exchange coupling of $J \cong -16$ K. Previous publications have used DFT methods with a Gaussian basis set to predict values of coupling constants within isolated binuclear⁶⁹ and polynuclear⁷⁰ transition-metal compounds, showing good correlation with the trends and sign of coupling constants. Also, plane-wave DFT methods have been applied to conducting molecular materials⁷¹ and continuous-lattice systems such as bulk metals.⁷² However, to the best of our knowledge, previous application of plane-wave DFT methods have never before been used to rationalise the magnetic properties and estimate coupling constants within extended-lattice molecular magnetic materials, such as in this work. It is interesting to note that the calculated values obtained for [2] are remarkably close to the experimental data showing a success of the method in reproducing and rationalising the empirical results in this case. This suggests that this novel approach of using DFT calculations to

obtain magnetic rationalisation for such materials could have great potential if applied to related materials.

The proposed coupling mechanism involving an exchange pathway via the $[BDTA]^{x+}$ counterion suggests that some non-zero spin density should be observed on the $[BDTA]^{x+}$ units. The calculated spin density within the unit cell is shown in figure 3. 10 and indicates spin density located principally on the nitrogen atom of the $[BDTA]^+$ cation, corresponding to a 0.011 electron difference, lending weight to the proposed coupling pathway and magnitude of J . The calculations also indicate that much of the spin density within the metal complex is located on the sulphur atoms and this is consistent with the observation of a larger magnetic coupling despite the large distance between copper centres in the material, as well as with the low value of g obtained from the EPR experiment. In summary, the DFT calculations fully support both the observation of an antiferromagnetic ground state with $J \cong -16$ K and also an unusual pathway of a counterion-mediated side-by-side magnetic interaction of metal dithiolene complexes to form a 1-D Heisenberg chain.

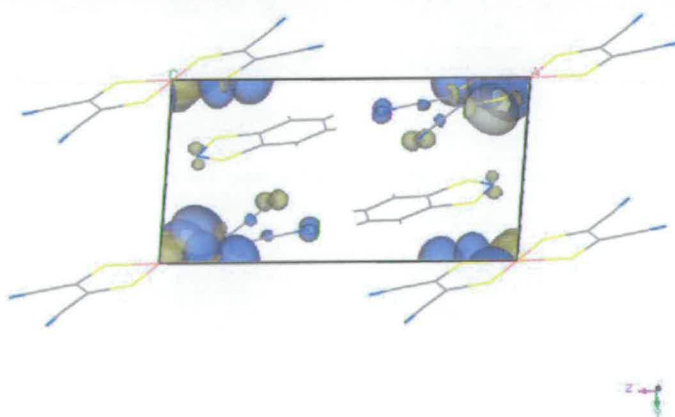


Figure 3. 10 Spin density distribution within the unit cell determined by DFT methods. The spin density on the N atom of the cation can be clearly seen. Electron density isosurfaces are set at $\pm 0.005 \text{ e}/\text{\AA}^3$.

3.2.1.6 Conclusions

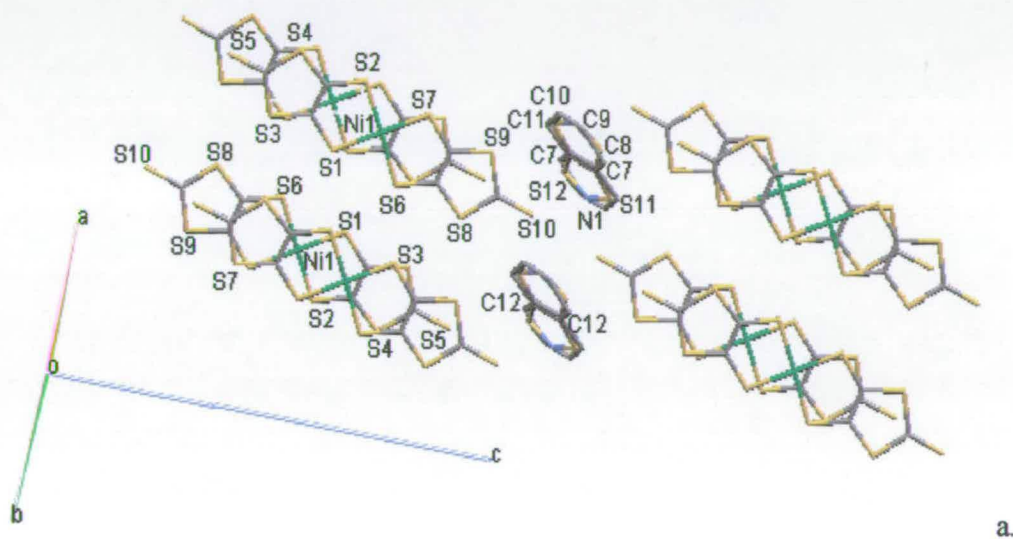
The salt [2] has been synthesised and structurally characterised. It was found to behave as an ideal 1-dimensional Heisenberg antiferromagnetic material from $2 \leq T \leq 300$, with a magnetic coupling constant of $J/k_B = -16.718 \pm 0.068$ K obtained from the Bonner-Fisher model. The data from 2-3 K were fitted to the Eggert model, that better accounts for the low temperature behaviour, with $J/k_B = -15.4 \pm 2$ K, in agreement with the value above. EPR studies confirmed the approximately isotropic nature of the magnetic copper centre and the temperature of the short range magnetic ordering.

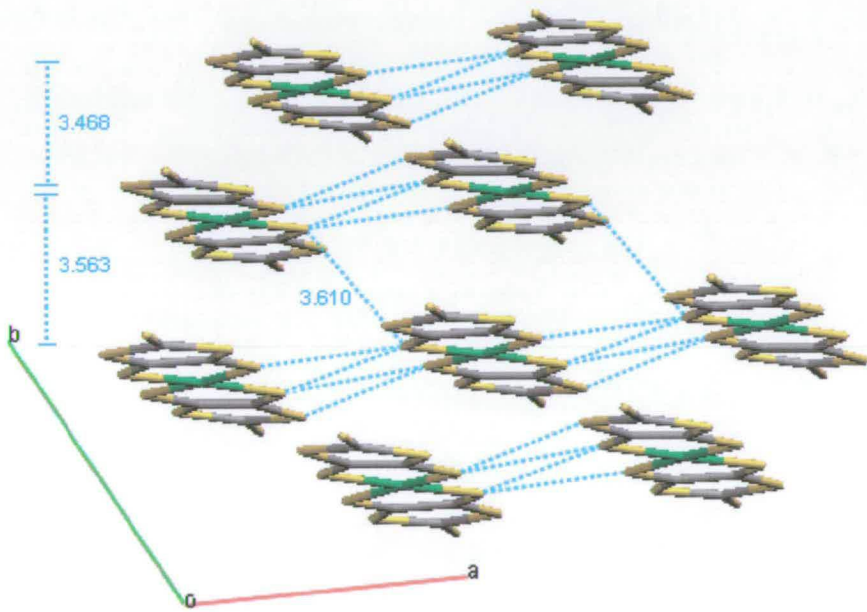
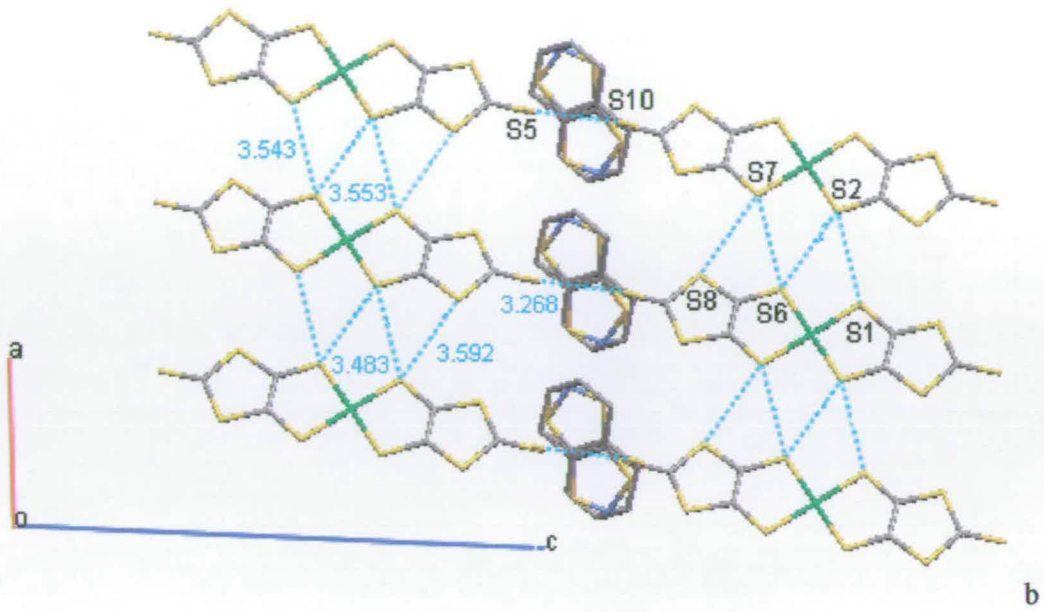
The structure is found to be an alternately stacked system in the b-c plane. Inspection of the X-ray structure suggests that magnetic exchange is propagated along the a-axis through the chain of dithiolene complexes via the (presumed) non-spin carrying [BDTA]^{x+} cation. Although the pathway between magnetic centres is unconventional and long, a relatively strong interaction is observed, attributed to the presences of spin density on the cation as well as the large side-by-side interaction between the sulphur atoms on both the anion and cation. These conclusions were supported by the use of plane-wave DFT computational methods that gave a good estimate of the sign and magnitude of J and also suggested a side-by-side exchange pathway involving some spin density on the [BDTA]^{x+} counterions.

3.2.2 [BDTA][Ni(dmit)₂]₂ [3]

3.2.2.1 Preparation and X-ray structure

Single crystals of [3] were prepared by a slow diffusion of a solution [BDTA]Cl in MeCN with [TBA][Ni(dmit)₂] in a DCM solution. Small, green, hexagonal plate shaped crystals were collected after 12 days.





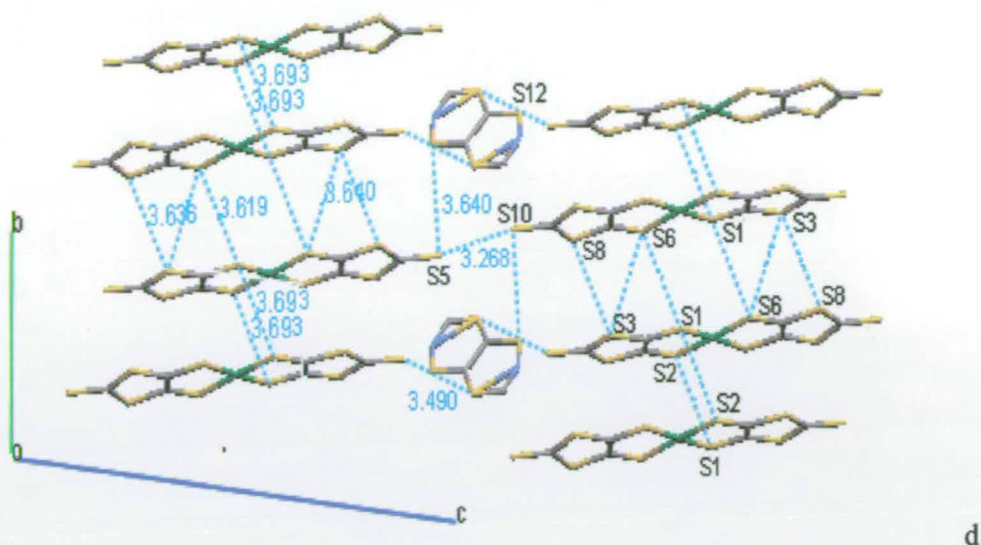


Figure 3. 11. Crystal structure of $[BDTA][Ni(dmit)_2]_2$ a) Viewed down the $[Ni(dmit)_2]$ stack, b) viewed along the b-axis and c) viewed along the c-axis d) viewed along the a-axis. Inter-molecular distances (\AA) smaller the sum of the Van der Waal radii (3.7) are shown.

[3] crystallises to form a 1:2 partially oxidised (charge transfer) material with one $[BDTA]^{x+}$ and two equivalent $[Ni(dmit)_2]^{x/2-}$ molecules per unit cell, suggesting a capacity for conduction. This stoichiometry is rationalised by the redox potentials of $E_{1/2} = +0.15 \text{ V (0/1+)}^{44}$ and $+0.316 \text{ V (1-/0)}^{22}$ for $[BDTA]^+$ and $[Ni(dmit)_2]^-$ which are sufficiently similar to suggest that electron transfer can accompany crystallisation. The crystals have the space group $P\bar{1}$ with one $[Ni(dmit)_2]^{x/2-}$ and half a $[BDTA]^{x+}$ cation per asymmetric unit, with a mirror plane down the $[BDTA]^{x+}$ creating an intrinsic disorder in the direction that each $[BDTA]^{x+}$ faces. $[Ni(dmit)_2]^{x/2-}$ stack along an axis diagonally between the a and b axis (figure 3. 11a.) with 2 molecules per repeat unit. It can be seen that they stack staggered to one another within the repeat unit (figure 3. 11a), which is not unusual in this sort of system. In fact the crystal's structural motif is very similar to that of $[Me_4N][Ni(dmit)_2]_2$.¹³ It can also be seen that there is a slight amount of

dimerisation within the stacks, as the intermolecular distances between each independent [Ni(dmit)₂]^{x-} plane alternates between 3.437 and 3.574 Å down the stack (Figure 3. 11c). Short contacts are seen between [Ni(dmit)₂]^{x/2-} complexes on the adjacent stacks, both side-by-side (figure 3. 11b & c. between S1-S2, S6-S2, S6-S7 and S8-S7) and diagonally (figure 3.11c. between S2-S2, and Figure 3.11d S8-S3, S6-S3 and S6-S1 {& symmetry equivalents}) as well as to the perpendicular adjacent stack through the terminal S5-S10 (figure 3.11b & d). Short contacts are also seen between the terminal sulphur atoms and the [BDTA]^{x+} cation (figure 3.11d) although only half of these are true contacts depending on the disorder. Thus it can be seen that the crystal structure of [BDTA][Ni(dmit)₂]₂ contains short contacts in all 3 dimensions (stacking, side-by-side, diagonally, and end-on) suggesting the possibility that the material could be a 3D conductor.

3.2.2.2 Conductivity.

The room temperature conductivity (σ_{RT}) of a compressed pellet of [BDTA][Ni(dmit)₂]₂ powder sample = $1.0 \times 10^{-1} \text{ S cm}^{-1}$. The temperature dependence of the conductivity was measured in the temperature range 80-200 K and the salt was found to be a small band gap semiconductor with an activation energy (E_a) of 0.19 eV (figure 3.12).

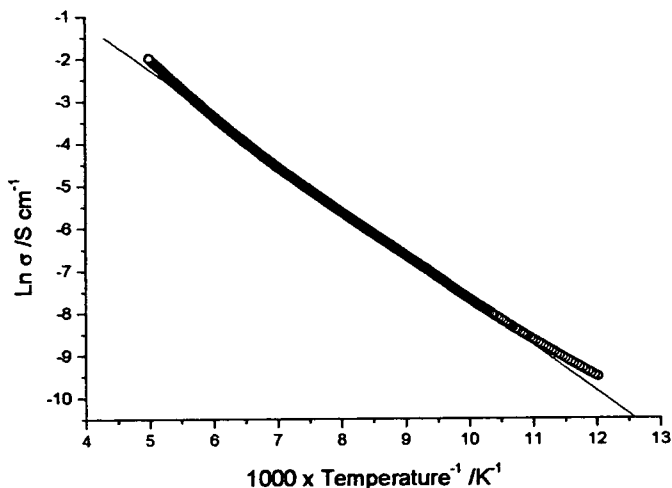


Figure 3. 12 Temperature dependence of conductivity (σ) of [3] at ambient pressure; \circ = experimental data and — = linear regression giving activation energy (E_a) = 0.19eV.

It can be seen from the plot that the data fits the linear regression well, showing that there are no phase transitions across the temperature range. Single crystals large enough to perform conductivity experiments on could not be obtained and so it is unclear as to whether or not the activation energy arises from grain boundaries within the pellet powder sample or is intrinsic to the material. Also no conclusions can be drawn concerning the relative magnitude of conductivity along different axes.

A band diagram of this material was calculated by Dr. Stewart Clark using recently developed plane-wave DFT methods, and as such is one of the very few molecular conducting systems to be modelled by this method to calculate a band structure. The band structure diagram of [3] shows considerable dispersion in the stacking and side-by-side directions (figure 3. 13) which can be expected as it is seen in many conducting $[\text{Ni}(\text{dmit})_2]^{x/2-}$ systems.⁸ Strong coupling through side-by-side interaction of $[\text{Ni}(\text{dmit})_2]^{x/2-}$, demonstrated by the large dispersion in this direction, is

less common than through the stacking direction but has been documented before through HOMO on the sulphur atoms of [BEDT-TTF]^{x+} in [BEDT-TTF][Ni(dmit)₂]⁶⁸. Although the intermolecular distances are the largest of the short contacts in the stacking direction, the band dispersion is the greatest. This is considered to be due to the large LUMO π orbital overlap that is common in [Ni(dmit)₂]^{x-} systems. There is negligible dispersion through the end-on interactions through the terminal S5-S10, despite the short contact distance, thought to be due to a lack of orbital overlap symmetry. Thus, overall this material is a 2D narrow band gap semiconductor. It is interesting to note that it is the HOMO of [BDTA]^{x+} that forms the frontier orbital at the Fermi level. This is very similar in energy to the LUMO of the [Ni(dmit)₂]^{x/2-}, and it is between these two bands that the very small band gap can be seen in the stacking direction. This band gap is actually the result of an avoided crossing, showing that conduction is propagated down the stack mediated by the [BDTA]^{x+} cation. It is assumed that [BDTA]^{x+} usually has a +1 oxidation state, making it diamagnetic and a closed shell cation. However this is not the case in this system, as the values of the charge calculated for each atom were summed and it was found that the anion carries a charge of -0.12, with the cation having a partial oxidation state of +0.24, making [3] the charge transfer salt [BDTA]^{0.24+}[Ni(dmit)₂]₂^{0.12-}.

Indeed, the band diagram shows that [BDTA]^{x+} must have a fractional charge to be open shell and participate in conduction. It was seen that [2] has magnetic interactions that rely on spin density being present on [BDTA]^{x+} (section 3.2.1.5) so a fractional charge on the cation in this material, although never seen prior to this work, is not unreasonable.

CASTEP Band Structure

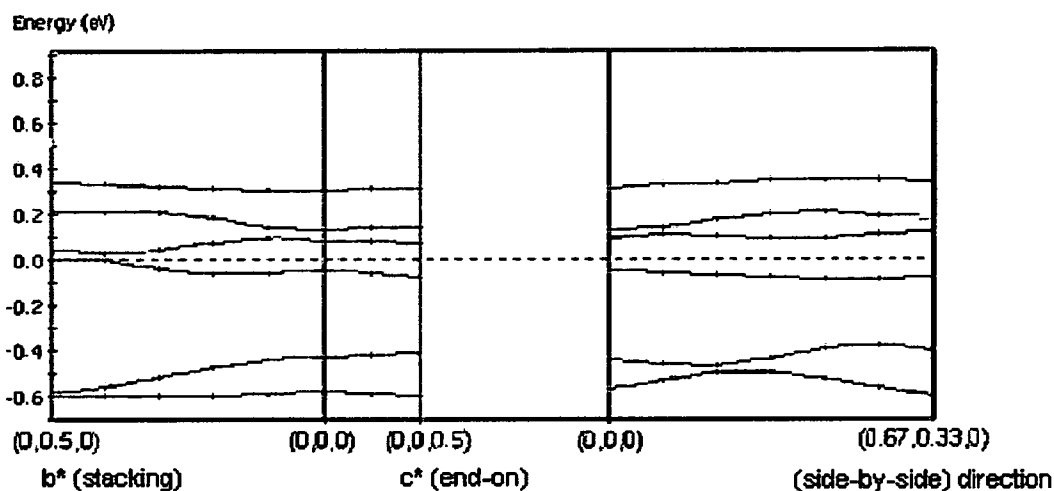


Figure 3. 13. Band structure of $[BDTA][Ni(dmit)_2]_2$. — = Fermi level.

3.2.2.3 Magnetic Susceptibility.

Figure 3.14 shows a plot of the molar magnetic susceptibility (χ_M) versus temperature of [3]. The data show a peak at 25 K, with an increase in susceptibility at lower temperatures. The characteristic magnetic susceptibility for a conducting material is usually very close being independent of temperature. However this is not the case with [3]. This can be rationalised by the fact that not all the electrons take part in conduction and many are localised. Thus, in order to model this magnetic data the system will be thought of as localised, with the intention of considering this discrepancy in light of future experimental data.

It can be seen from the results of the DFT calculations that $[BDTA]^{+0.24}$ carries a fraction of paramagnetic electron density that can be considered as approximately $\frac{3}{4}$ of an electron. As the cations are arranged at some distance from one another in the crystal structure, the magnetic effect from the cation can be predicted to be of Curie-

Weiss character. The peak at low temperature shows that low-dimensional short-range order is achieved. The dimensionality of this order cannot be ascertained completely with full confidence, as many different magnetic pathways could be possible. However, it would seem appropriate when considering both the magnetic and crystallographic data to use the Bonner-Fisher chain model to represent the fraction of the data that corresponds with the [Ni(dmit)₂]^{-0.12} stacking system (which, from the band diagram, seems to be the most prevalent interaction). For this reason and ease of interpretation, the formula weight used in the magnetic susceptibility will be [BDTA]₄[Ni(dmit)₂]₈ as this will provide approximately three electrons over the cations and one electron delocalised over the 8 anions to achieve the $S = \frac{1}{2}$ requirement. It is thus predicted that this magnetic data represents a mixture of Curie-Weiss behaviour from the cation and 1-D chain interaction down the anion stack.

The model fit gave a Curie constant of 0.375 emu K mol⁻¹, which is in exact agreement with the theoretical value for an unpaired electron. The ratio of Curie-Weiss to Bonner-Fisher electrons is approximately 3:1, reinforcing the DFT calculations that show a 3:1 electron ratio between the cation and anion, giving 3 electrons localised on 4 [BDTA]^{+0.24} with 1 electron delocalised over 8 [Ni(dmit)₂]^{-0.12} units within a stack. The magnetic coupling between electrons in this chain is strong with $J/k_b = -54.65$ K. This is also seen in the large dispersion shown in the [Ni(dmit)₂]^{-0.12} HOMO and LUMOs in the band diagram.

It must be reinforced that the models used to fit these data are only predicted to be good models and as such cannot be said to accurately represent the system. It could be that the system has more 2D character or that other equations can model the cation behaviour better than Curie-Weiss. The fact of the matter remains that when fitting data

to a combination of two equations, many parameters are used which makes it possible to fit many models to the same data set. In order to validate this fit further, the value of $g = 2$ was fixed, so it was only the coupling constant, Weiss constant and ratios that were varied in the fit. From the fact that the resulting parameters represent the observations made from the DFT calculations, it can be concluded that this was a reasonable model to use. However this does not dismiss the fact that other low dimensional models may represent the data more accurately.

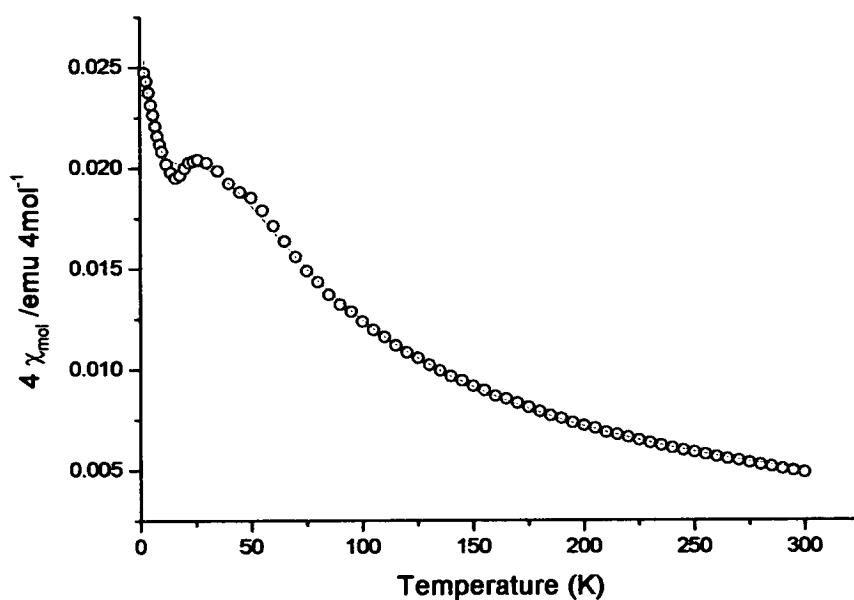


Figure 3. 14 Magnetic susceptibility χ_{mol} verse temperature of $4 \times [3]$; \circ = experimental data and $—$ = as fitted to $\chi_M(T) = 4((x) \chi_{Curie Weiss} + (1-x) \chi_{Bonner Fisher})$, with Curie constant = 0.375, Weiss constant = -8.05 and $J/k_b = -54.65$ K, with 73.3% of the contribution Curie Weiss character.

3.2.2.4 Conclusions.

Salt [3] was found to be a very narrow band gap 2D semiconductor with $\sigma_{RT} = 1 \times 10^{-1} \text{ S cm}^{-1}$. Conduction is thought to occur in the stacking direction and through side-by-side interaction in adjacent stacks. It was found from DFT calculations that [3] is a charge transfer salt with the cation carrying a charge of +0.24 and both anions having a charge of -0.12 each. The band diagram shows that the HOMO of cation [BDTA]^{+0.24} and the LUMO of [Ni(dmit)₂]^{-0.12} are the frontier orbitals with the narrow band gap lying between them in the stacking direction. This narrow band gap only occurs as the result of an avoided crossing and the band diagram indicates that conduction is propagated by both of these orbitals. This is the first reported incidence of the cation [BDTA]^{x+} carrying a partial charge and thus behaving as an open shell cation being involved in charge transfer and conduction. This situation has however been conceivable as [BDTA]^{x+} has been seen to carry spin density on material [2].

The magnetic data can be fitted to a combination of 73.3% Curie-Weiss and 26.7% 1-D, $S = \frac{1}{2}$ antiferromagnetic chain behaviour that reinforces the model presented in the DFT calculation.

3.2.3 [TBA]₄[Pd₈(dmit)₁₀][4]

3.2.3.1 Preparation and X-ray crystal structure

To complement the work carried out in section 3.2.2, crystallisations of the Pd and Pt analogues of [3] were attempted. This was performed using the same methods as

before as well as evaporation and cooling methods, but no crystals occurred in any of the [BDTA]_x[Pt(dmit)₂] crystallisation set ups. However, crystals were obtained from the [BDTA]_x[Pd(dmit)₂] crystallisation setup that diffused a solution of [BDTA]Cl in MeCN into [TBA][Pd(dmit)₂] in DCM at 263 K.

These crystals did not contain any [BDTA]^x cations, but instead were found to be a cluster rearrangement of the starting material of the form [TBA]₄[Pd₈(dmit)₁₀] [4]. In this structure four [Pd(dmit)₂]^{x-} units form an outer semicircular cage that are linked by four inner palladium metal ions. These four inner metals are also bound to two (dmit) units pointing out of the open semicircle. This structural motif is very unusual and the anionic part is shown in figure 3. 15. Unfortunately there is a very large amount of disorder in the cations, meaning that refining the structure to a high level would be very time consuming, (at present R = 15 %). As the structure of [4] shown that no [BDTA]⁺ cations have been incorporated and nor has a stacked system been achieved, the complete structural refinement and magnetic measurements have not been carried out.

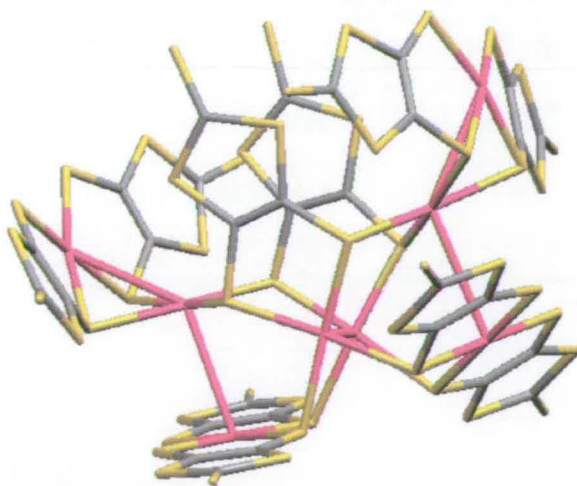
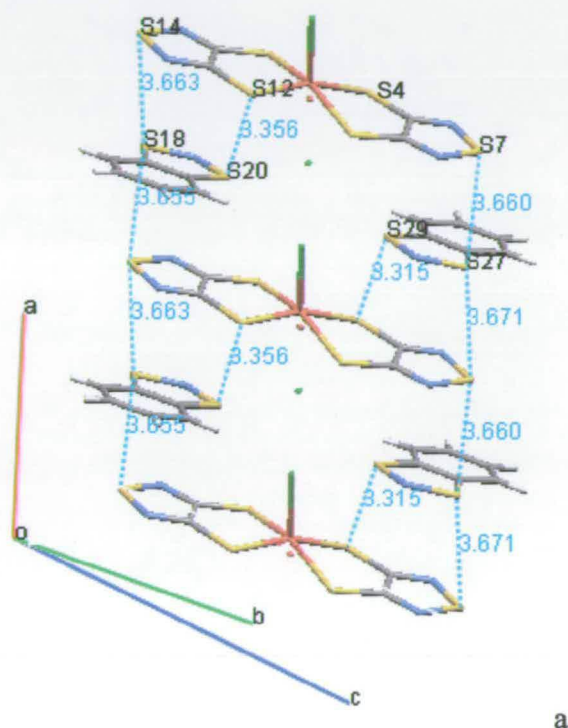


Figure 3. 15 Crystal structure of anionic cage structure of [Pd₈(dmit)₁₀]⁴⁻ cations not shown

3.2.4 [BDTA]2[Fe(tdas)2][Cl] [5]

3.2.4.1 Preparation and X-ray crystal structure

Single crystals of [5] were prepared by a slow diffusion of [BDTA]Cl in THF with [TBA][Fe(tdas)₂] in a DCM solution. Small, dark, rectangular shaped crystals were collected after 40 days.



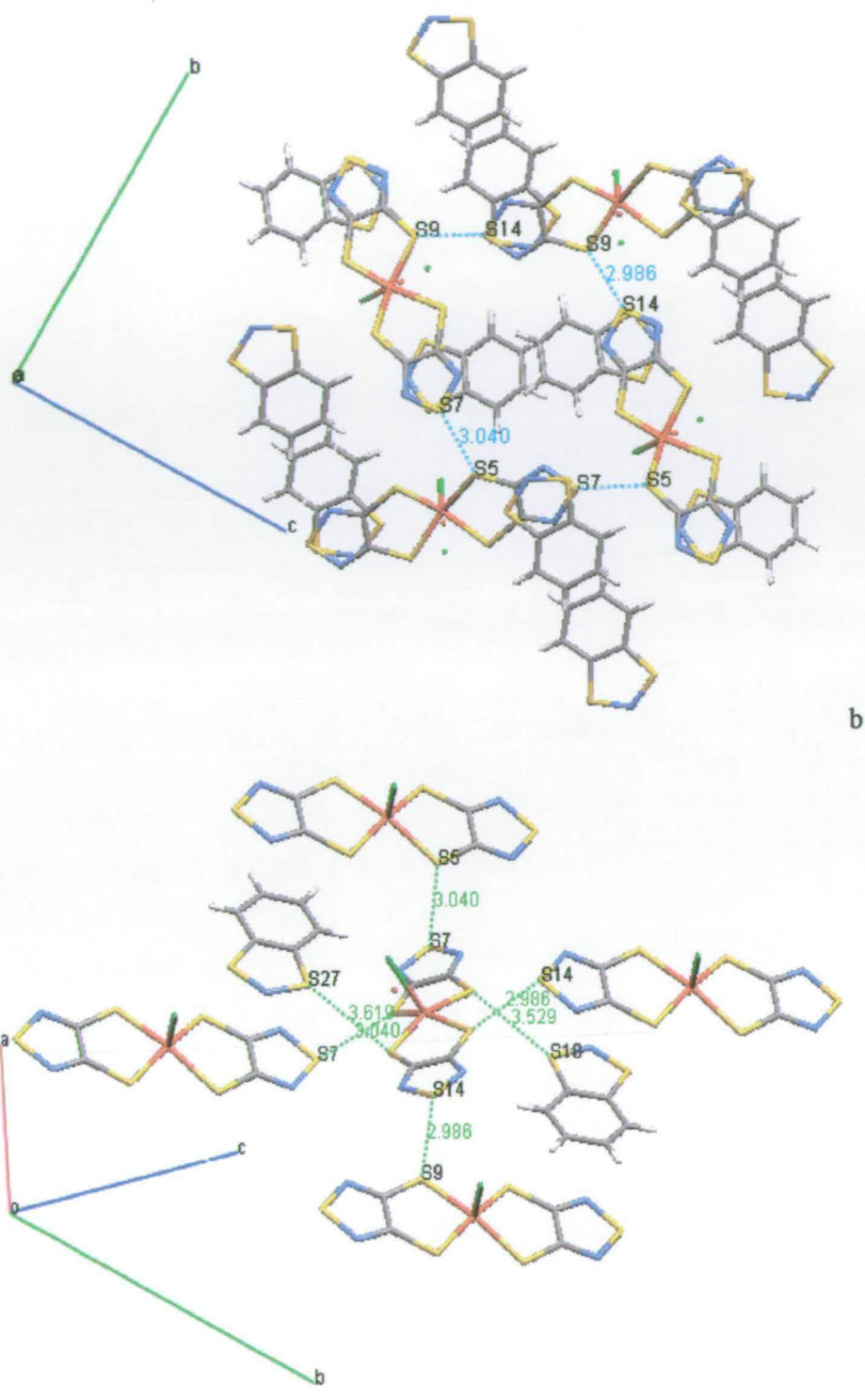


Figure 3.16 Crystal structure of [5] ($[BDTA]_2[Fe(tdas)_2][Cl]$) a) View of the a-axial stacking, b) viewed along the a-axis, c) Showing the interstack short contacts.

The salt [5] crystallises in a 2:1 stoichiometry of BDTA to [Fe(tdas)₂.Cl]. The iron centre is 5-coordinate, pyramidal and puckered towards the Fe-Cl bond. As a Cl atom is coordinated to the anion, the iron centre can be considered to be Fe³⁺ and thus paramagnetic. There is intrinsic disorder in the direction of this bond. This material crystallises in the space group *Pn* forming alternating stacks of [Fe(tdas)₂.Cl]²⁻ and pairs of [BDTA]⁺ cations between them along the a-axis (figure 3. 16a). The asymmetric unit can be seen to be a [BDTA]⁺ stacked below, at right angles to and, overlapping one side of the dithiolene complex, with the other [BDTA]⁺ molecule diagonally opposite and above the dithiolene plane, forming a “Z” shaped stacking unit in a zigzag motif if viewed down the stack (Figure 3. 16b). The view through the stack is shown in figure 3. 16a and depicts 2 asymmetric units per repeat unit. Short contacts are seen between the peripheral S7 and S14 on the dithiolene and S27 and S18 on the adjacent cation. There are also much shorter contacts between S4 and S12 on [Fe(tdas)₂.Cl] and adjacent S29 and S20 on opposite [BDTA]⁺ cations respectively. These contacts should be short enough to allow π -orbital overlap and hopefully magnetic interactions through the stack. Between each stacking unit there are short contacts between each terminal sulphur on the [Fe(tdas)₂.Cl] and the adjacent [Fe(tdas)₂.Cl] in the next “zigzag” (S7-S5, 3.040 Å and S14-S9, 2.980 Å, figure 3.16b). Each stack is tilted at an angle $\approx 16^\circ$ allowing the short contacts to form a 2D plane of interactions diagonally through the stacking systems (figure 3.16b & c). It should also be noted that each dithiolene complex forms a short contact with the nearest [BDTA]⁺ cation on the adjacent stack (S4-S18, S12-S27, figure 3. 16c). Thus it can be said that the solid state structure of [BDTA]₂[Fe(tdas)₂.Cl] is composed of mixed alternating cation-anion stacks with short contacts through the stacks, as well as in 3 dimensions between each stacking unit. It is worth noting here

that the structure of [5] obtained is ideal with respect to the original intention. An initial aim was to study magnetic interaction through a mixed cation-anion stack. Indeed this is the case here, with short contacts for intermolecular interactions continuous through the stacked system (which has not been previously achieved in any [M(tdas)₂]^{x-} material) as well as the added stability of short contacts in 3 dimensions. It is also worth noting that [M(tdas)₂]^{x-} is the most unlikely of the dithiolenes anions to be achieved this as [M(tdas)₂]⁻ complexes usually dimerise to form diamagnetic materials. Thus this is the first example of a [M(tdas)₂]⁻ anion containing material to form an integrated anion-cation, non-dimerised, stacking motif in the crystal structure.

3.2.4.2 Magnetic susceptibility

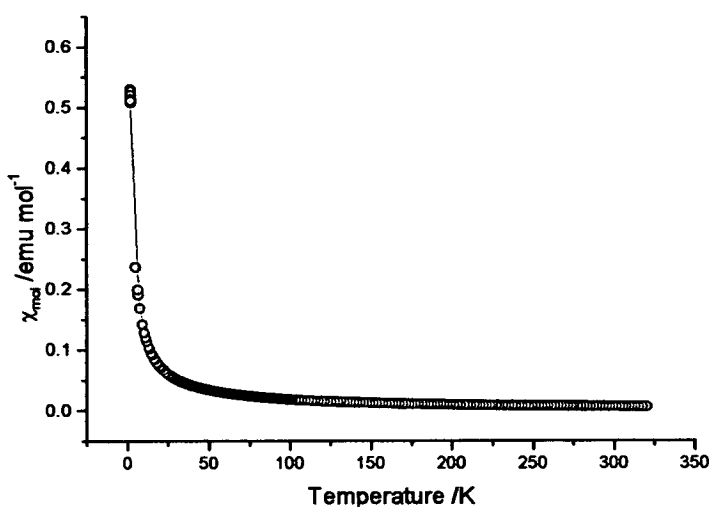


Figure 3. 17 Magnetic susceptibility χ_m versus temperature of [BDTA]₂[Fe(tdas)₂Cl] [5]; ○ = experimental data and — = as fitted to $\chi_M(T) = \chi_{\text{Curie Weiss}}$, with Curie constant = 1.50 ± 0.011 , Weiss constant = -0.95 ± 0.021 .

The molar magnetic susceptibility (χ_M) versus temperature of [BDTA]₂[Fe(tdas)₂Cl] is plotted in figure 3. 17. The data over the whole temperature range can be seen to fit the Curie-Weiss model very well, with a Curie constant = 1.50 ± 0.011 emu K mol⁻¹ and a Weiss constant = -0.95 ± 0.021 K. The high temperature data were also fitted to the Curie-Weiss model ($80 < T < 320$ K) to eliminate any deviations from the model at low temperature due to any potential long-range ordering. Constants obtained were $C = 1.94 \pm 0.005$ emu K mol⁻¹ and $\theta = -6.27 \pm 0.018$ K. As the iron centre is in an approximate square-planar site, one can expect 3 unpaired electrons, as degeneracy of higher energy d-orbitals is lost in this configuration. 3 unpaired electrons will give a theoretical spin-only Curie constant of 1.875 emu K mol⁻¹, which is in close agreement with the higher temperature experimental value. This, along with the small Weiss constant, implies that [5] behaves as a paramagnetic material with the possibility of antiferromagnetic interactions at very low temperature. However, it can be seen from the magnetic data that there are not the characteristic peaks usually seen at the onset of long-range antiferromagnetic order. It can thus be concluded that, despite the very promising crystal structure, [5] has no strong intermolecular interaction and behaves as a paramagnet in the solid state. It does appear that antiferromagnetic interactions do occur at very low temperature, but any characteristic peak must appear below 2 K so cannot be analysed any further.

3.2.5 [BDTA]₂[Ni(tdas)₂] [6]

3.2.5.1 Preparation and X-ray structure

Single crystals of [6] were prepared by a slow diffusion of [BDTA]Cl in either THF, MeCN or EtOH with [TBA][Ni(tdas)₂] in a DCM solution. Small, dark, needle shaped crystals were collected after between 20–43 days depending on the solvent.

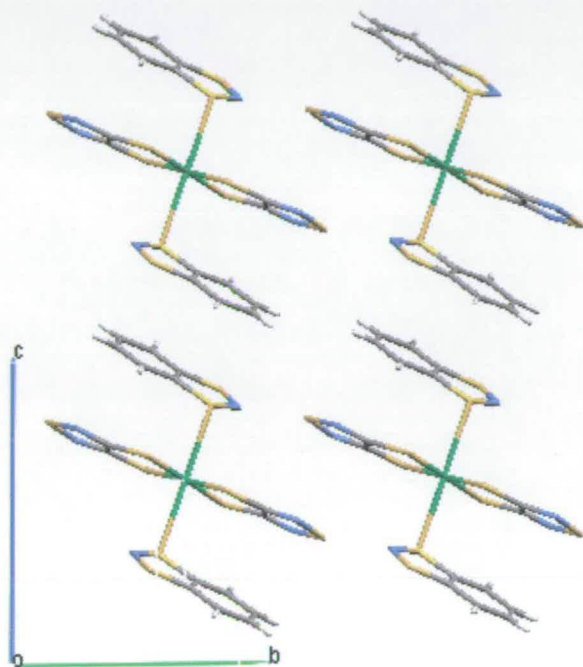


Figure 3. 18 Crystal structure of [BDTA]₂[Ni(tdas)₂] View along the a-axis.

Salt [6] was crystallised many times in different solvents and conditions and always yielded the 2:1 stoichiometric crystal structure shown in figure 3. 18. This was unintended, as the intended 1:1 stoichiometry would give a Ni³⁺ paramagnetic centre whereas this 2:1 material yields a Ni²⁺ complex, which is diamagnetic. Again, with

hindsight, this outcome is expected when one considers the redox potentials shown in table 3.1 (overleaf).

The salt [6] crystallises in the space group $P_{21/n}$ and takes the form of a stacked structure along the direction of the c axis. Each $[BDTA]_2[Ni(\text{tdas})_2]$ unit is tilted 23.12° out of the plane, perpendicular to the stacking axis, forming sheets of stacks, with alternate sheets tilted towards the b -axis then away from the b -axis. The structure does not display short contacts in the stacking direction. Thus, it could be assumed that even if the material were not diamagnetic, interesting long-range magnetic interactions would not be expected.

3.3 Summary and Conclusion

In summary, crystalline samples of $[BDTA]_x[M(\text{dithiolene})_2]$ salts were easily obtained through slow solution diffusion of each starting material into one another as a method of crystallisation. Using two different solvents that do not mix readily slowed the diffusion down and thus enhanced the crystallinity of the products. DCM was the chosen solvent for the bottom layer that contained the metal dithiolene starting material, and the solvent to dissolve $[BDTA].Cl$ to form the top layer could be varied greatly due to the extensive solubility of $[BDTA].Cl$. Out of these products [1]-[6] several surprises were encountered with respect to the stoichiometry of the salts. However, when one compared the redox potentials of the starting materials, the reason becomes obvious and these stoichiometries are simply a result of the preferred electrochemistry of the component cations and anions. This is summarised in table 3.1.

Cation	$E_{1/2 \text{ ox}} \text{ (V)} 0 \rightarrow 1+$		Reference		
[BDTA]	+ 0.15				44
Anions	$E_{1/2 \text{ ox}} \text{ (V)} 2- \rightarrow 1-$	$E_{1/2 \text{ ox}} \text{ (V)} 1- \rightarrow 0$	[BDTA] ⁺ : Anion ratio	Anion formal oxidation state	
[Ni(ddd _t) ₂] ^a [1]	-0.81	0	0:1	0	22
[Cu(mnt) ₂] [2]	+ 0.34	+1.28	2:1	-2	22, 75
[Ni(dmit) ₂] [3]	-0.19	+0.316	1:2	-0.12	22
[Pd(dmit) ₂] [4]	+0.10	-	N/A	[Pd ₈ (dmit) ₁₀] ⁻⁴	74
[Fe(tdas) ₂] [5]	-0.22	+0.94	2:1	[Fe(tdas) ₂ Cl] ⁻²	75
[Ni(tdas) ₂] [6]	+0.18	-	2:1	-2	22

Table 3. 1 Redox potentials of components of the salts, along with salt stoichiometry. All potentials (unless otherwise stated) measured in MeCN solvent with SCE reference electrode. (^a In DMF with Ag/AgCl reference electrode)

From this table it can be seen that [Ni(ddd_t)₂]⁻ easily oxidises to [Ni(ddd_t)₂]⁰ and [Ni(dmit)₂]⁻ can easily be partially oxidised to [Ni(dmit)₂]^{0.12-}. It can also be seen from the redox potentials that [Pd(dmit)₂]⁻ could have been reduced by [BDTA]⁺. However, due to the complexity of the structure of [4] it is difficult to tell if a redox reaction has occurred, or if the product is merely a result of a rearrangement in solution over a long period of time.

Out of the four [BDTA]^{x+} salts successfully synthesised ([2], [3], [5] and [6]), interesting low dimensional interactions were seen in two ([2] and [3]). The remaining two were found to be a diamagnetic [6] and a paramagnetic material [5]. However, all the [BDTA]^{x+} salt materials formed stacked crystal structures, and in all but one case ([3]), the stacks were comprised of a mixed arrangement of the anion and [BDTA]^{x+} cation. To this end, the choice of cation has been entirely successful. Two examples to highlight this success are the similar stacked structures of [2] and [5]. Both of these

structures are made up of tilted stacks of alternating layers of anions and cations, with [5] being the first example of such a motif for a [M(tdas)₂]^{x+} system. Unfortunately for both of these materials, the few short contacts present in the stacking direction were not enough to propagate magnetic interactions *through* the stack. Indeed, for [5] it is thought that an antiferromagnetic interaction occurs but at too low a temperature to readily analyse and state any definite pathway of interaction. [2] displays magnetic interaction transverse to the stacking direction. [6] is the other material to display alternating anion cation stacks, but these show one anion layer with two cation layers between, making any through stack interactions highly unlikely. No magnetic interactions are seen in this material as it was found to be diamagnetic.

Although [BDTA]^{x+} is not integrated into the stack, the structure of [3] shows stacked anions in close enough proximity to the cations to allow interactions. Thus [2] and [3] display overall long-range order in the solid state. [2] was found to have short contacts that provide intermolecular overlap between anions and cations in a side-by-side array along the a-axis between adjacent stacking motifs. The side-by-side interactions facilitate long-range antiferromagnetic order in the form of a near perfect 1D, spin ½, Heisenberg, antiferromagnetic chain with $J/k_b = 16.718 \pm 0.068$ K. Plane wave DFT calculations were used to model this system and confirmed the direction of interaction. The calculations also found some spin density on the nitrogen atom in the cation, dispelling the convention for [BDTA]^{x+} cations to be diamagnetic. The calculations also correctly predicted the value of coupling within a few degrees K. Such a strong side-by-side interaction over such a long pathway is unusual and thought to be achieved by a strong overlap of the dithiolene π -HOMOs as well as the involvement of the cation.

[3] was found to be a charge transfer salt capable of conduction. The material formed a 2D narrow band gap semiconductor with $\sigma_{RT} = 0.1 \text{ S cm}^{-1}$. Again, plane wave DFT calculations were utilised to rationalise the electronic properties, in this case to construct a band diagram of the materials electronic structure. The charges on each atom were summed to give an overall charge on the anion of -0.12 giving a partial charge of $+0.24$ on the cation. Thus, [3] is the first example of a material in which [BDTA]^{+0.24} carries a partial charge and is thus an open shell cation that can participate in conduction. In this structure, conduction is greatest through the stacking direction and through side-by-side interactions, but conduction is not observed through end-on interactions of the terminal sulphur atoms on [Ni(dmit)₂]^{-0.12}, despite the short contact distance. This is again due to the overlap symmetry of the sulphur π -HOMO and LUMOs being greatest in the stacking direction and providing no real overlap for an end-on interaction. Interestingly, it is the HOMO of [BDTA]^{+0.24} and a LUMO of [Ni(dmit)₂]^{-0.12} that are the frontier orbitals below and above the Fermi surface, forming a very small band gap as a result of an avoided crossing, inferring that conduction is propagated by these two orbitals, mainly in the stacking direction.

In conclusion, dithiolene salts of [BDTA]^{x+} have produced; a near perfect 1-D Heisenberg antiferromagnetic system, a paramagnetic and a 2D semiconducting material. These compounds exhibit several exciting characteristics. Firstly, the compounds were synthesised and crystallised by means of a very simple slow precipitation method. Secondly, the crystal structural motifs of integrated stacks are what was ideally sought and predicted for such salts. Thirdly, these materials display a number of unusual sulphur intermolecular interactions (side-by-side) that yield overlap to propagate long-range electronic cooperation through the structure. Fourthly, and

perhaps one of the most remarkable features of these materials is the role of the $[BDTA]^{x+}$ cation. Previously this cation was considered diamagnetic and closed shell, but here we see examples of the cation behaving as an open shell cation, carrying spin density to propagate a magnetic interaction, as well having the ability to carry a partial charge to form a conducting component of [3].

3.4 Experimental

All cations and anions used were synthesised by literature methods or bought from Sigma-Aldrich. The starting materials $BDTA.Cl$,⁷⁶ $TTTA$,¹⁷ and $bbDTDA$ ⁷⁷ were all synthesised by Yoshikatsu Umezono and other co workers of Prof. Kunio Awaga's group in Japan. The Starting materials $[TBA][Ni(\text{ddd}t)_2]$,⁷⁸ $[TBA]_2[Cu(\text{mnt})_2]$,⁷⁹ $[TBA][Pd(\text{dmit})_2]$, $[TBA][Pt(\text{dmit})_2]$, $[TBA][Ni(\text{dmit})_2]$,^{7, 80} $[TBA][Ni(\text{tdas})_2]$ and $[TBA][Fe(\text{tdas})_2]$ ¹⁸ were prepared by the author from literature methods.

3.4.1 Preparation of $[BDTA]_x[M(\text{dithiolene})_2]$ [1]-[6]

All $[BDTA]_x[M(\text{dithiolene})_2]$ salts were prepared by layering $BDTA.Cl$ in MeCN on top of $[TBA]_x[M(\text{dithiolene})_2]$ in a dichloromethane solution. The microcrystalline bulk sample was washed with MeCN and Ether and analysed by CHN. Further bulk samples were prepared by mixing stoichiometric solutions of each anion and cation starting material in MeCN to give a fast precipitation of product in a high yield (typically 90-98%). Powder X-ray diffraction was used to establish the sample was the same composition as the single crystal used to determine the structure. The bulk

sample was then used for the magnetic and EPR measurements. Products [1] and [4] were collected from crystallisations and no bulk sample was produced.

3.4.1.1 Analysis and Structures

3.4.1.1.1 [TBA][Ni(dddt)₂]

CHN for C₂₆H₄₈NNiS₈. Calculated; C, 45.30; H, 6.97; N, 2.03. Found; C, 46.21; H, 7.00; N, 2.00%

3.4.1.1.2 [TBA]₂[Cu(mnt)₂]

CHN for C₄₀H₇₂CuN₆S₄. Calculated; C, 57.96; H, 8.76; N, 10.14. Found; C, 57.65; H, 8.72; N, 10.12%

3.4.1.1.3 [TBA][Ni(dmit)₂]

CHN for C₂₂H₃₆NNiS₁₀. Calculated; C, 38.08; H, 5.23; N, 2.02. Found; C, 37.88; H, 5.48; N, 2.08 %

3.4.1.1.4 [TBA][Pd(dmit)₂]

CHN for C₂₂H₃₆NPdS₁₀. Calculated; C, 35.63; H, 4.89; N, 1.89. Found; C, 37.12; H, 5.11; N, 1.27 %

3.4.1.1.5 [TBA]₂[Ni(tdas)₂]

CHN for C₃₆H₇₂N₆NiS₆. Calculated; C, 51.47; H, 8.64; N, 10.00 Found; C, 51.54; H, 8.89; N, 9.93 %

3.4.1.1.6 [TBA][Fe(tdas)₂]

CHN for C₂₀H₃₆lFeN₅S₆. Calculated; C, 40.39; H, 6.10; N, 11.77. Found; C, 40.60; H, 6.35; N, 11.53 %

3.4.1.1.7 [Ni(dddtt)₂] [1]

Further analysis was not performed on [1] as the generic crystallisation procedure did not yield a [dithiazolyl]_x[M(dithiolene)₂] salt.

X-ray Crystallography C₁₀H₁₂NiS₁₈, M = 447.4, Orthorhombic, *a* = 7.5560(3), *b* = 13.0270(6), *c* = 16.1270(6) Å, α = β = γ = 90° U = 1587.41(11) Å³, T = 298 K, space group I₂₂₂, μ(Mo-Kα) = 1.91 mm⁻¹, 1890 reflections were measured, (R_{int} = 0.156) which were used in all calculations. The final wR(F²) was 0.358. (For full CIF appendix chapter 3)

3.4.1.1.8 [BDTA]₂[Cu(mnt)₂] [2]

CHN for C₂₀H₈CuN₆S₈. Calculated; C, 36.82; H, 1.24; N, 12.88. Found; C, 37.25; H, 1.21; N, 12.56%

X-ray Crystallography data- C₂₀H₈CuN₆S₈, M = 652.378, Triclinic, $a = 6.7870(4)$, $b = 7.1930(4)$, $c = 13.2820(10)$ Å, $\alpha = 83.347(2)$, $\beta = 81.029(2)$, $\gamma = 73.646(5)^\circ$ U = 612.79(7) Å³, T = 296 K, space group P1, Z = 1, $\mu(\text{Mo-K}\alpha) = 1.9 \text{ mm}^{-1}$, 4311 reflections were measured, 2621 independent reflections ($R_{\text{int}} = 0.0214$) which were used in all calculations. The final $wR(F^2)$ was 0.0798. (For full CIF appendix chapter 3)

3.4.1.1.9 [BDTA][Ni(dmit)₂]₂ [3]

CHN for C₁₈H₄NNi₂S₂₂. Calculated; C, 20.45; H, 0.38; N, 1.33. Found; C, 20.45; H, 0.27; N, 1.38 %

X-ray Crystallography data C₉H₂NiN_{0.5}S₁₁, M = 530.49, Triclinic, $a = 6.454(4)$, $b = 7.448(4)$, $c = 19.603(10)$ Å, $\alpha = 99.707(5)$, $\beta = 91.077(5)$, $\gamma = 115.569(6)^\circ$ U = 833.5(8) Å³, T = 293.1 K, space group P1, Z = 2, $\mu(\text{Mo-K}\alpha) = 0.7107 \text{ mm}^{-1}$, 4560 reflections were collected, 1803 independent reflections ($R_{\text{int}} = 0.0690$) which were used in all calculations. The final $wR(F^2)$ was 0.0320. (For full CIF appendix chapter 3)

3.4.1.1.10 [TBA]₄[Pd₈(dmit)₁₀]₂ [4]

Further analysis was not performed on [4] as the generic crystallisation procedure did not yield a [dithiazoly]_x[M(dithiolene)₂] salt.

X-ray Crystallography data C₉₄H₁₄₄Pd₈N₄S₃₀, M = 2779.36, $a = 17.7870(8)$, $b = 19.0871(8)$, $c = 23.4384(11)$ Å, $\alpha = 73.903(3)$, $\beta = 84.423(3)$, $\gamma = 88.132(3)^\circ$ U = 7609.1(6) Å³, T = 150 K, Z = 14, $\mu(\text{Mo-K}\alpha) = 0.7107 \text{ mm}^{-1}$, (For CIF appendix chapter 3)

3.4.1.1.11 [BDTA]₂[Fe(tdas)₂][Cl] [5]

CHN for C₁₆H₈ClFeN₆S₁₀. Calculated; C, 27.60; H, 1.16; N, 12.07. Found; C, 30.36; H, 1.48; N, 11.58 %

X-ray Crystallography data C₃₂H₁₆Cl₂Fe₂N₁₂S₂₀, M = 1390.03, Monoclinic, $a = 7.273$, $b = 13.969$, $c = 13.701$ Å, $\alpha = 90$, $\beta = 116.77$, $\gamma = 90^\circ$ U = 1242.78650(6) Å³, T = 150 K, space group *Pn*, Z = 1, $\mu(\text{Mo-K}\alpha) = 0.7107 \text{ mm}^{-1}$, 14793 reflections were collected, 5914 reflections were independent, ($R_{\text{int}} = 0.0505$) which were used in all calculations. The final $wR(F^2)$ was 0.1078. (For full CIF appendix chapter 3)

3.4.1.1.12 [BDTA]₂[Ni(tdas)₂] [6]

CHN for C₁₆H₈N₆NiS₁₀. Calculated; C, 28.96; H, 1.22; N, 12.66. Found; C, 28.74; H, 0.98; N, 12.62 %

X-ray Crystallography data C₁₆H₈N₆NiS₁₀, M = 663.59, Monoclinic, $a = 10.9893(11)$, $b = 9.1344(9)$, $c = 11.3177(11)$ Å, $\alpha = 90$, $\beta = 101.8420(10)$, $\gamma = 90^\circ$ U = 1111.90(19) Å³, T = 150 K, space group *P2₁/n*, Z = 2, $\mu(\text{Mo-K}\alpha) = 0.7107 \text{ mm}^{-1}$, 6787 reflections were measured, 2676 independent reflections ($R_{\text{int}} = 0.0252$) which were used in all calculations. The final $wR(F^2)$ was 0.0690. (For full CIF appendix chapter 3)

3.5 References

- 1 P. Cassoux, *Coord. Chem. Rev.*, 1999, **185-186**, 213.
- 2 N. Robertson and L. Cronin, *Coord. Chem. Rev.*, 2002, **227**, 93.
- 3 P. Romaniello and F. Lelj, *Chem. Phys. Lett.*, 2003, **372**, 51.
- 4 S. Alvarez, R. Vicente, and R. Hoffmann, *J. Am. Chem. Soc.*, 1985, **107**, 6253.
- 5 A. E. Underhill and M. M. Ahmad, *J. Chem. Soc., Chem. Commun.*, 1981, 67.
- 6 A. T. Coomber, D. Beljonne, R. H. Friend, J. L. Bredas, A. Charlton, N. Robertson, A. E. Underhill, M. Kurmoo, and P. Day, *Nature*, 1996, **380**, 144.
- 7 G. Steimecke, R. Kirmse, and E. Hoyer, *Zeits. Chemie*, 1975, **15**, 28.
- 8 P. Cassoux, L. Valade, H. Kobayashi, A. Kobayashi, R. A. Clark, and A. E. Underhill, *Coord. Chem. Rev.*, 1991, **110**, 115.
- 9 M. Bousseau, L. Valade, M. F. Bruniquel, P. Cassoux, M. Garbauskas, L. Interrante, and J. Kasper, *Nouv. J. Chim.*, 1984, **8**, 3.
- 10 L. Brossard, M. Ribault, L. Valade, and P. Cassoux, *Phys B+C* 1986, **143**, 378.
- 11 H. Tajima, M. Inokuchi, A. Kobayashi, T. Ohta, R. Kato, H. Kobayashi, and H. Kuroda, *Chem. Lett.*, 1993, 1235.
- 12 A. Kobayashi, H. Kim, Y. Sasaki, R. Kato, H. Kobayashi, S. Moriyama, Y. Nishio, K. Kajita, and W. Sasaki, *Chem. Lett.*, 1987, 1819.
- 13 H. Kim, A. Kobayashi, Y. Sasaki, R. Kato, and H. Kobayashi, *Chem. Lett.*, 1987, 1799.
- 14 T. Nakamura, T. Akutagawa, K. Honda, A. E. Underhill, A. T. Coomber, and R. H. Friend, *Nature*, 1998, **394**, 159.
- 15 H. Imai, T. Inabe, T. Otsuka, T. Okuno, and K. Awaga, *Phys. Rev. B: Condens. Matter*, 1996, **54**, R6838.
- 16 J. L. Morris and C. W. Rees, *J. Chem. Soc., Perkin Trans.*, 1987, 211.
- 17 G. Wolmershaeuser and R. Johann, *Angew. Chem.*, 1989, **101**, 952.
- 18 I. Hawkins and A. E. Underhill, *J. Chem. Soc., Chem. Commun.*, 1990, 1593.
- 19 D. Simao, H. Alves, I. C. Santos, V. Gama, and M. Almeida, *Inorg. Chem. Comm.*, 2003, **6**, 565.
- 20 N. Robertson, K. Awaga, S. Parsons, A. Kobayashi, and A. E. Underhill, *Adv. Mater. Optics & Electronics*, 1998, **8**, 93.
- 21 O. A. Dyachenko, S. V. Konovalikhin, A. I. Kotov, G. V. Shilov, E. B. Yagubskii, C. Faulmann, and P. Cassoux, *J. Chem. Soc., Chem. Commun.*, 1993, 508.
- 22 H. Yamochi, N. Sogoshi, Y. Simizu, G. Saito, and K. Matsumoto, *J. Mater. Chem.*, 2001, **11**, 2216.
- 23 S. Curreli, P. Deplano, M. L. Mercuri, L. Pilia, A. Serpe, J. A. Schlueter, M. A. Whited, U. Geiser, E. Coronado, C. J. Gomez-Garcia, and E. Canadell, *Inorg. Chem.*, 2004, **43**, 2049.
- 24 P. Deplano, L. Leoni, M. L. Mercuri, J. A. Schlueter, U. Geiser, H. H. Wang, A. M. Kini, J. L. Manson, C. J. Gomez-Garcia, E. Coronado, H. J. Koo, and M. H. Whangbo, *J. Mater. Chem.*, 2002, **12**, 3570.
- 25 K. Awaga, T. Okuno, Y. Maruyama, A. Kobayashi, H. Kobayashi, S. Schenk, and A. E. Underhill, *Inorg. Chem.*, 1994, **33**, 5598.
- 26 P. I. Clemenson, *Coord. Chem. Rev.*, 1990, **106**, 171.
- 27 J. E. Huyett, S. B. Choudhury, D. M. Eichhorn, P. A. Bryngelson, M. J. Maroney, and B. M. Hoffman, *Inorg. Chem.*, 1998, **37**, 1361.

- 28 K. W. Plumlee, B. M. Hoffman, M. T. Ratajack, and C. R. Kannewurf, *Solid State Commun.*, 1974, **15**, 1651.
- 29 K. W. Plumlee, PhD thesis, Chapters 1 & 2, Northwest Univ., Evanston, 1975.
- 30 K. W. Plumlee, B. M. Hoffman, J. A. Ibers, and Z. G. Soos, *J. Chem. Phys.*, 1975, **63**, 1926.
- 31 I. D. Parker, R. H. Friend, P. I. Clemenson, and A. E. Underhill, *Nature*, 1986, **324**, 547.
- 32 M. L. Allan, A. T. Coomber, I. R. Marsden, J. H. F. Martens, R. H. Friend, A. Charlton, and A. E. Underhill, *Synth. Met.*, 1993, **56**, 3317.
- 33 N. Robertson, C. Bergemann, H. Becker, P. Agarwal, S. R. Julian, R. H. Friend, N. J. Hatton, A. E. Underhill, and A. Kobayshi, *J. Mater. Chem.*, 1999, **9**, 1713.
- 34 J. Xie, X. Ren, S. Gao, and Q. Meng, *Chem. Lett.*, 2002, 576.
- 35 J. Xie, X. Ren, Y. Song, Y. Zou, and Q. Meng, *J. Chem. Soc., Dalton Trans.*, 2002, 2868.
- 36 J. Xie, X. Ren, S. Gao, W. Zhang, Y. Li, C. Lu, C. Ni, W. Liu, Q. Meng, and Y. Yao, *Eur. J. Inorg. Chem.*, 2003, 2393.
- 37 J. Xie, X. Ren, Y. Song, W. Zhang, W. Liu, C. He, and Q. Meng, *Chem. Comm.*, 2002, 2346.
- 38 X. Ren, Q. Meng, Y. Song, C. Lu, C. Hu, and X. Chen, *Inorg. Chem.*, 2002, **41**, 5686.
- 39 X. M. Ren, H. Okudera, R. K. Kremer, Y. Song, C. He, Q. J. Meng, and P. H. Wu, *Inorg. Chem.*, 2004, **43**, 2569.
- 40 J. Xie, X. Ren, Y. Song, W. Tong, C. Lu, Y. Yao, and Q. Meng, *Inorg. Chem. Comm.*, 2002, **5**, 395.
- 41 V. da Gama, R. T. Henriques, M. Almeida, and L. Alcacer, *J. Phys. Chem.*, 1994, **98**, 997.
- 42 M. Uruichi, K. Yakushi, Y. Yamashita, and J. Qin, *J. Mater. Chem.*, 1998, **8**, 141.
- 43 P. Kuppusamy, B. L. Ramakrishna, and P. T. Manoharan, *Inorg. Chem.*, 1984, **23**, 3886.
- 44 J. M. Rawson and G. D. McManus, *Coord. Chem. Rev.*, 1999, **189**, 135.
- 45 E. G. Awere, N. Burford, R. C. Haddon, S. Parsons, J. Passmore, J. V. Waszczak, and P. S. White, *Inorg. Chem.*, 1990, **29**, 4821.
- 46 T. M. Barclay, A. W. Cordes, N. A. George, R. C. Haddon, M. E. Itkis, M. S. Mashuta, R. T. Oakley, G. W. Patenaude, R. W. Reed, J. F. Richardson, and H. Zhang, *J. Am. Chem. Soc.*, 1998, **120**, 352.
- 47 A. J. Banister, N. Bricklebank, I. Lavender, J. M. Rawson, C. I. Gregory, B. K. Tanner, W. Clegg, M. R. J. Elsegood, and F. Palacio, *Angew. Chem., Int. Ed. Engl.*, 1996, **35**, 2533.
- 48 J. Luzon, J. Campo, F. Palacio, G. J. McIntyre, A. E. Goeta, C. M. Pask, and J. M. Rawson, *Polyhedron*, 2003, **22**, 2301.
- 49 L. Beer, R. C. Haddon, M. E. Itkis, A. A. Leitch, R. T. Oakley, R. W. Reed, J. F. Richardson, and D. G. VanderVeer, *Chem. Comm.*, 2005, 1218.
- 50 L. Beer, A. Wallace Cordes, R. C. Haddon, M. E. Itkis, R. T. Oakley, R. W. Reed, and C. M. Robertson, *Chem. Comm.*, 2002, 1872.
- 51 J. L. Brusso, O. P. Clements, R. C. Haddon, M. E. Itkis, A. A. Leitch, R. T. Oakley, R. W. Reed, and J. F. Richardson, *J. Am. Chem. Soc.*, 2004, **126**, 8256.
- 52 W. Fujita and K. Awaga, *Chem. Phys. Lett.*, 2002, **357**, 385.

- 53 W. Fujita, K. Awaga, Y. Nakazawa, K. Saito, and M. Sorai, *Chem. Phys. Lett.*, 2002, **352**, 348.
- 54 C. D. Bryan, A. W. Cordes, R. M. Fleming, N. A. George, S. H. Glarum, R. C. Haddon, C. D. MacKinnon, R. T. Oakley, T. T. M. Palstra, and A. S. Perel, *J. Am. Chem. Soc.*, 1995, **117**, 6880.
- 55 G. Teschmit, P. Strauch, A. Barthel, J. Reinhold, and R. Kirmse, *Inorg. Chim. Acta*, 2000, **298**, 94.
- 56 P. Basu, *J. Chem. Educ.*, 2001, **78**, 666.
- 57 B. A. Goodman and J. B. Raynor, *Adv. Inorg. Chem. Radiochem.*, 1970, **13**, 135.
- 58 I. S. Jacobs, J. W. Bray, H. R. Hart, Jr., L. V. Interrante, J. S. Kasper, G. D. Watkins, D. E. Prober, and J. C. Bonner, *Phys. Rev. B*, 1976, **14**, 3036.
- 59 C. Kittel, 'Introduction to Solid State Physics.' 7th Ed. New York, Wiley, 1996.
- 60 J.-L. Stanger, J.-J. Andre, P. Turek, Y. Hosokoshi, M. Tamura, M. Kinoshita, P. Rey, J. Cirujeda, and J. Veciana, *Phys. Rev. B*, 1997, **55**, 8398.
- 61 M. Oshikawa and I. Affleck, *Phys. Rev. Lett.*, 1999, **82**, 5136.
- 62 H. Ohta, S. Imagawa, H. Ushiroyama, M. Motokawa, O. Fujita, and J. Akimitsu, *J. Phys. Soc. Jpn.*, 1994, **63**, 2870.
- 63 K. Okuda, H. Hata, and M. Date, *J. Phys. Soc. Jpn.*, 1972, **33**, 1574.
- 64 S. Eggert, I. Affleck, and M. Takahashi, *Phys. Rev. Lett.*, 1994, **73**, 332.
- 65 R. B. Griffiths, *Phys. Rev.*, 1964, **133**, A768.
- 66 C. N. Yang and C. P. Yang, *Phys. Rev.*, 1966, **150**, 327.
- 67 S. Eggert, *Phys. Rev. B*, 1996, **53**, 5116.
- 68 H. Kobayashi, R. Kato, A. Kobayashi, and Y. Sasaki, *Chem. Lett.*, 1985, 191.
- 69 E. Ruiz, J. Cano, S. Alvarez, and P. Alemany, *J. Comput. Chem.*, 1999, **20**, 1391.
- 70 E. Ruiz, A. Rodriguez-Forteza, J. Cano, S. Alvarez, and P. Alemany, *J. Comput. Chem.*, 2003, **24**, 982.
- 71 C. Rovira, J. J. Novoa, J.-L. Mozos, P. Ordejon, and E. Canadell, *Phys. Rev. B*, 2002, **65**, 081104/1.
- 72 V. Cocula, F. Starrost, S. C. Watson, and E. A. Carter, *J. Chem. Phys.*, 2003, **119**, 7659.
- 73 S. P. Best, S. A. Ciniawsky, R. J. H. Clark, and R. C. S. McQueen, *J. Chem. Soc., Dalton Trans.*, 1993, 2267.
- 74 S. G. Liu, Y. Q. Liu, Y. F. Li, and D. B. Zhu, *Synth. Met.*, 2000, **114**, 139.
- 75 S. Schenk, 'tdas complexes'. Project report, University of Wales, Bangor.
- 76 G. Wolmershaeuser, M. Schnauber, and T. Wilhelm, *J. Chem. Soc., Chem. Commun.*, 1984, 573.
- 77 R. C. Haddon, *Nature*, 1975, **256**, 394.
- 78 R. D. Bereman and H. Lu, *Inorg. Chim. Acta*, 1993, **204**, 53.
- 79 I. G. Dance and T. R. Miller, *Inorg. Chem.*, 1974, **13**, 525.
- 80 G. Steimecke, H. J. Sieler, R. Kirmse, and E. Hoyer, *Phos. Sulf. Rel. Elem.*, 1979, **7**, 49.

Chapter 4

Complexes of [BDTA]₂[MCl₄]

4.1 Introduction

Metal halides have enjoyed a long history of low dimensional magnetic investigation. Considerable numbers of metal halide systems have been the subject of magnetic studies over the last 30 years, due to the fact they have displayed a range of interesting magnetic phenomena (reviewed in section 1.3.1). These properties have been observed across a large range of metal halide systems, due to the presence of strong M-X magnetic coupling combined with the ability to form a variety of structural motifs.¹

A₂MX₄ (A = organic counter cation, M = transition metal, X = Cl, Br and I) systems have been found to form 2D ferro- and antiferromagnetic Heisenberg lattices via halide bridging. These planes are separated by organic counter cations yielding a layered perovskite structure. The overall structure of the material tends to be dictated by the organic cation. An extended layered perovskite structure can only be formed when the organic cation has an acidic proton to hydrogen bond from the counterion to a halide, as well as having no bulky groups to interfere with the 2D network.¹ Some such functional dye counterions have been utilised for this role with the aim of creating mixed magneto-optical materials.²

There are also many materials with counterions that do not fulfil the above specifications and thus, there is also a large number of A₂MX₄ systems with discrete counter cations and MX₄²⁻ anions, with a range of short contacts and hydrogen bonding that yield molecular low dimensional magnetic behaviour.

As the counter cation influences the structure, the synthesis of A₂MX₄ systems with new counterions could yield materials with new structures and interesting magnetic properties.

Again, [BDTA]⁺ (described in chapter 3) was the chosen counterion and was found to form stable, crystalline, 2:1, molecular materials with [MCl₄]²⁻ (M = Cu, [7] Co [8] and Mn [9]). The materials were found to have layers of [MCl₄]²⁻ units in a square motif of metal centres, with weak coupling between neighbouring magnetic centres in 2D with [BDTA]⁺ cations separating the layers.

Square 2D lattice systems of Cu²⁺ ($S = \frac{1}{2}$) have been the subject of extensive investigation due to the fact that the family of superconductors with the highest values of T_c is based on cuprate compounds with a square lattice structure.³ A deeper understanding of the magnetic character of these systems holds out the possibility of describing aspects of the mechanism of high temperature superconductivity. It is thought that the mechanism of superconductivity is directly related to the fact that the magnetic ground state of these low dimensional $S = \frac{1}{2}$ systems is affected by quantum fluctuations⁴ and it is these magnetic fluctuations that probably play a role in superconduction. The current accepted model to describes these quantum effects is the resonating-valence-bonds model.⁵ This type of behaviour may be enhanced by applying a strong magnetic field.⁶ The magnitude of the saturated field is directly related to the magnetic coupling within the material ($H_{sat} = 4kJ/g\beta$) and as such, a material with a large magnetic coupling warrants an unrealistically large saturation field. For many of the 2D cuprate systems previously studied (e.g. Sr₂CuCl₂O₂) large magnetic coupling ($J/k = 1500$ K for Sr₂CuCl₂O₂) has made it almost

impossible to carry out studies in a saturation field. The strong magnetic exchange in such materials also makes it difficult to probe the full range of magnetic excitations by neutron scattering, which typically probes processes whose energy is up to about 1000 cm^{-1} . Therefore, a 2D square lattice material with *weak* magnetic coupling can be advantageous for this type of investigation as the energy scale is more accessible.

Molecular systems generally have much lower magnetic coupling than cuprate oxides, as the magnetic centres are generally further apart and exchange pathways are provided either by a series of covalent bonds, or less strong interactions such as hydrogen bonds and non-bonded interactions such as π - π interactions. Some molecular systems such as $\text{Cu}(\text{DCOO})_2 \cdot 4\text{D}_2\text{O}$ (CFTD)⁷ have weaker coupling ($J/k = 72 \text{ K}$) than the traditional cuprate compounds, as well as the propensity to form very large good quality crystals. This has allowed extensive neutron scattering experiments to be performed to provide a more in-depth magnetic characterisation, such as spin structure and, through the measurement of spin-wave dispersion, the determination of J in different directions (*i.e.* inter- and intraplanar exchange).⁸ However, neutron scattering measurements could not be performed in a saturated field for this material, as the size of the static field required is too great. The research that has been performed shows that the system adheres to a classical model, with some evidence of different behaviour, consistent with quantum fluctuations, occurring beyond the maximum experimental field available to date. Thus, in-depth magnetic characterisation cannot be performed to explore quantum effects at field saturation on this complex as the value of J is still too high.

Recently, two new quasi-square cuprate lattices of [2-amino-5-chloropyridinium]₂[CuX₄] (X = Cl (CAPCC) and Br (CAPCB)) have been synthesised and have readily yielded crystals. These have been found to have a much lower coupling constant with CAPCC being the lower ($J = 0.874$ K), providing a system with a saturated field of $H_{sat} = 2.6$ T which is accessible in neutron scattering experiments. Preliminary results show that perturbing the field of this system gives an antiferromagnetic isotropic ground state.⁹ Two disadvantages to this system are that the lattice is not a perfect square and the deuterated complex is expensive and inefficient to produce.

However, the new material [7] is a 2D, $S = \frac{1}{2}$, perfectly square lattice, with a very small J . There is also the added synthetic advantage that [BDTA].Cl can be easily produced and only contains two protons to deuterate for neutron experiments. Thus, [7] is a very exciting new model system that may have a low enough value of J to enable extensive measurements to be performed to lower temperatures in a saturated field. Future work on [7] could describe the magnetic quantum fluctuations that occur in the ground state of such materials and ultimately help to explain the mechanism of superconductivity.

4.2 Results and discussion of [BDTA]₂[MCl₄] (M = Cu [7], Co [8] and Mn [9])

4.2.1 Preparation and X-ray structure

Single crystals of [7], [8] and [9] were prepared by slow diffusion of [BDTA]Cl in EtOH with CuCl₂.2H₂O [7], CoCl₂.H₂O [8] or MnCl₂.H₂O [9] in HCl and EtOH solution. Small, yellow/orange [7], blue/green [8] or pale peach [9] plate shaped crystals were collected after 3, 10 and 8 days respectively.

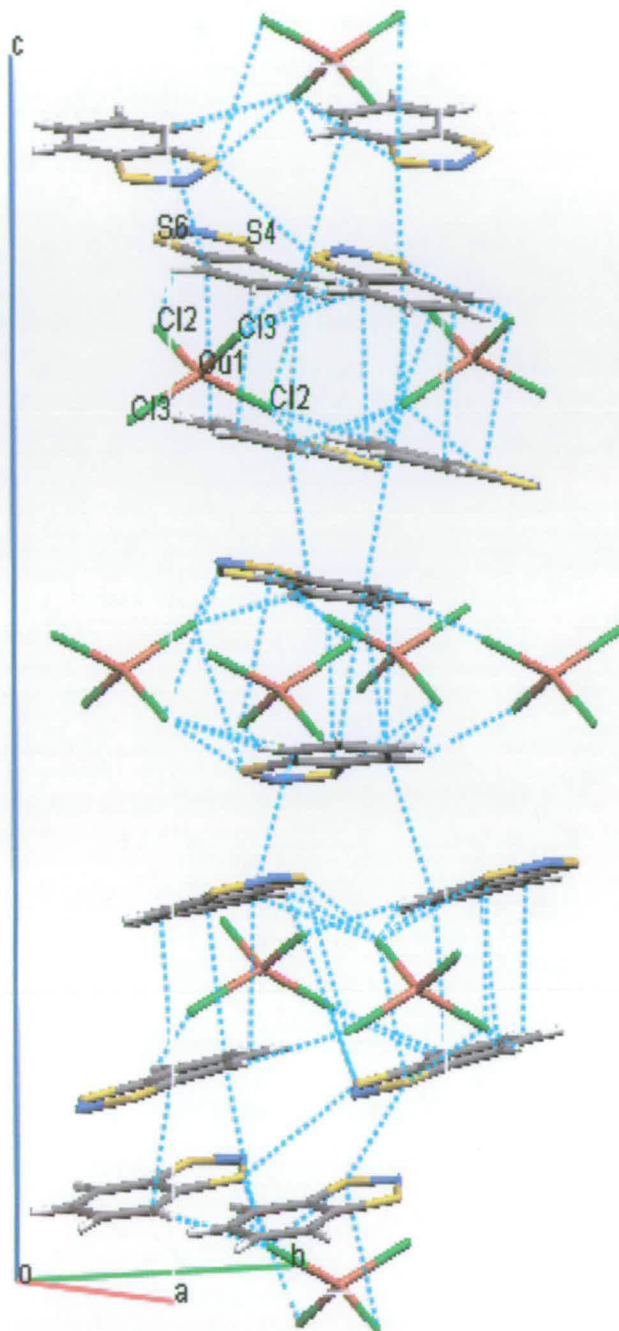


Figure 4. 1 Crystal structure of $[BDTA]_2[CuCl_4]$ [7] viewed perpendicular to the b - c plane.

Intermolecular distances shorter than the sum of the Van der Waals radii are shown. Distances are shown in table 4. 1

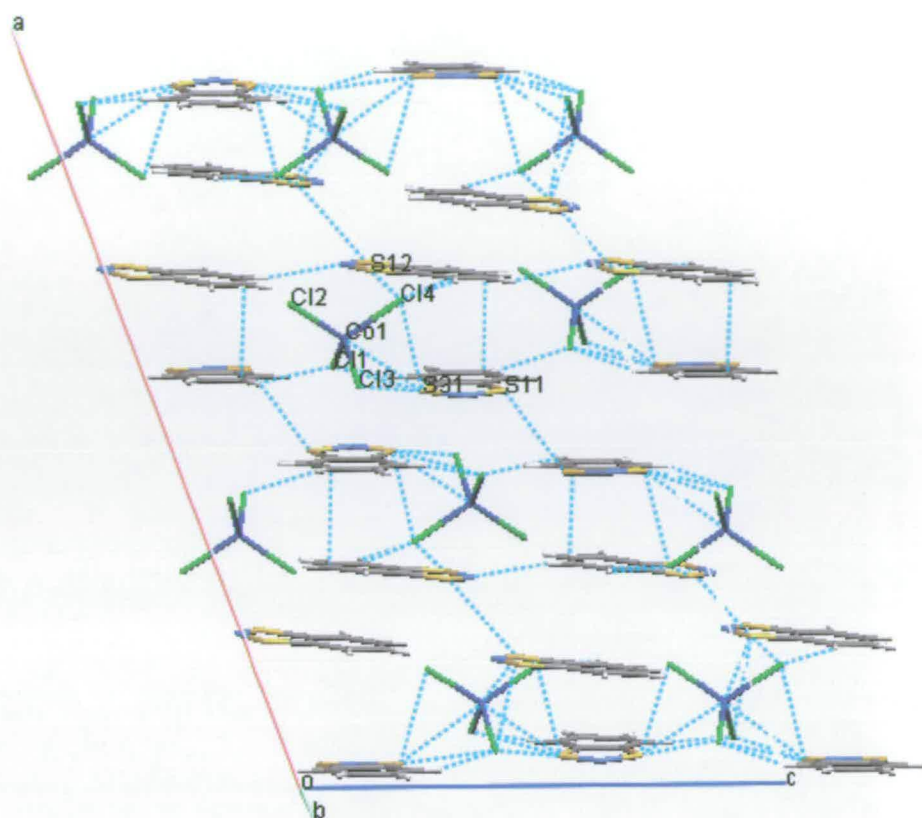


Figure 4. 2 Crystal structure of $[BDTA]_2[CoCl_4]$ [8] viewed perpendicular to the a-c plane.

Intermolecular distances shorter than the sum of the Van der Waals radii are shown. Distances are shown in table 4. 1

All three structures are molecular, yielding discrete anion and cation units, which is expected as $[BDTA]^+$ does not have acidic protons. It can also be seen that all the structures have many motifs in common, with [8] and [9] being isomorphic. For this reason only a figure of [8] is included to represent both [8] and [9] (Figure 4. 2). [8] and [9] crystallise in the space group $C2/c$ with [7] crystallising in the higher symmetry space group $P4_32_12$.

All the structures display a layered motif of two planes of [BDTA]⁺ ions with a square ([7]) and rectangular ([8] and [9]) lattice arrangement of [MCl₄]²⁻ units sandwiched between alternate layers. This gives rise to large numbers of short intermolecular contacts within the [MCl₄]²⁻ sandwiched layers with only one or two short contacts between the surrounding [BDTA]⁺ layers (Figure 4. 1 & Figure 4. 2). The [BDTA]⁺ cations within each layer align in a different orientation to adjacent layers and the motif of each layer is one difference between [7] and both [8] & [9]. In the structure of [7], the [BDTA]⁺ molecules within any one layer align in the same direction, but are orientated 180° and 90° to the molecules in the adjacent layers, and as such each identical layer is repeated every fourth layer (Figure 4. 1). The structures of [8] & [9] also have a repeat unit per four layers, however two adjacent layers in these structures have [BDTA]⁺ molecules aligned opposite to one another (Figure 4. 2). It can also be seen that [7] differs from the other two in the way that [BDTA]⁺ is tilted out of the plane by 10.96° as well as the fact that the [CuCl₄]²⁻ unit is much more distorted towards a square-planar geometry. [CuCl₄]²⁻ displays wide angles of 135.47° with the other four angles between 97.30° and 99.63°, whereas both [CoCl₄]²⁻ and [MnCl₄]²⁻ units are only very slightly distorted from tetrahedral, displaying angles between 106.91° and 112.38°. The fact that Cu²⁺ complexes have the ability to adopt more distorted geometries than Co²⁺ and Mn²⁺ complexes allows the Cu²⁺ complex to pack into a denser structure with [7] adopting a higher symmetry than [8] & [9].

The intermolecular interactions that are common to all the structures can be identified as 3 different types. Firstly, there is a short distance between the phenyl rings of [BDTA]⁺ in adjacent layers that can be attributed to phenyl π stacking. There is assumed to

be negligible interaction through this pathway. Secondly, there are numerous S---Cl and H---Cl short contacts between anions and cations within the sandwiched layers (as well as a S---M contact in [8] & [9]). These short contacts are the most significant with any magnetic correlation being communicated predominantly through S---Cl interactions. Thirdly and finally, short S---S contacts are observed between adjacent cation layers that do not have anions between them. This is the only short contact between these layers, and these interlayer distances are not expected to yield significant intermolecular interactions as they are very close to the van der Waal radii limit and so will provide very little overlap. All these distances are shown in Table 4. 1. From a direct comparison of these distances it can be seen that [7] has the shortest distances owing to its denser packing with [8] & [9] being comparable. Also, from inspection of the structures and from Table 4. 1 it can be seen that there is an intermolecular magnetic pathway between metal centres via Cl's and S on the [BDTA]⁺ cation within each sandwich layer (see Figure 4. 3 for a clear representation). This, along with the negligible or limited interactions between each layer, forms a square 2D magnetic lattice (these distances are shown in bold).

Bonds	Distance for [7] /Å		Distance for [8] /Å		Distance for [9] /Å	
C-C bonds π stacking	C(8)-C(11)''	3.256	C(62)-C(71)'	3.385	C(62)-C(71)'	3.392
	C(8)-C(10)'	3.362				
	C(9)-C(9)'	3.182				
	C(10)-C(8)'	3.362				
S-Cl	Cl(3)-S(6)	3.167	Cl(1)-S(31)	3.206	Cl(1)-S(31)	3.217
	Cl(3)-S(4)'	3.384	Cl(2)-S(11)'	3.387	Cl(3)-S(11)'	3.368
	Cl(3)-S(4)''	3.186	Cl(3)-S(11)'	3.322	Cl(2)-S(11)'	3.413
	Cl(2)-S(6)	3.472	Cl(3)-S(31)	3.528	Cl(2)-S(12)''	3.550

			Cl(3)-S(32) ^{''}	3.527	Cl(2)-S(32) ^{''}	3.549
			Cl(4)-S(12) ^{''}	3.083	Cl(4)-S(32) ^{''}	3.100
			Cl(4)-S(32) ^{''}	3.078	Cl(4)-S(31)	3.446
			Cl(4)-S(31)	3.400		
H-Cl	Cl(2)-H(111) [']	2.833	Cl(1)-H(51)	2.804	Cl(1)-H(51)	2.773
	Cl(2)-H(81)	2.854	Cl(1)-H(71) ^v	2.723	Cl(1)-H(71) ^v	2.712
	Cl(3)-H(111) [']	2.687	Cl(3)-H(61) ^v	2.905	Cl(3)-H(61) ^v	2.900
	Cl(3)-H(81)	2.780	Cl(3)-H(81) [']	2.826	Cl(3)-H(81) [']	2.840
			Cl(4)-H(52) ^{'''}	2.737	Cl(4)-H(52) ^{'''}	2.739
			Cl(4)-H(82) ^{v''}	2.709	Cl(4)-H(82) ^{v''}	2.704
S-M	-	-	Co-S(11) [']	3.217	Mn-S(11) [']	3.549
			Co-S(31)	3.427	Mn-S(31)	3.451
			Co-S(32) ^{''}	3.428	Mn-S(32) ^{''}	3.446
S-S	S(4)-S(6)	3.559	S(11)-S(11)	3.483	S(11)-S(11)	3.510
			S(31)-S(31)	3.494	S(31)-S(31)	3.540
			S(32)-S(32)	3.549	S(32)-S(32)	3.579

Table 4. 1 Intermolecular distances of all the short contacts in [7], [8] and [9]

The remainder of the structural discussion henceforth will only focus on [7], as the higher symmetry present provides a perfect square lattice system as opposed to the rectangular lattice of [8] and [9], which is of greater interest. This is owed to the flexibility of [CuCl₄]²⁻, that allows it to deviate from a tetrahedral geometry.

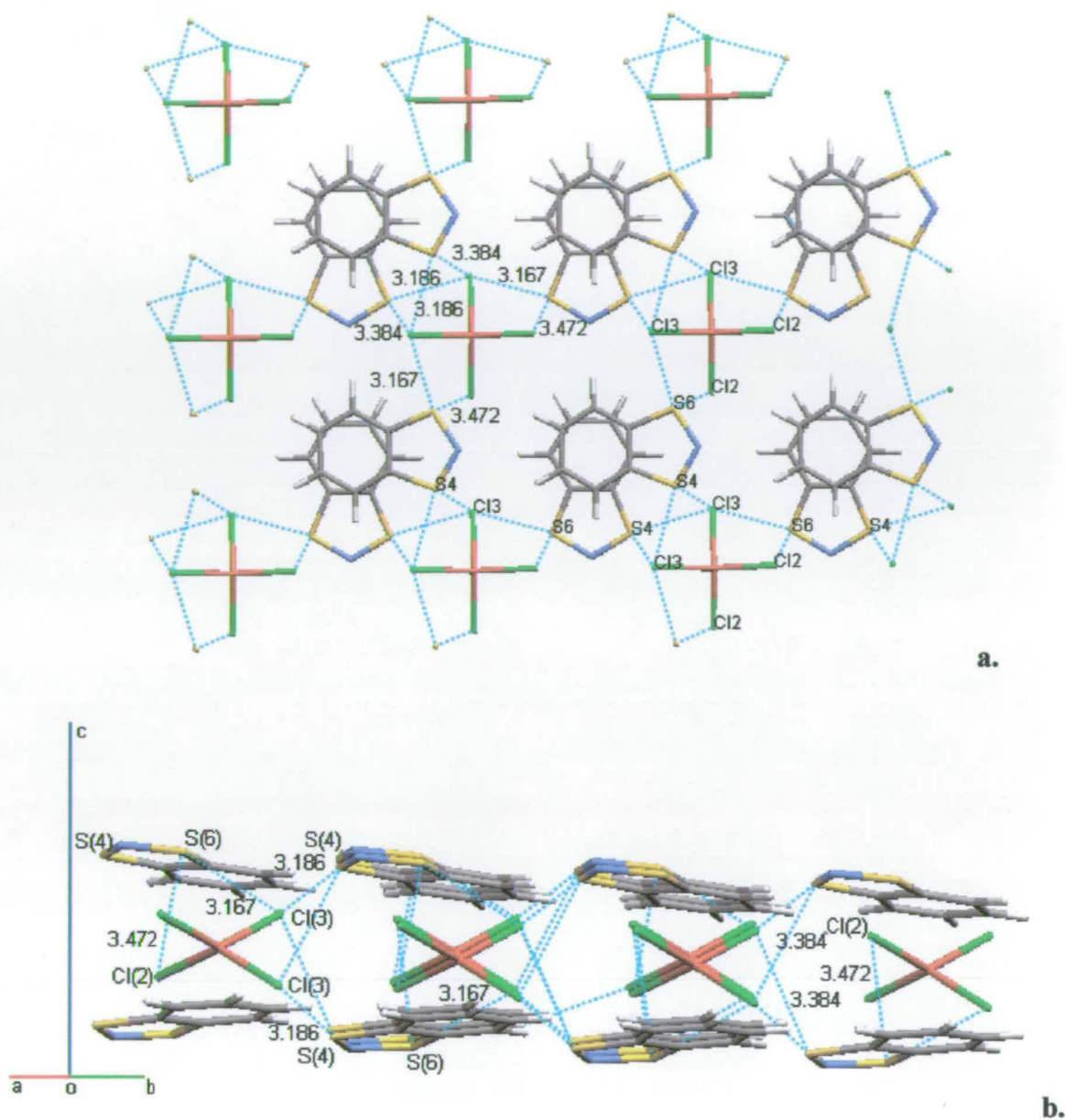


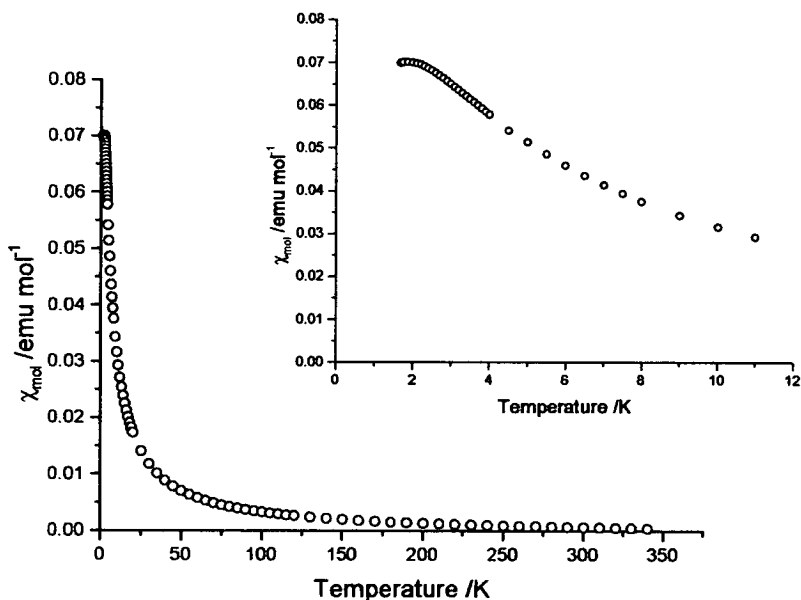
Figure 4.3 Crystal structure of $[BDTA]_2[CuCl_4]$ sandwich layer viewed; a) along the c-axis and b) perpendicular to the c-axis.

Close consideration of each 2D square lattice sandwich layer ($[BDTA]^+ [CuCl_4]^{2-}$ $[BDTA]^+$) will identify the square magnetic pathways which are displayed in Figure 4. 3.

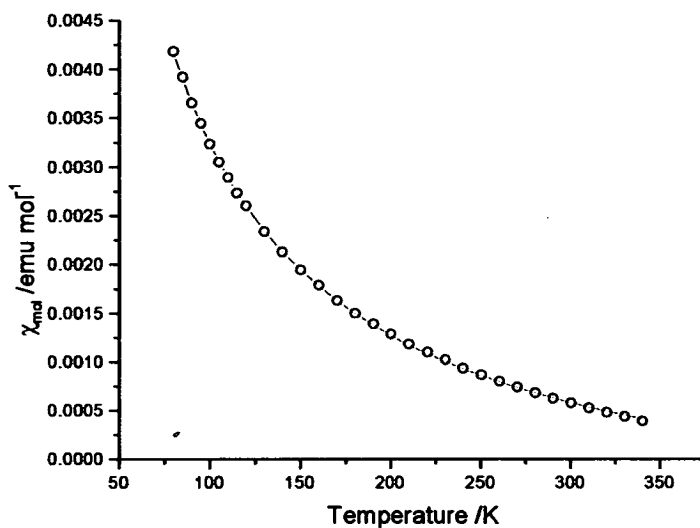
The magnetic intermolecular interactions occur in straight lines perpendicular to one another through a Cu—Cl---S short contact to [BDTA]⁺, linking to the next Cu²⁺ centre along the chain through the same interaction with the remaining S on the [BDTA]⁺ molecule. One such chain interaction is translated along the a-direction through the plane of [BDTA]⁺ cations below the [CuCl₄]²⁻ layer, while the other is propagated along the b-direction through interactions with the [BDTA]⁺ plane above the [CuCl₄]²⁻ unit (Figure 4.3.b) as the [BDTA]⁺ cations stack at 90° to one another. These short contacts are of alternating distances of 3.167 and 3.186 Å in both directions making a square of magnetic centres 8.229 Å apart. There are also short contacts of 3.384 Å between Cl(3) and 3.472 Å between Cl(2) and a [BDTA] in the opposing plane. This creates a perfectly symmetrical isolated 2D square lattice with a very large interatomic distance between magnetic centres and only a long pathway of magnetic coupling, suggesting a very low coupling constant *J*. It should be noted that systems [8] and [9] have similar motifs to [7], however the symmetry is not as high, with slightly different [BDTA]⁺ orientation in alternating layers.

4.2.2 Magnetic analysis

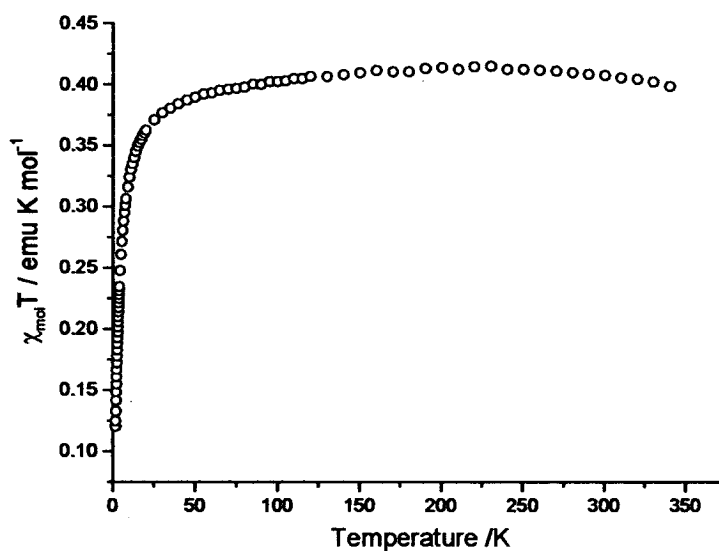
The magnetic susceptibility of [7]-[9] is shown in Figures 4. 4 – 4. 6 and shows behaviour similar to one another. All three materials can be modelled by the Curie-Weiss law at high temperature to give Curie constants of [7] = $0.4053 \pm 0.0002 \text{ emu K mol}^{-1}$, [8] = $2.357 \pm 0.001 \text{ emu K mol}^{-1}$ and [9] = $4.031 \pm 0.002 \text{ emu K mol}^{-1}$ which can be compared to the theoretical spin-only values of; $\text{Cu}^{2+} = 0.375 \text{ emu K mol}^{-1}$, $\text{Co}^{2+} = 1.875 \text{ emu K mol}^{-1}$ and $\text{Mn}^{2+} = 4.377 \text{ emu K mol}^{-1}$ (Table 4. 2). [7] and [9] have the closest value to the theoretical Curie constant with [8] being much higher than the spin-only value. This is to be expected, as higher values for Co^{2+} complexes are typical due to the mixing in of low-lying excited states when the symmetry of the complex is close to tetrahedral.



a.

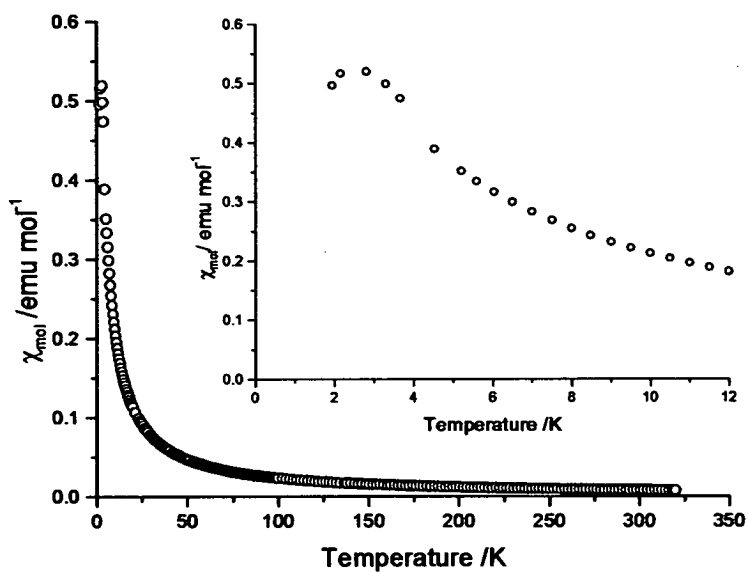


b.

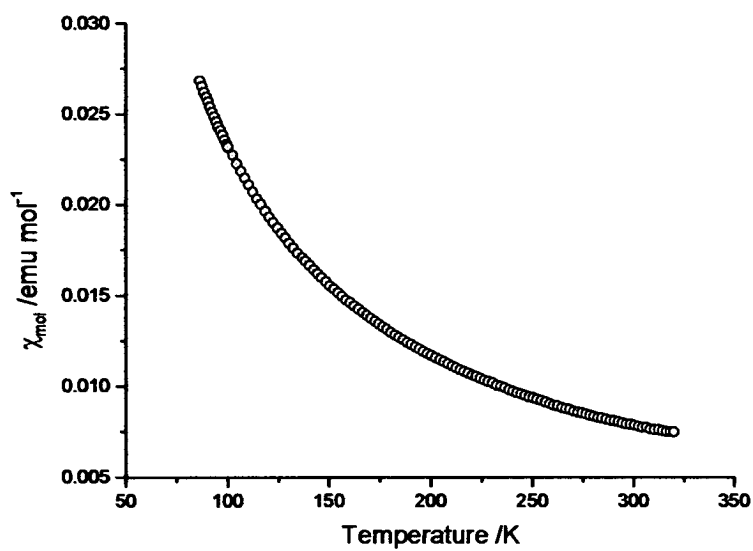


c.

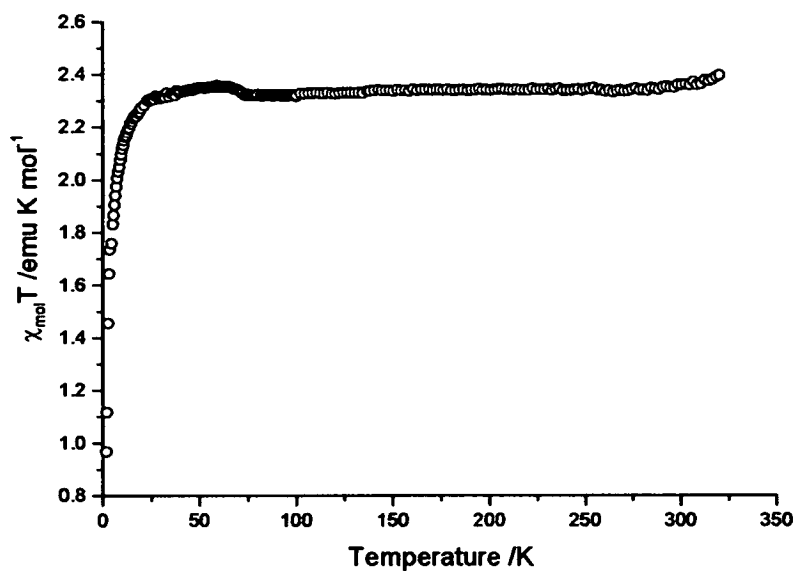
Figure 4. 4 Magnetic susceptibility χ_m versus temperature of $[BDTA]_2[CuCl_4]$; \circ = experimental data. a) over whole temperature range (1.8-320 K) with insert showing low temperature data (1.8-12 K) and b) higher temperature data (80-320 K) with — = fit to $\chi_M(T) = \chi_{Curie Weiss}$ with Curie constant = 0.4053 ± 0.0002 emu K mol $^{-1}$, Weiss constant = -2.46 ± 0.001 K. c) Magnetic susceptibility x temperature versus temperature.



a.

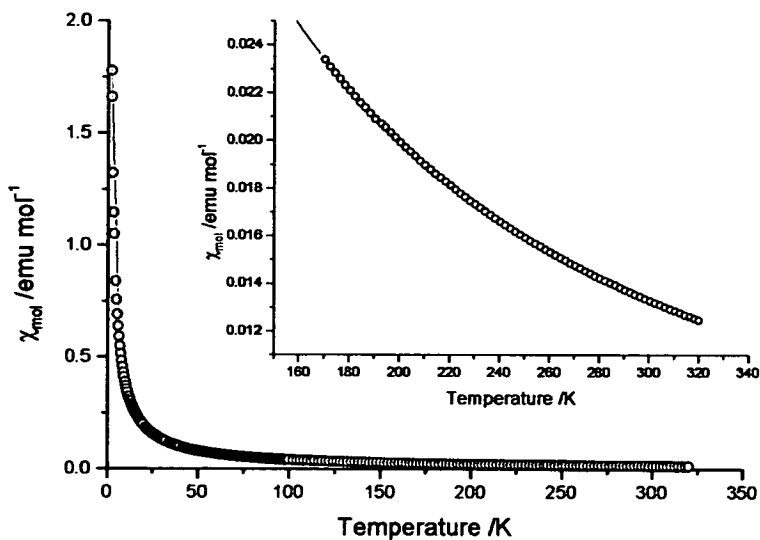


b.

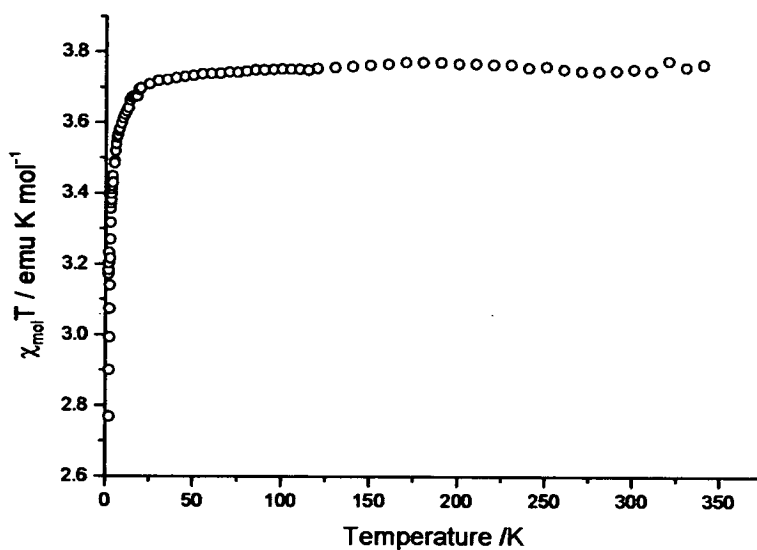


c.

Figure 4. 5 Magnetic susceptibility χ_m versus temperature of $[BDTA]_2[CoCl_4]$; \circ = experimental data. a) over whole temperature range (1.8-320 K) with insert showing low temperature data (1.8-12 K) and b) higher temperature data (80-320 K) with — = fit to $\chi_M(T) = \chi_{Curie Weiss}$ with Curie constant = 2.357 ± 0.001 emu K mol $^{-1}$, Weiss constant = -1.566 ± 0.074 K. c) Magnetic susceptibility x temperature versus temperature.



a.



b.

Figure 4. 6 a) Magnetic susceptibility χ_m versus temperature of $[BDTA]_2[MnCl_4]$; \circ = experimental data over whole temperature range (1.8-320 K) with insert showing higher temperature data (170-320 K) with — = fit to $\chi_M(T) = \chi_{Curie Weiss}$, with Curie constant = 3.973 ± 0.004 emu K mol $^{-1}$ (1.8-320 K) & 4.031 ± 0.002 emu K mol $^{-1}$ (170-320 K), Weiss constant = -0.217 ± 0.004 K (1.8-320 K) & -0.264 ± 0.130 K (170-320 K). b) Magnetic susceptibility x temperature versus temperature.

Compound	$C / \text{emu K mol}^{-1}$	$C_{s.o.} / \text{emu K mol}^{-1}$	θ / K
[7] ([BDTA] ₂ [CuCl ₄])	0.4053 ± 0.0002	0.375	-2.46 ± 0.001
[8] ([BDTA] ₂ [CoCl ₄])	2.357 ± 0.001	1.875	-1.566 ± 0.074
[9] ([BDTA] ₂ [MnCl ₄])	4.031 ± 0.002	4.377	-0.264 ± 0.130

Table 4. 2 Curie-Weiss constants from susceptibility data of [7]-[9].

The plots of $\chi_{mol}T$ versus temperature show the data to be a straight horizontal line over most of the temperature range, with a dramatic drop to lower values below approximately 20 K for [8] and [9] and approximately 35 K for [7]. This behaviour shows that the material is paramagnetic over most of the temperature range with short-range antiferromagnetic correlations below approximately 20-30 K. This can be further illustrated by the Weiss constants (θ) (shown in table 4. 2) that indicate all three materials have predominantly antiferromagnetic interactions at low temperatures. From the Weiss constants it can be seen that [7] has the highest ordering temperature with [9] having an almost negligible Weiss constant. Both [7] and [8] have a low temperature peak that can be assigned to 2D magnetic correlations, whereas [9] has no such feature, showing [9] to have negligible intermolecular magnetic coupling. This means that the susceptibility data of [9] over the entire temperature range can be fitted to the Curie-Weiss model accurately revealing [9] to behave as a spin-only paramagnet with no significant intermolecular magnetic exchange.

The fact that [8] has a clearer peak in the magnetic susceptibility at a slightly higher temperature than [7], even though [7] has the larger Weiss constant, can be explained by

the fact that that Co²⁺ complex has a larger value of S than the Cu²⁺ analogue. Also, Co²⁺ complexes are well know for having an increased single ion anisotropy, which will increase the temperature of a peak in the susceptibility.

The solid-state EPR spectra of [8] and [9] are silent, with only a broad characteristic Cu²⁺ single peak spectrum for [7]. These results are probably due to the fact that solid samples are used which increases any interactions and thus leads to rapid relaxation. [7] has a g -value = 2.12, and a linewidth = 21.8 G. The g -value is in close agreement with the g -value of characteristic [CuCl₄]²⁻ complexes such as [NH₄]₂[CuCl₄].¹⁰

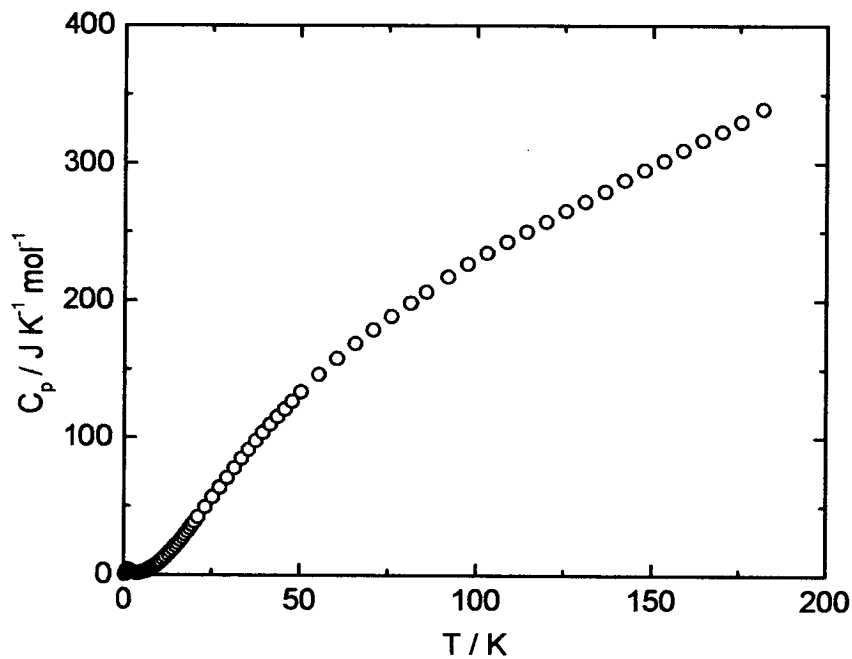
It was stated in section 4.2.1 that this study would focus on the magnetic properties of [7] as its structure makes it a perfect candidate for a model system to study the mechanism of low temperature quantum effects. This is due to its highly symmetric square lattice and low magnetic coupling, evident from the very low ordering temperature. Thus further analysis was carried out on [7] to test the suitability of this material for such studies.

An estimation of the value of J for [7] can be obtained from the susceptibility data. First, from the high-temperature data, the value of θ in the Curie-Weiss Law may be related to J using the mean-field approximation¹¹ $\theta = 2S(S+1)zJ/3k$ therefore $J/k = 3\theta/2S(S+1)z$, where z is the number of nearest-neighbour magnetic ions with which exchange occurs; this yields $|J| = 0.57(4) \text{ cm}^{-1}$. Alternatively, the temperature of the maximum in χ is related to spin and exchange on a $S=1/2$ square Heisenberg antiferromagnetic lattice through the expression:

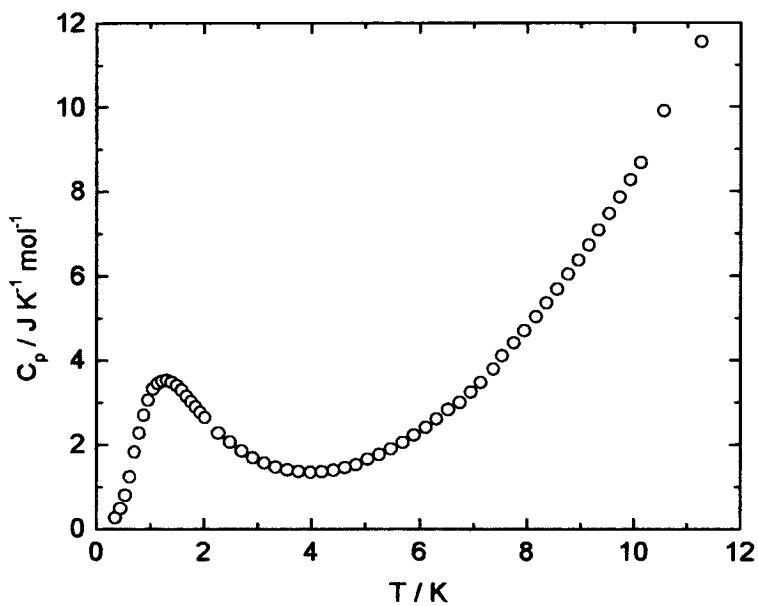
$$\frac{kT(\chi_{\max})}{|J|S(S+1/2)} = 2.53 \quad \text{Equation 4. 1}^{12}$$

This gives a value of $\Delta J/k = 1.0(1)$ K.

In order to establish whether [7] has a large degree of two dimensionality a heat capacity (C_p) versus temperature measurement was performed on [7] in the PPMS from 0.33-200 K to see if a distinct transition- indicative of magnetic long-range order, might occur. The results of this measurement are shown in figure 4.7.

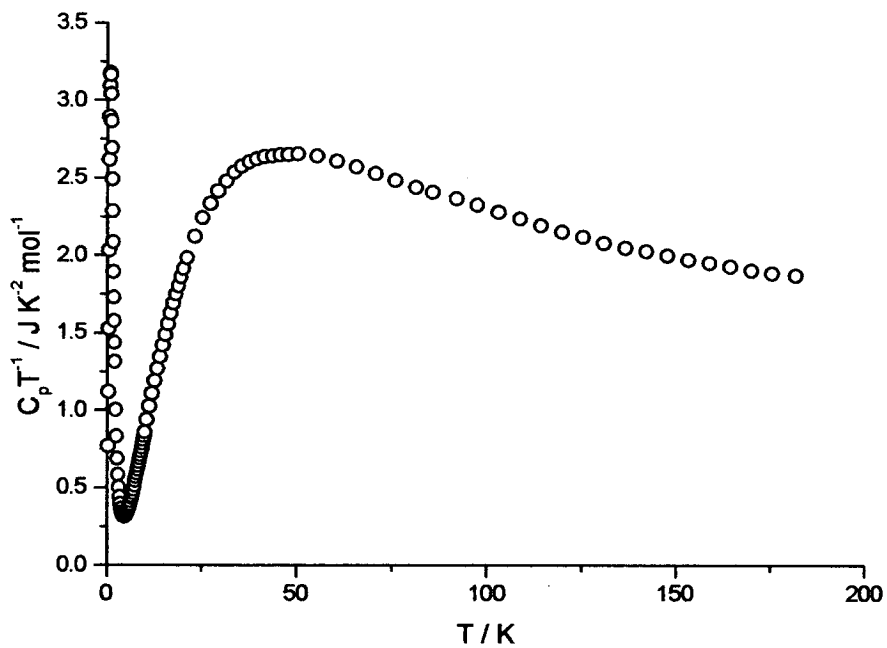


a.

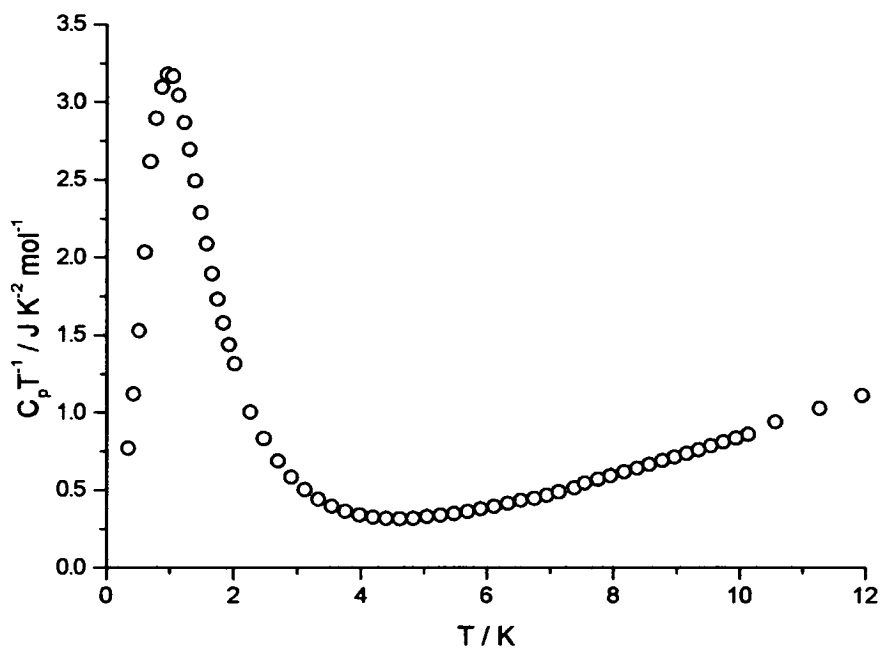


b.

Figure 4. 7 C_p versus Temperature of [7] from a) 0.33-200 K & b) 0.33-12 K



a



b.

Figure 4. 8 C_p/T versus Temperature of [7] from a) 0.33-200 K & b) 0.33-12 K

The entropy change, ΔS , associated with heating a system from temperature T_1 to T_2 is related to the heat capacity depicted in Equation 4. 2.

$$\Delta S = \int_{T_1}^{T_2} \frac{C_p}{T} dT \quad \text{Equation 4. 2}$$

This reflects the take-up of energy into the various degrees of freedom in the system (phonons and magnons), as well as that associated with any phase transitions. The peak in heat capacity at about 1.3 K will arise from magnetic degrees of freedom and at higher temperatures the phonon contribution will become more significant. In order to correct for the latter, an appropriate approximation was used to model C_p arising from phonons at temperatures well below the Debye temperature. For such temperatures the leading term in

the heat capacity is aT^3 , and the results of fitting this expression to low-temperature heat capacity data is shown in Figure 4. 9 (with the range in temperature for the fitting ranging from 6 – 10 K).¹³

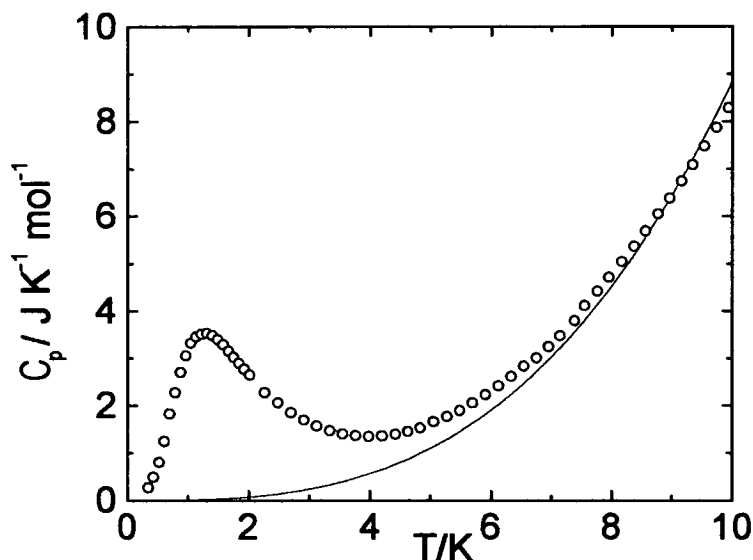


Figure 4. 9 Low temperature molar heat capacity of [7] = \circ , with a fit to an expression, $aT^3 = \text{---}$, representing the phonon contribution, over the temperature range 6 – 10 K.

The remaining contribution was taken to be magnetic in origin and is displayed in Figure 4. 10, along with the calculated change in magnetic entropy. Calculations based on spin-wave theory and high-temperature series expansions¹² predict a peak in the heat capacity for the 2D $S = \frac{1}{2}$ ferromagnet at approximately $|\theta|/2$ (i.e. at about 1.2 K), with a value of about 0.4 R (i.e. approximately $3.5 \text{ J K}^{-1} \text{ mol}^{-1}$); our data yield values of 1.22(2) K and $3.49(1) \text{ J K}^{-1} \text{ mol}^{-1}$ for these two quantities respectively, close to theoretical values. The limiting value of the magnetic entropy should correspond to $R \ln 2$ for a $S = \frac{1}{2}$ system, equal to $5.762 \text{ J K}^{-1} \text{ mol}^{-1}$; we find a value of $5.15 \text{ J K}^{-1} \text{ mol}^{-1}$. The reason for this small discrepancy could be

over-compensation for the phonon contribution to the heat capacity, and perhaps also the presence of continuing spin disorder and fluctuations (perhaps arising through quantum fluctuations), at low temperatures.

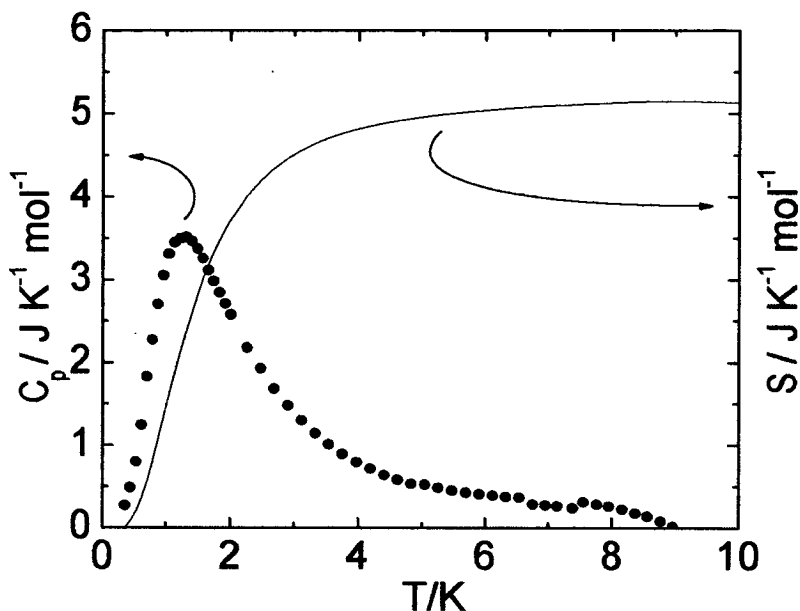


Figure 4. 10 Magnetic contribution to the heat capacity of [7] (\bullet), with the corresponding entropy (—)

Finally, with regard to the heat capacity data, there is no clear signature for three-dimensional long-range order. The peak in heat capacity is almost certainly due to 2D correlations, and one would expect a sharper feature to the low temperatures side of the broader cusp at the 3D ordering temperature. This part of the study needs more careful measurement of heat capacity, magnetic susceptibility and neutron or muon methods to confirm it.

This material would be an ideal candidate for a model system for future neutron studies as the counterion is easily synthesised and thus the deuterated form can be easily prepared for use in neutron scattering experiments. It is also useful to dilute these model systems with non-magnetic ions as another method of inducing quantum fluctuations. Usually it is the Zn²⁺ analogue that is used to dope the system. When Zn²⁺ ions are added to magnetically dilute the system, it rapidly goes into a quantum-disordered phase.¹⁴ It is thought that this effect has great significance in superconductivity, as the high temperature superconducting cuprates are all doped materials.

One main problem with zinc ion doping is that the crystal structure of the zinc material may be very different from the copper analogue. If this is the case, only very limited amounts of zinc doping can occur before the ideal crystal structure is altered by the inclusion of the zinc ions.

Thus the zinc analogue [BDTA]₂[ZnCl₄] [10] was synthesised by the same diffusion method as [7]-[9]. A pale yellow micro-crystalline product was isolated, washed and found to be pure from CHN analysis. Single crystals of a suitable size to gain a structure could not be obtained but an X-ray powder diffraction pattern was obtained from the sample (Figure 4. 11) and refined using the simulated powder patterns of the samples [7]-[9].¹⁵ From a comparison of the simulated powder pattern from the crystal structure of [9], it has been found that [10] has a structure very similar to [9] and this comparison is displayed in Figure 4. 12. The main differences in the patterns seem to be due to a discrepancy in peak heights and this is common when comparing a flat plate powder pattern to a simulated pattern as the microcrystalline powder has a degree of preferred orientation that will affect the peak heights.

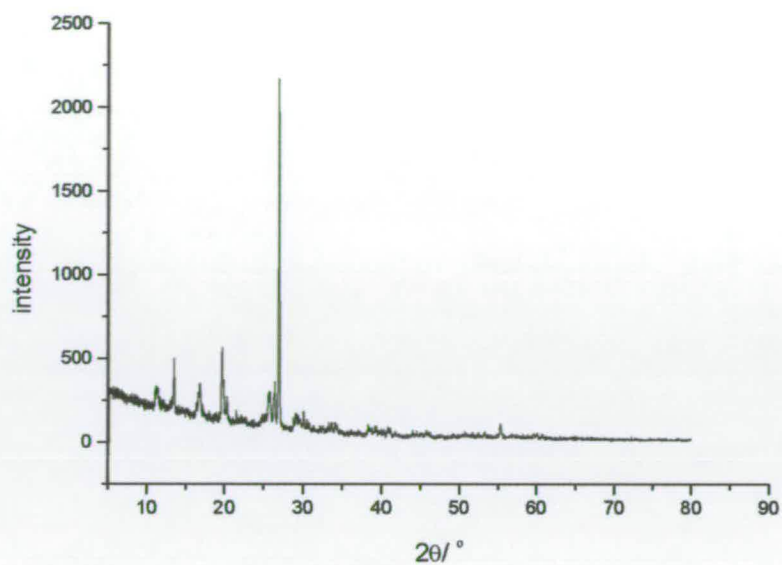


Figure 4. 11 Powder X-ray diffraction pattern of [10]

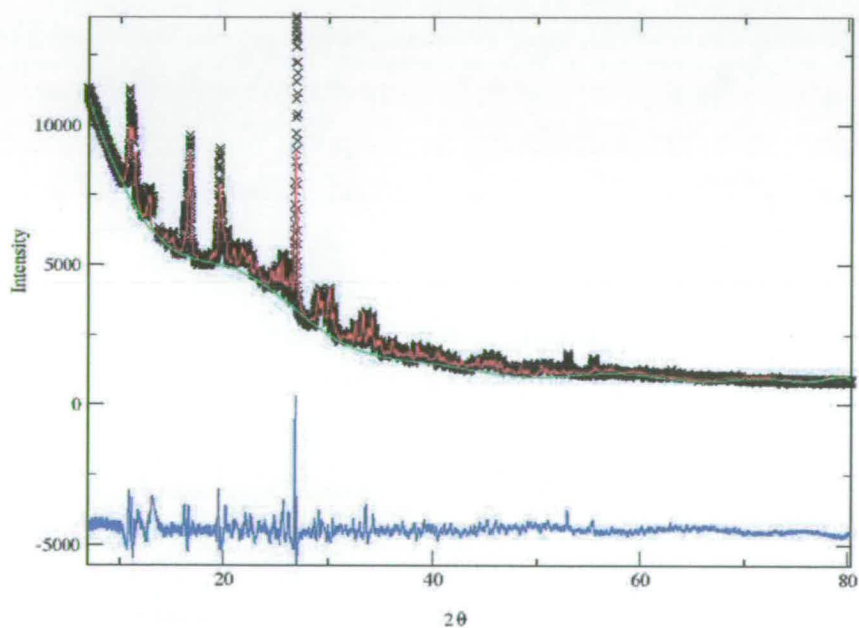


Figure 4. 12 Diffraction pattern of [10] (x) fitted to the calculated diffraction pattern of [9] (—), with the difference shown below (—). (Background (—))

All four structures are very similar so it can be predicted that any doping of [7] with [10] will not have a sizable impact on the overall structure. Thus, it appears that these materials fulfil all the specifications that are needed to study quantum disorder and other quantum magnetic effects, making them ideal model materials to study influences of magnetic fluctuations in the mechanism of superconductivity.

4.3 Conclusion

[BDTA]₂[MCl₄] (M = Cu [7], Co [8], Mn [9] and Zn [10]) were synthesised by a slow diffusion of the appropriate precursor salts in solution. Crystal structures were obtained for [7]-[9] and display a molecular structure of sandwich layers of [MCl₄]²⁻ between two [BDTA]⁺ layers. All three materials are paramagnetic with antiferromagnetic short-range correlations occurring at approximately 20-30 K with Curie constants very similar to the spin-only values for each metal. [9] was found to have a negligible Weiss constant and thus no onset of long-range order is seen in the susceptibility data. [7] and [8] form very weakly coupled magnetic 2D lattices with exchange pathways through the counterion with the greatest moment in [8] and the largest coupling in [7] ($J = 0.57 \text{ cm}^{-1}$). [7] has higher symmetry than the other two compounds and as such has a $S = \frac{1}{2}$, 2D square lattice motif. This should provide a good model material to investigate the way in which quantum fluctuations may be promoted in $S = \frac{1}{2}$ square Heisenberg antiferromagnets through diamagnetic dilution or the application of magnetic fields approaching the saturation field; in particular, the in-plane exchange is of the order of 1 K, and three-

dimensional long-range order sets in below this. Such information may provide new insights into the possible role of magnetic fluctuations in the mechanism of superconductivity in layered cuprates. A system diluted with non-magnetic dopants such as zinc is of great interest for this field of study. An X-ray powder diffraction of a microcrystalline sample [10] was found to have a very similar structure to [9] meaning that [7] could theoretically be doped with [10] without major deviations from the structure of [7], as the structure of all the materials is so similar. Thus, [7] appears to be an ideal material for such studies and will in the near future be the subject of neutron diffraction measurements and measurements to determine the magnetic effects of the inclusion of the dopant [10].

4.4 Experimental

All cations and anions used were synthesised by literature methods or bought from Sigma-Aldrich. The starting material [BDTA]Cl,¹⁶ was synthesised by Umezono Yoshikatsu and other co workers of Prof. Kunio Awaga's group in Japan.

4.4.1 Preparation of [BDTA]₂[MCl₄]

All [BDTA]_x[MCl₄] salts were prepared by layering [BDTA]Cl (2 equivalents) in EtOH on top of MCl₂.2H₂O (1 equivalent) dissolved in EtOH and HCl (2 equivalents 10 Molar). The microcrystalline bulk sample was washed with Water, EtOH and then Ether

(Yields 88-95%) and analysed by CHN and X-ray powder diffraction to compare with the crystalline samples. The bulk sample was then used for magnetic measurements.

4.4.2 Analysis and structure

4.4.2.1 [BDTA]₂[CuCl₄] [7]

CHN for C₁₂H₈Cl₄CuN₂S₄. Calculated; C, 28.05; H, 1.57; N, 5.45. Found; C, 27.94; H, 1.55; N, 5.22%

X-ray Crystallography data C₁₂H₈Cl₄CuN₂S₄, M = 513.83, Tetragonal, $a = 8.2295(3)$, $b = 8.2295(3)$, $c = 25.681(2)$ Å, $\alpha = 90$, $\beta = 90$, $\gamma = 90^\circ$ U = 1739.26(16) Å³, T = 150 K, space group $P4_32_12$, Z = 4, $\mu(\text{Mo-K}\alpha) = 0.7107 \text{ mm}^{-1}$, 2212 reflections were measured, 1148 independent reflections ($R_{\text{int}} = 0.0362$) which were used in all calculations. The final $wR(F^2)$ was 0.0734. (For full CIF, appendix Chapter 4)

4.4.2.2 [BDTA]₂[CoCl₄] [8]

CHN for C₁₂H₈Cl₄CoN₂S₄. Calculated; C, 28.05; H, 1.57; N, 5.45. Found; C, 27.61; H, 1.29; N, 3.90%

X-ray Crystallography data C₁₂H₈Cl₄CoN₂S₄, M = 509.17, Monoclinic, $a = 28.0151(8)$, $b = 8.4963(2)$, $c = 16.3222(5)$ Å, $\alpha = 90$, $\beta = 109.924(10)$, $\gamma = 90^\circ$ U =

3652.55(18) Å³, T = 150 K, space group C2/c, Z = 8, $\mu(\text{Mo-K}\alpha) = 0.71073 \text{ mm}^{-1}$, 13038 reflections collected, 3566 reflections were measured, 4027 independent reflections ($R_{\text{int}} = 0.0505$) which were used in all calculations. The final $wR(F^2)$ was 0.0953. (For full CIF, appendix Chapter 4)

4.4.2.3 [BDTA]₂[MnCl₄] [9]

CHN for C₁₂H₈Cl₄MnN₂S₄. Calculated; C, 28.05; H, 1.57; N, 5.45. Found; C, 28.18; H, 1.58; N, 5.55%

X-ray Crystallography data C₁₂H₈Cl₄MnN₂S₄, M = 505.18, Monoclinic, $a = 28.1046(9)$, $b = 8.5467(2)$, $c = 16.4017(5) \text{ \AA}$, $\alpha = 90$, $\beta = 109.973(2)$, $\gamma = 90^\circ$ U = 3702.75(19) Å³, T = 150 K, space group C2/c, Z = 8, $\mu(\text{Mo-K}\alpha) = 0.71073 \text{ mm}^{-1}$, 13108 reflections collected, 3963 reflections were measured, 4510 independent reflections ($R_{\text{int}} = 0.0405$) which were used in all calculations. The final $wR(F^2)$ was 0.0896. (For full CIF, appendix Chapter 4)

4.4.2.4 [BDTA]₂[ZnCl₄] [10]

CHN for C₁₂H₈Cl₄ZnN₂S₄. Calculated; C, 27.95; H, 1.56; N, 5.43. Found; C, 27.94; H, 1.57; N, 5.14 %

4.5 References

- 1 D. B. Mitzi, *Prog. Inorg. Chem.*, 1999, **48**, 1.
- 2 D. J. Nelson, K. Chan, I. Cervantes, and L. W. ter Haar, *J. Appl. Phys.*, 1996, **79**, 4715.
- 3 R. A. Fisher, J. E. Gordon, and N. E. Phillips, *Annu. Rev. Phys. Chem.*, 1996, **47**, 283.
- 4 G. Shirane, Y. Endoh, R. J. Birgeneau, M. A. Kastner, Y. Hidaka, M. Oda, M. Suzuki, and T. Murakami, *Phys. Rev. Lett.*, 1987, **59**, 1613.
- 5 P. W. Anderson, *Science*, 1987, **235**, 1196.
- 6 M. E. Zhitomirsky and A. L. Chernyshev, *Phys. Rev. Lett.*, 1999, **82**, 4536.
- 7 S. J. Clarke, A. Harrison, T. E. Mason, G. J. McIntyre, and D. Visser, *J. Phys.: Condens. Matter*, 1992, **4**, L71.
- 8 H. M. Ronnow, D. F. McMorrow, and A. Harrison, *Phys. Rev. Lett.*, 1999, **82**, 3152.
- 9 F. Coomer, 'unpublished work', 2004.
- 10 B. A. Goodman and J. B. Raynor, *Adv. Inorg. Chem. Radiochem.*, 1970, **13**, 135.
- 11 J. S. Smart, 'Effective Field Theories of Magnetism', Saunders 1966.
- 12 R. L. Carlin, 'Magnetochemistry', Berlin, Springer-Verlag, 1986.
- 13 C. Kittel, 'Introduction to Solid State Physics.' 7th Ed. New York, Wiley, 1996.
- 14 A. L. Chernyshev, Y. C. Chen, and A. H. Castro Neto, *Phys. Rev. Lett.*, 2001, **87**, 067209/1.
- 15 M. De Vries, in 'Private Communication', Edinburgh, 2005.
- 16 G. Wolmershaeuser, M. Schnauber, and T. Wilhelm, *J. Chem. Soc., Chem. Commun.*, 1984, 573.

Chapter 5

Complexes of [BBDTA]_x[M(dithiolenes)₂]

5.1 Introduction

The work carried out in Chapter 3 was repeated with the same metal dithiolene complexes as before, but using the cation [BBDTA]^{•+}. [BBDTA]^{•+} (shown in figure 3. 2) is of great magnetic significance as it is a paramagnetic cation that has been involved in the formation of organic ferromagnetic materials (see section 3.1.2). Although [BBDTA]^{•+} is a radical it is considerably more stable than other dithiazolyl radical such as [TTTA][•]. Single crystals of [BBDTA]^{•+} have been obtained as [BBDTA][FeCl₄] and a structure determined. Thus it was anticipated that [BBDTA]^{•+} would be stable enough to form novel and magnetically interesting materials, as well as being stable enough in solution to form crystalline materials for a full structural analysis.

5.2 Results and discussion of

[BBDTA]_x[M(dithiolene)₂]

Similar to chapter 3, the dithiolene complexes [Cu(mnt)₂]²⁻, [Ni(dmit)₂]⁻ and [Fe(tdas)₂]⁻ were co-precipitated with [BBDTA]^{•+} along with the additional dithiolenes [Ni(mnt)₂]⁻ and [Co(mnt)₂]²⁻. A dark solid was formed in all five reactions, which were found to be [BBDTA]₂[Cu(mnt)₂] [11], [BBDTA][Ni(dmit)₂] [12], [BBDTA][Fe(tdas)₂] [13], as well as the impure products [BBDTA]_x[Ni(mnt)₂] [14] and [BBDTA]_x[Co(mnt)₂] [15].

5.2.1 Preparation and X-ray analysis

All salts were synthesised by rapid co-precipitation of [BBDTA][FeCl₄] in MeCN and the [TBA]⁺ salt of each dithiolene complex in MeCN. For all reactions a very dark powder was obtained almost immediately. These were washed and found (by CHN analysis) to be pure compounds of the formula given in the previous page (with the exception of [14] and [15]). Single crystal growth was attempted by layering a solution of [BBDTA][FeCl₄] in either MeCN, EtOH, acetone, chlorobenzene or benzonitrile on top of each [TBA]_x[M(dithiolene)₂] in a DCM solution at various temperatures (193 K-298 K). Single crystals were obtained for what were thought to be [13] and [15] using chlorobenzene as solvent at 253 K, but these were not the desired salts. [BBDTA]⁺⁺ was not incorporated into the crystallised salts as the structures were found to be composed of the dimerised dithiolene starting materials, shown in Figure 5. 1. Both of these structures are known in the literature and in this case appear to have crystallised out of solution as the anions dimerised in solution over a long period of time. The [BBDTA]⁺⁺ cation also appears to decompose over this time as a fine solid, different in appearance from the products, was deposited within the crystallisations involving benzonitrile. To conclude, [BBDTA]⁺⁺ appears to be unstable in solution over a long period of time which prevents the growth of crystals by this method. Thus, [TBA][Fe(tdas)₂] and [TBA][Co(mnt)₂] were crystallised from the solutions instead of [13] and [15]. However, [BBDTA]⁺⁺ is present in the powder samples, emphasising that the composition and structure of the powder cannot be the same as the crystals.

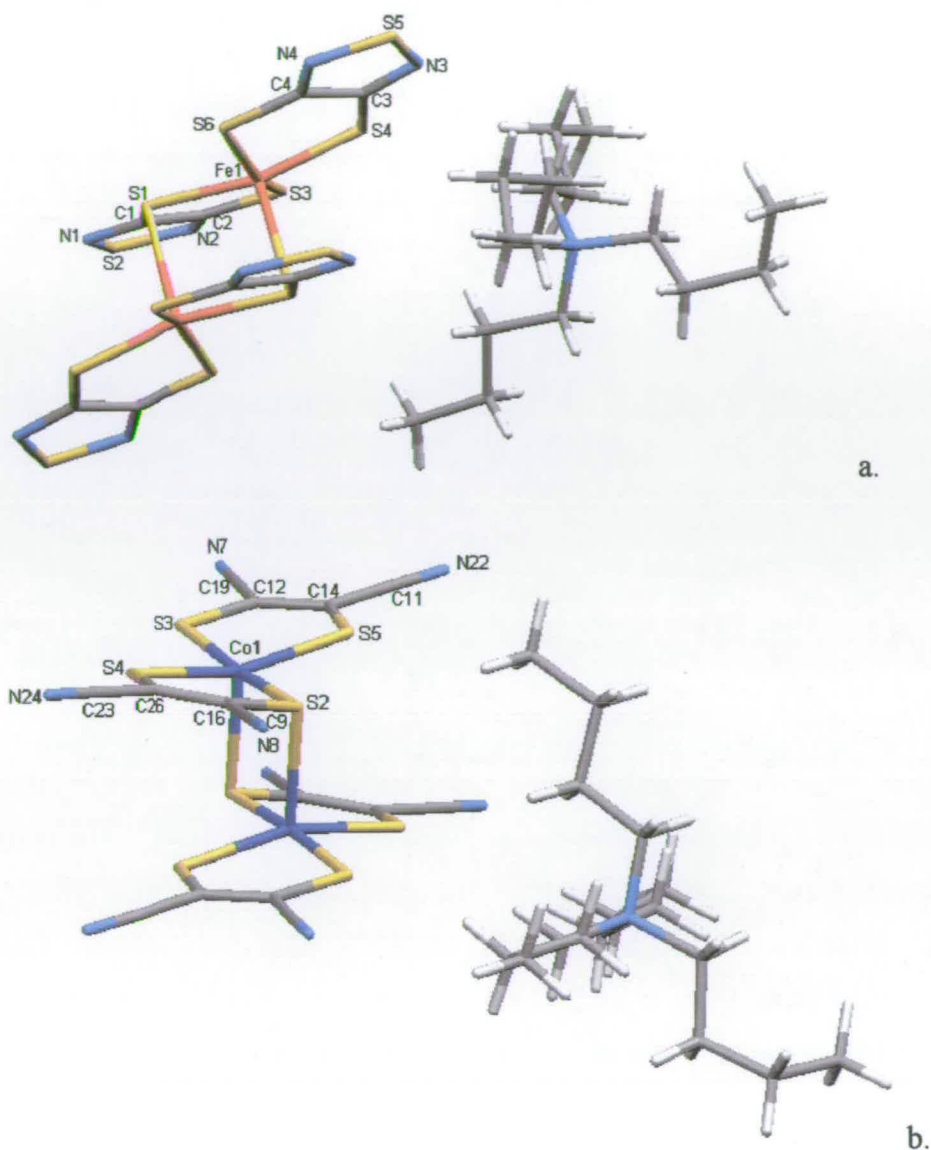


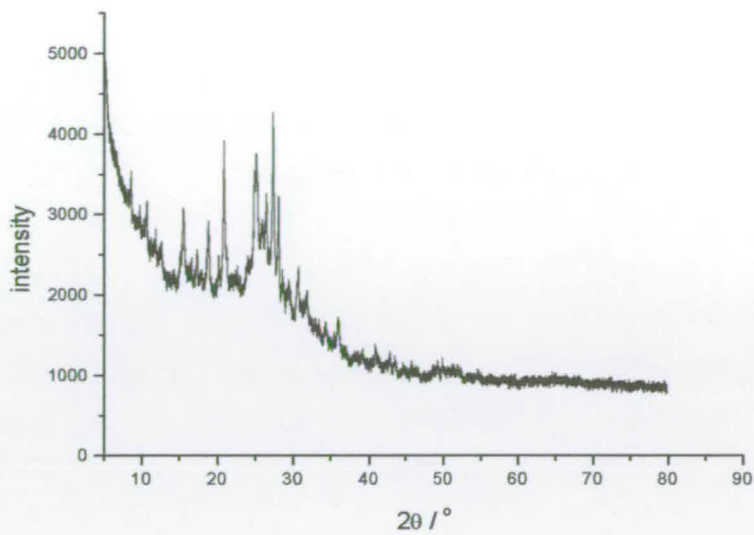
Figure 5. 1 Crystal structures of a) product obtained from attempted crystallisation of [13], found to be $[TBA][Fe(tdas)_2]$, b) product obtained from attempted crystallisation of [15], found to be $[TBA][Co(mnt)_2]$.

To overcome the potential instability of $[BBDTA]^{*+}$, an *in situ* method of obtaining single crystals was then undertaken, designed to exploit the redox reaction that occurs in the synthesis of the $[BBDTA][FeCl_4]$ from $BBDTA.Cl_2$. For this *in situ* approach,

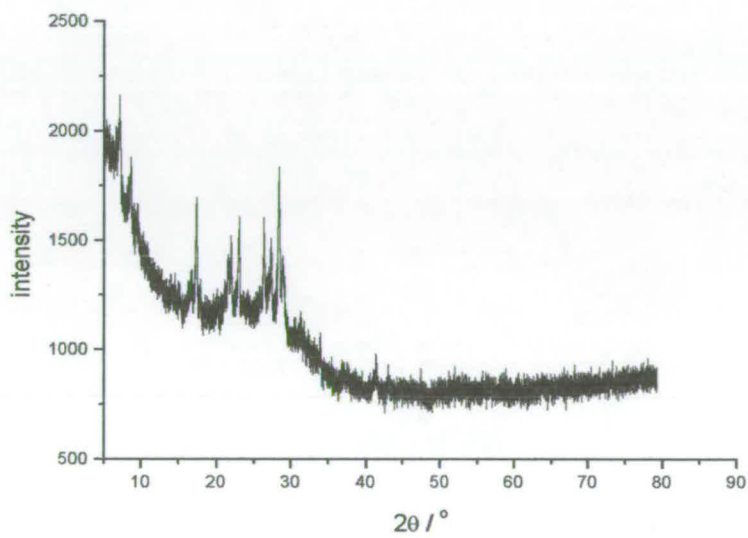
BBDTA.Cl₂ was suspended in MeCN and a solution of [TBA]₂[Ni(dmit)₂] or [TBA]₂[Ni(tdas)₂] in MeCN was added slowly. A redox reaction to reduce the cation and oxidise the anion to produce the desired salts was then expected to take place (just as when FeCl₂ and BBDTACl₂ are mixed in solution). Crystals of [12] and [14] should then have formed when the reaction mixture was cooled. The redox reaction did not occur to the same extent (if at all) as the production of [BBDTA][FeCl₄] and as such it was virtually impossible to separate out the solid starting material [BBDTA]Cl₂ from any insoluble desired product. Thus this method was also abandoned.

It became apparent that the best opportunity to obtain structural data that did not depend on crystal growth was to perform X-ray powder diffraction on fast precipitation powder products of [11]-[15].

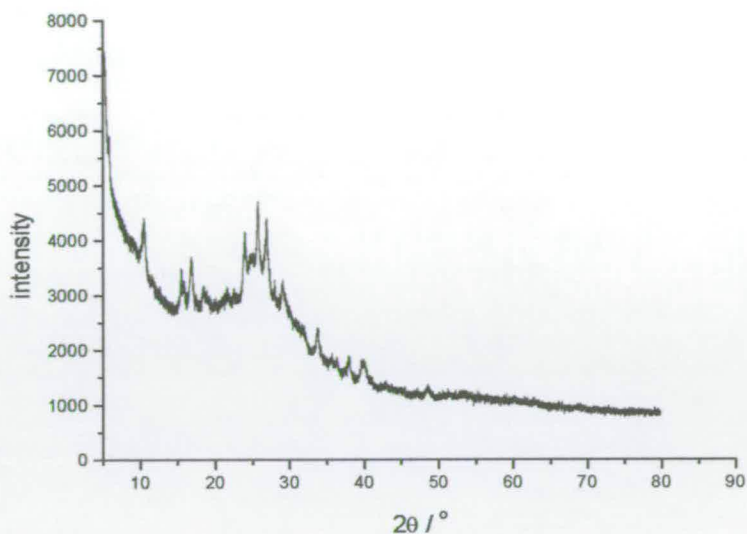
X-ray powder diffraction patterns were collected for all 5 samples and it was found that the samples [14] and [15] were amorphous and so no structural information could be obtained for these samples. For this reason, along with the uncertainty over purity and composition, magnetic data were not collected for these two samples. Salts [11]-[13] yielded diffraction data that is shown in figure 5. 2.



a



b.



c

Figure 5. 2. Powder x-ray diffraction patterns for a) [11], b) [12] and c) [13].

The X-ray powder patterns show crystalline material. However, the quality of the samples are not ideal, as the peaks are quite poorly defined. Even taking this into consideration, the full crystal structure solutions for these compounds can be attempted from this data as the individual molecules within the structure are rigid and are present in other known structures, so distances and angles can be predicted. For molecules such as these the most difficult part of solving a structure from powder diffraction data is the initial stage of indexing to obtain the unit cell. Once this has been achieved the remaining stages are relatively straightforward, as there are no degrees of freedom in each ion, so it is simply a case of fitting them into the unit cell. This said, the samples are proving very difficult to solve as the unit cell cannot be identified and so attempts to resolve the solid-state structures from these data are still underway.

5.2.2 Magnetic and EPR Studies

5.2.2.1 EPR Analysis

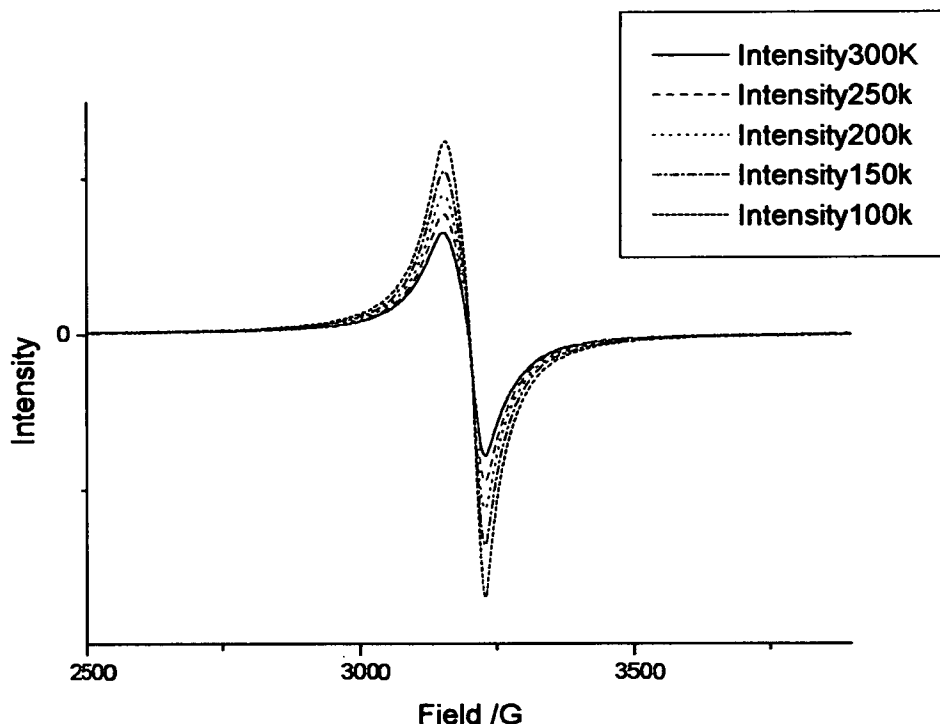


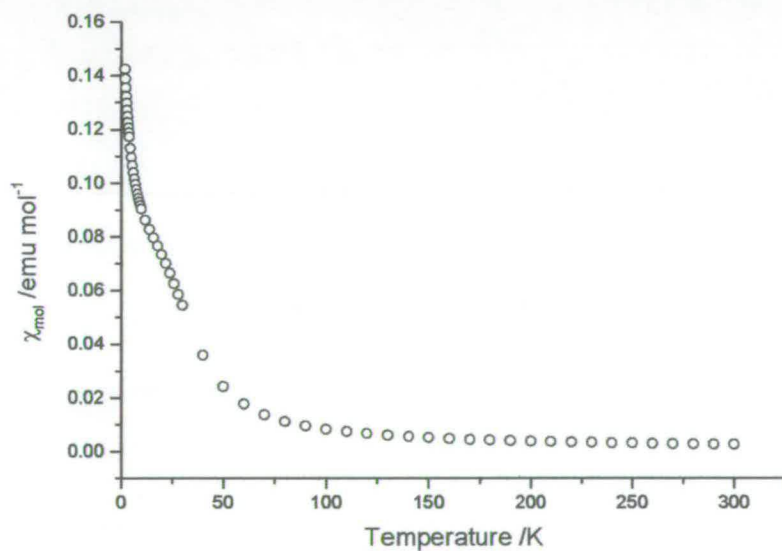
Figure 5. 3 Variable temperature EPR spectra of [11] from 100-300 K.

Variable temperature EPR measurements were performed on the solid samples [11]-[13] between 4-300 K (Figure 5. 3 shows EPR measurements of [11] from 100-300 K {lower temperature values are omitted for clarity, as the intensity increases dramatically at lower temperature}). The spectrum obtained showed a single peak, characteristic of an organic radical with $g = 2.02$ for samples [11] and [12]. Sample [11] showed the strongest signal, with sample [12] being quite noisy at room temperature. [13] displayed a similar

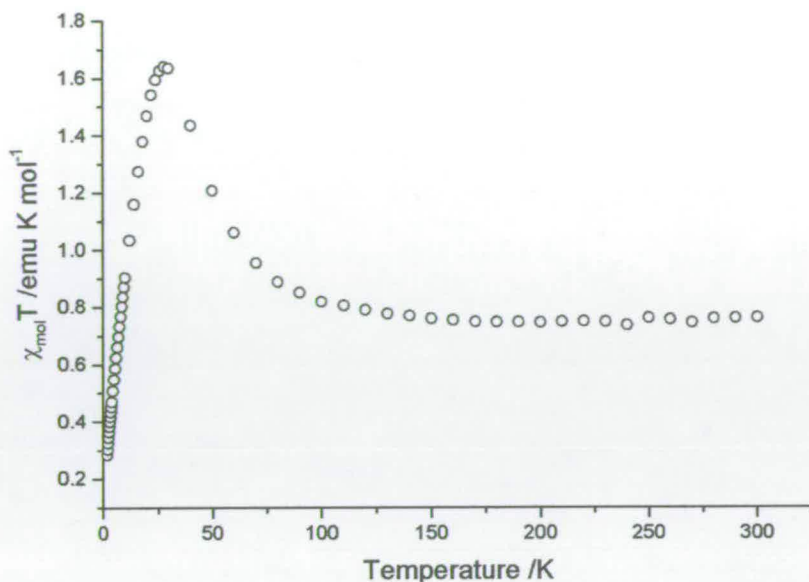
pattern but of much reduced intensity. The signal is very noisy, even at 4 K, with the signal diminishing to silence at room temperature. It is only the organic radical that is seen in all the samples, with no visible peaks or coupling to the dithiolene anions.

5.2.2.2 Magnetic susceptibility

As the solid state structure of compounds [11]-[13] have not yet been resolved from the X-ray powder data, any discussion of magnetic interactions within these materials will be on a speculative basis until structural information becomes available. The magnetic analysis is further complicated by the presence of paramagnetic cations as well as anions.



a.



b.

Figure 5.4. Magnetic data for [11] from 2-300K a) Molar magnetic susceptibility, b) $\chi_{mol}T$ versus temperature.

The data collected for [11] show a magnetic susceptibility curve that increases with decreasing temperature, with a shoulder at 13 K. This behaviour is most probably due to a mixture of two magnetic systems: a combination of a peak depicting intermolecular magnetic interaction, as well as a Curie-Weiss curve showing the presence of isolated paramagnets. A better idea of the magnetic behaviour within this material can be obtained from a plot of $\chi_{mol}T$ versus temperature that will show the values of a Curie constant at any given temperature (figure 5. 4). The plot shows a horizontal line at high temperatures with a peak occurring 25 K, the plot then drops off to lower values at lower temperature. [11] is a system with one $[\text{Cu}(\text{mnt})_2]^{2-}$ anion and two $[\text{BBDTA}]^{+}$ cations per formula unit that will have one unpaired electron associated with each ion in the absence of any intermolecular

interactions. The first observation to note is that the value of $\chi_{mol}T$ at high temperature is lower than expected for three non-interacting unpaired electrons ($C_{expected} = 1.125 \text{ emu K mol}^{-1}$) suggesting there is some antiferromagnetic interaction. At approximately 35-20 K $\chi_{mol}T$ peaks to a value of $1.65 \text{ emu K mol}^{-1}$ which is greater than the value expected for three unpaired electrons suggesting the onset of some ferromagnetic alignment. Below this temperature the value of $\chi_{mol}T$ decreases to $0.3 \text{ emu K mol}^{-1}$ suggesting the onset of global antiferromagnetic exchange.

In the absence of any structural data, there are numerous postulates that could describe a magnetic mechanism that conforms to these specifications. For example, if the structure of **[11]** is similar to that of **[2]** then antiferromagnetic trimers could account for the high temperature data, while these could form ferromagnetic chains at 25 K with antiferromagnetic interchain interactions occurring at very low temperatures. However any number of combinations of interacting ferromagnetic and antiferromagnetic systems could be present and the true mechanism can only be ascertained when a crystal structure is obtained.

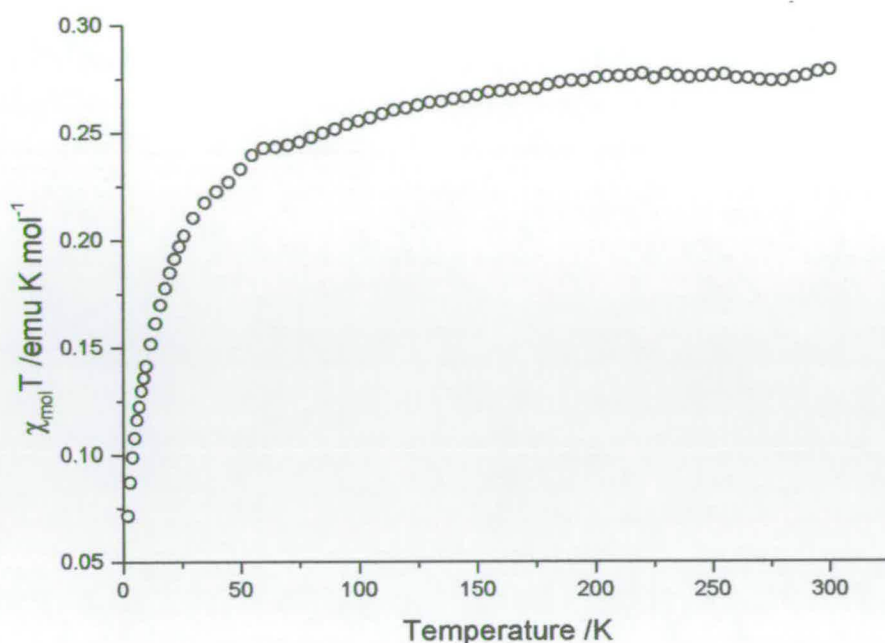
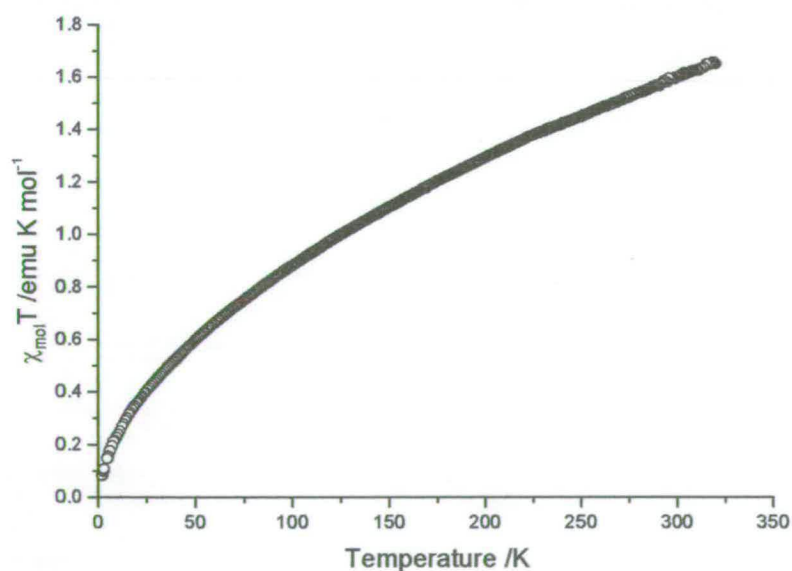


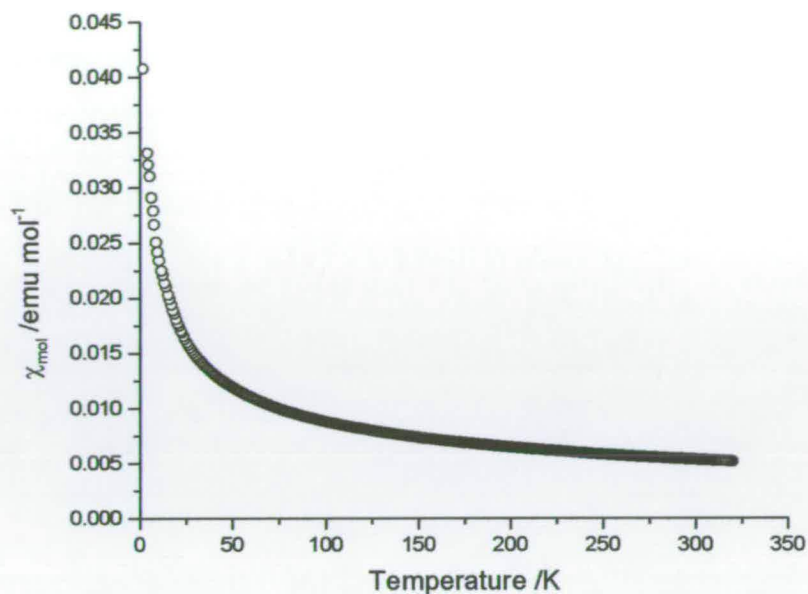
Figure 5. 5 Magnetic data of [12]. $\chi_{mol}T$ versus temperature.

The $\chi_{mol}T$ versus temperature plot for [12] is simpler and depicts a curve that decreases at low temperature, which is the classic pattern for a material with an antiferromagnetic ground state (figure 5. 5). The magnetic susceptibility of [12] shows a characteristic Curie-Weiss curve with no visible peaks or shoulders. In this case a Curie constant of approximately $0.26 \text{ emu K mol}^{-1}$ is seen above approximately 100 K. The CHN analysis shows the composition of the salt to be 1:1 and from this ratio one unpaired electron is expected on each of the ions at high temperatures which should give a Curie constant ($= 0.75 \text{ emu K mol}^{-1}$) much higher than $0.26 \text{ emu K mol}^{-1}$. The redox potential ($E_{1/2}$) of $[BBDTA]^{0/+} = +0.16$ which is comparable to that of $[BDTA]^{0/+}$ (+0.15) so it is not

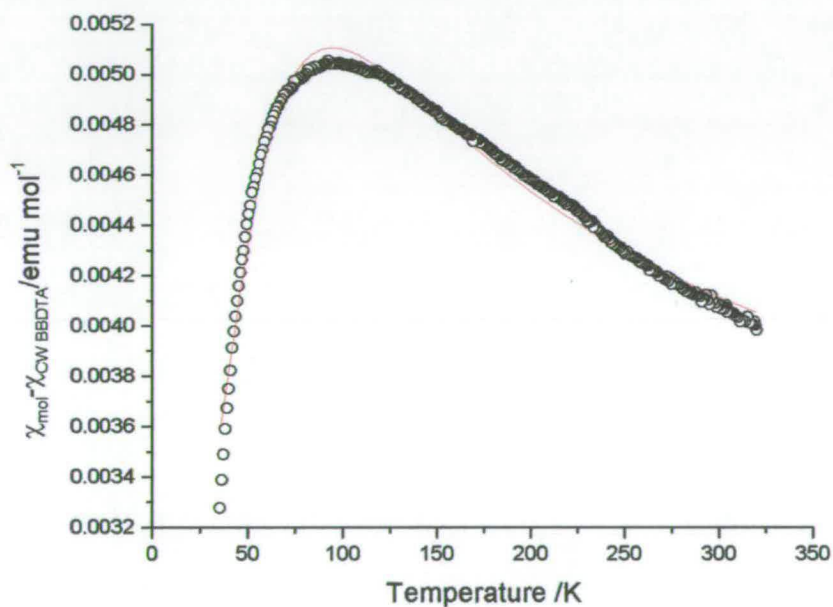
unreasonable to suggest that charge transfer may have occurred in [12] that could have reduced the value of the Curie constant, similar to the $[BDTA]^+$ analogue [3] (although it is not the analogous 1:2 salt $[BBDTA][Ni(\text{dmit})_2]_2$). The value of $0.26 \text{ emu K mol}^{-1}$ is closer to a value for one unpaired electron, and as such some degree of partial oxidation and charge transfer cannot be ruled out. In the absence of a structure it is impossible to say whether or not there is more than one type of cation or anion. Different oxidation states for different fractions of the material could explain the low spin density, with some ions charged and some neutral. It is also a possibility that dimerisation is occurring in this material that would also reduce the spin density, as both of these ions have been known to form such dimeric species in the literature.^{1, 2} Thus, the low value of $\chi_{mol}T$ can be interpreted as potentially arising from a number of sources that include dimerisation and possible charge transfer.



a



b.



c.

Figure 5. 6 Magnetic data for [13] versus temperature (2-320 K) a) $\chi_{\text{mol}}T$, b) Molar magnetic susceptibility, c) Molar magnetic susceptibility with a Curie component of $[BBDTA]^{*+}$ subtracted. —

= Bleaney-Bower fit for a dimer with $J/k = -76 \pm 0.2$ K

Similar to [11] and [12], [13] displays some mixed magnetic effects. This is apparent from the fact that $\chi_{mol}T$ versus temperature shows increasing $\chi_{mol}T$ with increasing temperature and does not show signs of levelling to a constant value (figure 5.6.a). This activated signal shows that magnetic interactions are seen, even at high temperatures. [13] is composed of one [BBDTA]^{•+} cation and one [Fe(tdas)₂]⁻ anion. All examples of [Fe(tdas)₂]⁻ (with the exception of [5], {chapter 3 in this work}) have a crystal structure that has dimerised [Fe(tdas)₂]₂ units. It is therefore reasonable to assume that the [Fe(tdas)₂]⁻ anions within [13] also dimerise with a strong coupling. The molar magnetic susceptibility plot (figure 5.6.b) looks very much like a Curie-Weiss curve but can not be fitted to this model, as a result of the intermolecular interactions. Unlike [11] there is no visible peak or shoulder in the susceptibility plot of [13]. However, if the Curie component of the [BBDTA]^{•+} cation is subtracted from the magnetic susceptibility data the plot shown in figure 5.6.c is observed. Here one can clearly see a peak due to antiferromagnetic dimerisation. This can be fitted to the Bleaney-Bower model to give a predictably strong magnetic coupling of $J/k = -76 \pm 0.2$ K which is comparable to the coupling of other literature examples of [Fe(tdas)₂]₂ dimers ($J/k = -108$).³ Thus, the suggested magnetic structure of [13] is a mixed model of a Curie-Weiss component to represent the non-interacting paramagnetic cation [BBDTA]^{•+} with $C = 0.375$ emu K mol⁻¹, along with [Fe(tdas)₂]⁻ anions forming dimers with a strong antiferromagnetic coupling interaction with $J = -76$ K.

5.3 Conclusion

Samples [11]-[15] were synthesised by rapid precipitation in MeCN. Crystal growth proved to be very problematic, perhaps due to $[BBDTA]^{*+}$ decomposition in solution over a crystal growth time frame. Thus attempts to obtain structural information from X-ray powder diffraction were implemented. Compound [14] and [15] were found to be amorphous, as well as their purity being lower than the other samples. This reduced purity made it difficult to identify the salt composition as there is little elemental difference between a 2:1 and 1:1 salt. These samples thus offered no information to elude to any structure or true composition. For these reasons no further studies were carried out on these samples. X-ray powder diffraction patterns were collected for the pure microcrystalline samples [11]-[13] and attempts to obtain a full structure for these compounds is currently underway. As no structural data is yet known for these, the analysis of the magnetic and EPR data can only be conjectural. The EPR data show an organic radical signal of varying intensity for each compound that can be assigned to the $[BBDTA]^{*+}$ cation. This shows the magnetic data has an element of paramagnetic behaviour from the cations. Analysis of the magnetic data shows a combination of paramagnetic behaviour from the cation mixed with; antiferromagnetic and ferromagnetic order occurring in [11], and antiferromagnetic dimerisation of $[\text{Fe}(\text{tdas})_2]^-$ anions ($J/k = -76 \text{ K}$) in [13]. [12] displayed magnetic data with a very low spin density that could be the result of dimerisation or charge transfer. However, these magnetic mechanisms cannot be clarified until structural data is obtained.

5.4 Experimental

All starting material salts used were synthesised by literature methods. The starting materials [BBDTA][FeCl₄]MeCN,⁴ [BBDTA]Cl₂,⁵ were synthesised by Umezono Yoshikatsu and other co workers of Prof. Kunio Awaga's group in Japan. [BBDTA][FeCl₄] was also prepared by the author in Edinburgh. The salts [TBA]₂[Co(mnt)₂], [TBA]₂[Cu(mnt)₂], [TBA][Ni(mnt)₂],⁶ [TBA][Ni(dmit)₂],^{7, 8} and [TBA][Fe(tdas)₂]⁹ were prepared by the author from literature methods.

5.4.1 Preparation of [BBDTA]_x[M(dithiolene)₂] [11]-[15]

All [BBDTA]_x[M(dithiolene)₂] salts were prepared by mixing x equivalents of [BBDTA][FeCl₄] (≈ 17 mg) in MeCN (5 ml) with one equivalent of [TBA]_x[M(dithiolene)₂] (≈ 30mg) in MeCN (5 ml). The powder sample was washed with MeCN and ether and analysed by CHN. The bulk sample was then used for the magnetic and EPR measurements.

5.4.2 Analysis

5.4.2.1 [BBDTA][FeCl₄]

CHN for C₆H₂Cl₄FeN₂S₄ Calculated; C, 16.84; H, 0.47; N, 6.55. Found; C, 16.65; H, 0.74; N, 6.42%

5.4.2.2 [TBA]₂[Co(mnt)₂]

CHN for C₄₀H₇₂CoN₆S₄. Calculated; C, 49.58; H, 6.25; N, 12.04. Found; C, 52.04; H, 6.91; N, 11.8%

5.4.2.3 [TBA]₂[Cu(mnt)₂]

CHN for C₄₀H₇₂CuN₆S₄. Calculated; C, 57.96; H, 8.76; N, 10.14. Found; C, 57.65; H, 8.72; N, 10.12%

5.4.2.4 [TBA][Ni(mnt)₂]

CHN for C₂₄H₃₆N₅NiS₄. Calculated; C, 49.57; H, 6.24; N, 12.04. Found; C, 50.57; H, 5.96; N, 6.63%

5.4.2.5 [TBA][Ni(dmit)₂]

CHN for C₂₂H₃₆NNiS₁₀. Calculated; C, 38.08; H, 5.23; N, 2.02. Found; C, 37.88; H, 5.48; N, 2.08 %

5.4.2.6 [TBA][Fe(tdac)₂]

CHN for C₂₀H₃₆FeN₅S₆. Calculated; C, 40.39; H, 6.10; N, 11.77. Found; C, 40.60; H, 6.35; N, 11.53 %

5.4.2.7 [BBDTA]₂[Cu(mnt)₂] [11]

CHN for C₂₀H₄CuN₈S₁₂. Calculated; C, 29.85; H, 0.50; N, 13.93. Found; C, 29.78; H, 0.47; N, 13.03%

5.4.2.8 [BBDTA][Ni(dmit)₂] [12]

CHN for C₁₂H₂NiS₁₄. Calculated; C, 21.14; H, 0.30; N, 4.11. Found; C, 21.80; H, 0.48; N, 4.50%

5.4.2.9 [BBDTA] [Fe(tdas)₂] [13]

CHN for C₁₀H₂FeN₆S₁₀. Calculated; C, 20.61; H, 0.35; N, 14.78. Found; C, 21.64; H, 0.10; N, 10.60%

5.4.2.10 [BBDTA]_x[Ni(mnt)₂] [14]

CHN for C₁₄H₂N₆NiS₈. Calculated; C, 29.53; H, 0.35; N, 14.76. Found; C, 21.19; H, 0.96; N, 9.07%

5.4.2.11 [BBDTA]_x[Co(mnt)₂] [15]

CHN for C₂₀H₄CoN₈S₁₂. Calculated; C, 30.03; H, 0.50; N, 14.01. Found; C, 23.56; H, 1.13; N, 10.51%

5.5 References

- ¹ T. M. Barclay, A. W. Cordes, R. H. de Laat, J. D. Goddard, R. C. Haddon, D. Y. Jeter, R. C. Mawhinney, R. T. Oakley, T. T. M. Palstra, G. W. Patenaude, R. W. Reed, and N. P. C. Westwood, *J. Am. Chem. Soc.*, 1997, **119**, 2633.
- ² H. Oshio, *Inorg. Chem.*, 1993, **32**, 4123.
- ³ K. Awaga, T. Okuno, Y. Maruyama, A. Kobayashi, H. Kobayashi, S. Schenk, and A. E. Underhill, *Inorg. Chem.*, 1994, **33**, 5598.
- ⁴ G. Wolmershaeuser, G. Wortmann, and M. Schnauber, *J. Chem. Res., Synop.*, 1988, 358.
- ⁵ G. Wolmershaeuser, M. Schnauber, T. Wilhelm, and L. H. Sutcliffe, *Synth. Met.*, 1986, **14**, 239.
- ⁶ I. G. Dance and T. R. Miller, *Inorg. Chem.*, 1974, **13**, 525.
- ⁷ G. Steimecke, R. Kirmse, and E. Hoyer, *Zeits. Chem.*, 1975, **15**, 28.
- ⁸ G. Steimecke, H. J. Sieler, R. Kirmse, and E. Hoyer, *Phos. Sulf. Rel. Elem.*, 1979, **7**, 49.
- ⁹ I. Hawkins and A. E. Underhill, *J. Chem. Soc., Chem. Commun.*, 1990, 1593.

Chapter 6

Thiophosphine Complexes

6.1 Introduction

A thiophosphine is a bidentate ligand system of the form $((\text{SPR}_2)_2\text{N})$ comprising a conjugated heterocyclic six-membered ring when complexed to a metal, with organic R groups bound to each phosphorus, shown in Figure 6. 1. Complexes of the form $[\text{M}((\text{SPR}_2)_2\text{N})_2]$ have aroused great interest, due to their unusual geometry. Structural determination of these complexes with a variety of metal centres and R groups has displayed an MS_4 core from tetrahedral to square-planar geometries along with distorted intermediates.

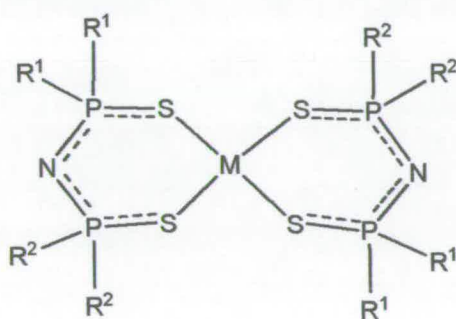


Figure 6. 1 $[\text{M}((\text{SPR}_2)_2\text{N})_2]$

Complexes with an MS_4 core of distorted geometry, are of particular interest as mimics of biological systems,^{1, 2} since metalloenzymes are usually coordinated with some strain or unusual geometry. The intermediate between square-planar and tetrahedral geometries is utilised in biological processes as it represents the transition state of a reaction and allows fast electron transfer to and from the metal centre. In addition, many of these systems coordinate to the metal ion via the sulphur donors of residues such as cystine. One example of such an enzymatic system is the Ni-Fe

hydrogenase. This system oxidises a molecule of H_2 to $2H^+ + 2$ electrons by cleaving the H-H bond and thus allowing fast electron transfer away from the H^+ . The nickel ion is bound by four cysteine residues and a computer model has shown that the optimum transition state for the reaction has a distorted geometry very similar to that of the natural system.³ Thus $[M((SPR_2)_2N)_2]$ complexes have been studied extensively as they display similar distorted geometry to those of natural systems and can be used as simplified models to mimic metalloenzymatic processes. It is for this reason that most of the previous research on these complexes has been largely concerned with the structural and enzymatic properties, involving crystal structure determination and probing with IR and UV-Vis spectroscopy as well as some EPR studies.⁴⁻⁹

Transition metal complexes previously studied are those where $M = Ni(II)$,^{4, 5, 7, 10}, $Co(II)$,^{7, 8} $Fe(II)$,⁷ $Zn(II)$,⁴ $Cu(II)$ ⁶ and $Cd(II)$ ⁴ and these have shown a variety of geometries, mainly tetrahedral/ pseudo-tetrahedral with some pseudo-square-planar complexes. The Ni^{2+} complexes are of particular interest as Ni^{2+} has a geometric preference to form square-planar complexes with strong-field ligands such as these (see results section 6.2.2.1), making the tetrahedral form unusual.

No previous studies have concentrated on magnetic analysis of these complexes, but $[M((SPR_2)_2N)_2]$ would lend themselves ideally to an in-depth magnetic study as they are easy to synthesise and crystallise, and so magnetic interpretation can be performed with reference to the structures. Within this context, it will be especially interesting to observe the effect of the distorted geometry on the magnetism. The geometry of a system has a profound effect on the magnetism as the energy of the d-orbitals are altered, leading to different numbers of unpaired electrons and variation in the energy of orbitals. For example Ni^{2+} is paramagnetic in a tetrahedral geometry and diamagnetic in

a square-planar geometry.

The reasoning for different $[M((SPR_2)_2N)_2]$ complexes to adopt different geometries has not been fully explained in every case. The preference of a specific metal to adopt a certain geometry will be a factor, however, there are examples of complexes that do not conform to the typical geometry for these M^{2+} systems, with Ni^{2+} being the most pronounced example. From an examination of previously studied Ni^{2+} complexes, it has been found that complexes with the same $M = Ni$ but different R groups may have different geometries. Many examples of tetrahedral complexes have $R = Ph^{5,7}$ and steric hindrance of the Ph group was initially thought to be the cause for this geometry. The steric hindrance hypothesis was found to be incorrect as tetrahedral examples were found for $R = Me^{7,10}$ and iPr^4 as well as square-planar examples of $R = Ph^9$ and the asymmetric case of $R = Me \& Ph^5$. Thus, $M = Ni$ and $R = Ph$ can adopt both square-planar and tetrahedral geometries in different conditions^{5,9} and the factors that control the geometry remain unexplained.

In this context, the magnetic analysis, along with EPR, NMR, structural analysis, computer modelling and X-ray spectroscopy, of $[M((SPR_2)_2N)_2]$ complexes of varying geometry was performed. The results were used to help elucidate the reasons behind the formation of various geometries of this family of compounds by monitoring the distribution of electron density and nature of bonding. In this work $M = Co, Mn, Ni$, $R = Ph, iPr$ and (Ph, iPr) have been studied. The crystal structures for these complexes are known with the exception of $M = Mn$ and $R = iPr$, and the asymmetric example ($R = (Ph, iPr) M = Co, Mn, Ni$), which have been determined and are reported herein.

6.2.1 Literature crystal structures of $[M((SPR_2)_2N)_2]$ [16], [19], [20], [22] & [23] and the structural determination for [17], [18], [21] & [24]

The structures of [16], [19], [20], [22], and [23] have been determined previously and are reported in the literature.^{4, 5, 8, 9, 11, 12} A summary of these structures is shown in Table 6. 2. All the systems are pseudo-tetrahedral with the exception of [22] which adopts both pseudo-tetrahedral and square-planar geometries. It can be seen that the M-S bond lengths are typical of each system and that the Ni-S bond is shorter in the square-planar than the tetrahedral system. It is also worth noting that all the endocyclic angles are larger than the perfect geometrical angle ($109.5^\circ =$ tetrahedral, $90^\circ =$ square-planar) by up to 3° in the tetrahedral complexes and approximately 8° in the square-planar. The M = Mn complex [16] has an MS_4 core very close to tetrahedral geometry. Although the endocyclic bond angles are some degree larger, the two S-Mn-S planes have dihedral angles very close to 90° . This creates a molecule with approximate S_4 point symmetry with the four-fold rotation about the c-axis N(1)-Mn-N(2). Thus, although they are not crystallographically equivalent, the a and b axis can be said to be very nearly equivalent with an elongation in the c-axis (example of [23] shown in Figure 6. 2). This axial symmetry is mirrored in the M = Co complexes [19] and [20] along with M = Ni complexes [22] and [23], with [23] being the most symmetrical. [19] and [22] can be said to be isostructural to one another as well as being the most unsymmetrical of these five complexes.

Single crystal X-ray crystallography was carried out on [17], [18], [21] and [24] and these structures are also summarised in Table 6. 2.

M	Mn			Co			Ni			
	16	17	18	19	20	21	22	23	24	
Approx. MS ₄ geometry	tet.	tet.	tet.	tet.	tet.	tet.	tet.	sq. pl.	tet.	sq. pl.
Space Group	P1	P $\bar{1}$	P1	P $\bar{1}$	I4 ₁ /a	C2/c	P $\bar{1}$	P $\bar{1}$	I4 ₁ /a	P $\bar{1}$
M-S mean /Å	2.443	2.443	2.447	2.323	2.317	2.321	2.299	2.234	2.284	2.230
P-S mean /Å	2.013	2.028	2.021	2.015	2.028	2.028	2.028	2.032	2.027	2.034
Endocyclic S-M-S °	111.68 112.08	109.59 110.82	109.19 110.04	113.20 113.78	110.48	110.60	111.32- 112.39	98.36	109.86	97.86- 98.17
Exocyclic S-M-S °	106.32- 110.82	107.34- 111.53	96.94- 117.04	106.25- 108.39	108.97	95.84- 114.22	103.25- 113.88	81.60 180.00	108.69	81.83 180.00
References	¹²			⁸	⁸		⁵	⁹	⁴	

Table 6. 2 Summary of structural feature of complexes [16]-[24]

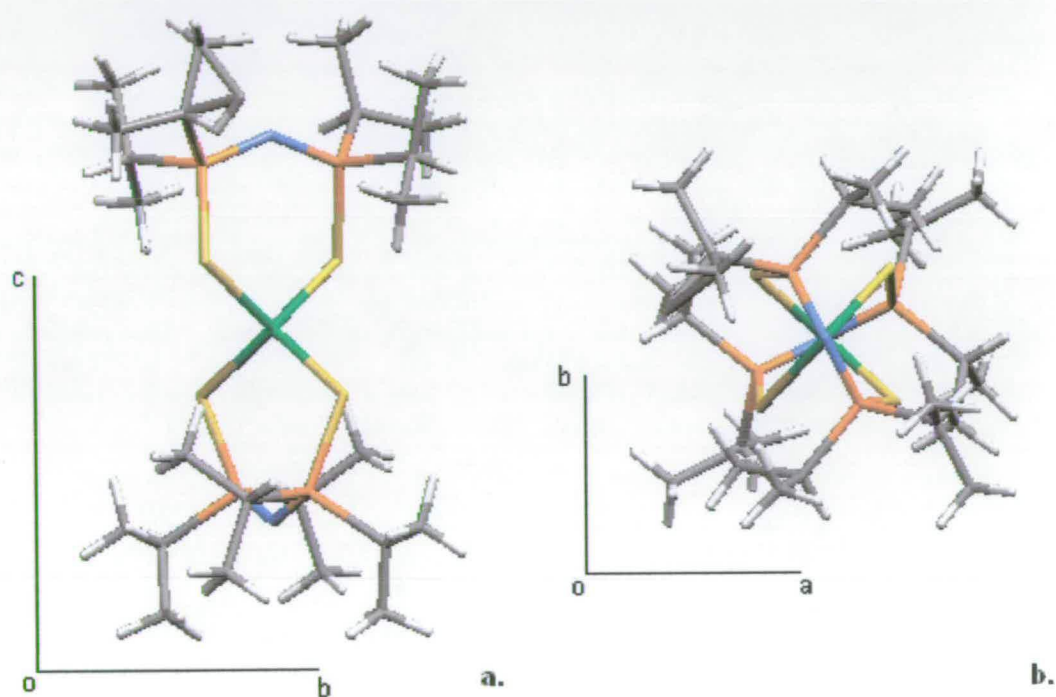


Figure 6. 2. Molecular crystal structure of [23]. Viewed a) along the a-axis and b) along the c-axis.

6.2.1.1 Crystal structure of $[\text{Mn}((\text{SP}(\text{iPr})_2)_2\text{N})_2]$ [17]

[17] was crystallised in the space group $P\bar{1}$ with one molecule per unit cell (shown in Figure 6.3). The structure shows Mn-S bond lengths of 2.438 (S2), 2.441 (S3), 2.444 (S4) and 2.447 (S1) Å which are typical of Mn-S unstrained bonds. It should also be noted that the lengths are not symmetrical. The S(1)-Mn-S(2) and S(3)-Mn-S(4) have bond angles of 109.59 and 110.82 respectively, which are close to the ideal value for a tetrahedral geometry. The planes of both S-Mn-S unit are nearly exactly perpendicular to one another with an S-Mn-S dihedral angle of 91.5° , showing that the molecule is very close to having tetrahedral symmetry and it is only the slight deviation from the tetrahedral angle and asymmetric bond lengths that breaks this symmetry. The six-membered ring is slightly puckered with P(1) and P(2) atoms lying at 40.4° above and below the M, S(1), N(1), S(2) plane, and P(3) and P(4) atoms lying at 39.9° and 42.1° above and below the M, S(3), N(2), S(4) plane.

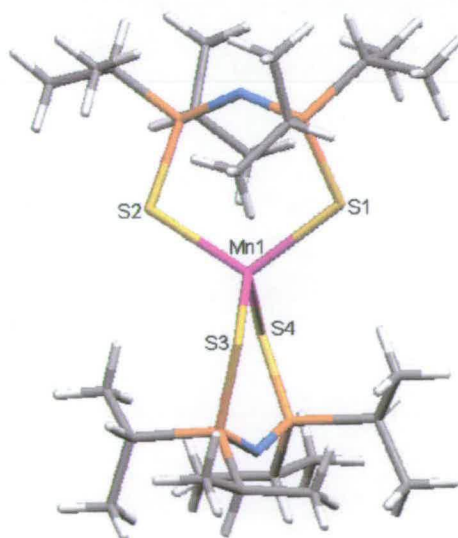


Figure 6.3 Molecular structure of [17]

6.2.1.2 Crystal structure of $[\text{Mn}((\text{SPPh}_2)(\text{SP}^i\text{Pr}_2\text{N})_2)]$ [18]

Similarly to [17], [18] was crystallised with one molecule per unit cell in the space group P1. However unlike [17], [18] has an MS_4 core that is much more distorted pseudo-tetrahedral. The Mn-S bond lengths are again unsymmetrical and in the region typical of unstrained Mn-S bonds, but vary in length by a greater degree with values of 2.438, 2.440, 2.450 and 2.459 Å. The most striking difference between [17] and [18] is the conformation of the six-membered rings. The ring systems of [18] have a boat conformation and it has a degree of strain about the metal centre, which has a very unusual pseudo-tetrahedral motif. The endocyclic angles of 109.19° and 110.04° are close to tetrahedral, however the intersect between each S-Mn-S plane deviates by 10° from the ideal 90° , as each boat shaped ring bends towards the ^iPr groups on the adjacent ligand (shown in Figure 6. 4).

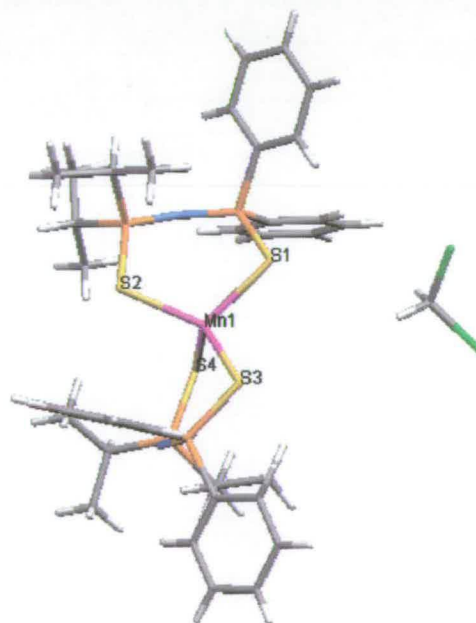


Figure 6. 4 Molecular structure of [18]

6.2.1.3 Crystal structure of $[\text{Co}((\text{SPPh}_2)(\text{SP}^i\text{Pr}_2)\text{N})_2]$ [21]

[21] has an MS_4 core that has a distorted pseudo-tetrahedral geometry similar to that of the previous asymmetric-ligand manganese complex, [18], but with 4 molecules per unit cell. [21] similarly has the cyclic rings arranged in a boat conformation, although [21] is not quite so distorted as [18]. The bond lengths and angles of each ligand of [21] are identical to one another showing Co-S bond lengths of 2.336 Å (S1) and 2.306 Å (S2) and an endocyclic angle of 110.60° . However, the geometry around the metal centre is distorted from tetrahedral as the ligands bend toward the ^iPr groups similarly to the manganese analogue displaying exocyclic angles of 95.84° , 110.70° , 110.70° and 114.22° (shown in Figure 6.5)

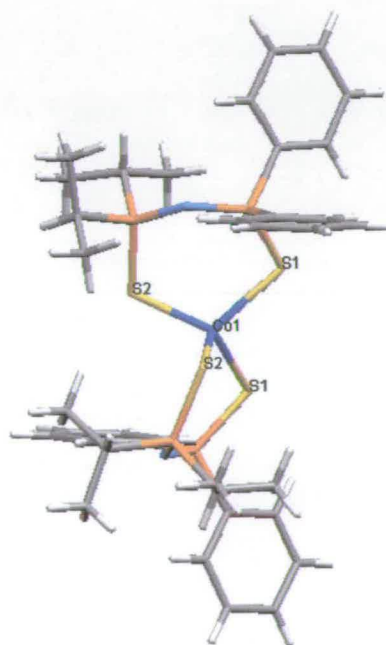


Figure 6. 5 The Molecular Structure of [21]

6.2.1.4 Crystal structure of $[\text{Ni}((\text{SPPPh}_2)(\text{SP}(\text{Pr})_2\text{N})_2)]$ [24]

[24] crystallises with a slightly distorted square-planar geometry in the space group $P\bar{1}$ with three molecules per unit cell of two crystallographically independent molecules that are very similar with only minor deviations in symmetry, bond lengths and angles. Thus the asymmetric unit in this structure is made up of $1\frac{1}{2}$ molecules with the centre of inversion lying on the one centrosymmetric complex, labelled with a Ni(2) centre, and the other two acentric complexes labelled with a Ni(1) centre. Both structures have boat-shaped ring systems, shown in Figure 6. 6, that are very similar to that of the previously-studied asymmetric analogue $[\text{Ni}((\text{SPPPh}_2)(\text{SP}(\text{Me})_2\text{N})_2)]$.⁵ Both structures are distorted from square-planar geometry, as the endocyclic angle is much greater than the ideal 90° . The complex with higher symmetry is Ni(2) and is perfectly planar as it lies on the inversion centre. It has Ni-S bonds of 2.223 (S(5)) and 2.236 Å (S(6)) which are shorter than the Ni-S tetrahedral bond and comparable with other literature examples of Ni-S square-planar bond lengths. This complex has an endocyclic angle of 98.17° (S(5)-Ni(2)-S(6)) and an exocyclic angle of 81.83° . The complex that contains Ni(1) is of a lower symmetry with four different Ni-S bond lengths of 2.243 (S(1)), 2.217 (S(2)), 2.239 (S(3)), 2.226 Å (S(4)), which are again comparable with other square-planar Ni-S bond lengths. The endocyclic bond angles of 97.86° (S(1)-Ni(1)-S(2)) and 98.08° (S(3)-Ni(1)-S(4)), and exocyclic angles of 81.86° (S(1)-Ni(1)-S(4)) and 82.38° (S(2)-Ni(1)-S(3)) deviate only slightly from the Ni(2) complex. However, in the Ni(1) complex the NiS₄ core unit is not perfectly planar with an S(1)-Ni(1)-S(3) angle of 177.03° .

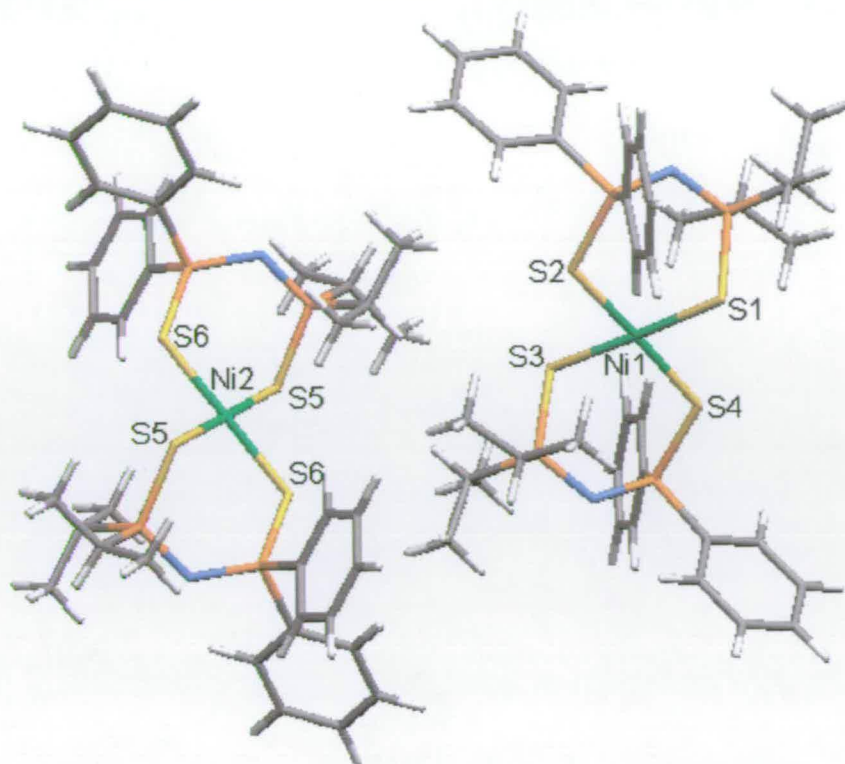


Figure 6. 6 Molecular structure of [24]

6.2.2 Magnetic, EPR and spectroscopic analysis

Magnetisation versus temperature was recorded for [16]-[24] from 2-340K at 0.1 T. The molar magnetic susceptibilities were calculated and corrected for a diamagnetic contribution.

X-band EPR analysis was carried out on samples [16]-[23] in a solution of DMF at room temperature and as a frozen solution at 77 K. The measurements were carried out at a frequency of 9.70 GHz and 9.48 GHz respectively over a field of 2800- 3800 Gauss.

6.2.2.1 Analysis of Co²⁺ and Mn²⁺ complexes [16]-[21].

[16] – [21] showed very similar magnetic data to each other and were found to fit to the Curie-Weiss model (Figure 6. 7) with Curie constants of: C = 4.42 ± 0.01 emu K mol⁻¹ [16], C = 4.25 ± 0.01 emu K mol⁻¹ [17], C = 4.17 ± 0.005 emu K mol⁻¹ [18], C = 1.88 ± 0.003 emu K mol⁻¹ [19], C = 2.17 ± 0.07 emu K mol⁻¹ [20] and C = 1.86 ± 0.01 emu K mol⁻¹ [21]. High spin Mn (II) and Co (II) have 5 and 3 unpaired electrons respectively and no first order orbital contribution, giving a theoretical spin-only Curie constant of 4.377 and 1.875 emu K mol⁻¹ respectively, which are in very close agreement with the experimental results. The slightly higher value for [20] can be explained by the mixing in of low-lying excited states and is supported by literature examples of tetrahedral cobalt complexes that have higher Curie constants up to approximately 2.6 emu K mol⁻¹. The effect of this mixing is greater when the symmetry is higher which is why [20] has this higher value but [19] and [21] do not, as they have a greater deviation from a tetrahedral geometry. All the complexes [16]-[21] show a negligible Weiss constant indicating no significant intermolecular interactions. This is to be expected as the crystal structures show only limited short contacts between peripheral R groups, which do not efficiently mediate spin interactions. Thus the R groups effectively shield the metal centres from intermolecular interaction and the M-M distance is large between molecules (approximately 10 Å). It can thus be seen that [16]-[21] are near perfect paramagnetic materials.

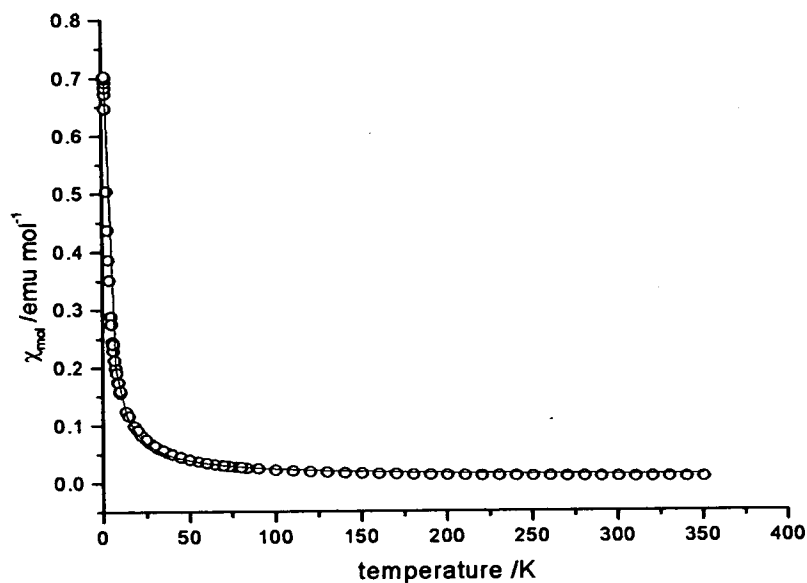


Figure 6. 7 Magnetic susceptibility (χ) of [19]. \circ = experimental data

— = Curie-Weiss fit.

NIR-UV-Vis spectroscopy was performed on [19] and [20] from 5000-30000 cm^{-1} . There are three d-d transitions to observe, between 4A_2 to 4T_2 , ${}^4T_1(F)$ and ${}^4T_1(P)$ labelled ν_1 , ν_2 and ν_3 respectively. Only transition ν_2 and ν_3 are seen in the spectrum as ν_1 occurs too far into the IR region to be in this range as well as being difficult to distinguish from vibrational absorptions at such low energy. However, ν_2 and ν_3 can be used to calculate the value of Δ_t , B and β (nephelauxetic parameter = $B/B_{\text{free ion}}$) from the simultaneous equations found in reference 13. These results are shown in table 6. 3 and show that both complexes have a ligand field splitting of approximately 4000 cm^{-1} . Studies of a series of Co(II) complexes show that Γ has the weakest ligand field of approximately 1500 cm^{-1} with a strong ligand field giving a splitting of approximately 4000 cm^{-1} .^{13, 14} Thus the thiophosphine ligands of [19] and [20] are strong-field ligands.

The values of Δ_t and μ_{eff} (corrected for temperature independent paramagnetism) were used to calculate the spin-orbit coupling (λ) for [20] (using equation 6. 1 for a perfect tetrahedral Co^{2+} complex). This equation can be reasonably applied to [20], as it has the closest symmetry to tetrahedral. The other two complexes [19] and [21] deviate too far from this geometry and thus yield values of λ that are unrealistically low. For [20] $\lambda = -189 \text{ cm}^{-1}$ which is close to the free ion value (-173 cm^{-1}). The value of λ is expected to be slightly smaller than the free ion value, however, there is a large error associated with the values of ν as a value is extracted from very broad peaks and there is uncertainty as to what part of the peak values should be taken from.¹⁵ It is therefore reasonable to obtain a value slightly higher than the free ion as a result of this large error.

An equation has also been derived to relate the average susceptibility to the spin-orbit coupling of an axial distorted tetrahedral complex shown in Equation 6. 2¹⁶ where k is the orbital reduction factor (explained in 6.2.2.3), δ is the zero-field splitting (very small $\approx 10 \text{ cm}^{-1}$) and Δ_1 and Δ_2 are the two values of the ligand-field splitting as the tetrahedral triplet d-orbitals split to form non-degenerate energy levels. In order to collect the data needed for this equation, an orientated single crystal magnetic susceptibility measurement is needed to obtain the values of Δ_1 and Δ_2 in each distorted and equivalent direction (see nickel treatment in 6.2.2.3). This is not possible in the cases of [19] and [21] as single crystals large enough for this measurement could not be grown. Thus, [19] and [21] were fitted successfully to this model using sensible assumed parameters. However, a fit could not converge on a real solution, as there are too many unknown parameters. Thus the magnetic data were seen to represent the model, showing that the data are reasonable for complexes with λ close to the free ion value. More precise analysis could not be performed due to the asymmetric nature of [19] and [21] and the lack of magnetic information from

single crystals.

	ν_2 / cm^{-1}	ν_3 / cm^{-1}	$\Delta_t / \text{cm}^{-1}$	B / cm^{-1}	β	λ / cm^{-1}
[19]	6613	14258	4027	586	0.61	-
[20]	6630	14740	3980	660	0.68	-189

Table 6. 3 Ligand field parameters for [19] and [20].

$$\mu_{\text{eff}} = \mu_{\infty} \left(1 - \frac{4\lambda}{\Delta_t} \right) \quad \text{Equation 6. 1}^{15}$$

$$\bar{\chi} = \frac{N\beta^2}{3kT} \left[5 \left(1 - \frac{4k\lambda}{\Delta_1} \right)^2 + 10 \left(1 - \frac{4k\lambda}{\Delta_2} \right)^2 + \frac{2\delta}{kT} \left(\left(1 - \frac{4k\lambda}{\Delta_1} \right)^2 - \left(1 - \frac{4k\lambda}{\Delta_2} \right)^2 \right) \right] \quad \text{Equation 6. 2}^{16}$$

$$+ \frac{8N\beta^2 k^2}{3} \left[\frac{1}{\Delta_1} + \frac{2}{\Delta_2} \right]$$

Room temperature EPR studies of [16]-[18] revealed a characteristic 6 peak Mn^{2+} pattern for all three samples (Figure 6. 8). Frozen glass EPR studies of [16]-[18] all showed the characteristic low temperature signal of Mn^{2+} in a tetrahedral site^{17, 18} of 16 lines. The 16 lines comprise of 6 main peaks with 5 sets of doublets due to spin forbidden transitions (Figure 6. 9). This pattern is typical and the hyperfine coupling constants are comparable with those of MnCl_4^{2-} , demonstrating that the spin density is mainly on the metal centre and not the ligands. It can also be concluded that the metal centre is isotropic with a g value of approximately 2 for all 3 complexes and hyperfine splitting values of approximately 90 G for the main peaks and 23 G splitting for the forbidden transition doublets for all complexes (table 6. 4).

Complex	g	A_1 / G (main line splitting, average)	A_2 / G (Doublet splitting, average)
[16]	2.06	89.5	22.1
[17]	2.07	93.7	23.4
[18]	2.01	90.9	25.2
$MnCl_4^{2-17}$	2.00	89.4	21.5

Table 6. 4 Summary of EPR values of the manganese complexes [16]-[18], compared with $MnCl_4^{2-}$

The $M = Co$ samples [19]-[21] were also studied but yielded no EPR signal. This response is unusual but has occurred previously in the literature.¹⁹ It is most likely to arise from excessive broadening of the signal as the spin lattice relaxation is rapid due to the fact there is a small separation between the ground state and the first excited state.¹⁹

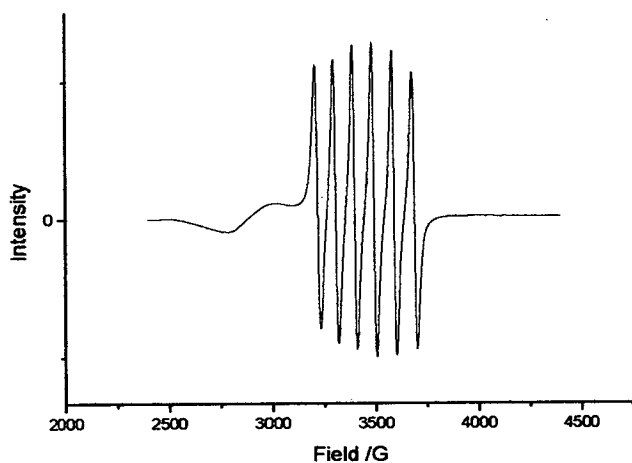


Figure 6. 8 Room temperature solution EPR spectrum of [17] at 9.70 GHz

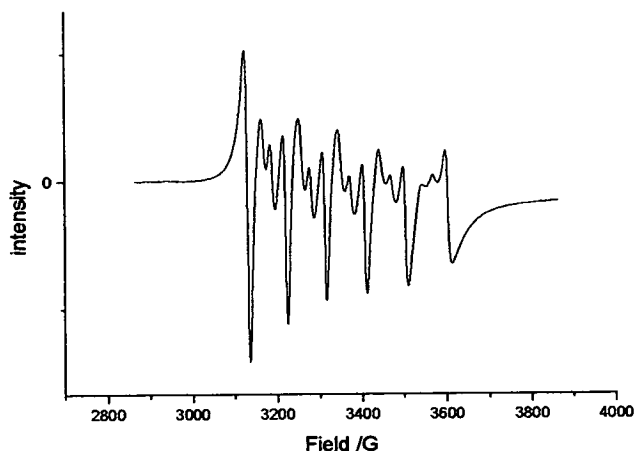


Figure 6. 9. Frozen glass EPR spectrum at 9.48 GHz of [17] at 100 K.

6.2.2.2 Analysis of Ni²⁺ complexes [22]-[24]

Ni(II) is a d⁸ ion that is diamagnetic in the square-planar conformation and paramagnetic in a tetrahedral geometry that yields 2 unpaired electron spins. It has been noted in Table 6. 2 that complex [22] can exist in both pseudo-square-planar and tetrahedral geometries. It should also be noted from Section 6.2.1.4 and Table 6. 2 that [24] has a square-planar geometry. It is thus predicted that the square-planar form of [22] and [24] will be diamagnetic and will give no signal in a magnetic measurement. This was indeed the case, and results of the magnetic analysis of the square-planar form of [22] showed that 95.2% of the sample was diamagnetic with 4.8% of this complex giving a paramagnetic signal from the tetrahedral conformation present as an impurity. This was also to be expected, as the square-planar form of [22] seemed to be decidedly unstable and reverted

back to the tetrahedral form over time and with increased temperature. Again a similar, mainly diamagnetic signal was seen for [24]. Analysis of the magnetic susceptibility showed a diamagnetic signal with a small Curie tail giving 3% paramagnetic impurity. This square-planar material seems to be more stable with no visible changes to its appearance over time or temperature. However, a paramagnetic signal was detected for [24] in solution, showing that the complex reverts to tetrahedral geometry when solvated. [24] however, still gave no EPR signal and as such there was no further magnetic or EPR analysis to be performed on either of these square-planar examples. It can thus be concluded that the geometric preference of [22] and [24] is finely balanced. It appears that [22] is only stable in a square-planar geometry at very low temperatures and in the crystal form with specific solvents of crystallisation. The square-planar form of [24] is more stable but will revert to a paramagnetic geometry in different media.

Complex [22] can also be crystallised in a pseudo-tetrahedral geometry just as [23] does (whose structure is discussed in section 6.2.1). The d-orbital splitting in a tetrahedral crystal field gives a 3T_1 ground state. Thus a complex of perfect tetrahedral symmetry will have an angular momentum quantum number (L) = 1 and the total spin quantum number (S) = 1, so the ground state (J) will be non-magnetic ($J = L - S = 0$).¹⁶ This type of behaviour is also true for the pseudo-tetrahedral complexes [22] and [23].

Like [16]-[21], the plots of the magnetic susceptibility versus temperature of both [22] and [23] are almost identical to each other, but differ greatly from [16]-[21]. The magnetic susceptibility of both the nickel complexes can be seen to have a shoulder present at low temperature due to spin-orbit coupling (Figure 6. 10).

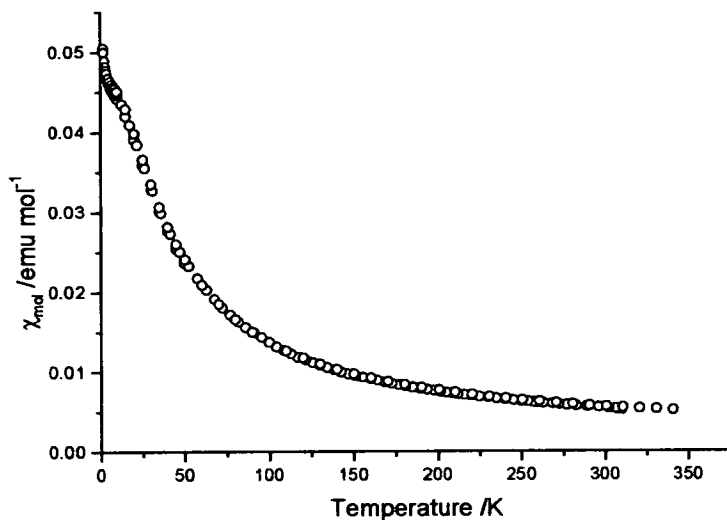


Figure 6. 10 Magnetic susceptibility of [22]. \circ = experimental data

When μ_{eff}^2 is plotted against temperature the non-magnetic ground state is clearly seen, as μ_{eff}^2 tends towards zero at temperatures below 50 and 75 K for [22] and [23] respectively (Figure 6. 11.). These data were fitted to a tetrahedral model for a 3T_1 system in a cubic crystal field to determine an approximate value of the spin-orbit coupling constant (Equation 6.3).¹⁶

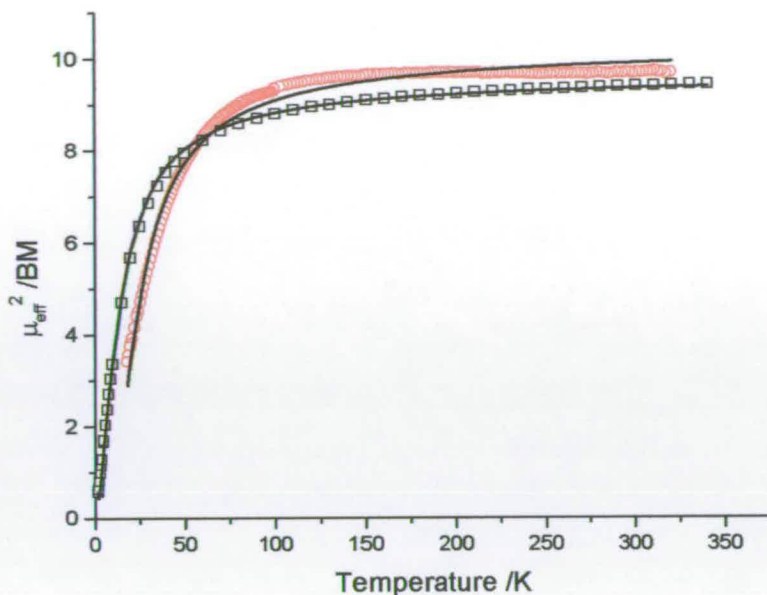


Figure 6.11. μ_{eff}^2 versus temperature of [22] (\square) and [23] (\circ), — Theoretical plot with $\lambda/k = 8.125$ K and 15.09 K respectively.

$$\mu^2 = \frac{3 \left[0.625x + 6.8 + (0.125x + 4.09) \exp(-3x) - 10.89 \exp\left(-\frac{9x}{2}\right) \right]}{x \left[5 + 3 \exp(-3x) + \exp\left(-\frac{9x}{2}\right) \right]} \quad \text{Equation 6.3}$$

In equation 6.3 $x = \lambda/k(T-\theta)$, where T is temperature, with a Weiss constant (θ) and λ is the strength of spin-orbit coupling. This equation was derived from the Van Vleck equation by considering the Zeeman perturbations in a cubic crystal field.¹⁶ It should be emphasised here that [22] and [23] are not perfectly tetrahedral and as such, Equation 6.3 is only an approximation to these systems. The systems deviate from the equation to such an extent that the data could only be fitted when the equation was multiplied by a correction factor of approximately 0.9. The inaccuracy of the model can also be seen in Figure 6.11 in that the experimental data of [23] cannot conform accurately to the model.

However it can be seen from this fit that [22] and [23] have negligible Weiss constants showing that there are no significant intermolecular interactions, and that the approximated spin-orbit coupling constants for [22] and [23] from this model are 1.14×10^{-22} J (5.74 cm^{-1} , $\lambda/k = 8.125 \text{ K}$) and 2.08×10^{-22} J (10.46 cm^{-1} , $\lambda/k = 15.09 \text{ K}$) respectively. These are extremely low spin-orbit coupling energies compared to literature values that give λ values for most Ni(II) complexes in the region of 300 cm^{-1} .¹⁶ Although the fitting of the magnetic data to this model is crude, it has provided a good initial understanding of the systems and shown the unusually low values for λ which will be investigated more accurately and are discussed in the subsequent sections.

6.2.2.3 Orientated crystal magnetic analysis

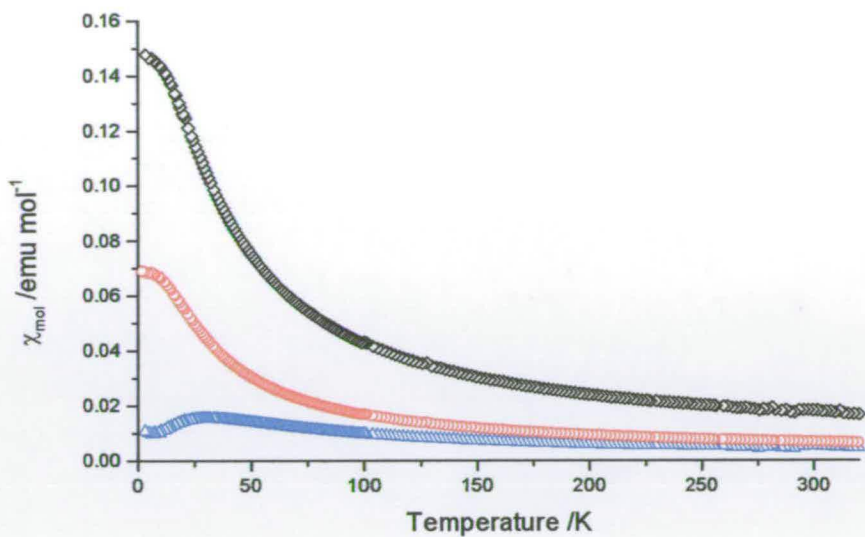
As was previously seen with the cobalt complexes [19]-[21], susceptibility data for a complex with a distorted tetrahedral geometry cannot be fitted perfectly to a tetrahedral model to find the value of the spin-orbit coupling constant. When the crystal structure of [23] is examined (in figure 6. 2) it can be clearly seen that the molecular symmetry is slightly distorted to give approximately axial symmetry, being elongated in the c-axis with the a and b axes being almost equivalent. This is true for both [22] and [23] as both structures are anisotropic in the c-direction. If large single crystals are available, it is beneficial to measure the magnetic susceptibility along both the c and either of the equivalent axes as the difference between these measurements can provide the parameters needed to extract a more precise value of λ for these axial systems.

Although there are only a few degrees of deviation from the tetrahedral angle in

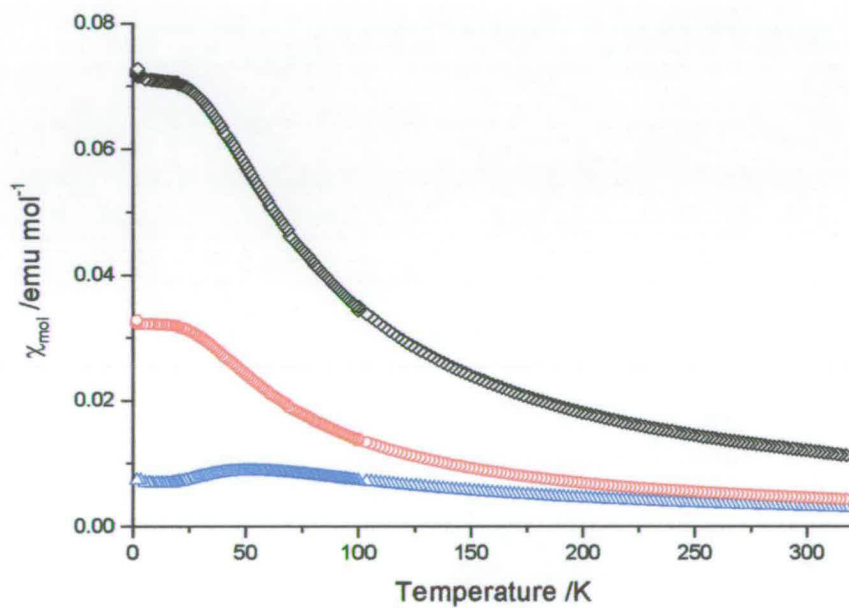
these complexes, it has a pronounced effect on the magnetism.²⁰ Thus the degree of axial distortion is also of importance when fitting the data.

In Equation 6. 3 and in the discussion so far, λ has been used to represent the spin-orbit coupling of the complex, which was found to be very low. More accurately the parameter used in equation 6. 3 for the spin-orbit coupling should be the multiple λk , where k is the orbital reduction factor. The orbital reduction factor is the fraction of spin density that resides on the metal centre with k having a value of 1 when all the spin density is on the metal and a value of 0 when all the spin density is located on the ligand. The variable k is usually omitted from equations such as equation 6. 2 as it is usually approximated to 1 and so can be neglected. It is thus hypothesised that the apparent value of the spin-orbit coupling is so low because k must have a small value illustrating that a large amount of spin density is located on the ligands of complexes [22] and [23]. This hypothesis can be tested, as the value of k can be extracted from the axial model that describes the specific geometry of the complexes to which the parallel and perpendicular orientated crystal magnetic data are fitted.

[22] forms large long needle-shaped crystals and the needle axis was found to correspond to the c-axis of the complex. Large single crystals of [23] take on the form of compressed octahedra, with the shortest axis corresponding to the c-axis of this complex. Thus, a magnetic susceptibility versus temperature measurement was collected for crystals of [22] and [23] orientated along and perpendicular to the unique axis of the crystals, corresponding to the c-axis and perpendicular to the c-axis of the complexes.



a.



b.

Figure 6. 12 Magnetic susceptibility of orientated single crystal of; a) [22] and b) [23]. Δ = crystal orientated parallel to the needle (c) axis, \circ = crystal orientated perpendicular to the needle axis \diamond = total ($\Delta + 2x\circ$).

The orientated crystal magnetic data were analysed using a mathematical treatment derived using perturbation theory. A free ion d^8 system was placed in a cubic tetrahedral field and the system was perturbed to accommodate a tetragonal distortion and spin-orbit coupling. A further perturbation was considered to account for a magnetic field applied along the unique axis and then perpendicular to the unique axis. This treatment was derived following the procedure carried out by Figgis *et al.*²⁰ and the data can be described using variables for a tetragonal distortion (Δ), spin-orbit coupling (λ), and the orbital reduction factor (k). The measure of tetragonal distortion is represented by the energy level splitting parameter Δ (in cm^{-1}) that increases as the complex distorts in the z-direction.

Initially it can be seen that when the free ion (3P) is subjected to a cubic crystal field a lower energy 3T_1 ground state term is formed, and only this term need be considered, as higher terms are not thermally populated. It must however be noted that there is an excited state 3T_1 term in this crystal field available for second-order orbital mixing and this is accounted for using a parameter that describes the strength of the cubic crystal field (A) and hence the degree of mixing. For a weak-field ligand the value of $A = 1.5$ and for a strong field ligand the value of $A = 1$. The effects of tetragonal distortion and spin-orbit coupling on the 3T_1 ground state were then treated simultaneously as their energies are comparable. This resulted in 9 energy levels, 6 of which are degenerate. This energy level diagram is shown in figure 6. 13.

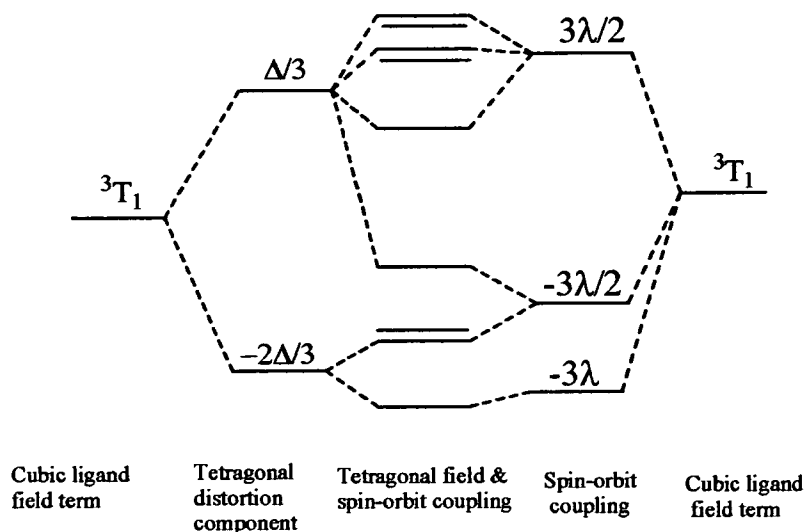


Figure 6. 13 Splitting orbital pattern for a tetrahedral 3T_1 term after a tetragonal distortion and spin-orbit coupling is applied.²⁰

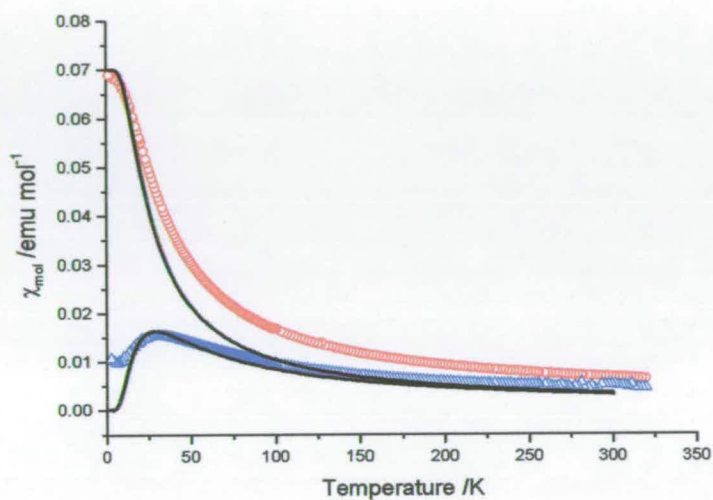
A further perturbation was then carried out on these new wavefunctions to account for the Zeeman splitting in a magnetic field to obtain first and second order coefficients to substitute into the Van Vleck equation. It is from this equation that the magnetic susceptibility in both the x and z direction can then be calculated. These terms are complex and so an exact equation was not defined, as they could not be readily simplified into a manageable formula. Thus, solutions were simulated numerically by inputting logical variables into a computer program (Appendix chapter 6) that calculated the parallel and perpendicular susceptibility using the method above. The results obtained were then compared to the magnetic susceptibility data collected for [22] and [23] to get the best fit to the simulation. It should be noted that there is a small discrepancy of approximately 10% between the results obtained from our computer program and the published results for related complexes.²⁰ The discrepancy is small enough however for it to have no significant influence over the principle conclusions drawn from this calculation. It should also be noted

that resolution of this discrepancy will be subsequently required to clarify whether an error(s) remains in our procedure or that of the published calculations.

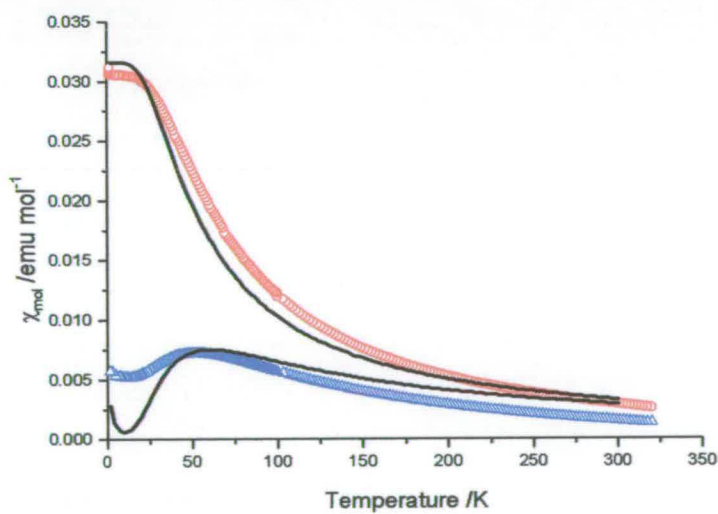
The parameters A , Δ , λ and k were varied until a suitably close fit to each orientated crystal susceptibility data was found. The complex was found to be weak-field complex and so the parameter A was only varied between 1.5 and 1.48 with the optimum value being fixed at 1.499. It was found that both Δ and λ affect the magnitude of the magnetic susceptibility dramatically. An increasing magnitude of λ decreases the value of the magnetic susceptibility for both the x and z directional data, whereas an increasing value of Δ increases the value of the magnetic susceptibility in both directions. The value of λ should be approximately the same for both complexes and should have a value between -200 cm^{-1} and -300 cm^{-1} to be in agreement with similar complexes. Thus, an optimum value of $\lambda = -210\text{ cm}^{-1}$ was found and then the value of Δ was adjusted accordingly to converge on a solution. As the main difference between [22] and [23] is the degree of distortion from a tetrahedral geometry, the different values of Δ are the main difference in the parameters that fit to the data. The values of Δ for [22] and [23] that best fit the data were 3900 cm^{-1} and 2000 cm^{-1} respectively. The value for [22] is considerably larger than the value for [23] which is expected as [23] deviates by approximately 1° in the endocyclic angle from the tetrahedral and [22] has a greater deviation between 2 and 3° . The position of the peak in the z-orientated susceptibility data is related to the value of k and this was found to fit the data best when $k = 0.03$ for [22] and 0.04 for [23]. All of these values are summarised in table 6. 5 and the solutions containing these parameters are shown along with the orientated crystal susceptibility data in figure 6. 14.

	$X-\chi_{\max}$	$Z-\chi_{\max}$	A	λ	Δ	k
[22]	0.070	0.016	0.1499	-210	3900	0.03
[23]	0.031	0.008	0.1499	-210	2000	0.04

Table 6. 5 Summary of the parameters of the simulated orientated susceptibility data



a



b

Figure 6. 14 Magnetic susceptibility of orientated single crystal and data simulation of; a) [22] and b) [23]. Δ = crystal orientated parallel to the needle (c) axis, \circ = crystal orientated perpendicular to the needle axis, — = the simulated pattern using parameters shown in table 6. 5.

It can be seen in figure 6. 14 that the simulated data do not fit the experimental data perfectly and this is to be expected as the complexes are not perfectly distorted solely in the z-direction. [23] is the most symmetrical and thus the simulated data fits the susceptibility data for this complex better than [22]. However, the value of k strongly correlates with the peak in the z-direction susceptibility data and thus is a reliable parameter to extract from the data. The values of $k = 0.03$ and 0.04 correlate well to the estimated spin-orbit coupling constants obtained from the equation for a perfect tetrahedron if these values are taken to be the multiple of λk . The multiple of λk from the simulated data is 6.3 cm^{-1} and 8.4 cm^{-1} for [22] and [23] respectively which are in good agreement with the values of 5.74 cm^{-1} and 10.46 cm^{-1} from the previous estimation. The fact that the values of k are very small confirms the fact that the majority of the spin density is delocalised on the ligand with only a very small amount (3-4%) residing on the nickel centre.

6.2.2.4 Structural analysis of Ni compounds

The results from the orientated crystal analysis give low orbital reduction factors of 0.03 and 0.04 that show that the majority of the spin density is delocalised on the ligands. If the majority of the spin density is based on the ligand, and not the metal, the spin coupling with d-orbitals on the metal is minimal. It is possible for spin density to be stabilised on the ligand due to the delocalised nature of the ligand. The ligand can be regarded as non-innocent and able to form stable complexes of the form $[\text{Ni}^{2+}\text{L}_2^-]$ through to $[\text{Ni}^0\text{L}_2]$, where the unpaired spin density is located solely on the ligand.

The fact that these complexes are closer to being organic radical in character can

also explain why nickel thiophosphine complexes adopt a tetrahedral geometry so readily. A Ni^{2+} complex with such strong-field ligands as these has a preference to adopt a square-planar geometry, whereas a complex that contains Ni^0 has no such preference, so sterically, a tetrahedral geometry will be favoured.

The hypothesis that these complexes are closer to the $[\text{Ni}^0\text{L}_2]$ form when they possess a tetrahedral geometry and closer to the $[\text{Ni}^{2+}\text{L}_2^-]$ form when they possess a square-planar geometry, was analysed by comparing bond lengths of the crystal structures of all known Ni thiophosphine systems. If the ligand is of a radical character, the S-P bond can be thought of as a double bond and thus shorter. If more ionic, a delocalised single to 1.5 bond character is expected and a longer bond length. When comparing the bond lengths of complexes with the two different geometries this is indeed observed. With a maximum standard deviation of 0.0009 Å across the structures, the difference in the measured lengths (0.0091-0.0214 Å) is statistically significant, supporting our analysis. This is further supported by ^{31}P NMR spectroscopy performed by Dimitrios Maganas shown in Table 6. 6.

^{31}P NMR /ppm		Ph /ppm	Pr /ppm
KL (Ph)		36.8	
KL (Pr)			61
KL (Ph, Pr)		36.0	51.5
CoL_2	[19]	-32.8	
	[20]		-331
	[21]	-87.3	-188.3
NiL_2	[22]	-436	
	[23]		-724
	[24]	-553	-510

Table 6. 6 Table of ^{31}P NMR of complexes [19]-[24]

Here we see that the peaks for the non-complexed K^+ salt shift dramatically to a lower frequency on complexation. This is to be expected as the presence of a paramagnetic metal so close to the P atom affects the signal in this way. Interestingly though, a large difference is seen between the shift for the cobalt complexes compared to the nickel complexes. The nickel complexes show a much larger shift than is expected for complexation and this can be explained by the fact that spin density is induced on the ligand in the nickel complexes, forming paramagnetic character on the ligand and thus the P atom. It should be noted [24] has the same paramagnetic shifts and this is because the measurement is from a solution, so the square-planar solid-state crystal structure does not represent this material. In this state [24] is paramagnetic.

This trend of the nickel ligands having radical character with the cobalt ligands being more ionic, is further illustrated by the X-ray absorption spectra (XAS) of [16], [19], and [22]. The character of the three different M-S bonds (M = Mn, Co and Ni) were compared using the R = Ph complexes. The spectra (again performed by Dimitrios Maganas) reveal that the Mn-S bond is the most ionic in character with the Co-S bond being covalent and the Ni-S bond has a more radical character,²¹ demonstrating that the Ni complexes have more spin density on the ligand.

Indeed, the variety of geometries adopted by this family of complexes can be explained by the different location of spin density with respect to different geometry. It would appear that competing factors of electronic preference and geometric strain are finely balanced to be the dominant influence over the geometry.

Geometric strain can be analysed by comparing ideal bond lengths and angles of unstrained literature complexes with all the known Ni^{2+} thiophosphine complexes of both square-planar and tetrahedral geometries and considering any deviations from the ideal.²² It

was found that the Ni-S bond in square-planar complexes [22] and [24] were shorter ($\approx 2.23 \text{ \AA}$) than those in tetrahedral complexes [22] and [23] ($\approx 2.29 \text{ \AA}$), but this was found to be the representative of all non-strained Ni-S₄ core systems of each geometry, displaying no strain in bond length. The S-Ni-S bite angles of [22]-[24] were then compared to see if there was any deviation from the ideal angles for tetrahedral and square-planar complexes (109° and 90° respectively). The bite angles were found to deviate by over 8° for the square-planar complex, whereas the tetrahedral conformation had a bite angle deviation of only $0\text{-}3^\circ$. This suggests that the square-planar system displays a great degree of ring strain and this must be an opposing force favouring a tetrahedral conformation over the electronic strong-ligand-field preference of a square-planar geometry. Thus, we conclude that a tetrahedral conformation is favoured to reduce any geometric strain that would occur in the square-planar complex. The spin density is then transferred onto the ligand to form a complex with Ni⁰ character, which is preferable to a Ni²⁺ complex that would have the conflicting preference to form a square-planar complex with such a strong-field ligand.

6.3 Conclusions

		$C_{so} / \text{emu K mol}^{-1}$ (Theoretical)	$C / \text{emu K mol}^{-1}$	EPR, g Splitting /G		$k\lambda / \text{cm}^{-1}$
M = Mn	[16]	4.375	4.42 ± 0.005	2.06	89.5, 22.1	-
	[17]		4.25 ± 0.001	2.07	93.7, 23.4	-
	[18]		4.17 ± 0.005	2.01	90.9, 25.2	-
M = Co	[19]	1.875	1.88 ± 0.003	-	-	-
	[20]		2.17 ± 0.07	-	-	-189
	[21]		1.86 ± 0.01	-	-	-
M = Ni	[22]	1	-	-	-	-5.74 ($k = 0.03$)
	[23]		-	-	-	-10.46 ($k = 0.04$)

Table 6. 7 Summary of magnetic data for pseudo-tetrahedral complexes [16]-[23].

Thiophosphine complexes of $[M((\text{SPR}^{1,2})_2\text{N})_2]$ (M = Mn, [16], [17], [18], Co, [19], [20], [21], Ni [22], [23], [24], R = Ph [16], [19], [22], ⁱPr [17], [20], [23], Ph and ⁱPr [18], [21] and [24]) were all analysed structurally and magnetically. The structures of [16], [19], [20], [22] and [23] are already reported in the literature and have a pseudo-tetrahedral geometry with the addition of the fact that [22] can adopt both a tetrahedral and a square-planar geometry. The crystal structures of [17], [18], [21] and [24] were determined for this study and the first three complexes were once again found to have pseudo-tetrahedral geometry with [24] adopting square-planar geometry. All the pseudo-tetrahedral complexes

were magnetically analysed (results summarised in table 6. 6) with the square-planar complexes being found to be diamagnetic with a small amount of paramagnetic impurities. EPR studies were also carried out on all complexes and these only yielded results for the $M = \text{Mn}$ complexes as the Co and Ni samples were found to be EPR silent. The EPR signal of the $M = \text{Mn}$ complexes were all very similar and could be directly compared to other Mn^{2+} tetrahedral complexes such as the ionic complex MnCl_4^{2-} , showing the manganese complexes to be ionic in character. The magnetic analysis of the $M = \text{Mn}$ and Co complexes ([16]-[21]) found them to be near perfect paramagnets with no significant intermolecular interactions. NIR-UV-Vis spectroscopy was performed on the $M = \text{Co}$ complexes and revealed the ligands to be strong-field ligands with $\Delta_t \approx 4000 \text{ cm}^{-1}$ and with $\beta = 0.61$ and 0.68 , showing these complexes to be covalent. A spin-orbit coupling constant $= -189 \text{ cm}^{-1}$ could also be extracted for [20] from the ligand field strength and magnetic data and this is similar to the free ion value of -173 cm^{-1} . A value of λ could not be obtained for [19] and [21] as their geometries both deviate too far from the tetrahedral model used to acquire λ .

The $M = \text{Ni}$ complexes [22] and [23] were also found to be paramagnetic with both showing no significant intermolecular interactions. The magnetic data could not be fit to the Curie Weiss law due to the fact that [22] and [23] displayed spin-orbit coupling leading to a non-magnetic ground state. Approximate spin-orbit coupling constants were found to be 5.74 cm^{-1} and 10.46 cm^{-1} respectively, which are unusually low. This is believed to be because the amount of spin density on the metal centre is reduced as the majority of the spin density in the complexes is transferred on the ligands, reducing the d-orbital effect. This is supported by the calculation of the orbital reduction factor from magnetic data collected for an orientated crystal. The values of k were found to be 0.03 and 0.04 for [22]

and [23] respectively showing there to be 3-4% of spin density on the metal.

Strong-field nickel complexes normally have a propensity to form square-planar complexes. These thiophosphine systems are unusual as they are known to form both square-planar and tetrahedral geometries with tetrahedral complexes in the majority. This can now be explained by the fact that there is a significant ring strain in the square-planar complexes that favours the formation of a less strained tetrahedral geometry. This is aided (or perhaps induced) by the fact that in the tetrahedral case, the spin density lies predominately on the ligand leaving the nickel centre in a Ni^0 form. This has been supported with analysis of bond lengths, bond angles, values of λ , k and ^{31}P NMR spectroscopy, although it is not clear whether or not the movement of spin density induces the formation of a tetrahedral geometry, or the steric strain induces a tetrahedral geometry and as a result spin density is moved onto the ligands to stabilise the system. X-ray spectroscopy shows the covalency of the M-S bond. This measurement showed that the M = Mn complexes have an ionic M-S bond, with the majority of the spin density lying on the metal, which is supported by the EPR measurements. The measurement showed that the M = Co complexes have a typical covalent M-S bond, also shown by the value of β from the NIR-UV-Vis measurements. The X-ray spectroscopy also revealed that the M = Ni complexes have an M-S bond with a large radical character, having the majority of the spin density residing on the ligand, which is reiterated in the other measurements. Interestingly, it is only really M = Ni complexes that appear in natural enzyme systems bonding to sulphur out of these three metals, and this is probably due to this distinction between the different types of M-S bonding and the effect this has on the geometry and electron transfer.

6.4 Experimental

All the compounds used in this chapter were synthesised by the group of Dr. Panyotis Kyritsis of Athens University from literature methods.^{7, 23-27}

[17] *X-ray Crystallography data-* $C_{24}H_{56}MnN_2P_4S_4$, $M = 679.81$, Triclinic, $a = 9.2498(3)$, $b = 12.7938(4)$, $c = 16.3398(5)\text{\AA}$, $\alpha = 79.2030(10)$, $\beta = 78.1480(10)$, $\gamma = 69.0760(10)^\circ$ $U = 1753.84(10)\text{\AA}^3$, $T = 150\text{ K}$, space group $P\bar{1}$, $Z = 2$, $\mu(\text{Mo-K}\alpha) = 0.814\text{ mm}^{-1}$, 8179 reflections were collected, ($R_{\text{int}} = 0.0352$) which were used in all calculations. The final $wR(F^2)$ was 0.0413. (For full CIF, Appendix chapter 6)

[18] *X-ray Crystallography data-* $C_{37}H_{50}Cl_2MnN_2P_4S_4$, $M = 900.75$, Triclinic, $a = 9.9405(3)$, $b = 10.2453(3)$, $c = 11.2043(3)\text{\AA}$, $\alpha = 96.560(2)$, $\beta = 101.4900(10)$, $\gamma = 100.4150(10)^\circ$ $U = 1086.35(5)\text{\AA}^3$, $T = 150\text{ K}$, space group $P1$, $Z = 1$, $\mu(\text{Mo-K}\alpha) = 0.795\text{ mm}^{-1}$, 11470 reflections were collected, ($R_{\text{int}} = 0.0421$) which were used in all calculations. The final $wR(F^2)$ was 0.1035. (For full CIF, Appendix chapter 6)

[21] *X-ray Crystallography data-* $C_{36}H_{48}CoN_2P_4S_4$, $M = 819.81$, Monoclinic, $a = 12.6570(3)$, $b = 15.6482(4)$, $c = 21.4667(6)\text{\AA}$, $\alpha = 90$, $\beta = 103.356(2)$, $\gamma = 90^\circ$ $U = 4136.69(18)\text{\AA}^3$, $T = 150\text{ K}$, space group $C 2/c$, $Z = 4$, $\mu(\text{Mo-K}\alpha) = 0.799\text{ mm}^{-1}$, 30143 reflections were collected, ($R_{\text{int}} = 0.0327$) which were used in all calculations. The final $wR(F^2)$ was 0.0901. (For full CIF, Appendix chapter 6)

[24] *X-ray Crystallography data-* $C_{36}H_{48}NiN_2P_4S_4$, $M = 819.66$, Triclinic, $a =$

9.1329(2), $b = 17.0596(4)$, $c = 19.1631(4)$ Å, $\alpha = 87.8670(10)$, $\beta = 88.2800(10)$, $\gamma = 89.7280(10)^\circ$ $U = 2982.25(11)$ Å³, $T = 150$ K, space group $P\bar{1}$, $Z = 3$, $\mu(\text{Mo-K}\alpha) = 0.887$ mm⁻¹, 25269 reflections were collected, ($R_{\text{int}} = 0.0592$) which were used in all calculations. The final $wR(F^2)$ was 0.1365. (For full CIF, Appendix chapter 6)

6.5 References

- ¹ R. S. Giordano and R. D. Bereman, *J. Am. Chem. Soc.*, 1974, **96**, 1019.
- ² R. S. Giordano, R. D. Bereman, D. J. Kosman, and M. J. Ettinger, *J. Am. Chem. Soc.*, 1974, **96**, 1023.
- ³ S. Niu and M. B. Hall, *Inorg. Chem.*, 2001, **40**, 6201.
- ⁴ D. Cupertino, R. Keyte, A. M. Z. Slawin, J. D. Woolins, and D. J. Williams, *Polyhed.*, 1996, **15**, 4441.
- ⁵ R. Roesler, C. Silvestru, G. Espinosa-Perez, I. Haiduc, and R. Cea-Olivares, *Inorg. Chim. Acta*, 1996, **241**, 47.
- ⁶ R. D. Bereman, F. T. Wang, J. Najdzionek, and D. M. Braitsch, *J. Am. Chem. Soc.*, 1976, **98**, 7266.
- ⁷ A. Davison and E. S. Switkes, *Inorg. Chem.*, 1971, **10**, 837.
- ⁸ L. M. Gilby and B. Piggott, *Polyhed.*, 1999, **18**, 1077.
- ⁹ E. Simon-Manso, M. Valderrama, and D. Boys, *Inorg. Chem.*, 2001, **40**, 3647.
- ¹⁰ M. R. Churchill, J. Cooke, J. Wormald, A. Davison, and E. S. Switkes, *J. Am. Chem. Soc.*, 1969, **91**, 6518.
- ¹¹ O. Siimann, M. Wrighton, and H. B. Gray, *J. Coord. Chem.*, 1972, **2**, 159.
- ¹² O. Siiman and H. B. Gray, *Inorg. Chem.*, 1974, **13**, 1185.
- ¹³ F. A. Cotton and M. Goodgame, *J. Am. Chem. Soc.*, 1961, **83**, 1777.
- ¹⁴ R. H. Holm and F. A. Cotton, *J. Chem. Phys.*, 1960, **32**, 1168.
- ¹⁵ F. A. Cotton, O. D. Faut, D. M. L. Goodgame, and R. H. Holm, *J. Am. Chem. Soc.*, 1961, **83**, 1780.
- ¹⁶ F. E. Mabbs and D. J. Machin, 'Magnetism and Transition Metal Complexes', London, Chapman and Hall, 1973.
- ¹⁷ B. T. Allen and D. W. Nebert, *J. Chem. Phys.*, 1964, **41**, 1983.
- ¹⁸ F.-D. Tsay, S. L. Manatt, and S. I. Chan, *Chem. Phys. Lett.*, 1972, **17**, 223.
- ¹⁹ R. Stahl-Brada and W. Low, *Phys. Rev.*, 1959, **116**, 561.
- ²⁰ B. N. Figgis, J. Lewis, F. E. Mabbs, and G. A. Webb, *J. Chem. Soc. A: Inorg., Phys., Theor.*, 1966, 1411.
- ²¹ D. Maganas, 'Masters dissertation', University of Athens, Athens, 2004.
- ²² F. H. Allen, *Acta Crystallo. B: Structural Science*, 2002, **B58**, 380.
- ²³ E. Fluck and F. L. Goldmann, *Ber.*, 1963, **96**, 3091.
- ²⁴ A. Schmidpeter, R. Boehm, and H. Groeger, *Angew. Chem.*, 1964, **76**, 860.
- ²⁵ A. Schmidpeter and H. Groeger, *Z. Anorg. Allg. Chem.*, 1966, **345**, 106.
- ²⁶ A. Schmidpeter and H. Groeger, *Chem. Ber.*, 1967, **100**, 3979.
- ²⁷ A. Schmidpeter and J. Ebeling, *Chem. Ber.*, 1968, **101**, 815.

Chapter 7

[M(C_nH_{2n}(C₃S₅))₂] materials

7.1 Introduction

7.1.1 Low dimensional magnetic materials and spin ladders

Low dimensional magnetism is of enormous theoretical interest as it is a phenomenon that is not fully understood. 1-dimensional and 2-dimensional systems can be well described theoretically. However, there is much more mystery shrouding those material that lie between these dimensions. The interest in 2D magnetic lattices is great due to the fact that high temperature superconductivity has been achieved mainly in materials that have 2D magnetic lattices. Materials with magnetic dimensionality between the 1st and 2nd-dimensions are known as spin ladders (Figure 7. 1) which contain a finite number of 1D magnetic chains coupled together. The magnetic understanding of these materials is limited as they display very unusual magnetic characteristics.

It was assumed that these intermediate compounds could show a theoretical transition between one and two-dimensional models of magnetism. However, the study of these compounds yielded surprising results that show a far from smooth transition.¹ It was found that when a 1D structure was extended to a ladder, a very unusual system occurs. With the apparent lack of any frustration within the system, the magnetism becomes dependant on whether there is an odd or even number of “legs” (number of chains). If there is an odd number of legs on the ladder the material behaves like the 1D chain showing gapless spin excitations. However when there is an even number of legs the material displays a spin liquid ground state with a finite energy gap.

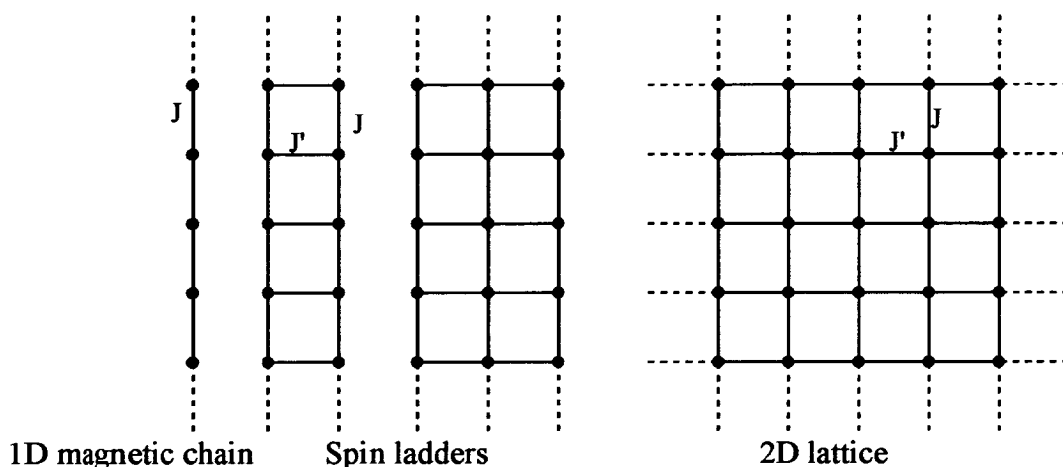


Figure 7. 1. schematic diagram of low dimensional magnetic lattices.

For clarity, a few terms used in the last paragraph will be defined. Magnetic frustration is a characteristic that occurs when magnetic centres interact in such a way that straightforward antiparallel coupling cannot be achieved, as there are conflicting coupling orientation preferences. Examples of such situations are shown in Figure 7. 2. A frustrated system can be identified by the fact that the Weiss constant may be up to 10 times larger than the ordering temperature, as long-range order is more difficult to achieve. Long-range order is usually achieved by adopting a configuration similar to Figure 7. 2c. However, in many frustrated materials long-range order is not achieved and a spin liquid ground state is formed. This is one of the alternating ground states that occurs in spin ladder systems and is thus why it is important to dispel the occurrence of a spin liquid state as a consequence of any frustration in the system. Spin liquid states have been called “cooperative paramagnets” as they behave like a paramagnetic system with a short-range order. Thus the spin system

mimics a molecular liquid with a dynamic system of spins randomly orientated over long-range, but ordered in the short-range with a finite spin gap.

The other magnetic state that occurs in spin ladders with an odd number of legs is a 1D chain and this is described in Chapter 1, section 1.2.5 with examples in section 1.3.1.

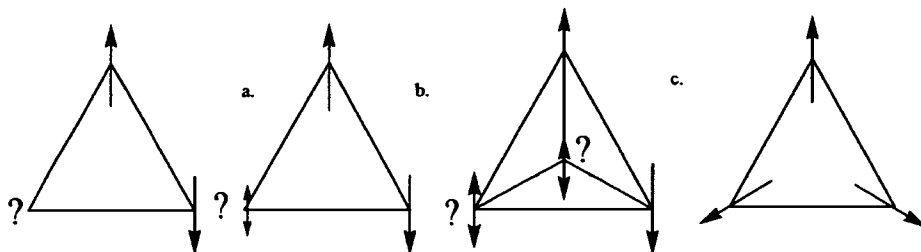


Figure 7. 2. Schematic representation of a frustrated magnetic system. a) equilateral triangular, b) tetrahedron, all showing fluctuation, c) triangular showing a long range order.

The majority of spin ladder systems synthesised to date have been based on the building blocks of CuO_4 as this square-planar configuration can be corner sharing or edge sharing to make up a ladder system. These are most commonly of the form $Sr_{n-1}Cu_{n+1}O_{2n}$ ($n = 3, 5, \dots$). They have very strong antiferromagnetic overlap, with a σ -overlap having a typical $|J/k| = 1500-2500$ K. Sr_2CuO_3 is the basic 3D starting point of ladder materials and this material has $|J/k| = 2200$ K. The planar forms of this material form the two and three legged ladder materials $SrCu_2O_3$ and $Sr_2Cu_3O_5$ respectively.^{2,3}

7.1.2 New molecular approach using modified dithiolenes ligands

The two spin ladder materials mentioned in the previous section ($SrCu_2O_3$ and $Sr_2Cu_3O_5$) were synthesised by high temperature solid-state chemical methods. Materials created by this synthetic route can have disadvantages as they form extended lattices with many fractures and defects. These materials are also very difficult to probe as they do not tend to be soluble or form single crystals. The synthetic method itself also limits the type of materials made as it gives very little control over the design of the product. Even $Sr_{n-1}Cu_{n+1}O_{2n}$ analogues $(VO)_2P_2O_7$ and $LaCuO_{2.5}$ have structures that suggest they may form spin ladders, but inelastic neutron scattering experiments showed that they do not.

A molecular approach opens the door to an extensive amount of new systems that could form spin ladders. This method also has the advantage of producing materials with features that make them much easier to probe, as molecular materials are generally more soluble and as such much easier to analyse and isolate as single crystals. There is also an added advantage that the magnetic coupling between intermolecular bonds are generally weaker than the chemical bonds that exist in lattice systems and this can be of great advantage when probing for some magnetic features (see section 4.1). The stoichiometric salt $[p\text{-EPYNN}][Ni(\text{dmit})_2]$ was the first molecular magnetic material to form a spin ladder system. In this material $[p\text{-EPYNN}]^+$ forms a one dimensional ferromagnetic chain whereas the $[Ni(\text{dmit})_2]^-$ units form the first molecular antiferromagnetic spin ladder.⁴

From this example it can be seen that the $(\text{dmit})^{2-}$ ligand $((C_3S_5)^{2-})$, when complexed, is a good candidate to form spin ladder materials. This is because dithiolenes

are planar and have extensive conjugation that can propagate magnetic interactions. The planarity means they generally form a stacked motif in the solid state. $(C_3S_5)^{2-}$ is a ligand rich in sulphur and these sulphur atoms can give large intermolecular overlap that can mediate strong magnetic interactions. From literature examples, this type of interaction can be mediated strongly through the stack and through side-by-side interaction, but not through the terminal sulphur atoms (see figure 7. 4). This is thought to be due to the symmetry of overlapping π orbitals (see Section 3.2.2).

There are very few molecular spin ladder materials at present⁵ because they are very difficult to produce since interaction must be limited to specific directions, with all other interaction being blocked. There is the danger that weak interactions may occur in unwanted directions. For example there are a few pseudo spin ladders that have additional weak interactions, such as the dithiolene salt $[(DT-TTF)_2][Au(mnt)_2]$ which has the configuration of a spin ladder but the interladder distance is relatively short and there is a small interaction between ladders.⁶

There are two ways to consider constructing a spin ladder. The first is to connect chain systems and the second is to stack up dimer molecules, illustrated in Figure 7. 3. The perfect spin ladder system would be the intermediate with interactions in both directions being very similar.

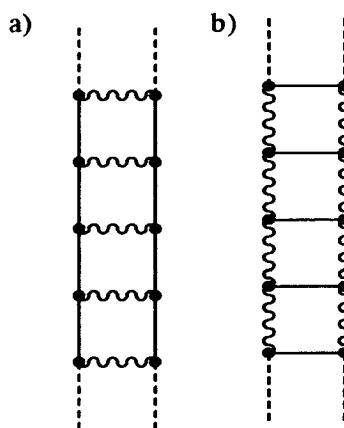


Figure 7. 3 Two synthetic strategies of crystallising a spin ladder a) joining 1D chains & b) connecting dimers.

This work will attempt to assemble spin ladders from modified $[M(\text{dmit})_2]^{x-}$ complexes as these show strong side-by-side and stacking interactions, so can form materials considered to be the perfect intermediate between the two models in figure 7. 3. To modify these complexes further to create a spin ladder material, a blocker must be added on one side of the $[M(\text{dmit})_2]^{x-}$, so only one side-by-side interaction can occur to form a dimer. This blocking unit will be an alkyl bridge between the two ligands so the stack will be the leg of the ladder with the dimer interaction forming the rung (figure 7. 4). Initially $M = \text{Cu}$ will be chosen, as the magnetic ion has 1 unpaired electron and this will simplify analysis of the magnetic data obtained. However, once an understanding of this system is obtained, analogous complexes containing other first row transition metals could be synthesised.

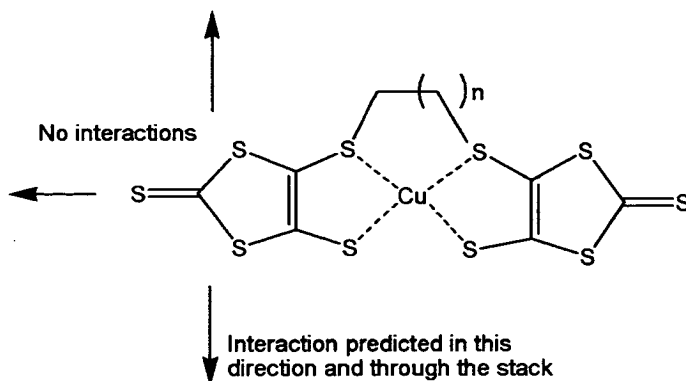


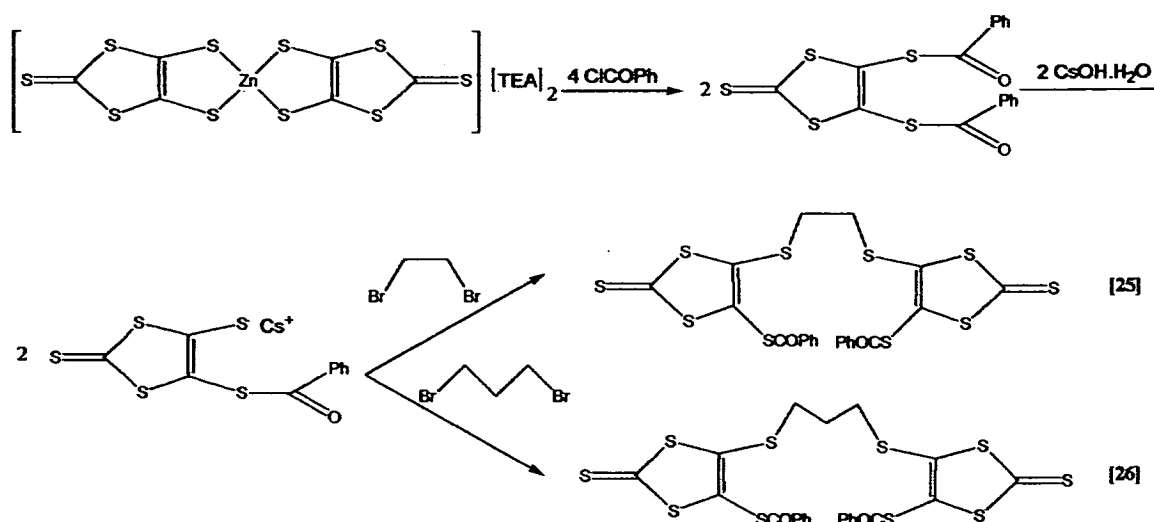
Figure 7.4. The general molecular design of the copper complex and the predicted directions of interaction to form dimer stacks

7.2 Results and discussion

7.2.1 Preparation and structure of ligands $(C_nH_{2n}(C_3S_5)_2)^{2-}$ ($n = 2$ & 3) ([25]-[28])

There are several proposed synthetic routes to this ligand in which various steps have been shown to be viable in the literature. The first synthesis attempted is shown in Scheme 7. 1. It involves the acylation of $[TEA]_2[Zn(dmit)_2]$, followed by the deprotection of one S^- to form the mono-cesium salt. The linking alkyl unit can then be bound at these sites to form $(C_nH_{2n}(C_3S_5(COPh))_2)$, ($n = 2$ and 3). The value of n is chosen as 2 and 3 to ensure that planarity of the ligand is maintained after complexation, as any longer bridges

could form several types of metal complexes, such as oligomeric and twisted forms.



Scheme 7.1 Synthetic route to [25] and [26]

The synthetic scheme was followed to produce $(C_3H_6(C_3S_5(COPh))_2)$ [26] in a low yield (32.7%) with the major product being the $C_6H_6S_5$ molecule 4,5-bis(propylthio)-1,3-dithiole-2-thione (Figure 7. 5). Unfortunately this preparation could not be used to synthesise the $(C_2H_4(dmit(COPh))_2)$ [25] analogue as the capped $C_5H_4S_5$ molecule, 4,5-bis(ethylthio)-1,3-dithiole-2-thione (Figure 7. 5) was found to be the major product with [25] being in such a minority it proved very difficult to separate, also due to similarities in solubility of the products.

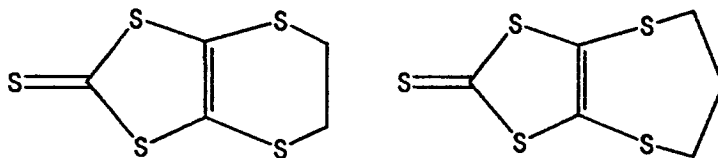
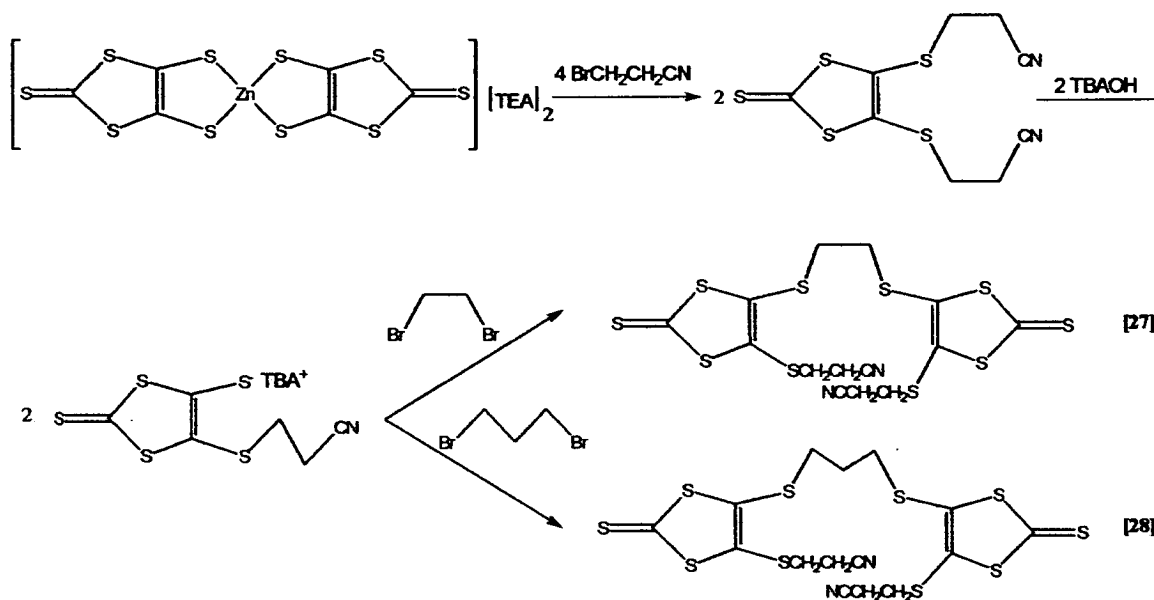


Figure 7.5. 4,5-bis(alkylthio)-1,3-dithiole-2-thiones

An alternative method to synthesise this ligand, which ultimately proved more successful, was to use a cyano intermediate synthesised by R. Berridge *et al*^{7, 8} shown in Scheme 7. 2. This differed by using $[TEA]_2[Zn(dmit)_2]$ to synthesise the $C_3S_5^{2-}$ ligand with cyano protecting groups, then deprotecting one S^- with base and adding the bridging group in one step. This method is an improvement on the previous one as it reduces the number of synthetic steps as well as only giving the desired compounds [27] and [28] as the major products. In contrast to the previous method the cyano protecting group is not as labile as the acyl group and is thus more difficult to remove, avoiding formation of a cyclic by-product.



Scheme 7. 2 Synthetic route to [27] and [28]

This method gave large crystalline yields of both [27] and [28]. Crystals large enough for single crystal X-ray diffraction were obtained for [28] and this structure is

shown in Figure 7. 6.

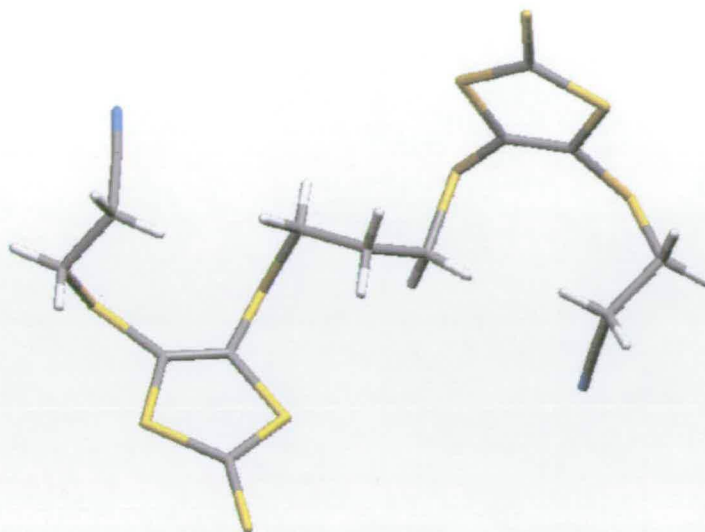


Figure 7. 6 Crystal structure of [28].

7.2.2 Preparation and structure of $[M(C_nH_{2n}(dmit)_2)]$ [29]-[32] (M = Cu, n = 2 [29], 3 [30]. M = Fe, n = 2 [31], 3 [32])

The complexation reaction of both [27] and [28] with $CuCl_2$ to form [29] and [30] involved a straightforward deprotection with base followed by the addition of $CuCl_2$. Upon the addition of EtOH, a red precipitate formed that was found to be the product. This was also true for the formation of [31] and [32] with $FeCl_2$.

Other complexation reactions, that were not so straightforward, were attempted with $MnCl_2$ and $CoCl_2$. It appeared that these metals preferred a higher oxidation state and would not precipitate out of solution. Counterions were added but the products proved very

difficult to work up and purify.

All four products [29]-[32] were obtained analytically pure directly from the reaction mixture and only needed washing. This was fortunate as they were found to be very insoluble with [29] being the most insoluble (only soluble in DMF) and [32] being most soluble (in DMF, CS₂ and partially soluble in many common solvents). The trend seems to be that the Fe²⁺ complexes have greater solubility than the Cu²⁺ complexes and n = 3 complexes are more soluble than n = 2 complexes leading to a solubility of [32] > [31] ≅ [30] > [29]. Crystallisations of [29]-[32] were attempted by numerous methods, such as slow precipitation from DMF, and slow *in situ* diffusion of the deprotected ligand and MCl₂. In all cases only very fine powders were obtained. Attempts to obtain structural information from the powders were executed using powder X-ray diffraction. The typical powder pattern of [30] (shown in Figure 7. 7) is representative of all four materials. The powder pattern has a broad characteristic peak of an amorphous material with only very small peaks from a crystalline phase. It can thus be concluded that the majority phase of these materials is amorphous which shows that no long-range order is achieved in the majority of the material and thus no long-range, crystalline, spin ladder system can be identified.

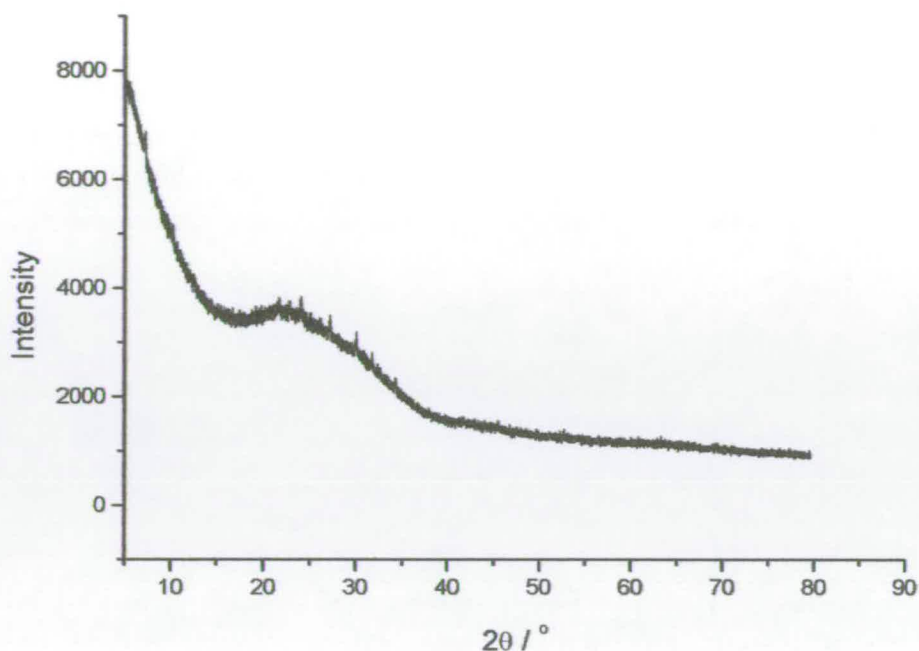


Figure 7. 7. X-ray powder diffraction pattern of [30]

7.2.3 Magnetic and EPR analysis

As no structural data have been obtained, analysis of magnetic data for [29]-[32] is speculative. Magnetic data were collected for [29]-[32] and are shown in Figures 7. 8 -7. 11. EPR data were also collected for [29]-[32] and each was EPR silent. This could be due to rapid exchange between interacting spin centres.

The magnetic data generally can be described as a curve with a broad peak/shoulder occurring at approximately 30 K. This peak shows that magnetic intermolecular interactions are occurring within the material. The presence of an increase in susceptibility

at low temperatures show that there is also a degree of Curie-Weiss paramagnetism in the material. Thus the magnetic data were fitted to a mixed model incorporating elements of the Curie-Weiss model for a simple paramagnet, and the Bleaney-Bowers dimer interaction model, as this is the simplest model to represent interacting magnetic spins. Parameter x and y are included to give the percentage amount of each model present. The overall model is shown in Equation 7.1

$$\chi = x \left(\frac{C}{T - \theta} \right) + y \left(\frac{2Ng^2\beta^2}{3kT} \right) \left[\frac{1}{1 + \frac{1}{3} \exp\left(\frac{-2J}{kT}\right)} \right] + (1 - x - y) \text{Dimagnetism} \quad \text{Equation 7.1}$$

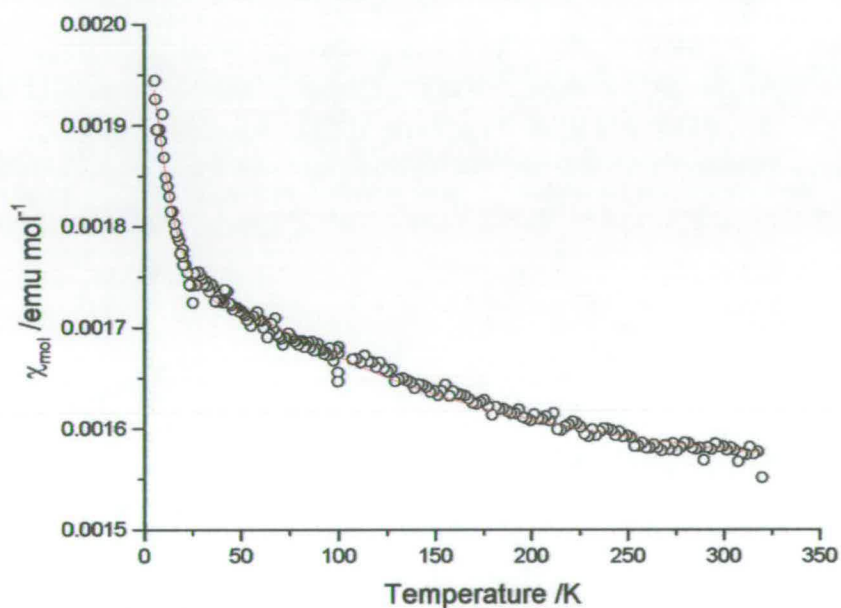


Figure 7.8. Molar magnetic susceptibility χ_{mol} vs temperature of [29] \circ = experimental data (1.8-320 K)

— = fit to $\chi_M(T) = x\chi_{Curie\ Weiss} + y\chi_{Bleaney-Bowers}$. Parameter shown in table 7.1.

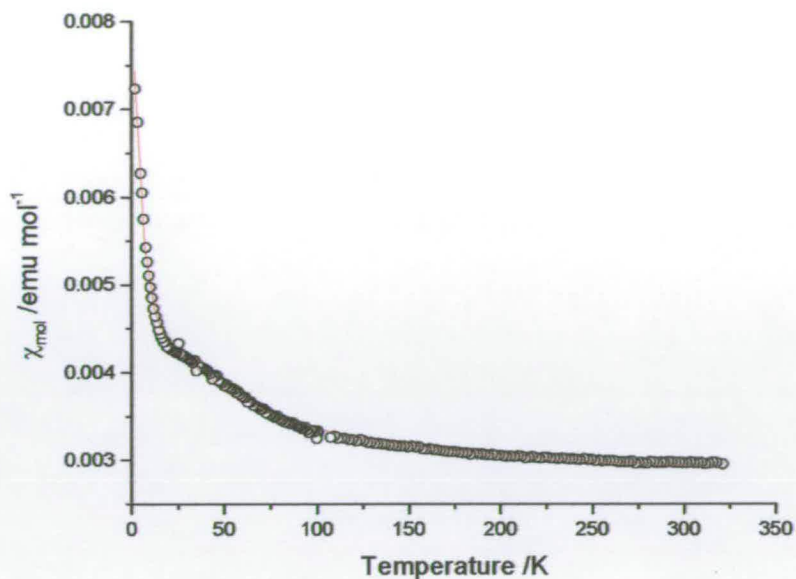


Figure 7. 9. Molar magnetic susceptibility χ_{mol} vs temperature of [30] \circ = experimental data (1.8-320 K)

— = fit to $\chi_M(T) = x \chi_{Curie Weiss} + y \chi_{Bleaney-Bowers}$. Parameter shown in table 7.1.

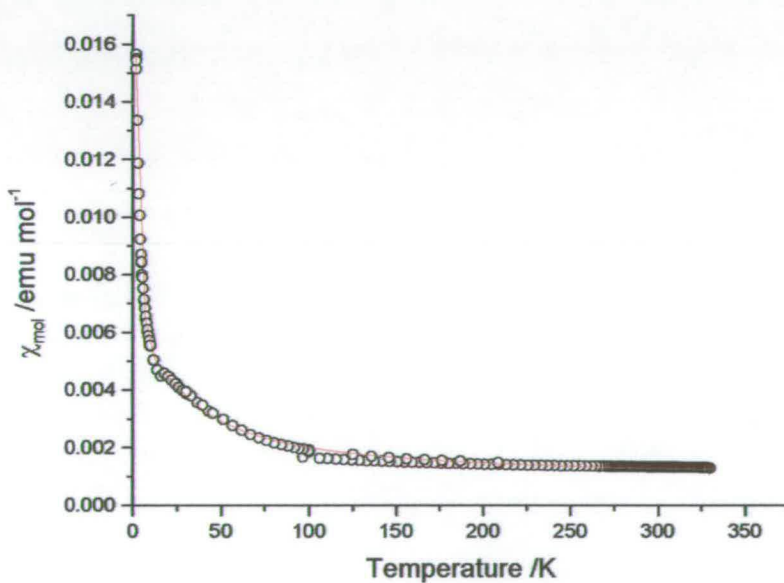


Figure 7. 10. Molar magnetic susceptibility χ_{mol} vs temperature of [31] \circ = experimental data (1.8-320

K) — = fit to $\chi_M(T) = x \chi_{Curie Weiss} + y \chi_{Bleaney-Bowers}$. Parameter shown in table 7.1.

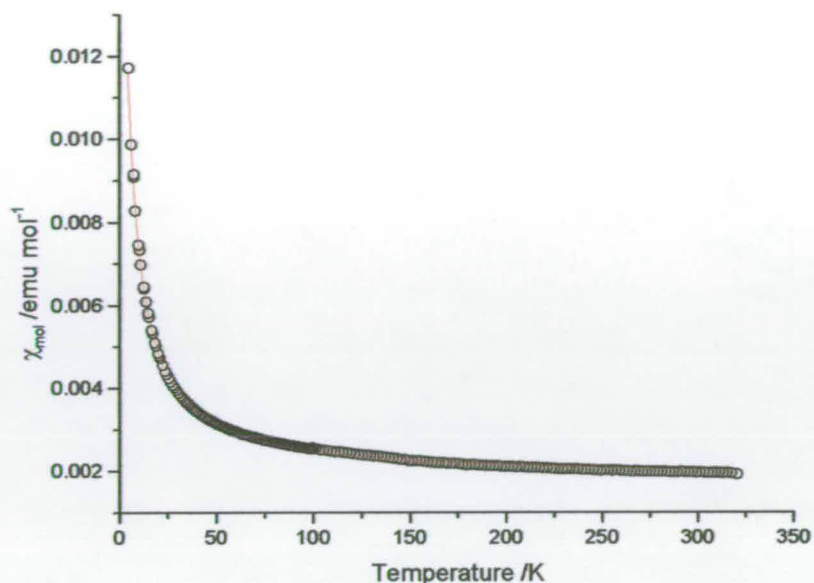


Figure 7. 11. Molar magnetic susceptibility χ_{mol} vs temperature of [32] \circ = experimental data (1.8-320

K) — = fit to $\chi_M(T) = x \chi_{Curie Weiss} + y \chi_{Bleaney-Bowers}$ Parameter shown in table 7.1.

Material			C /emu K mol ⁻¹	θ /K	Curie Weiss %	J/k /K	Bleaney- Bowers %	Diamagnetic %
M	n	name						
Cu	2	[29]	0.375	-18.0	2.7	-67.6	2.0	95.3
	3	[30]	0.375	-5.7	9.9	-34.6	6.5	83.6
Fe	2	[31]	1	-1.2	5.1	-18.6	8.5	86.4
	3	[32]	1	-1.3	4.2	-0.5	6.1	89.7

Table 7. 1. Summary of parameters used to fit figures 7.9-7.12 to the mixed model $\chi_M(T) = x \chi_{Curie Weiss} + y \chi_{Bleaney-Bowers}$

It is worth noting that this model requires six parameters and so to obtain a more realistic fit the value of g was fixed to 2 throughout, which also fixed the value of C if the spin-only values are used. Thus the number of variable parameters are reduced to four and are shown in Table 7. 1. The most striking observation for all four materials is the very large diamagnetic component (83-95%). This fact suggests that the majority of these

mainly amorphous materials do not contain discrete units but are forming intermolecular bonds; either dimerising or forming much more complex structural motifs that allow strong M-M bonding, forming a predominately diamagnetic material. As the material is amorphous, no further conclusions can be drawn. However, it is interesting to note that the strength of coupling between magnetic centres obtained from the Bleaney-Bowers fit shows the copper samples to have a greater value than the iron with $n = 2$ having a larger coupling than $n = 3$. Although these actual values are of limited significance without structural data they do mimic the same trend as the solubility of the products. These trends are probably due to the fact that Cu^{2+} and $n = 2$ compounds have a greater ability to form more rigid planar complexes. Planar complexes are known for poor solubility as well as being able to forming strong intermolecular bonds between M—S on adjacent complexes. If the bond is strong enough a diamagnetic complex can be formed. Iron complexes do not have such a strong preference to form square-planar compounds as well as the fact that the compounds with $n = 3$ have much more flexibility. Thus any intermolecular coupling will be weaker. This is most evident for [32] where J is so small that there is no visible broad peak.

7.3 Conclusion

Attempts to synthesise molecular spin ladders based on dithiolene complexes were undertaken, as dithiolenes have already yielded spin ladder systems. Materials were synthesised using Cu^{2+} and Fe^{2+} complexes of alkyl bridged (C_3S_5) ligands. Unfortunately, the materials were found to be mainly amorphous with structural data being impossible to

obtain. This also meant that the desired long-range ordered spin ladders structure was not obtained in the materials. The magnetic data show that the majority of the four compounds are diamagnetic with a signal showing a Curie tail with some aspect of intermolecular interactions. The evidence suggests that there is little or no structural order within the four materials and as such little to no information can be gleaned from the magnetic data.

7.4 Experimental

7.4.1 $(Et_4N)_2[Zn(dmit)_2]$ ⁹

Synthesis CS₂ (240ml, 303.84g, 4 mol) was dissolved in DMF (480ml, 451.2g). The vessel was cooled to 0°C under N₂ and stirring was maintained via an overhead mechanical stirrer. Na (14.5g, 0.63 mol) was then added over 6 hours in the form of thin flakes. The solution turned red and was stirred overnight. Any remaining Na was destroyed by addition of MeOH (100ml), then MeOH/H₂O (100ml), then H₂O (100ml). A solution of ZnCl₂ (21.3g in NH₃ solution (360ml) and H₂O (100ml)) was then added over an hour, followed by a solution of Et₄NBr (66g in H₂O (500ml)) added dropwise over 2 hours giving a bright red precipitate. This was left to stir overnight, and the product was filtered off and washed with propan-2-ol then ether. (Yield 78.68g, 76%).

Analysis CHN for C₂₂H₄₀N₂S₁₀Zn. Calculated; C, 36.77; H, 5.61; N, 3.90. Found; C, 37.18; H, 5.76; N, 3.69 %

7.4.2 (COPh)₂(C₃S₅)¹⁰

Synthesis (Et₄N)₂[Zn(dmit)₂] (16g, 0.014 mol) was dissolved in acetone (200ml) and filtered to remove some yellow impurity. C₆H₅COCl (40ml, 48.44g, 0.35 mol) was added dropwise to the filtrate overnight, under N₂. A yellow precipitate was formed and this was filtered off and washed with acetone. The solid was refluxed in CHCl₃ (100ml) and filtered while hot. An excess of EtOH was added to the filtrate. The precipitate was then filtered and washed with EtOH Et₂O. (Yield 13.15g, 64.78%).

Analysis CHN C₁₇S₅O₂H₁₀ calc. C 50.2 H 2.46 found C 51.1 H 2.36, ¹H NMR (CDCl₃/TMS): δ = 7.95 (m, 2H), 7.65 (m, 1H), 7.5 (m, 2H), MS m/z⁺ 407.

7.4.3 [Cs⁺][(COPh)(C₃S₅)]⁻¹¹

Synthesis (COPh)₂(dmit) (0.812g, 0.002 mol) was dissolved in CHCl₃ (20ml) under N₂. To this, a solution of CsOH.H₂O (0.34g, 0.002 mol) in MeOH (4ml) was added. The solution turned dark red then orange. After 30 sec. a yellow precipitate formed and Et₂O was added (60ml). The solid was filtered off, washed with Et₂O and dried in air. (Yield 0.84g, 96.8%).

Analysis C₁₀S₅H₅OCs calc. C 27.65 H 1.15 found. C 28.13 H 1.10, ¹H NMR (CDCl₃/TMS): δ = 7.95 (m, 2H), 7.7 (m, 1H), 7.55 (m, 2H), ¹³C NMR (CDCl₃/TMS): δ = 135.79, 134.27, 129.49, 129.37, 127.13, 40.61, 40.27, 39.94, 39.61, 39.27, 38.94, 38.61),

MS $mz^+ = 133$ $mz^- = 301$

7.4.4 $[C_2H_4((C_3S_5)COPh)_2]$ [25]

Synthesis $[Cs][[(COPh)(dmit)]]$ (0.1g, 0.00023 mol) was dissolved in EtOH (8ml) under N_2 . A solution of 1,2-dibromoethane (0.0216g, 0.01ml, 0.000115 mol) in EtOH (10ml) was added dropwise over 10 hours and stirred for 24 in total. Solvent was reduced to $\frac{1}{3}$ volume and an excess of H_2O was added. The precipitate was collected by filtration and re-dissolved in DCM and H_2O . The remaining solid was removed by filtration. The solvent was removed by rotary evaporation from the remaining filtrate and the resulting solid was collected (Yield 0.012g, 1.9×10^{-5} mol, 16.5%).

Analysis CHN $C_{22}S_{10}O_2H_{14}$ calc. C 41.9, H 2.22 found C 45.25 H 2.71, 1H NMR ($DCCl_3/TMS$): $\delta = 8.05$ (m. 4.25H), 7.8 (m. 2.125H), 7.6 (m. 4.25H), 3.41 (s. 1H) 1.65 (s. 0.75H)) Mpt. $118^\circ C$,

7.4.5 $[C_3H_6((C_3S_5)COPh)_2]$ [26]

Synthesis Procedure as 7.4.4, but using 1,3-dichloropropane (0.058g, 0.000288 mol) (instead of 1,2-dibromoethane) in EtOH (10ml). (Yield: 0.0606g, 0.000094 mol, 32.7%).

Analysis CHN $C_{23}S_{10}O_2H_{16}$ calc. C 42.8, H 2.48, found C 41.46, H 2.27, 1H NMR

(DCCl₃/TMS): $\delta = 7.9$ (m. 4H), 7.55 (m. 2H), 7.32 (m. 4H), 2.75 (t. 4H) 2.4 (q. 2H)

7.4.6 $[Cu(C_3H_6(C_3S_5)_2)]$ from $[C_3H_6((C_3S_5)COPh)_2]$ [30]

Synthesis $C_3H_6((C_3S_5)COPh)_2$ (0.04g, 6.21×10^{-5} mol) was dissolved in MeOH (10ml) under N₂ and stirred. NaOMe (0.00671g (1.24×10^{-4} mol) in MeOH (3ml)) was added followed by CuCl₂ (0.00835g, 6.21×10^{-5} mol) dissolved in MeOH (3ml). A dark precipitate formed and this was removed by filtration and washed with MeOH and DCM. (Yield: 0.0064g, 20.72%),

Analysis CHN C₉S₁₀H₆Cu calc. C 21.7, H 1.2, found C 18.61, H 0.51.

7.4.7 $(C_2H_4CN)_2(C_3S_5)^{12}$

Synthesis (Et₄N)₂[Zn(dmit)₂] (4.32g, 0.006 mol) was dissolved in MeCN (100ml) and filtered to remove some yellow impurity. 3-bromopropionitrile (2.49ml, 4.02g, 0.03 mol) was added to the filtrate and refluxed for 1 hour under N₂. This was then cooled to room temperature and the inorganic salts were removed by filtration. The filtrate was concentrated by rotary evaporation and redissolved in DCM. This was then washed 4x with water and dried over MgSO₄. DCM was then removed and the solid produce was then recrystallised from toluene/petroleum ether. (Yield 3.093g, 84.5%).

Analysis CHN C₉ H₈N₂S₅ calc. C 35.53 H 2.63 N 9.21 found C 35.46 H 2.59 N

8.89%, $^1\text{H NMR}$ (CDCl_3/TMS): $\delta = 3.16$ (t, 4H), 2.76 (t, 4H), , MS mz^+ 305.

7.4.8 $[\text{C}_2\text{H}_4((\text{C}_3\text{S}_5) \text{C}_2\text{H}_4\text{CN})_2]$ [27]^{7, 12}

Synthesis $[(\text{C}_2\text{H}_4\text{CH})_2(\text{C}_3\text{S}_5)]$ (0.2g, 0.00066 mol) was dissolved in THF (30ml) under N_2 and cooled to -5°C . Tetrabutylammonium hydroxide (0.79 ml of 1M solution in MeOH) was added in MeOH (10ml) over 20mins and the solution turned purple. A solution of 1,2-dibromoethane (0.062g, 0.0284 ml, 0.00033 mol) in MeOH (10ml) was added dropwise and stirred for 16 hours at room temperature. The solvent was reduced to minimal volume then re-dissolved in DCM. This was then filtered and the filtrate was layered with EtOH and placed in the freezer overnight. Yellow crystalline solid was then collected by filtration and washed with EtOH and Ether. (Yield 0.092g, 1.74×10^{-4} mol, 52.8%).

Analysis CHN $\text{C}_{14}\text{H}_{12}\text{N}_2\text{S}_{10}$ calc. C 31.79, H 2.29, N 5.30 found C 31.56, H 2.18, N 5.12% $^1\text{H NMR}$ (DMSO/TMS): $\delta = 3.31$ (s, 4H), 3.26 (4. 4H), 2.94 (t, 4H), MS mz^+ 529

7.4.9 $[\text{C}_3\text{H}_6((\text{C}_3\text{S}_5) \text{C}_2\text{H}_4\text{CN})_2]$ [28]^{7, 12}

Synthesis $[(\text{C}_2\text{H}_4\text{CH})_2(\text{C}_3\text{S}_5)]$ (0.4g, 0.00131 mol) was dissolved in THF (50ml) under N_2 and cooled to -5°C . Tetrabutylammonium hydroxide (1.58 ml of 1M solution in MeOH) was added in MeOH (10ml) over 20mins and the solution turned purple. A

solution of 1,3-dibromopropane (0.133g, 0.00066 mol) in MeOH (10ml) was added dropwise and stirred for 16 hours at room temperature. The solution was rotary evaporated to dryness then re-dissolved in DCM. This was layered with EtOH and placed in the freezer overnight. A yellow sticky solid was then collected by filtration and washed with EtOH and Ether. (Yield 0.221g, 4.077×10^{-4} mol, 61.8%).

Analysis CHN $C_{15}H_{14}N_2S_{10}$ calc. C 33.18, H 2.60, N 5.16 found C 33.12, H 2.52, N 4.56% NMR 1H NMR ($CDCl_3/TMS$): $\delta = 3.05$ (m, 8H), 2.70 (t, 4H), 2.0 (q, 4H), MS mz^+ 543

7.4.10 $[Cu(C_2H_4(C_3S_5)_2)] [29]$ from $[C_2H_4((C_3S_5)C_2H_4CN)_2]$

Synthesis $C_2H_4((C_3S_5)C_2H_4CN)_2$ (0.05g, 9.47×10^{-5} mol) was dissolved in THF (10ml) under N_2 and stirred. Tetramethylammonium hydroxide (0.189 ml of 1M solution in MeOH (1.89×10^{-4} mol)) in MeOH (3ml) was added and stirred for 1 hour and the solution turned red. The a solution of $CuCl_2$ (0.0127g, 9.47×10^{-5} mol) dissolved in THF (5ml) and a drop of MeOH was then added over 1 hour. An excess of EtOH was added and a red precipitate formed in a yellow solution. The solid was collected by centrifugation and washed with EtOH and ether. (Yield: 0.0089g, 19.28%)

Analysis $C_8H_4S_{10}Cu$ calc. C 19.85, H 0.83, found C 20.61, H 1.29.

7.4.11 [Cu(C₃H₆(C₃S₅)₂)] [30] from [C₃H₆((C₃S₅)C₂H₄CN)₂]

Synthesis C₃H₆((C₃S₅)C₂H₄CN)₂ (0.05g, 9.225x10⁻⁵ mol) was dissolved in THF (10ml) under N₂ and stirred. Tetramethylammonium hydroxide (0.1845 ml of 1M solution in MeOH (1.845x10⁻⁴ mol)) in MeOH (3ml) was added and stirred for 1 hour and the solution turned red. A solution of CuCl₂ (0.012g, 9.22x10⁻⁵ mol) dissolved in THF (5ml) and a drop of MeOH was added over 1 hour. An excess of EtOH was added and a red precipitate formed in a yellow solution. The solid was collected by centrifugation and washed with EtOH and ether. (Yield: 0.033g, 71.9%)

Analysis CHN C₉H₆S₁₀Cu calc. C 21.7, H 1.2, found C 21.37, H 1.31.

7.4.12 [Fe(C₂H₄(C₃S₅)₂)] [31] from [C₂H₄((C₃S₅)C₂H₄CN)₂]

Synthesis Procedure as 7.4.10, but replace CuCl₂ with FeCl₂ (0.012g, 9.47x10⁻⁵ mol). Yellow product. (Yield: 0.021g, 4.3 x 10⁻⁵ mol, 45.6%).

Analysis CHN C₈H₄S₁₀Fe calc. C 20.16, H 0.85, found C 21.51, H 1.12.

7.4.13 [Fe(C₃H₆(C₃S₅)₂)] [32] from [C₃H₆((C₃S₅)C₂H₄CN)₂]

Synthesis Procedure as 7.4.11, but replace CuCl₂ with FeCl₂ (0.012g, 9.47x10⁻⁵ mol). Yellow product. (Yield: 0.031g, 6.28 x 10⁻⁵ mol, 66.3%).

Analysis C₉H₆S₁₀Fe calc. C 22.03, H 1.23, found C 23.52.37, H 1.59.

7.5 References

- 1 E. Dagotto and T. M. Rice, *Science*, 1996, **271**, 618.
- 2 C. Berthier, L. P. Levy, G. Martinez, and Editors, 'High Magnetic Fields: Applications in Condensed Matter Physics and Spectroscopy. [In: Lect. Notes Phys., 2002; 595]', 2002.
- 3 S. Haddad, S. Charfi-Kaddour, M. Heritier, and R. Bennaceur, *J. de Phys IV: Proc.*, 2000, **10**, Pr3/225.
- 4 H. Imai, T. Inabe, T. Otsuka, T. Okuno, and K. Awaga, *Phys. Rev. B: Condens. Matter*, 1996, **54**, R6838.
- 5 C. Rovira, *Struct. & Bond.*, 2001, **100**, 163.
- 6 C. Rovira, *Chem.-Europ. J.*, 2000, **6**, 1723.
- 7 D. W. Allen, R. Berridge, N. Bricklebank, E. Cerrada, M. E. Light, M. B. Hursthouse, M. Laguna, A. Moreno, and P. J. Skabara, *J. Chem. Soc., Dalton Trans.*, 2002, 2654.
- 8 R. Berridge, N. Bricklebank, D. W. Allen, P. J. Skabara, K. M. A. Malik, S. J. Coles, and M. B. Hursthouse, *Synth. Met.*, 2001, **120**, 1023.
- 9 C. S. Wang, A. S. Batsanov, M. R. Bryce, and J. A. K. Howard, *Synthesis*, 1998, 1615.
- 10 T. K. Hansen, J. Becher, T. Jorgensen, K. S. Varma, R. Khedekar, and M. P. Cava, *Organic Syntheses*, 1996, **73**, 270.
- 11 S. Zeltner, R.-M. Olk, M. Wagner, and B. Olk, *Synthesis*, 1994, 1445.
- 12 N. Svenstrup, K. M. Rasmussen, T. K. Hansen, and J. Becher, *Synthesis*, 1994, 809.

Chapter 8

Appendices

Appendices are on CD in the envelope inside the back cover.

List of Publications

Sarah S. Staniland; Wataru Fujita; Yoshikatsu Umezono; Kunio Awaga; Philip J. Camp; Stewart J. Clark and Neil Robertson. **[BDTA]₂[Cu(mnt)₂]: An Almost Perfect One-Dimensional Magnetic Material.** *Inorganic Chemistry* (2005), 44(3), 546-551. CODEN: INOCAJ ISSN:0020-1669. CAN 142:308599 AN 2005:27001 CAPLUS

Sarah S. Staniland; Wataru Fujita; Yoshikatsu Umezono; Kunio Awaga; Stewart J. Clark; HengBo Cui; Hayao Kobayashi; and Neil Robertson **A unique new multiband molecular conductor: [BDTA][Ni(dmit)₂]₂.** *Journal of the Royal Society of Chemistry; Chemical Communication.* (2005) (In press.)

Sarah S. Staniland. **Magnetic Properties of New Metal Dithiolene-Dithiazolyl Salts.** Conference Oral presentation. *ICCC36*, 2004, Merida, Mexico,